Development of Dual-Phase Oxygen Transport Membranes for Carbon Capture Processes

Pirou, Stéven; Kiebach, Wolff-Ragnar; Hendriksen, Peter Vang; Kaiser, Andreas

Publication date:
2017

Document Version
Publisher's PDF, also known as Version of record

Development of Dual-Phase Oxygen Transport Membranes for Carbon Capture Processes

Ph.D Dissertation

By

Stéven Pirou

In partial fulfilment of the requirements for the degree of Ph.D

Department of Energy Conversion and Storage

Technical University of Denmark

September 2017

Preface

This thesis is the result of the PhD study “Development of Dual-Phase Oxygen Transport Membranes for Carbon Capture Processes” conducted from September 15th 2014 to September 14th 2017 and submitted to the Technical University of Denmark.

The study was part of the project entitled “Graded Membranes for Energy Efficient New Generation Carbon Capture Process (GREEN-CC)” financed by the European Union (Grant agreement no. 608524). The aim of the GREEN-CC project was to demonstrate a high-efficiency carbon capture process based on oxy-fuel combustion. To achieve this, thermally integrated separation modules based on ceramic oxygen transport membranes (OTMs) have been developed for the oxygen production. This thesis focuses on (i) the development of thin (10-20 μm) dual-phase membranes, and (ii) oxygen permeation tests of the developed membranes in conditions expected in power plants.

The work presented in the thesis was carried out at three places. Most of the research took place at the Technical University of Denmark in the Department of Energy Conversion and Storage (Section for Mixed Conductors), under the main supervision of Senior Researcher Martin Søgaard (September 2014 – April 2015) and Senior Researcher Ragnar Kiebach (May 2015-September 2017), and the co-supervision of Professor Peter Vang Hendriksen and Senior Researcher Andreas Kaiser. Three months (October 2016 – December 2016) were spend at the Institute of Chemical Technology, a research centre created by the Politechnic University of Valencia and the Spanish National Research Council (in Spanish: Consejo Superior de Investigaciones Científicas). During this period, work related to the improvement of the performance of the OTMs was conducted in the group of Professor José M. Serra. Finally, a two-month collaboration (March 2017 – April 2017) took place at the Korea Institute of Energy Research (KIER) in the group of Dr. Ji Haeng Yu. During this period, thin supported membranes were optimized and tested.

Acknowledgements

First, I would like to express my sincere gratitude to my supervisors: Dr. Martin Søgaard and Dr. Ragnar Kiebach. Thank you Martin for giving me the opportunity to join DTU, first as a visiting Master student, and later as a PhD student. I appreciated your guidance, your patience and your sincerity. I have been fortunate to receive your advices, which put me on good tracks for my PhD. Thank you Ragnar for accepting to become my supervisor after Martin's departure, you have been a great supervisor, always available giving me many wise advices. Thank you for your dynamism and your optimism, which made my working environment very pleasant. I appreciated all our discussions at Risø or abroad, scientific or not.

Beside my supervisors, I would like to thank my co-supervisors: Prof. Peter Vang Hendriksen and Dr. Andreas Kaiser, for their insightful comments and encouragement, for answering my questions during my supervisor meetings and for bringing new questions to answer. Thank you for your valuable scientific advices making our meetings very fruitful.

I also would like to thank the GREEN-CC project, funded from the European Community's Seventh Framework Program. This project gave me the opportunity to meet formidable scientists and persons, with who I learnt a lot. Among all research groups, I would like to thank the people from *Instituto de Tecnología Química (UPV-CSIC)*, *Imperial College*, *Forschungszentrum Jülich* and *Ricerca sul Sistema Energetico (RSE S.p.A.)*, which are the people I worked with the most.

My thanks and regards shall go to Prof. José M. Serra from the *Instituto de Tecnología Química* of the Politechnic University of Valencia. Thank you for offering me the opportunity to come and work in your group. I had a very good experience from it, both academically and personally. Many thanks to all the post-docs and PhDs, you made me feel very comfortable at ITQ from the first to the last day of my stay in Valencia. Special thanks to María Belaguer, which helped me planning my external stay and performed some experiments with me, and to Julio García-Fayos, for guiding me from the beginning to the end of my stay in Valencia. I really appreciated your help, both in the lab and outside.

My sincere thanks also goes to Dr. Ji Haeng Yu form the *Korea Institute of Energy Research (KIER)*. Thank you for enabling me to work in your group for two months. I have been very

lucky to work with you and learn from your knowledge on ceramic processing. I fully enjoyed my stay in Korea, both academically and personally. It was a great chance for me to learn scientifically in a great laboratory, while in a same time discovering a new culture. Many thanks to Beom Tak Na, for your great help, both at work and outside. If you come in Europe for your PhD, I hope to be able to help you as much as you helped me.

My acknowledgment also goes to DTU colleagues. Thanks to Jonas, Vanesa, Astri, Shiyang, Simona, Karen, Søren F., etc. for your help, discussions, advices and the good moments spent together. Special thanks to Jens F.S. Borchsenius, which always repaired the membrane testing rigs after that I broke them (sorry for that), and to Henrik Paulsen, which put a billion of membrane samples in epoxy for me (sorry for that too). Many thanks also to our awesome secretary Heidi Adler Berggren for helping me in diverse tasks and for always finding answers to my questions.

Many thanks to all my PhD friends: Yu, Christophe, Kosova, Fabrizio, Megha, Alexandra, Jan, Roberto, Ilaria, Katrine, Salvo, Lev, etc. for all the lunches, coffee breaks, Friday bar and other good moments spent together.

Finally my deepest acknowledgement and love to my parents and my brother for their support and love, which are very precious to me, also for understanding and accepting my choice of studying abroad for more than three years. I extend my acknowledgment to all my friends and family in France, for understanding my distance and lack of communication, and to Julia for her wonderful support, comprehension and love, which give me a lot of strength and energy.

Stéven Pirou

Roskilde, Denmark, September 2017

Abstract

Fossil fuel based power plants and industrial production of cement and steel are major sources of anthropogenic CO_2 emissions. One of the most promising approaches to capture and store CO_2 from such large point sources is the oxy-fuel combustion route, where pure oxygen instead of air is used in the combustion, which greatly facilitates the down-stream CO_2 capture. The main energy penalty for the oxy-fuel process is related to the production of the oxygen, which today commonly is done in cryogenic air separation units (ASUs). An alternative approach, which requires significant less energy is the use of oxygen transport membranes (OTMs), which has the potential to reduce the cost and energy penalty associated with the CO_2 capture and storage.

This thesis focusses on the development and characterization of highly efficient and chemically stable planar asymmetric OTMs for direct integration in oxy-fuel combustion power plants. For the case of direct integration considered here the permeate side of the OTMs will be swept with recirculated flue gas whereby a driving force for oxygen transport through the membrane, which is fed with air on the other side, is directly established. It further facilitates thermal integration and thermal management in the combustion and avoids the need to handle pure oxygen. However, a direct integration scheme impose quite severe conditions on the membrane materials, such as stability towards both CO_2 and SO_2 and at low pO_2 (1-10 mbar).

The development of planar asymmetric membranes in this work, required the parallel development of (i) stable porous supports, (ii) thin dense membrane layers, (iii) porous catalytic backbones and (iv) meso-porous nano-particulate catalytic coatings. For the dense membrane layers, dual-phase composites consisting of a stable ionic and a stable electronic conductor were used to overcome the stability limitations commonly observed with single-phase membrane materials (e.g. $La_{1-x}Sr_xCo_{1-y}Fe_yO_{3-\delta}$ (LSCF), $Ba_{1-x}Sr_xCo_{1-y}Fe_yO_{3-\delta}$ (BSCF)) in CO_2 and SO_2. Three composite materials, $(ZrO_2)_{0.89}(Y_2O_3)_{0.01}(Sc_2O_3)_{0.10}$ - $MnCo_2O_4$ (10Sc1YSZ-MCO), $(ZrO_2)_{0.89}(Y_2O_3)_{0.01}(Sc_2O_3)_{0.10}$ - $Al_{0.02}Zn_{0.98}O_{1.01}$ (10Sc1YSZ-AZO) and $(ZrO_2)_{0.89}(Y_2O_3)_{0.01}(Sc_2O_3)_{0.10}$ - $LaCr_{0.85}Cu_{0.10}Ni_{0.05}O_{3-\delta}$ (10Sc1YSZ-LCCN) were

prepared and applied in planar dual-phase asymmetric OTMs and finally characterized and tested in clean as well as flue-gas like atmospheres.

The work dedicated to 10Sc1YSZ-MCO (70-30 vol.%) dual-phase membranes entailed development and characterisation of of 7 µm thin asymmetric membranes supported on zirconia supports as well as 0.5 mm thick self-standing membranes. The thin asymmetric membranes were prepared by tape-casting, lamination, and fired in a two-step sintering process in order to obtain fully dense thin membrane layers in a sintering regime that avoids excessive Co and Mn diffusion and/or decomposition of the MCO phase. Long-term stability tests over 1700 h in pure CO_2 and 170 h in oxy-fuel conditions (250 ppm of SO_2, 3 vol.% of H_2O, 5 vol.% of O_2 balanced with CO_2) demonstrated the stability of the composite membranes under relevant application conditions. Oxygen permeation fluxes of 1.41 $mL_N\ cm^{-2}\ min^{-1}$ and 2.23 $mL_N\ cm^{-2}\ min^{-1}$ at 940 °C in air/N_2 and O_2/N_2 atmospheres, respectively, were obtained. To further improve the membrane performance, catalytic surface layers were developed and tested by electrochemical impedance spectroscopy (EIS). Oxygen permeation tests were realized on 10Sc1YSZ-MCO (70-30 vol.%) membranes coated with these porous catalytic layers. The tests demonstrated that layers based on mixed ionic and electronic conducting backbones worked best (e.g. $Ce_{0.8}Tb_{0.2}O_{2-\delta}$ (CTO)-$NiFe_2O_4$ (NFO) (40-60 vol.%)); increases in the oxygen permeation of about 50 % were observed for membranes coated with a such compared to those based on purely ionically conducting backbones.

10Sc1YSZ-AZO (50-50 vol.%) dual-phase composite membranes were also developed and characterized as thick (1 mm) self-standing membranes and thin (8 µm) supported membranes. The stability of these membranes in gas streams containing CO_2, SO_2 and H_2O was found to be excellent. However, the high volatility of the Zn in the AZO phase under mildly reducing atmospheres makes the fabrication of thin asymmetric membranes challenging. Very limited oxygen permeation fluxes were measured through the 8 µm thick supported membrane (0.16 $mL_N\ cm^{-2}\ min^{-1}$ at 925 °C in air/N_2), while 1 mm thick membranes, in which the Zn depleted part was removed by polishing, displayed higher oxygen permeation fluxes (0.33 $mL_N\ cm^{-2}\ min^{-1}$ at 925 °C in air/N_2).

Finally, self-supported dual-phase membranes made of 70 vol.% of 10Sc1YSZ and 30 vol.% of LCCN were prepared and characterized (oxygen permeation measurements

and stability tests under oxy-fuel conditions). Analyses using several characterization techniques (X-ray diffraction (XRD), X-ray fluorescence (XRF), attenuated total reflection Fourier transform infrared spectroscopy (ATR-FTIR), Raman spectroscopy and scanning electronic microscopy with energy dispersive X-ray spectroscopy (SEM-EDX) underlined the excellent stability of the materials under application relevant atmospheres. Oxygen permeation fluxes of 0.27 $mL_N\ cm^{-2}\ min^{-1}$ and 1.02 $mL_N\ cm^{-2}\ min^{-1}$ were obtained at 950 °C in air/N_2 gradient for a 1000 µm thick and a 110 µm thick membrane, respectively. To further improve the oxygen permeation through 10Sc1YSZ-LCCN membranes, thin asymmetric and symmetric supported membranes were developed on 10Sc1YSZ-LCCN (40-60 vol.%) porous structures. Fully dense thin membrane layers (10-60 µm) were obtained, but the porous structures (support and activation layers) became to dense in the co-firing process. Consequently, further research and development is required to realize the full potential of this promising material combination.

Papers Included in the Thesis

Paper I. Oxygen permeation flux through 10Sc1YSZ-$MnCo_2O_4$ asymmetric membranes prepared by two-step sintering

S. Pirou, J. Gurauskis, V. Gil, M. Søgaard, P.V. Hendriksen, A. Kaiser, S. Ovtar, R. Kiebach

*Fuel Process. Technol. 152 (**2016**) 192–199*

Contribution: The PhD student was responsible for the experiments and wrote the manuscript (first and corresponding author of the paper).

Paper II. Improving the performance of oxygen transport membranes in simulated oxy-fuel power plant conditions by catalytic surface enhancement

S. Pirou, J. García-Fayos, M. Balaguer, R. Kiebach, J.M. Serra

In manuscript

Contribution: The PhD student contributed to the article by: (1) producing 7 μm thick 10Sc1YSZ-MCO asymmetric membranes; (2) performing several experiments together with the second author (J. García-Fayos): (i) long-term stability test on a 7 μm thick membrane under oxy-fuel conditions, (ii) XRD and SEM analyses, (iii) EIS measurements on 8YSZ activated backbone and 10Sc1YSZ-MCO (70-30 vol.%) activated & non-activated backbone, (iv) developing 0.5 mm thick 10Sc1YSZ-MCO membranes and (v) performing all oxygen permeation tests. The PhD student (first and corresponding author of the paper) wrote the manuscript except the description of the characterization techniques devices (XRD, SEM-EDX, Raman spectra, oxygen permeation reactor, gas chromatography).

Paper III. Stability and performance of robust dual-phase $(ZrO_2)_{0.89}(Y_2O_3)_{0.01}(Sc_2O_3)_{0.10}$-$Al_{0.02}Zn_{0.98}O_{1.01}$ oxygen transport membranes

S. Pirou, J.M. Bermudez, P.V. Hendriksen, A. Kaiser, T.R. Reina, M. Millan, R. Kiebach

*J. Memb. Sci. 543 (**2017**) 18–27*

Contribution: The PhD student was responsible for all experiments except the chemical stability of 10Sc1YSZ-AZO composite material under relevant flue gas conditions in power plants (section 3.1.1.). The PhD student wrote the manuscript except the thermochemical stability and characterization of 10Sc1YSZ-AZO composites (section 2.1.) and the chemical stability of 10Sc1YSZ-AZO composite material under relevant flue gas conditions in power plants (section 3.1.1.). The PhD student was responsible for organizing the paper (first and corresponding author of the paper).

Paper IV. Performance and stability of $(ZrO_2)_{0.89}(Y_2O_3)_{0.01}(Sc_2O_3)_{0.10}$-$LaCr_{0.85}Cu_{0.10}Ni_{0.05}O_{3-\delta}$ oxygen transport membranes under conditions relevant for oxy-fuel combustion

S. Pirou, J. M. Bermudez, B.T. Na, J.H. Yu, P.V. Hendriksen, A. Kaiser, M. Millan, R. Kiebach

In manuscript

Contribution: The PhD student was responsible for all experiments except the chemical stability of 10Sc1YSZ-LCCN under conditions relevant for oxy-fuel combustion (section 3.1.). The PhD student wrote the manuscript except the thermochemical stability and characterization of 10Sc1YSZ-LCCN composite (section 2.1.) and chemical stability of 10Sc1YSZ-LCCN under conditions relevant for oxy-fuel combustion (section 3.1.). The PhD student was responsible for organizing the paper (first and corresponding author of the paper).

Papers Not Included in the Thesis

Paper V. Hydrothermal synthesis, characterization, and sintering behavior of core-shell particles: a principle study on lanthanum strontium cobaltite coated with nanosized gadolinium doped ceria

Y. Xu, P. Zielke, N.V. Nong, **S. Pirou**, R. Reolon, S.B. Simonsen, P. Norby, H. Lühmann, W. Bensch, R. Kiebach

J. Solid State. Chem., ***Revised***

Contribution: The PhD student performed the conventional sintering of the samples and reviewed the manuscript before submission.

Paper VI. Continuous hydrothermal flow synthesis of $LaCrO_3$ in supercritical water and its application in dual-phase oxygen transport membranes

Y. Xu, **S. Pirou**, P. Zielke, S.B. Simonsen, P. Norby, P.V. Hendriksen, R. Kiebach

In manuscript

Contribution: The PhD student performed the oxygen permeation measurements, wrote the sections 2.5 (Oxygen permeation measurements) and 3.2.2 (Oxygen permeability) and reviewed the manuscript.

List of participated activities

1. Oral presentations

S. Pirou, J. Gurauskis, V. Gil, M. Søgaard, P.V. Hendriksen, A. Kaiser, P.S. Jørgensen, S. Ovtar and R. Kiebach. *Asymmetric dual phase* $(ZrO_2)_{0.89}(Y_2O_3)_{0.01}(Sc_2O_3)_{0.10}$-$MnCo_2O_4$ *oxygen membranes prepared by two-step sintering.* 14th International Conference on Inorganic Membranes. Atlanta, USA (2016).

R. Kiebach, **S. Pirou**, S. Ovtar, A.B. Haugen and P.V. Hendriksen. *Research and Development on Oxygen Transport Membranes at the Technical University of Denmark from Materials to Modules*. PRiME 2016, Honolulu, USA (2016).

R. Kiebach, **S. Pirou**, J. Gurauskis, V. Gil, M. Søgaard, P.V. Hendriksen, A. Kaiser, P.S. Jørgensen, S. Ovtar, J. Garcia-Fayos and J. M. Serra. *Long-Term Stability of Oxygen Transport Membranes in simulated Flue Gas Environments*. AMPEA workshop: "Materials for membranes in energy applications: gas separation membranes, electrolysers and fuel cells". Olso, Norway (2017).

P.V. Hendriksen, S. Ovtar, **S. Pirou**, A.B. Haugen, R. Kiebach, S. Cheng, J. Gurauskis and A. Kaiser. *Dense Gas Separation Membranes – Current Status and Future Challenges*. 229th ECS Meeting. San Diego, USA (2016).

M. Søgaard, S. Ovtar, **S. Pirou**, S. Cheng, A.B. Haugen, J. Gurauskis, A. Kaiser, P.V. Hendriksen and R. Kiebach. *Dual Phase Membranes for Oxygen Separation*. 20th International Conference on Solid State Ionics (SSI-20). Keystone, USA (2015).

Y. Xu, P. Zielke, **S. Pirou**, R. Kiebach, S.B. Simonsen, P. Norby, P.V. Hendriksen. *Continuous Hydrothermal Flow Synthesis of* $LaCrO_3$. 5th International Conference from Nanoparticles and Nanomaterials to Nanodevices and Nanosystems. Porto Heli, Greece (2016).

2. Posters

S. Pirou, J.M. Bermúdez, B.T. Na, J.H. Yu, P.V. Hendriksen, A. Kaiser, T. R. Reina, M. Millan and R. Kiebach. *Stability and Performance of Robust $(ZrO_2)_{0.89}(Y_2O_3)_{0.01}(Sc_2O_3)_{0.10}$-$LaCr_{0.85}Cu_{0.10}Ni_{0.05}O_{3-\delta}$ Oxygen Transport Membranes*. International Congress on Membranes and Membrane Processes. San Francisco, USA (2017).

S. Pirou, J. Gurauskis, M. Søgaard, A. Kaiser, P.V. Hendriksen, V. Gil and R. Kiebach. *Oxygen permeation flux through 10Sc1YSZ-$MnCo_2O_4$ asymmetric membranes developed by two-step sintering.* Summer School: "Ionic and protonic conducting ceramic membranes for green energy applications". Valencia, Spain (2015).

S. Pirou, J. Gurauskis, M. Søgaard, A. Kaiser, P.V. Hendriksen, V. Gil and R. Kiebach. *Oxygen permeation flux through 10Sc1YSZ-$MnCo_2O_4$ asymmetric membranes developed by two-step sintering.* 3rd DTU Energy's Annual PhD Symposium with Industrial Participation, Lyngby, Denmark (2015).

S. Pirou, M. Søgaard, A. Kaiser, P.V. Hendriksen and M. Salehi. *Development and Testing of Planar Oxygen Transport Membranes for Carbon Capture in Power Plants and Cement Industry*. 2nd DTU Energy's Annual PhD Symposium with Industrial Participation, Lyngby, Denmark (2014).

Y. Xu, R. Kiebach, **S. Pirou**, P. Zielke, S.B. Simonsen, P. Norby, P.V. Hendriksen. *Continuous Hydrothermal Flow Synthesis of $LaCrO_3$ for the Use in Solid Oxide Fuel Cells and Oxygen Separation Membranes*. 5th International Solvothermal and Hydrothermal Association Conference, Tainan City, Taiwan (2016).

Table of Contents

Lists of Figures and Tables

1. List of Figures

2. List of Tables

Lists of Acronyms and Symbols

1. List of Acronyms

Acronym	Definition
10Sc1YSZ	$(ZrO_2)_{0.89}(Y_2O_3)_{0.01}(Sc_2O_3)_{0.10}$
3YSZ	$(ZrO_2)_{0.97}(Y_2O_3)_{0.03}$
8YSZ	$(ZrO_2)_{0.92}(Y_2O_3)_{0.08}$
AC	Alternating Current
ASU	Air Separation Unit
ATR-FTIR	Attenuated Total Reflection-Fourier Transform Infrared Spectroscopy
AZO	$Al_{0.02}Zn_{0.98}O_{1.01}$
BBP	Butyl Benzyl Phthalate
BET	Brunauer–Emmett–Teller
BSCF	$Ba_{1-x}Sr_xCo_{1-y}Fe_yO_{3-\delta}$
BYS32	$Bi_{1.5}Y_{0.3}Sm_{0.2}O_3$
CCD	Charged Coupled Device
CCS	Carbon Capture and Storage/Sequestration
CCU	Carbon Capture and Utilization
CFO	$CoFe_2O_4$
CGO	$Ce_{1-x}Gd_xO_{2-\delta}$
CGO91	$Ce_{0.9}Gd_{0.1}O_{1.9}$
CGPO811	$Ce_{0.8}Gd_{0.1}Pr_{0.1}O_{2-\delta}$
CPO	$Ce_{1-x}Pr_xO_{2-\delta}$
CPO91	$Ce_{0.9}Pr_{0.1}O_{2-\delta}$
CSO	$Ce_{1-x}Sm_xO_{2-\delta}$
CSO82	$Ce_{0.8}Sm_{0.2}O_{1.9}$
CSO8515	$Ce_{0.85}Sm_{0.15}O_{1.925}$
CSO91	$Ce_{0.9}Sm_{0.1}O_{1.95}$
CTO	$Ce_{0.8}Tb_{0.2}O_{2-\delta}$
DBP	Di Butyl Phthalate
DTU	Danmarks Tekniske Universitet
EIS	Electrochemical Impedance Spectroscopy
GC	Gas Chromatography
GDC	Gadolinium Doped Ceria

GREEN-CC	GRaded membranes for Energy Efficient New generation Carbon Capture process
ITQ	Instituto de Tecnología Química
KIER	Korea Institute of Energy Research
LCCN	$LaCr_{0.85}Cu_{0.10}Ni_{0.05}O_{3-\delta}$
LNC	$LaNi_{0.6}Co_{0.4}O_{3-\delta}$
LSC82	$La_{0.8}Sr_{0.2}CrO_3$
LSCF	$La_{1-x}Sr_xCo_{1-y}Fe_yO_{3-\delta}$
LSCF6428	$La_{0.6}Sr_{0.4}Co_{0.2}Fe_{0.8}O_{3-\delta}$
LSCrF8255	$La_{0.8}Sr_{0.2}Cr_{0.5}Fe_{0.5}O_{3-\delta}$
LSF64	$La_{0.6}Sr_{0.4}FeO_{3-\delta}$
LSF6498	$(La_{0.6}Sr_{0.4})_{0.98}FeO_{3-\delta}$
LSM	$La_{1-x}Sr_xMnO_{3-\delta}$
LSM73	$La_{0.7}Sr_{0.3}MnO_{3-\delta}$
LSM82	$La_{0.8}Sr_{0.2}MnO_{3-\delta}$
LVDT	Linear Variable Displacement Transducer
MCN55	$MnCo_{1.5}Ni_{0.5}O_4$
MCO	$MnCo_2O_4$
MCO55	$Mn_{1.5}Co_{1.5}O_{4+\delta}$
MFC	Mass Flow Controller
MFO	$MnFe_2O_4$
MIEC	Mixed Ionic and Electronic Conductors
NAS	Sodium aluminosilicate (Na_2O: 17.8 mol.%, Al_2O_3: 9.4 mol.% and SiO_2: 72.8 mol.%)
NFO	$NiFe_2O_4$
OOR	Oxygen Oxidation Reaction
ORR	Oxygen Reduction Reaction
OTM	Oxygen Transport Membrane
PEG	PolyEthylene Glycol
PID	Proportional Integral Derivative
PMMA	Poly(Methyl MethAcrylate)
PPG	PolyPropylene Glycol
PSA	Pressure Swing Adsorption
PSD	Particle Size Distribution
PVB	PolyVinyl Butyral
PVP	PolyVinylPyrrolidone
SCF	$SrCo_{1-x}Fe_xO_3$

ScYSZ	$(ZrO_2)_{1-(x+y)}(Y_2O_3)_x(Sc_2O_3)_y$
SEM-EDX	Scanning Electronic Microscopy with Energy Dispersive X-ray spectroscopy
SiC	Silicon Carbide
SOFC	Solid Oxide Fuel Cell
SSAF6437	$Sm_{0.6}Sr_{0.4}Al_{0.3}Fe_{0.7}O_3$
SSF64	$Sm_{0.6}Sr_{0.4}FeO_3$
TEC	Thermal Expansion Coefficient
UPV	Universitat Politècnica València
WDS	Wavelength Dispersive X-ray spectroscopy
WIP	Warm Isostatic Press
XRD	X-Ray Diffraction
XRF	X-Ray Fluorescence
YSZ	Yttria Stabilized Zirconia
ZYO82	$Zr_{0.8}Y_{0.2}O_{2-\delta}$
ZYO8416	$Zr_{0.84}Y_{0.16}O_{1.92}$

2. List of Symbols

Symbol	Definition	Units
A	Effective area	cm^2
C_{O_2}	Concentration of oxygen	mol m^{-3}
d	Density	kg m^{-3}
D	Chemical diffusion coefficient	$cm^2\ s^{-1}$ / $m^2\ s^{-1}$
D_{1m}	Binary diffusion coefficient	$cm^2\ s^{-1}$ / $m^2\ s^{-1}$
D_k	Knudsen diffusion coefficient	$m^2\ s^{-1}$
d_p	Particle size	µm
D_S	Self-diffusion coefficient	$cm^2\ s^{-1}$
e	Volume void fraction	-
E	Electrode potential	V
E_a	Apparent activation energy	kJ mol^{-1}
f	Frequency	Hz
F	Faraday constant	C mol^{-1}
h	Height (of a sample)	m
I	Current	A
J_{O2}	Oxygen permeation flux	mL $cm^{-2}\ min^{-1}$ / mol $m^{-2}\ s^{-1}$
k_S	Surface exchange coefficient	cm s^{-1}

l	Distance (between electrodes in the conductivity probe)	cm
L	Membrane thickness	m / mm / μm
L_c	Membrane characteristic thickness	cm / μm
M_{O_2}	Molar weight of O_2	kg mol^{-1}
$\dot{n}$	Molar flow rate	mol s^{-1}
p	Equilibrium pressure	Pa / bar / atm
p_0	Saturation pressure	Pa / bar / atm
pO_2	Oxygen partial pressure	Pa / bar / atm
R	Gas constant	J mol^{-1} K^{-1}
R_{ABCD}	Resistance (between four points)	Ω
R_p	Polarization resistance	Ω cm^{-2}
r_{pore}	Pore radius	m
t	Support thickness	μm / mm
t	Time	h
T	Temperature	K / °C
T_G	Glass transition temperature	K / °C
V	Voltage	V
w	Width (of a sample)	m
ω	Angular frequency	rad s^{-1}
x_{O_2}	Oxygen mole fraction	-
Z	Impedance	Ω
Z’	Real impedance	Ω cm^{-2}
Z’’	Imaginary impedance	Ω cm^{-2}
α	Cross sectional area	cm^2
Δx	Thickness of the stagnant gas layer	m / mm / μm
$\Delta_{\mu O_2}$	Chemical potential drop	J mol^{-1}
λ	Wavelength	Å
ρ	Resistivity	Ω cm^{-1} / Ω m^{-1}
σ_{amb}	Ambipolar conductivity	S cm^{-1}/ S m^{-1}
σ_e / σ_{el}	Electrical conductivity	S cm^{-1}/ S m^{-1}
σ_i / σ_{ion}	Ionic conductivity	S cm^{-1}/ S m^{-1}
τ	Tortuosity	-
φ	Phase shift	rad

Chapter 1: Introduction

This chapter gives a general introduction into oxygen transport membranes (OTMs) in the context of carbon capture and storage (CCS) and utilization (CCU).

1.1. Oxygen transport membranes in the context of Carbon Capture and Utilization or Storage

The increase of the global population and the fast-growing economies of the developing countries are the main drivers which predict an increasing demand for energy in future decades. Despite all efforts focused on the development of clean and renewable energies, it clearly appears that in all realistic scenarios fossil fuel energy (coal, gas and oil) will still represent an important part of the energy sources in the near future, and it is predicted that more than 60 % of future electricity generation will be based on fossil fuels [1]. However, fossil fuel use is the primary source of greenhouse gas emissions as shown in Figure 1. 1 [2]. Fossil power plants are by far the biggest point sources of CO_2 emissions; therefore, Carbon Capture and Utilization (CCU) or Storage (CCS) in fossil power plants is an important strategy to reduce CO_2 emissions in order to counteract global warming and allow future electricity supply to be environmentally safe as recommended by the Kyoto Protocol and the Energy Technology Strategic Plan of the European Union [3].

Post-combustion capture, pre-combustion fuel decarbonisation and oxy-fuel combustion are the three main CO_2 capture technologies in advanced power generation [4]. Post-combustion relates to CO_2 capture from the exhaust of a combustion process by absorbing CO_2 in chemical or physical solvents (e.g. amine scrubbling). The pre-combustion fuel decarbonisation process removes CO_2 from the fuel before the combustion is completed. This process involves two main steps: (i) converting fuel into a mixture of CO_2 and H_2 using processes like reforming or gasification and (ii) separating CO_2 and H_2. This separation can be done by absorbing CO_2 into solvents or by adsorption (pressure swing adsorption). In the oxy-fuel process the fuel is combusted in oxygen unlike the two other processes using air (pure oxygen can also be used for the pre-combustion process). By eliminating nitrogen from the oxidant gas stream, it is possible to produce a CO_2-enriched flue gas (90 – 95 % CO_2 in the dried flue gas) and the non-circulated part of the CO_2 can be compressed and

stored [5]. This approach makes the CO_2 capture much easier and cheaper than using air for combustion. The main additional energy demand in this method results from the oxygen production, which is usually done using cryogenic air separation units (ASUs), the only available technology for large-scale production. ASUs cool incoming air to a sufficiently low temperature to liquefy oxygen. While the freezing technique produces a pure stream of oxygen, the process is particularly expensive and consumes a considerable amount of energy [6, 7]. This energy demand can substantially be lowered using thermally integrated separation modules based on ceramic oxygen transport membranes (OTMs) [8].

OTMs are made of dense mixed ionic and electronic conductor (MIEC) materials permitting the transport of oxygen ions via oxygen vacancies and the transport of electron via defects or polaron hopping in the material crystal lattice. Thus, OTMs can extract O_2 from air and produce a flux of pure oxygen. The separation process is based on a driving force created by the difference between partial pressures of oxygen (pO_2) on the two sides of the membrane. More details on the working principle and OTM materials are given in **Chapter 2**.

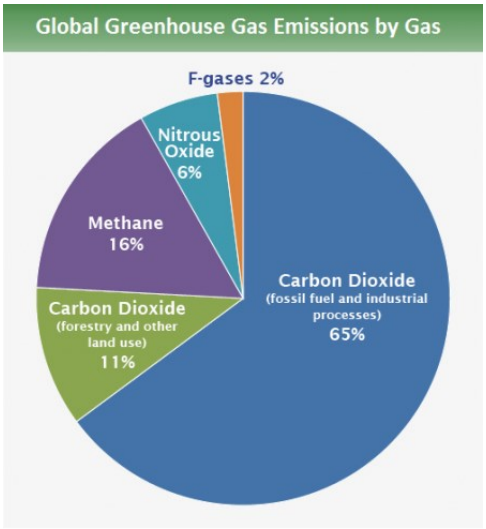

Figure 1. 1: Global greenhouse gas emissions sorted by gas and based on global emission data from 2010. Figure taken from the Fifth Assessment Report of the Intergovernmental Panel: Climate change 2014 [2].

1.2. Integration of oxygen transport membranes in oxy-fuel combustion power plants

Oxy-fuel combustion is considered to be an energy-efficient process for CCS in power plants. The process requires high purity oxygen in large quantities that can be produced by

distillation (ASU), adsorption (Pressure Swing Adsorption [PSA]) or membrane (OTM) technology. As mentioned above, a cryogenic distillation of air is the most mature of the three technologies and allows for both high purities (> 99 %) and large-scale productions [9]. With OTMs, the effective energy demand for oxygen production can be reduced compared to cryogenic air separation. Several studies reported the effective energy demand values of 147 kWh/tO_2 [10] and 185 kWh/tO_2 [11] for plants equipped with the OTM technology, while the energy consumption for cryogenic distillation has been put at 220 – 245 kWh/tO_2 for large scale production [12 – 14], and 280 – 340 kWh/tO_2 for small- to medium-scale plants [11]. The reduction of the energy demand is the main advantage of the membrane technology.

The integration of oxygen transport membranes in the oxy-fuel combustion process can be applied in two ways called the 4-end mode and the 3-end mode. Figure 1. 2.a and 1. 2.b illustrate the two options, respectively. The two processes can be distinguished according to two parameters: the membrane integration (direct/indirect) and the operation mode (sweep gas/vacuum). The 3-end mode membrane module is indirectly integrated to oxy-fuel combustion power plants. In this configuration, the membrane module generates pure oxygen, which is subsequently diluted with recirculated flue gas in order to control the combustion process in the boiler. The membrane module is, therefore, not in direct contact with the flue gas. Vacuum pumps or exhausters are required to remove the oxygen from the membrane. Conversely, the 4-end mode integrates the membrane module in direct contact with the flue gas. The recirculated flue gas is used as a sweep gas on the permeate side of the membrane and is thus directly diluting the oxygen and ready for combustion [15]. Consequently, the 4-end mode membrane module does not require additional turbomachines and consumes less energy than the 3-end mode. Up to 60 % reduction in capture energy demand compared to cryogenic air separation can be achieved by using thermally integrated separation modules (4-end mode) based on ceramic oxygen transport membranes [10, 14].

However, OTM technology is not developed at an industrial scale nowadays. One of the major limitations is the availability of materials with high permeability and chemical stability [16]. For example, cerium oxide-based compounds are stable at CO_2-containing atmospheres but result in a very low oxygen permeation flux [17]. On the other hand, in the last years, very high oxygen fluxes were obtained in particular with $Ba_{1-x}Sr_xCo_{1-y}Fe_yO_{3-\delta}$ or

$La_{1-x}Sr_xFe_{1-y}Co_yO_{3-\delta}$-based membranes. Baumann *et al.* reported oxygen fluxes between 12.2 and 67.7 mL min^{-1} cm^{-2} at 1000 °C depending on the oxygen gradient [18]. Unfortunately, these compounds decomposed in carbonates when it is exposed to CO_2-rich atmospheres [19 – 25]. The composition of the flue gas of oxy-fuel power plants, to which the membrane is exposed, is influenced by several parameters: oxygen purity, fuel composition and false air intrusion. Therefore, the composition of the flue gas varies from case to case. Nevertheless, it is commonly composed mainly of CO_2 (80 – 90 mol.%) and contains a limited amount of N_2 (8 – 10 mol.%), H_2O (2 – 3 mol.%), O_2 (2 – 3 mol.%) and SO_2 (200 – 500 ppm) [26]. No OTMs exhibited sufficiently high performances under such conditions to be commercialized. Therefore, the main effort required for the integration of the OTM technology in oxy-fuel combustion power plants is to develop highly performant and stable membranes in realistic power plant conditions.

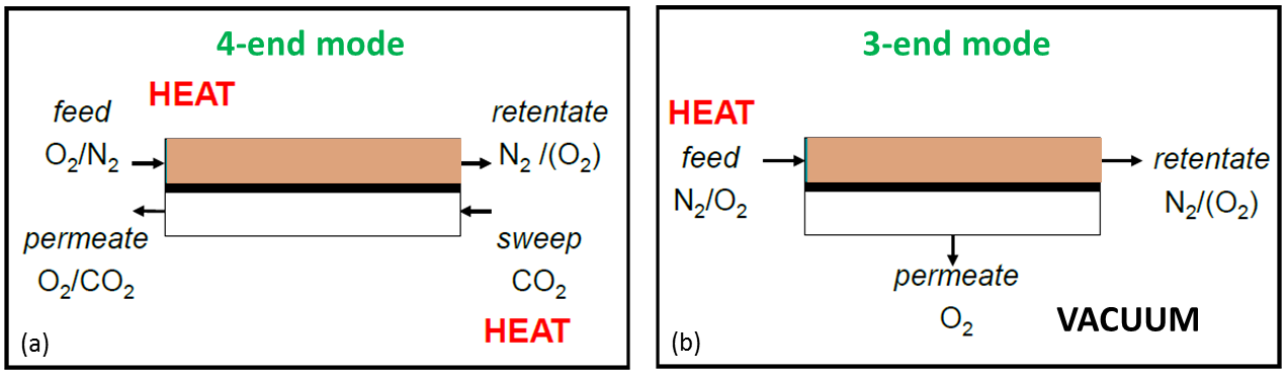

Figure 1. 2: Illustrations of (a) 4-end mode (direct) and (b) 3-end mode (indirect) integration of oxygen transport membranes into oxy-fuel combustion power plants.

References

[1] International Energy Agency, World Energy Outlook 2011, 2011. doi:10.1049/ep.1977.0180.

[2] O. Edenhofer, R. Pichs-Madruga, Y. Sokona, J.C. Minx, E. Farahani, S. Kadner, K. Seyboth, A. Adler, I. Baum, S. Brunner, P. Eickemeier, B. Kriemann, J. Savolainen, S. Schlömer, C. von Stechow, T. Zwickel, Climate Change 2014: Mitigation of Climate Change: Working Group III Contribution to the Fifth Assessment Report of the Intergovernmental Panel on, 2014. http://www.ipcc.ch/index.htm.

[3] Commition of the European communities, Towards a low carbon future, 2007.

[4] R. Bredesen, K. Jordal, O. Bolland, High-temperature membranes in power generation with CO_2 capture, Chem. Eng. Process. Process Intensif. 43 (2004) 1129–1158. doi:10.1016/j.cep.2003.11.011.

[5] H. Stadler, F. Beggel, M. Habermehl, B. Persigehl, R. Kneer, M. Modigell, P. Jeschke, Oxyfuel coal combustion by efficient integration of oxygen transport membranes, Int. J. Greenh. Gas Control. 5 (2011) 7–15. doi:10.1016/j.ijggc.2010.03.004.

[6] S.M. Hashim, A.R. Mohamed, S. Bhatia, Current status of ceramic-based membranes for oxygen separation from air, Adv. Colloid Interface Sci. 160 (2010) 88–100. doi:10.1016/j.cis.2010.07.007.

[7] S. Smart, C.X.C. Lin, L. Ding, K. Thambimuthu, J.C. Diniz da Costa, Ceramic membranes for gas processing in coal gasification, Energy Environ. Sci. 3 (2010) 268–278. doi:10.1039/b924327e.

[8] M. Czyperek, P. Zapp, H.J.M. Bouwmeester, M. Modigell, K. Ebert, I. Voigt, W.A. Meulenberg, L. Singheiser, D. Stöver, Gas separation membranes for zero-emission fossil power plants: MEM-BRAIN, J. Memb. Sci. 359 (2010) 149–159. doi:10.1016/j.memsci.2010.04.012.

[9] T. Burdyny, H. Struchtrup, Hybrid membrane/cryogenic separation of oxygen from air for use in the oxy-fuel process, Energy. 35 (2010) 1884–1897. doi:10.1016/j.energy.2009.12.033.

[10] T.L. Ochs, D.B. Oryshchyn, C.A. Summers, Proceedings of Electric Utilities Environmental Conference, in: Tucson, 2005.

[11] P. Kauranen, Nanotechnology, Presentation at Materials and New Production - NMP, in: Helsinki, 2008.

[12] A. Seltzer, Z. Fan, H. Hack, Oxyfuel Coal Combustion Power Plant System Optimization, in: 7th Annu. COAL-GEN Conf., Milwaukee, 2007.

[13] J. Davison, Performance and costs of power plants with capture and storage of CO_2, Energy. 32 (2007) 1163–1176. doi:10.1016/j.energy.2006.07.039.

[14] J. Hong, G. Chaudhry, J.G. Brisson, R. Field, M. Gazzino, A.F. Ghoniem, Analysis of oxy-fuel combustion power cycle utilizing a pressurized coal combustor, Energy. 34 (2009) 1332–1340. doi:10.1016/j.energy.2009.05.015.

[15] R. Kneer, D. Toporov, M. Förster, D. Christ, C. Broeckmann, E. Pfaff, M. Zwick, S. Engels, M. Modigell, OXYCOAL-AC: Towards an integrated coal-fired power plant process with ion transportmembrane-based oxygen supply, Energy Environ. Sci. 3 (2010) 198–207. doi:10.1039/B908501G.

[16] S. Diethelm, J. Van herle, P.H. Middleton, D. Favrat, Oxygen permeation and stability of $La_{0.4}Ca_{0.6}Fe_{1-x}Co_xO_{3-\delta}$ (x= 0, 0.25, 0.5) membranes, J. Power Sources. 118 (2003) 270–275. doi:10.1016/S0378-7753(03)00098-3.

[17] M. Balaguer, C. Solís, J.M. Serra, Study of the transport properties of the mixed ionic electronic conductor $Ce_{1-x}Tb_xO_{2-\delta}$ + Co (x = 0.1, 0.2) and evaluation as oxygen-transport membrane, Chem. Mater. 23 (2011) 2333–2343. doi:10.1021/cm103581w.

[18] S. Baumann, J.M. Serra, M.P. Lobera, S. Escolástico, F. Schulze-Küppers, W.A. Meulenberg, Ultrahigh oxygen permeation flux through supported $Ba_{0.5}Sr_{0.5}Co_{0.8}Fe_{0.2}O_{3-\delta}$ membranes, J. Memb. Sci. 377 (2011) 198–205. doi:10.1016/j.memsci.2011.04.050.

[19] M. Arnold, H. Wang, A. Feldhoff, Influence of CO_2 on the oxygen permeation performance and the microstructure of perovskite-type $(Ba_{0.5}Sr_{0.5})(Co_{0.8}Fe_{0.2})O_{3-\delta}$ membranes, J. Memb. Sci. 293 (2007) 44–52. doi:10.1016/j.memsci.2007.01.032.

[20] X. Tan, N. Liu, B. Meng, J. Sunarso, K. Zhang, S. Liu, Oxygen permeation behavior of $La_{0.6}Sr_{0.4}Co_{0.8}Fe_{0.2}O_3$ hollow fibre membranes with highly concentrated CO_2 exposure, J. Memb. Sci. 389 (2012) 216–222. doi:10.1016/j.memsci.2011.10.032.

[21] S. Engels, T. Markus, M. Modigell, L. Singheiser, Oxygen permeation and stability investigations on MIEC membrane materials under operating conditions for power plant processes, J. Memb. Sci. 370 (2011) 58–69. doi:10.1016/j.memsci.2010.12.021.

[22] J. Gao, L. Li, Z. Yin, J. Zhang, S. Lu, X. Tan, Poisoning effect of SO_2 on the oxygen permeation behavior of $La_{0.6}Sr_{0.4}Co_{0.2}Fe_{0.8}O_{3-\delta}$ perovskite hollow fiber membranes, J. Memb. Sci. 455 (2014) 341–348. doi:10.1016/j.memsci.2013.12.073.

[23] E. Bucher, A. Egger, G.B. Caraman, W. Sitte, Stability of the SOFC Cathode Material $(Ba,Sr)(Co,Fe)O_{3-\delta}$ in CO_2-Containing Atmospheres, J. Electrochem. Soc. 155 (2008) B1218. doi:10.1149/1.2981024.

[24] S.J. Benson, D. Waller, J.A. Kilner, Degradation of $La_{0.6}Sr_{0.4}Fe_{0.8}Co_{0.2}O_{3-\delta}$ in Carbon Dioxide and Water Atmospheres, J. Electrochem. Soc. 146 (2000) 1305–1309.

[25] M. Schulz, R. Kriegel, A. Kämpfer, Assessment of CO_2 stability and oxygen flux of oxygen permeable membranes, J. Memb. Sci. 378 (2011) 10–17. doi:10.1016/j.memsci.2011.02.037.

[26] E.S. Rubin, A.B. Rao, M.B. Berkenpas, Technical Documentation : Oxygen-based Combustion Systems (Oxyfuels) with Carbon Capture and Storage (CCS), 2007.

Chapter 2: Background

In this chapter the basic operating principle of OTMs is explained (**sub-chapter 2.1.**) and the underlying transport processes of the oxygen through the membranes is described (**sub-chapter 2.2.**). Additionally, an overview of the typical membrane geometries is presented (**sub-chapter 2.3.**) and a brief literature review on membrane materials (single + dual-phase membranes) is done (**sub-chapter 2.4.**).

2.1. Basic working principle of oxygen transport membranes

Oxygen transport membranes consist of gastight mixed ionic and electronic conductors (MIEC) that allow simultaneously the transport of oxygen ions via oxygen vacancies and electrons via defects and polaron hopping in the crystal lattice. OTMs produce a flux of pure oxygen, based on a driving force created by the difference between partial pressures of oxygen (pO_2) on the two sides of the membrane. In general, such membranes work at high temperature (> 700 °C) because of the demand of energy for the movement of charge carriers (oxygen ions and electrons). The high pO_2 side (called feed side) corresponds usually to air flow while a variety of mildly or harsh reducing gases (e.g. N_2, CO_2, Ar) can be used at the low pO_2 side (called sweep side). The oxygen flux through the membrane is for the case of fast surface exchange given by the Wagner Equation (1):

$$J_{O_2} = \frac{RT}{16F^2L} \int_{pO_2^{permeate}}^{pO_2^{feed}} \frac{\sigma_e \sigma_i}{\sigma_e + \sigma_i} (pO_2)\, d \ln pO_2 \quad (1)$$

where J_{O_2} is the oxygen permeation flux (mol m^{-2} s^{-1}), R is the gas constant, F is the Faraday constant, L is the membrane thickness, σ_e and σ_i are the electronic and the ionic conductivities, and pO_2^{feed} and $pO_2^{permeate}$ are the oxygen partial pressures at the high-pressure side and low-pressure side, respectively.

Accordingly, in order to obtain a high oxygen flux, the membrane thickness L should be as low as possible (cf. Eq. (1)). Asymmetric membranes made of a thin selective membrane layer (10 – 30 µm) supported on a relatively thick porous support (200 – 500 µm) are promising architecture to minimize the actual membrane thickness while ensuring mechanical robustness. For this reason, this thesis focuses on the development of

asymmetric supported membranes. Some specific details on the transport of oxygen through asymmetric membranes are given in the following section.

2.2. Transport of oxygen through asymmetric membranes

Oxygen permeation through asymmetric MIEC membranes can be divided into 6 different steps. Figure 2. 1 shows the assembly model of the steps represented as resistances in series. Zones I and VI represent the concentration polarization in the gas phases (feed gas and sweep gas); zone V corresponds to the concentration polarization in the pores of the porous support; zone II symbolizes the surface exchange including oxygen reduction, dissociation and incorporation into the oxide lattice at the high oxygen partial pressure side while zone IV illustrates the reactions in the opposite order at the low-oxygen partial pressure side in order to reconstitute the oxygen molecule. Finally, zone III represents the bulk transport of the oxygen ions into the dense selective membrane layer. The dominating rate-limiting process (largest resistance) governs the overall performance. The rate-limiting process depends on several parameters such as the membrane material, the membrane geometry or the operating conditions. In the following sections the various rate-limiting processes will be quickly presented.

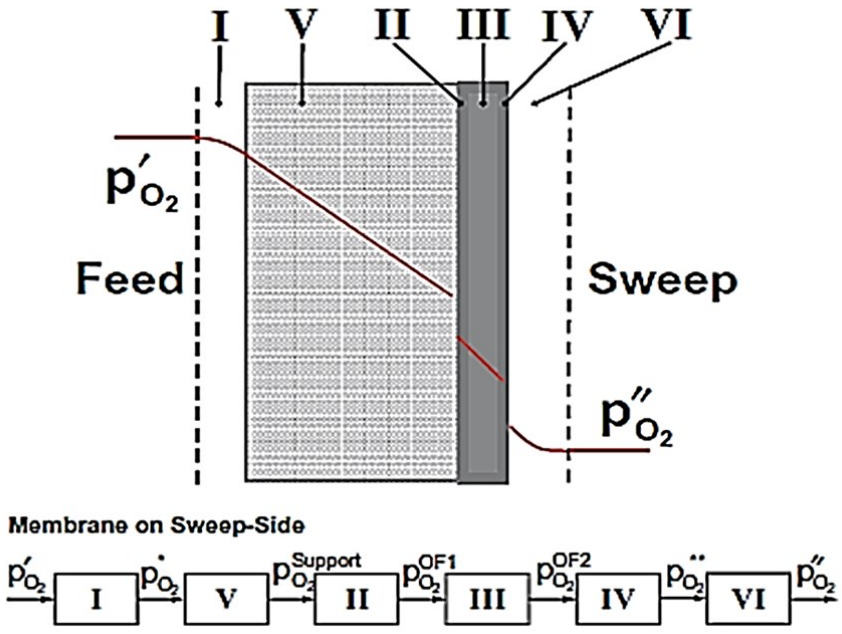

Figure 2. 1: Model of resistances representing the steps of the oxygen permeation through asymmetric membranes. Figure taken from [1].

2.2.1. Gas diffusion limitation

In the case of high oxygen flux and high driving force, an oxygen gradient occurs adjacent to the porous support because of the existence of a stagnant gas layer. This phenomenon is called gas diffusion layer and corresponds to a decline of the chemical potential starting from gases (feed or sweep gases) to the surface of porous layers (zones I and VI, Figure 2. 1). The flux through a stagnant gas layer will be proportional to the concentration gradient through the layer:

$$J_{O_2} = -D_{O_2-N_2} \frac{\Delta C_{O_2}}{\Delta x} \quad (2)$$

where Δx is the thickness of the stagnant gas layer, $D_{O_2-N_2}$ is the binary diffusion coefficient of oxygen in nitrogen, and ΔC_{O_2} is the concentration difference across the layer. The fast diffusion of the oxygen in air (large values of $D_{O_2-N_2}$) commonly leads to a negligible loss of oxygen activity.

The diffusion of the gas through the porous support (zone V, Figure 2. 1) usually induces a more significant loss of the driving force. The associated resistance is highly dependent on the microstructure of the support material (porosity, pore size, pore connectivity, tortuosity, etc.). In a porous support, Knudsen and surface diffusion govern the mass transfer. Both of them are functions of the pore size of the support. The expression for the mass transfer across a porous support is given below [1]:

$$J_{O_2} = \frac{\frac{1}{\frac{1}{D_k} + \frac{1-x_{O_{2S}}}{D_{1m}}} (C_{O_{2S}} - C'_{O_{2S}})}{t\frac{-e}{\tau}} \quad (3)$$

where the Knudsen diffusion coefficient D_k is expressed as:

$$D_k = \frac{2}{3} r_{pore} \sqrt{\frac{8RT}{\pi M_{O_2}}} \quad (4)$$

M_{O_2} is the molar weight of O_2, T is the temperature, r_{pore} the radius of the pore, t the support thickness, and e the volume void fraction. D_{1m}, the binary diffusion coefficient, takes into account the diffusivity of oxygen inside the stream on the sweep side, e.g. in the case reported in this work, the diffusivity of the species oxygen inside CO_2. $x_{O_{2S}}$ is the oxygen

mole fraction in the gas at the surface of the support, and $C_{O_{2S}}$ and $C'_{O_{2S}}$ are the concentration of oxygen, respectively, at the two sides of the support.

2.2.2. Bulk diffusion limitation

When the thickness of the selective membrane layer is in the range of 200–300 μm or higher, it is typically estimated that the limiting step of the oxygen permeation is the bulk transport in the selective layer (zone III) [2]. The bulk transport is very well understood and can be described by the Wagner equation (Eq. 1). In this equation, the term $\frac{\sigma_e \sigma_i}{\sigma_e + \sigma_i}$ corresponds to the ambipolar conductivity. In most of the MIECs or dual-phase materials, the electronic conductivity is, at least, an order of magnitude higher than the ionic conductivity ($\sigma_e \gg \sigma_i$); therefore, the Wagner's equation can be simplified to:

$$J_{O_2} = \frac{RT}{16F^2L} \int_{pO_2^{permeate}}^{pO_2^{feed}} \sigma_i \, (pO_2) \, d \ln pO_2 \quad (5)$$

2.2.3. Surface exchange limitation

Under the 200–300 μm thresholds, the thickness of the membrane has a weak influence on the flux. The critical value is defined as the condition when the bulk diffusion and the surface exchange resistance are equivalent. For thicknesses below the critical value, surface reactions should be considered [3]. For such thin membranes, the losses associated with oxygen incorporation from the gas into the bulk material may become limiting for the transport over the membrane. The oxygen surface exchange process occurs through a series of reaction steps, including oxygen reduction, dissociation and incorporation into the oxide lattice at the high-oxygen partial pressure side (zone II, Figure 2. 1) such as [4]:

$$O_2 + e^- \longrightarrow O_2^- \quad (6)$$

$$O_2^- + e^- \longrightarrow O_2^{2-} \quad (7)$$

$$O_2^{2-} \longrightarrow 2O^- \quad (8)$$

$$2O^- + 2e^- \longrightarrow 2O^{2-} \quad (9)$$

$$2O^{2-} + 2V_{\ddot{O}} \longrightarrow 2O_O^x \quad (10)$$

At the low-oxygen partial pressure side (zone IV, Figure 2. 1), the reactions occur in the opposite order, representing thus the desorption, recombination and oxidation of the oxygen. Each of these reactions can be the limiting rate step for the overall surface exchange reaction. In the steady state, the oxygen flux across the membrane is assumed to be proportional to the chemical potential drop over the interface (linear kinetics):

$$J_{O_2} = -\frac{k_S c_O}{4RT} \Delta\mu_{O_2}^{int} \quad (11)$$

$\Delta\mu_{O_2}^{int}$ is the chemical potential drop across the interface, k_S is the surface exchange coefficient, and c_O denotes the oxide ion concentration at the surface.

Bouwmeester and Burggraaf [5, 6] introduced the characteristic thickness L_c to define the membrane thickness corresponding to transition from predominant bulk diffusion limitation to the state when the oxygen permeation is governed by the surface exchange. L_c is defined by the ratio between the self-diffusion coefficient of oxygen (D_S) and the surface exchange coefficient (k_s):

$$L_c = \frac{D_S}{k_s} \quad (12)$$

when the membrane thickness (L) is much smaller than L_c, the oxygen permeation is mainly limited by the surface-exchange kinetics, while for $L \gg L_c$ the bulk diffusion is the main rate limiting factor. It has to be noted that L_c is not an intrinsic property of the material but is also dependent on a variety of extrinsic conditions, i.e. temperature [7], oxygen-partial pressure [8, 9], roughness and the surface porosity [10]. A modified Wagner equation, considering the bulk diffusion and surface exchange kinetics limitations, can be written as [10]:

$$J_{O_2} = -\frac{1}{1+\left(\frac{2L_c}{L}\right)} \frac{RT}{16F^2L} \int_{pO_2^{permeate}}^{pO_2^{feed}} \sigma_{ion}\,(pO_2) d\ln pO_2 \quad (13)$$

2.3. Geometry structure

The most common geometric shapes of OTMs are planar, tubular and hollow fibres. Each geometry presents advantages and disadvantages. They will be described briefly here.

The planar design presents the advantages of being well-established and relatively easy to fabricate by using low-cost and reproducible methods like powder pressing or tape casting.

The mechanical strength of the planar design is another advantage compared to the other configurations. On the other hand, the membrane sealing is more critical for the planar design than the tubular and hollow fibre configurations due to the large seal areas and the large pressure differential applied through the membranes [11].

The tubular configuration is relatively easy to fabricate and operate. The porous support can be prepared in large scale by extrusion methods at relatively low cost. The dense layer can be applied using conventional methods such as dip coating. The sealing procedure is difficult due to the high-pressure differential applied through the tubes but the sealing area per unit of membrane surface is small. A disadvantage of the tubular design is that it results in an expensive system since the membrane surface area per unit volume is low compared to a planar structure. Moreover, during testing every tube needs to be sealed to the testing manifold, and this is expensive. One way to reduce the cost is to increase the length of the tubes, which unfortunately decreases the reliability of the membranes [11].

Compared to planar or tubular designs, hollow fibre membranes have a higher surface-to-volume ratio [12]. Such membranes can be prepared by extruding or pumping methods. Moreover, the thinner membrane walls and asymmetric structure of hollow fibre membranes are more favourable for getting higher oxygen permeation flux than with the other geometric configurations. However, the complexity of sealing the membranes to the manifold still exists with this design, and the membranes' mechanical strength is not as good as with the planar configuration.

Considering all pros and cons of the different geometric configurations as well as the in-house experience and the facilities of the laboratory, the planar design has been selected for the development of the OTMs of this thesis.

2.4. State of the art of oxygen transport membrane materials

Asymmetric oxygen transport membranes consist of different layers that require different material proprieties. Table 2. 1 summarizes the requirements that the porous support, the catalyst activation layers and the dense membrane layers have to fulfil.

Table 2. 1: Requirements for porous support, catalyst activation layers and dense membrane layers. Targeted values are mentioned in brackets

Porous support	Catalyst activation layers	Dense membrane
Chemical, thermal and mechanical stability	Chemical, thermal and mechanical stability	Chemical, thermal and mechanical stability
Gas permeability ($\geq 10^{-14}$ m^2)	Gas permeability ($\geq 10^{-14}$ m^2)	Gas-tightness (d > 95 %)
Suitable pore size, pore connectivity and surface roughness	Suitable pore size, pore connectivity and surface roughness	Minimum thickness (10-30 µm)
Good mechanical strength (Flexural strength ≥ 80MPa)	Buffer layer in case of chemical incompatibility or thermal expansion coefficient mismatch between membrane layer and porous support	High ionic and electronic conduction

The performances of oxygen transport membranes are highly related to the material properties of the material(s) composing the dense and selective membrane layer. Consequently, this section will give a review of the most studied materials used as dense membranes for oxygen separation applications. Among these membrane materials, two categories can be distinguished: the single-phase materials and the dual-phase materials.

2.4.1. Single-phase membranes

Since decades, membranes based on single phase MIEC materials have been highly studied, showing high oxygen permeation flux [13 – 22]. The oxygen conduction phenomenon exhibited by MIEC materials is attributed to their ability to support oxygen vacancies and lattice disorder, which allows the relatively rapid and sustainable transport of oxygen ions under the appropriate conditions [23 – 27]. Most MIEC membrane materials can be classified into two groups based on their crystal structure: the perovskite and Ruddlesden–Popper phases.

- Perovskites

Perovskite materials are defined by the general formula ABO_3, corresponding in general to $A^{2+}B^{4+}O_3$ ($A^{1+}B^{5+}O_3$ or $A^{3+}B^{3+}O_3$ are also possible). In this formula, A and B correspond to two cations of very different sizes. The “A” atoms are larger than the “B” atoms. The ideal cubic-symmetry structure has the “B” cation in 6-fold coordination, surrounded by an octahedron of oxygen anions, and the “A” cation in 12-fold cuboctahedral coordination. Figure 2. 2 presents two views of the unit cell of such materials. In Figure 2. 2.a, the type “A” atom sits at cube corner positions (0, 0, 0), the type “B” atom sits at the body centre position (½, ½, ½), and the oxygen atoms sit at face-centred positions (½, ½, 0). Conversely, the Figure 2. 2.b presents the structure with the “A” atom at the body centre position and the “B” atom at the cube corner positions, surrounded by oxygen octahedrons.

The ionic conductivities can be enhanced greatly by substituting lower valence cations for both A and B sites because the deficiency from the substitution brings an increase of oxide ion vacancies. The electronic conductivity can also be increased by the addition of aliovalent cations. The “B” cation is oxidized and thus formed an electron hole. After doping with other metal cations, the perovskite can be symbolized by the formula $A_{1-x}A'_xB_{1-y}B'_yO_{3-\delta}$. Usually, “A’” ions are alkaline-earth metals such as Ca^{2+}, Sr^{2+} and Ba^{2+}, and “B” ions are transition metals such as Co^{3+} and Fe^{3+}. Among the various combination of chemical compounds, $Ba_{1-x}Sr_xCo_{1-y}Fe_yO_{3-\delta}$ (BSCF) and $La_{1-x}Sr_xCo_{1-y}Fe_yO_{3-\delta}$ (LSCF) appear to be the materials with the highest oxygen permeation flux [13, 28 – 35].

BSCF is a derivative of the commonly studied material $SrCo_{1-x}Fe_xO_3$ (SCF). Teraoka *et al.* revealed that $SrCo_{0.8}Fe_{0.2}O_3$ exhibits 5.10^{-6} mol cm^{-2} s^{-1} at 800 °C (air/He) [36]. This high flux is a consequence of the high concentration of oxygen vacancies in the crystalline structure of SCF. Nevertheless, the stability of the material at high temperatures is problematic. Indeed, SCF presents a structural transformation from perovskite to brownmillerite at 700 °C [37]. The substitution of Sr by Ba (BSCF) is a way to stabilize the cubic structure of the perovskite and to enhance the oxygen permeation flux [31, 38]. Despite its good performances, BSCF has several drawbacks that limit its use as a membrane material. One of the most critical is its instability under CO_2 and SO_2 containing atmospheres [30, 39, 40]. BSCF also has high chemical and thermal expansion [41]. The lattice expansion arising from the phase transition (cubic to hexagonal) occurs in the 850–

900 °C temperature range in which OTMs are usually operated and results in chemical instability and mechanical failure [42].

During the past decade, LSCF has been intensively investigated as a membrane material for oxygen separation from air [43, 44] and cathode material for solid oxide fuel cells [45 – 48]. This material is a mixed ionic electronic conductor showing high electronic conductivity (310 S cm^{-1} for $La_{0.2}Sr_{0.8}Co_{0.8}Fe_{0.2}O_{3-\delta}$ at 900 °C) and good ionic conductivity (0.87 S cm^{-1} for $La_{0.2}Sr_{0.8}Co_{0.8}Fe_{0.2}O_{3-\delta}$ at 900 °C) [46]. Teraoka *et al.* demonstrated that the performance of the material increases with Sr and Co content while its stability decreased [36]. Previous studies proved its stability in CO_2 if the Sr-content is limited [43, 44] but also its instability in SOx-containing atmospheres due to the formation of $SrSO_4$ [49, 50]. This makes LSCF an inappropriate candidate material for OTMs developed for oxy-fuel combustion applications.

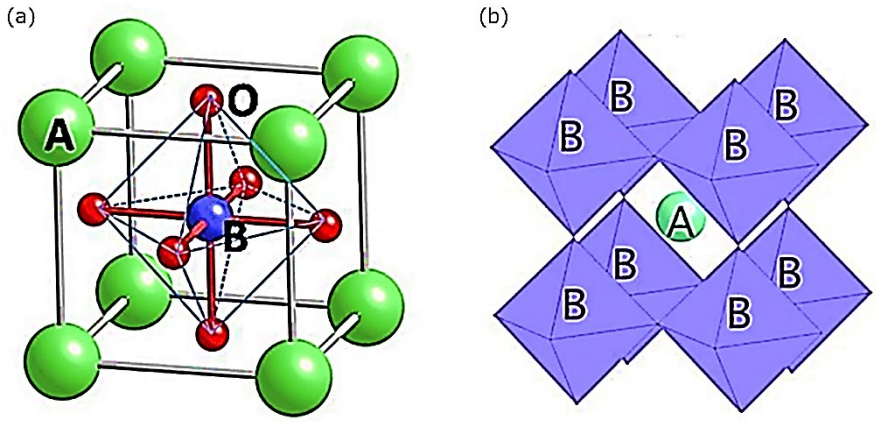

Figure 2. 2: Schema of an ABO_3 perovskite structure with the body centre position occupied by the "B" atom (a) and by the "A" atom (b).

- The Ruddlesden–Popper phases

Ruddlesden–Popper phases are materials with the general formulation $A_{n+1}M_nO_{3n+1}$ (with n = 1, 2, 3, …∞), where A is a cation of large ionic radius (lanthanide or alkaline earth) and M a transition metal (M= Co, Ni, Cu, etc). Figure 2. 3 presents the $A_2MO_{4+\delta}$ structure corresponding to the first term (n=1) of the Ruddlesden–Popper series. The structure belongs to the K_2NiF_4 model. It can be simplified as a succession of perovskite-type MO_6 octahedra layers, shifted relative to each other by a vector (½, ½, ½) so that they appear linked together by a NaCl-type AO sheets. In reality, due to the Jahn–Teller effect, the octahedra are not regular and the structure consists more as a succession of square MO_2 plan sheets and A_2O_2 layers. This layered structure admits a deviation from the oxygen

stoichiometry and makes it possible to incorporate an excess of oxygen. This phenomenon is due to the size difference of A and M cations which induces distortions within the crystal structure. This distortion is partly compensated by a natural insertion of interstitial oxygen [51, 52] and results in a mixed valence of the metal (M^{2+}/M^{3+}). The presence of two degrees of oxidation confers good electronic conduction on the material. Thus, Ruddlesden–Popper phase materials are good ionic and electronic conductors.

$La_2NiO_{4+\delta}$ and its derivative materials $La_{2-x}Sr_xNi_{1-y}M_yO_{4+\delta}$ (M= Fe, Cu, Co) are the Ruddlesden–Popper materials that have been investigated as an oxygen transport membrane material [53 – 63]. These materials exhibit high oxygen diffusion and surface exchange coefficients at intermediate temperatures together with moderate thermal expansion coefficients around 13.0 10^{-6} K^{-1} [58]. Several studies attest that the substitution of strontium for lanthanum ($0 \leq x \leq 0.75$) results in an increase of the electrical conductivity [54, 62, 63]. Indeed, Aguadero *et al.* demonstrated that $La_{1.25}Sr_{0.75}NiO_{4+\delta}$ exhibits a conductivity of 235 S cm^{-1} in air at 850 °C, while $La_2NiO_{4+\delta}$ displays only 60 S cm^{-1} under the same operating conditions [54].

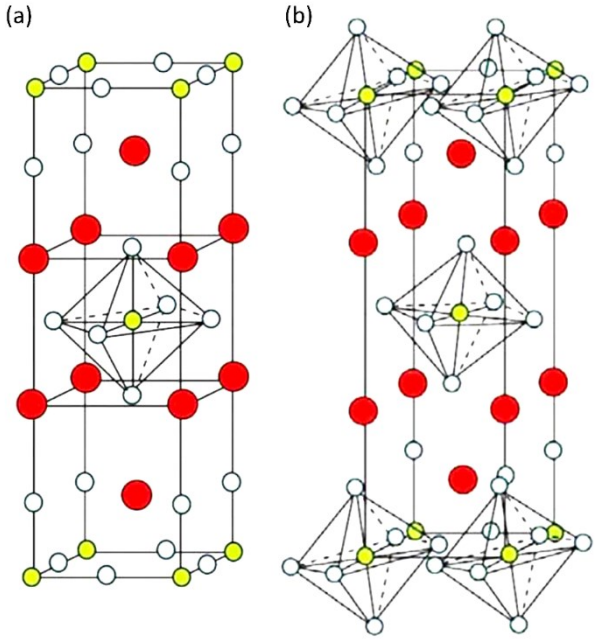

Figure 2. 3: (a) A_2MO_4 tetragonal structure and (b) A_2MO_4 orthorhombic structure. Figure taken from [51]. A-site cations are in red, M-site in yellow and oxygen in white.

2.4.2. Dual-phase membranes

As mentioned, most of the flux-wise promising single-phase MIEC materials are not chemically stable under oxy-fuel combustion power plant conditions. Conversely, the stable ones do not present sufficiently high oxygen permeation fluxes to be commercialized. Dual-phase systems, where the membrane consists of a composite of a stable ionic conductor and a stable electronic conductor, can overcome the disadvantages of single phase membranes. Ideally, they combine the best characteristics of compounds to achieve both a large oxygen permeability and good chemical and mechanical stabilities at elevated temperatures. A good percolation of both ionic and electronic conducting phases is fundamental for dual-phase composites in order to show high oxygen permeation fluxes. Figure 2. 4 presents a schematic draw of an asymmetric dual-phase membrane.

The first dual-phase membranes were made of oxygen conductors and noble metals: $(Bi_2O_3)_{0.24}SrO_{0.26}$-Ag [64], $Bi_{1.5}Er_{0.5}O_3$-Ag [65], $Bi_{1.6}Y_{0.4}O_3$-Ag [66], $Bi_{1.5}Y_{0.3}Sm_{0.2}O_3$-Ag [67, 68], and YSZ-Pd [69]. However, the application of these materials is limited due to high material costs, a mismatch of the thermal expansion coefficient (TEC) between the ceramic and the metallic materials, and poor oxygen permeability. More recently, perovskite, spinels or fluorite type oxides have been used instead of noble metals as electronic conductors [70 – 79].

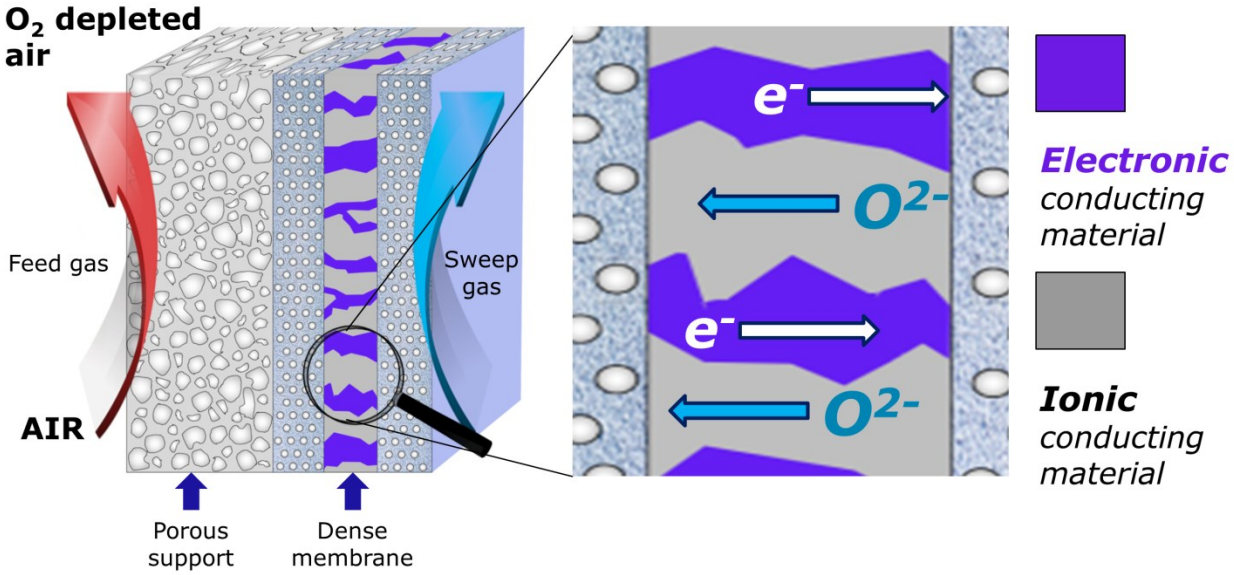

Figure 2. 4: Schematic draw of an asymmetric dual-phase membrane.

2.4.2.1. Ionic conductors

Materials for which the conduction is predominated by ions, rather than by electrons and holes (negligible electronic conductivity) are considered as purely ionic conductors. Fluorite-type oxides represent the most common ionic conducting materials. The fluorite structure is represented by AO_2, where A is the large tetravalent cation such as Zr^{4+} or Ce^{4+}. Fluorite contains oxygen anions in simple cubic packing, with half of the interstices occupied by metal cations. The metal cations are surrounded by oxygen anions tetrahedrally coordinated to the metal cations. Two fluorite oxides have particularly been investigated for use as oxygen transport membrane materials: ZrO_2 and CeO_2.

At room temperature, ZrO_2 has a monoclinic crystal structure. Nevertheless, when the temperature increases, the crystal structure of ZrO_2 transforms to the tetragonal (>1000 °C) and cubic structures (>2300 °C) [80]. Trivalent cation oxides can be added to pure ZrO_2 in order to stabilize the cubic phase at room temperature [80 – 82]. The cubic ZrO_2 presents the advantage of having a higher ionic conductivity than the monoclinic crystal structure. Yttria-doped zirconia has been particularly investigated as an oxygen transport membrane material or an electrolyte material for solid oxide fuel cells due to its high ionic conductivity, its thermodynamic stability in oxidizing and reducing atmospheres and its good mechanical properties [83]. The highest ionic conductivity for $(ZrO_2)_{1-x}(Y_2O_3)_x$ materials is obtained for x = 0.08 (8YSZ), with 0.03 S cm^{-1} at 850 °C [84]. Further addition of yttria will decrease the ionic conductivity due to enhanced association of the oxygen vacancies and dopant cations, which results in defective complexes with low mobility [85]. During the past decades, other zirconia-based oxide ion conductors consisting of aliovalent dopants substituting zirconia such as $(ZrO_2)_{1-x}$-$(M_2O_3)_x$ (M= Sc [86 – 97], Yb [87, 89, 91, 92, 94, 95, 97], Gd [89, 91, 92, 94, 97], Dy [89, 91, 92, 94, 97], Eu [89, 91, 92, 94], Er [87, 91, 92, 94, 97], Nd [87, 94], La [87; 94], Sm [87, 94], Ce [86, 91], Ho [94], Pr [94], Tb [94], Lu [94]) and tertiary systems of two oxides co-doping zirconia like $(ZrO_2)_{1-(x+y)}$-$(M_2O_3)_x$-$(M'_2O_3)_y$ have been studied. Artemov *et al.* reported that the ionic conductivity of $(ZrO_2)_{0.89}(Sc_2O_3)_{0.10}(Y_2O_3)_{0.01}$ corresponds to 0.12 S cm^{-1} at 850 °C [98], which makes it a significantly better ionic conductor than 8YSZ.

Unlike ZrO_2, CeO_2 has a stable cubic fluorite structure at room temperature and, therefore, the structure does not need to be stabilized. However, the partial substitution of Ce^{4+} by divalent or trivalent ions is desired because it creates oxygen vacancies in the structure, due

to the lower valence of the doping ions compared with Ce^{4+} [99 – 101]. Over the past decades, many substitutions of ceria with alkaline earth or rare earth oxides have been attempted in order to increase its ionic conductivity. Systems based on CeO_2–M_2O_3 (M= Gd [87, 89 – 91, 101 – 104], Sm [89, 90, 101 – 103, 105], Y [89, 90, 101, 103], Dy [103], Nd [103], Eu [103], Yb [103], La [90, 101, 103], Sc [101]) and CeO_2–M'O (M'=Mg [101, 103], Sr [101, 103], Ba [101, 103], Ca [89]) were reported. Gadolinia and Samaria-doped ceria show the highest conductivities among the doped ceria materials. The high performances were attributed to the good match in ionic radii [106]. Figure 2. 5 shows the dependence of the ionic conductivity on ionic radius of M^{3+} for $(CeO_2)_{0.8}(M_2O_3)_{0.2}$ systems at 800 °C. The oxygen vacancies make gadolinium-doped ceria (CGO) one of the fastest oxide ion conductors, in spite of being an electronic conductor at high temperature in reducing atmosphere. Ionic conductivities of 0.06 S cm^{-1} and 0.078 S cm^{-1} were found at 800 °C and 850 °C for a dopant level of 20 mol.% Gd ($Ce_{0.8}Gd_{0.2}O_{2-\delta}$), respectively [107 – 109].

Bi_2O_3-doped metal oxides are another significant class of ionic conductors with high conductivity in comparison to doped ZrO_2 and CeO_2 [110]. Nevertheless, most bismuth oxide materials have extremely poor strength and tend to reduce in low partial pressure atmosphere, making them unsuitable for the intended power plant and industrial applications [97, 111].

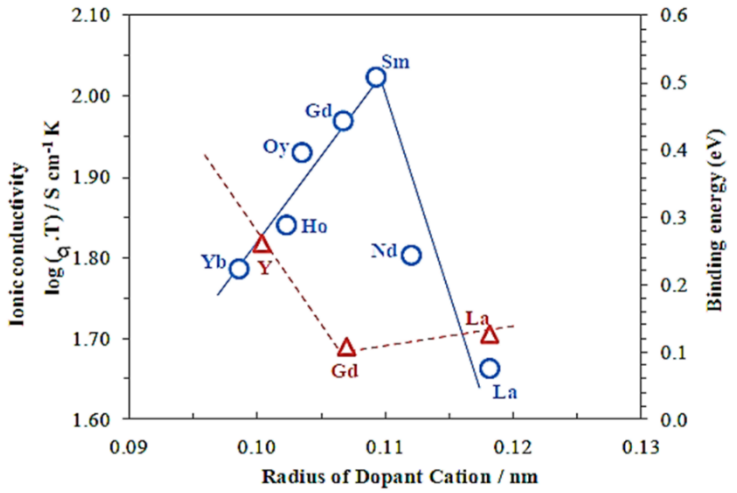

Figure 2. 5: Dependence of the ionic conductivity on ionic radius of M^{3+} for $(CeO_2)_{0.8}(M_2O_3)_{0.2}$ systems at 800 °C. Figure taken from [89].

2.4.2.2. Electronic conductors

Electronic conducting oxides have been investigated as electronic conductors for dual-phase membranes as replacements for the expensive noble metals originally used. These oxide can mainly be regrouped in two category of materials: spinel oxides type and perovskites.

- Spinels

Oxide spinels are described by the general formula AB_2O_4, where in most of the cases A and B are tetrahedral and octahedral cation sites in a cubic close packing of oxygen (Figure 2. 6). Nevertheless, some spinels such as $NiCr_2O_4$, $MgMn_2O_4$ or $ZnMn_2O_4$ have a tetragonal structure due to the Jahn–Teller distortion [112]. The conductivity of spinels originates from hopping of charges between octahedral sites [113]. Consequently, the presence of aliovalent octahedral cation is beneficial to conduction. Thus, Fe_3O_4, which is an inverse spinel with tetrahedral sites occupied by Fe^{3+} and octahedral sites filled by an equal proportion of Fe^{2+} and Fe^{3+} ions, has a conductivity over 100 S cm^{-1} at room temperature, the highest of all spinels [112]. On this basis, the strong octahedral site preference energies of Al^{3+} and Cr^{3+} explain why aluminium and chromium spinels are not good conductors. On the other hand, manganite and cobaltite families of spinels are the best-suited as high-temperature conductors because of their multiple valence states. Petric *et al.* showed that among a selection of twenty-six spinels, $MnCo_2O_4$ and $Mn_{1.7}Cu_{1.3}O_4$ present the two highest electrical conductivities with 60 S cm^{-1} at 800 °C and 225 S cm^{-1} at 750 °C, respectively [112].

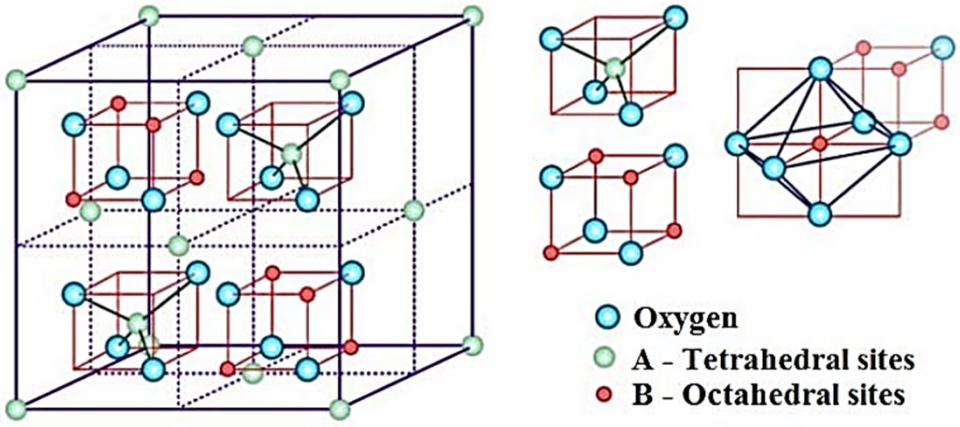

Figure 2. 6: Schematic drawing representing a unit cell of spinel structure.

- Perovskites

Over the past years, perovskites consisting of La as A-site cation and transition metals (Cr, Mn, Fe, Co and Ni) as B-site cation have been extensively investigated [114 – 117]. Manganites, ferrites, nickelates and cobaltites present higher electrical conductivities than chromates but also a lower stability in reducing atmospheres, which is one of the key requirement for some OTM applications (e.g. biomass gasification, partial oxidation of methane into syngas) [118]. For this reason, lanthanum chromite-based materials are also considered as interconnect materials for Solid Oxide Fuel Cells (SOFC) [119 – 125]. Moreover, the electrical conductivity of $LaCrO_3$ (0.6-1.0 S cm^{-1} at 1000 °C) [118] can be improved by using suitable dopants. These last may also help to densify the lanthanum chromite-based materials usually refractory to densification. Thus A-site and B-site dopants can be introduce to the formula $LaCrO_3$, forming the derivative formula $La_{1-x}A_xCr_{1-y}M_yO_{3-\delta}$, where A is an alkaline earth metal (A= Sr, Ca) and M is a transition metal (M= Mn, Fe, Co, Ni, Ti, Cu and Al). A-site dopants are generally acceptor type, they enhance densification and improve the electrical conductivity [126 – 130]. These studies showed that calcium and strontium doping on the A-site enhance the $LaCrO_3$ sintering by the formation of liquid phase ($CaCrO_4$/$SrCrO_4$) which dissolves back into the lattice with increase in temperature. Accordingly, $LaCrO_3$ has a relative low density of 50 % at 1450 °C, while $(La_{0.6}Ca_{0.4})_{1.02}CrO_3$ is 95 % dense at 1350 °C [131]. B-site dopants also enhance the conductivity but also maintain the thermal and crystal structured stability [118].

2.4.2.3. Performances of dual-phase oxygen transport membranes

Table 2. 2 gives an extensive list of dual-phase membrane performances investigated in literature. Most of the ionic and electronic conductors composing these dual-phase membranes have been discussed in the previous sections (2.4.2.1 and 2.4.2.2). The table provides the oxygen permeation fluxes permeating through the composite membranes and indicates the geometry and the thickness of the membranes as well as the atmosphere and the temperatures used during the tests.

From oxygen permeation fluxes reported in literature (temperature range 700–1000 °C), graphs gathering the performances of planar and tubular/capillary dual-phase membranes for transporting oxygen were plotted in Figures 2. 7 and 2. 8, respectively. Two parameters especially influence the performance of the membranes during a test: (i) the thickness of the

dense and selective membrane layer, and (ii) the driving force used through the membrane. In order to fairly compare the performances of dual-phase membranes for transporting oxygen, these two parameters need to be evaluated separately. Therefore, all dual-phase OTMs plotted in Figures 2. 7 and 2. 8 are composed of a dense separation layer of 300 µm or thinner and were tested using air as a feed gas and an inert gas as a sweep gas (He, Ar, N_2 or CO_2).

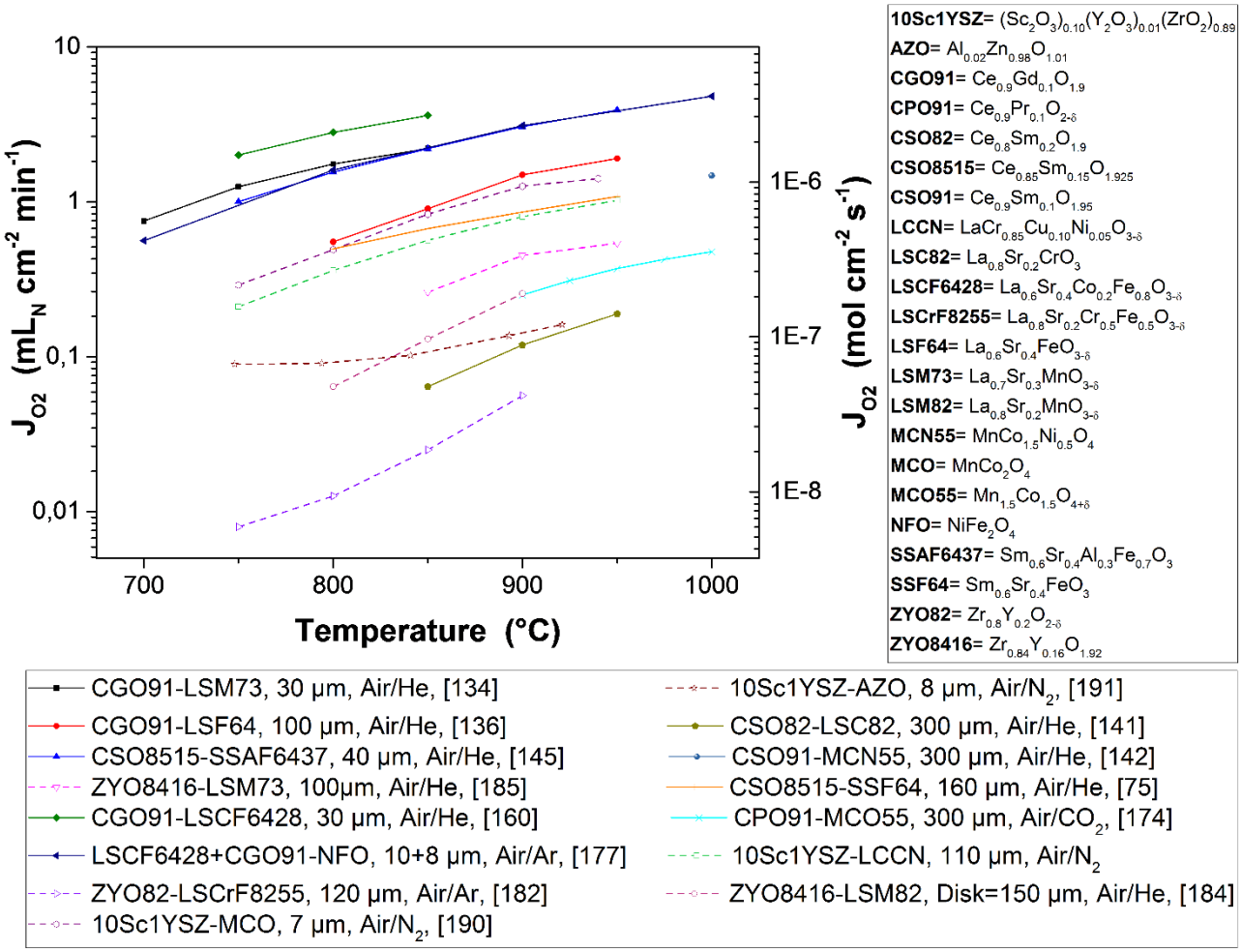

Figure 2. 7: Oxygen permeation flux of various thin (L ≤ 300 µm) planar dual-phase OTMs as a function of the temperature.

As demonstrated by Figures 2. 7 and 2. 8, most of the thin (L ≤ 300 µm) dual-phase OTMs reported in literature are planar (15 planar membranes, 6 tubular/hollow fiber membranes). In general, ceria-based membranes (solid lines) display higher oxygen permeability than zirconia-based membranes (dashed lines). It is a 8 µm thick $Ce_{0.9}Gd_{0.1}O_{2-\delta}$ – $NiFe_2O_4$ dual-phase membrane (containing also a 10 µm thick $La_{0.6}Sr_{0.4}Co_{0.2}Fe_{0.8}O_{3-\delta}$ dense layer)

developed by Gaudillere *et al.* that present the highest oxygen permeation flux with 3.58 µmol cm^{-2} s^{-1} at 1000 °C in Air/Ar. Among the zirconia-based membranes, the 10Sc1YSZ-MCO and 10Sc1YSZ-LCCN composites developed in this thesis display the two highest oxygen permeability, multiplying by 2 the highest oxygen permeation flux previously reported in the literature.

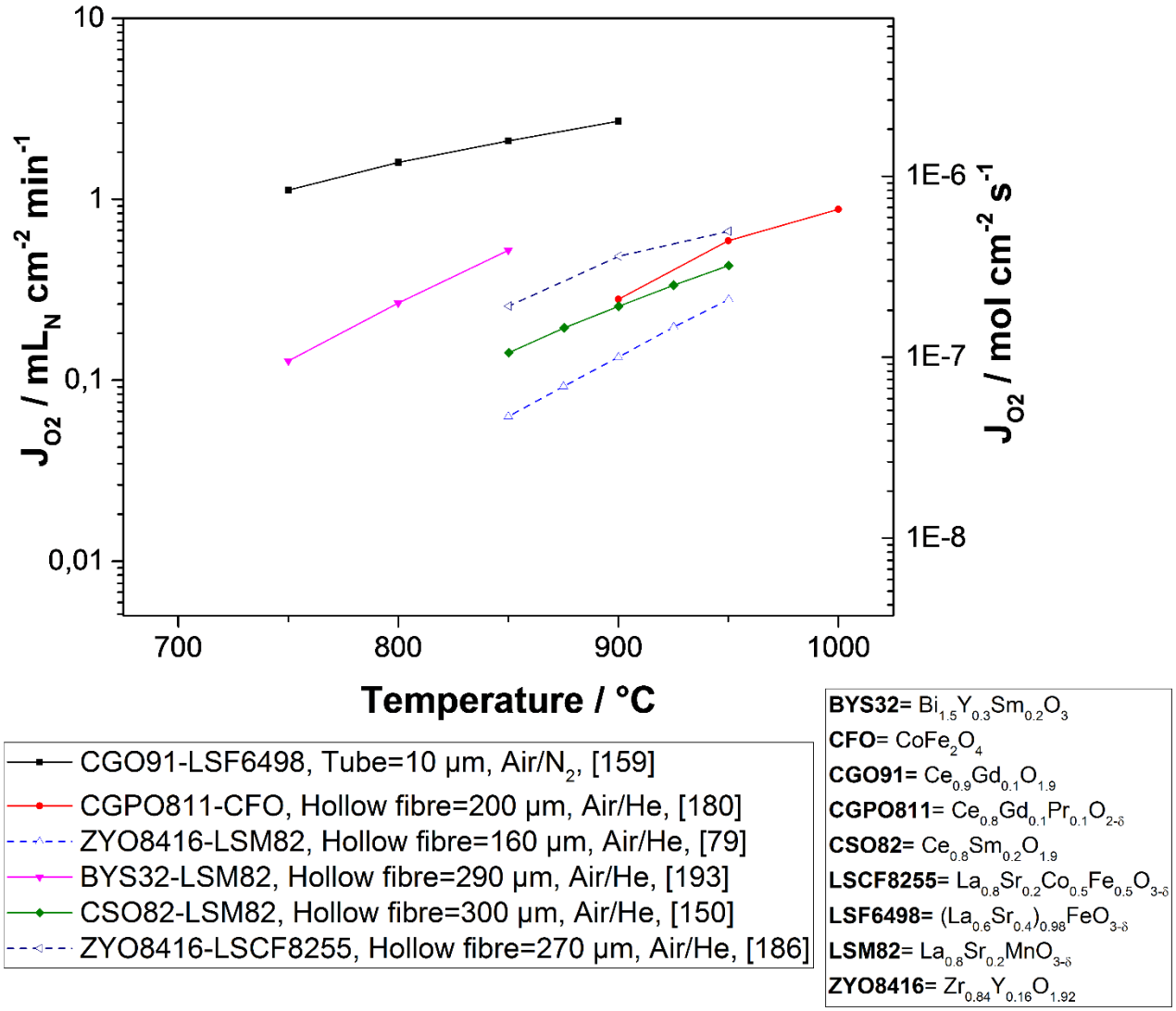

Figure 2. 8: Oxygen permeation flux of various thin (L ≤ 300 µm) tubular and capillary dual-phase OTMs as a function of the temperature.

Table 2. 2: Performance of various dual-phase OTMs investigated in the literature. L corresponds to the thickness of the dual-phase membrane.

	Materials	Geom.	L (μm)	Flux (μmol $cm^{-2}s^{-1}$)	T (°C)	Atm. $pO_2^{feed}/pO_2^{permeate}$	Ref.
1	$Ce_{0.8}Gd_{0.2}O_{1.9}$ - $La_{0.7}Sr_{0.3}MnO_3$	Planar	600	0.08	950	Air/He 0.21/0.01	[132]
2	$Ce_{0.8}Gd_{0.2}O_{1.9}$ - $La_{0.7}Sr_{0.3}MnO_3$	Planar	1000	0.040	950	Air/He 0.2/0.01	[133]
	$Ce_{0.8}Gd_{0.2}O_{1.9}$ - $La_{0.8}Sr_{0.2}Fe_{0.8}Co_{0.2}O_3$	Planar	1000	0.063	950	Air/He 0.2/0.01	
3	$Ce_{0.9}Gd_{0.1}O_{2-\delta}$ - $La_{0.7}Sr_{0.3}MnO_{3-\delta}$	Planar	30	1.64	850	Air/He	[134]
4	$Ce_{0.9}Gd_{0.1}O_{1.95}$ - Ag -CuO	Planar	1000	0.103	800	Air/N_2	[135]
	$Ce_{0.9}Gd_{0.1}O_{1.95}$ -$LaCoO_3$	Planar	1000	0.0742	800	Air/N_2	
	$Ce_{0.9}Gd_{0.1}O_{1.95}$ - $La_{0.6}Sr_{0.4}CoO_{3-\delta}$	Planar	1000	0.153	800	Air/N_2	
	$Ce_{0.9}Gd_{0.1}O_{1.95}$ - $La_{0.6}Sr_{0.4}FeO_{3-\delta}$	Planar	1000	0.0926	800	Air/N_2	
	$Ce_{0.9}Gd_{0.1}O_{1.95}$ – $(La_{0.6}Sr_{0.4})_{0.99}Co_{0.2}Fe_{0.8}O_{3-\delta}$	Planar	1000	0.136	800	Air/N_2	
	$Ce_{0.9}Gd_{0.1}O_{1.95}$ – $La_{0.75}Sr_{0.25}Cr_{0.97}V_{0.03}O_{3-\delta}$	Planar	1000	0.0448	800	Air/N_2	
5	$Ce_{0.9}Gd_{0.1}O_{1.95}$ - $La_{0.6}Sr_{0.4}FeO_{3-\delta}$	Planar	100	1.052	900	Air/He	[136]
6	$Ce_{0.75}Nd_{0.25}O_{1.875}$ - $Nd_{1.8}Ce_{0.2}CuO_4$	Planar	600 1030 1030 1030 1030	0.2 0.12 0.07 0.04 0.02	900 900 900 850 800	0.1/0.003 0.1/0.003 0.1/0.01 0.1/0.01 0.1/0.01	[137]
7	$Ce_{0.9}Nd_{0.1}O_{2-\delta}$ – $Nd_{0.6}Sr_{0.4}FeO_{3-\delta}$	Planar	600	0.358	950	Air/CO_2	[138]
8	$Ce_{0.8}Sm_{0.2}O_{2-\delta}$ – $SrCo_{0.9}Nb_{0.1}O_{3-\delta}$	Planar Planar	800 800	1.15 0.388	950 950	Air/He Air/CO_2	[139]
9	$Ce_{0.8}Sm_{0.2}O_{2-\delta}$ – $Ba_{0.95}La_{0.05}Zr_{0.1}Fe_{0.5}Co_{0.4}O_{3-\delta}$	Planar	1000	0.313	925	Air/He	[140]
10	$Ce_{0.8}Sm_{0.2}O_{1.9}$ - $La_{0.8}Sr_{0.2}CrO_3$	Planar	300	0.14	950	0.21/0.0092	[141]
11	$Ce_{0.9}Sm_{0.1}O_{1.95}$ -$MnCo_{1.5}Ni_{0.5}O_4$	Planar Planar	300 300	1.1 7	1000 1000	Air/He	[142]

	$Ce_{0.9}Sm_{0.1}O_{1.95}$ -$MnFe_2O_4$	Planar Planar	300 133	6 10	1000 1000	Air/Ar,CH_4 Air/Ar,CH_4 Air/Ar,CH_4	
12	$Ce_{0.8}Gd_{0.2}O_{1.9}$ - $Gd_{0.2}Sr_{0.8}FeO_3$	Planar Planar Planar Planar Planar	500 500 1000 1000 500	0.55 0.25 0.3 0.14 3.41	950 850 950 850 950	0.21/0.005 0.21/0.005 0.21/0.005 0.21/0.005 Air/syngas	[143]
13	$Ce_{0.85}Sm_{0.15}O_{1.925}$ - $Sm_{0.6}Sr_{0.4}FeO_3$	Planar Planar Planar	500 500 160	0.340 2.700 0.746	950 950 950	0.21/0.005 Air/Syngas Air/He	[144] [75]
14	$Ce_{0.85}Sm_{0.15}O_{1.925}$ - $Sm_{0.6}Sr_{0.4}Al_{0.3}Fe_{0.7}O_3$	Planar	40	2.910	950	Air/He	[145]
15	$Ce_{0.8}Sm_{0.2}O_{1.9}$ - $LaBaCo_2O_5$	Planar	600	0.46	950	0.21/0.005	[146]
16	$Ce_{0.8}Gd_{0.2}O_{1.9}$ - $CoFe_2O_4$	Planar	1000 1000	0.006 0.135	700 950	0.21/0.0001 Air/He	[147] [148]
17	$Ce_{0.9}Sm_{0.2}O_{1.9}$ - $La_{0.8}Sr_{0.2}CrO_3$	Tubular	1100	0.86	950	Air/CO $0.21/10^{-15}$	[149]
18	$Ce_{0.8}Sm_{0.2}O_{1.9}$ - $La_{0.8}Sr_{0.2}MnO_3$	Capillary Capillary	300 300	0.32 0.3	950 950	Air/He Air/CO_2	[150]
19	CeO_2 - $La_{0.2}Sr_{0.8}CoO_3$	Tubular	10	0.007	850	Air /He 0.21/0.001	[151]
20	$Ce_{0.8}Tb_{0.2}O_{2-\delta}$ - $NiFe_2O_4$	Planar	680	0.15	1000	Air/CO_2	[152]
21	$Ce_{0.8}Sm_{0.2}O_{2-\delta}$ - $PrBaCo_2O_{5+\delta}$	Planar	600	0.238	925	Air/He	[153]
22	$Ce_{0.9}Gd_{0.1}O_{1.95}$ - $Al_{0.02}Ga_{0.02}Zn_{0.96}O_{1.02}$	Planar Planar	1100 1100	0.16 0.40	860 940	Air/N_2 Air/N_2	[154]
23	$Ce_{0.8}Gd_{0.2}O_{2-\delta}$ - $GdBaCo_2O_{5+\delta}$	Planar	620	0.21	950	Air/He	[155]
24	$Ce_{0.8}Gd_{0.15}Cu_{0.05}O_{2-\delta}$ - $SrFeO_{3-\delta}$	Planar Planar	500 500	0.63 0.42	900 900	0.9/CO_2 Air/He	[156]
25	$Ce_{0.85}Gd_{0.1}Cu_{0.05}O_{2-\delta}$ - $La_{0.6}Ca_{0.4}FeO_{3-\delta}$	Planar Planar	500 500	0.52 0.65	950 950	Air/CO_2 Air/He	[157]
26	$Ce_{0.9}Gd_{0.1}O_{2-\delta}$ - $(La_{0.6}Sr_{0.4})_{0.98}Fe_{0.02}O_{3-\delta}$	Tubular	15	0.75	900	0.21/0.01	[158]
27	$Ce_{0.9}Gd_{0.1}O_{2-\delta}$-$(La_{0.6}Sr_{0.4})_{0.98}FeO_{3-\delta}$	Tubular Tubular	10 10	1.567 11.12	850 850	Air/N_2 Air/H_2	[159]
28	$Ce_{0.9}Gd_{0.1}O_{2-\delta}$ - $La_{0.6}Sr_{0.4}Co_{0.2}Fe_{0.8}O_{3-\delta}$	Planar	30	2.69	850	Air/He	[160]

29	$Ce_{0.8}Sm_{0.2}O_{2-\delta}$ - $La_{0.7}Ca_{0.3}CrO_{3-\delta}$	Planar	1000	0.11	950	Air/He	[161]
30	$Ce_{0.9}Gd_{0.1}O_{2-\delta}$ - $SrCo_{0.8}Fe_{0.1}Nb_{0.1}O_{3-\delta}$	Planar Planar	1000 600	0.36 0.60	900 900	Air/He Air/He	[162]
31	$Ce_{0.8}Sm_{0.2}O_{2-\delta}$ - $SrCO_3$ - Co_3O_4	Planar	500	0.694	900	Air/He	[163]
32	$Ce_{0.9}Gd_{0.1}O_{2-\delta}$ - Ag	Planar Planar	1000 1000	0.011 0.13	700 700	Air/Ar Air/CH_4	[164]
33	$Ce_{0.8}Sm_{0.2}O_{1.9}$ - $Y_{0.8}Ca_{0.2}Cr_{0.8}Co_{0.2}O_3$	Planar	1300	0.23	950	Air/N_2	[165]
34	$Ce_{0.8}Sm_{0.2}O_{3-\delta}$ - $Sm_{0.5}Sr_{0.5}Cu_{0.2}Fe_{0.8}O_{3-\delta}$	Planar Planar Planar	600 600 600	0.754 0.948 0.836	950 1000 1000	Air/He Air/He Air/CO_2	[166]
35	$Ce_{0.8}Sm_{0.2}O_{3-\delta}$ - $Sm_{0.3}Sr_{0.7}Cu_{0.2}Fe_{0.8}O_{3-\delta}$	Planar Planar Planar	600 600 600	0.776 1.01 0.858	950 1000 1000	Air/He Air/He Air/CO_2	[166]
36	$Ce_{0.8}Gd_{0.2}O_{2-\delta}$ - $FeCo_2O_4$	Planar	1000	0.082	850	Air/Ar	[167]
37	$Ce_{0.8}Sm_{0.2}O_{1.9}$ - $Sm_{0.8}Ca_{0.2}CoO_3$	Planar Planar	500 500	0.172 0.119	950 950	Air/He Air/CO_2	[168]
38	$Ce_{0.8}Sm_{0.2}O_{1.9}$ - $Sm_{0.6}Ca_{0.4}CoO_3$	Planar	500	0.41	950	0.21/0.0066	[169]
39	$Ce_{0.8}Sm_{0.2}O_{1.9}$ - $Sm_{0.6}Ca_{0.4}FeO_3$	Planar	500	0.336	950	0.21/0.006	[169]
40	$Ce_{0.8}Sm_{0.2}O_{1.9}$ - $Sm_{0.8}Ca_{0.2}Mn_{0.5}Co_{0.5}O_3$	Planar Planar Planar	500 500 500	0.187 0.254 0.463	850 900 940	0.21/0.005 0.21/0.005 0.21/0.005	[170]
41	$Ce_{0.8}Sm_{0.2}O_{2-\delta}$ – $La_{0.9}Sr_{0.1}FeO_{3-\delta}$	Planar Planar Planar	1100 1100 1100	0.642 0.159 0.159	900 950 950	Air/CO Air/CO_2 Air/He	[171]
42	$Ce_{0.9}Pr_{0.1}O_{2-\delta}$ – $Pr_{0.6}Sr_{0.4}FeO_{3-\delta}$	Planar Planar	600 600	0.194 0.134	950 950	Air/He Air/CO_2	[172]
43	$Ce_{0.8}Gd_{0.2}O_{2-\delta}$ - $Pr_{0.6}Sr_{0.4}Co_{0.5}Fe_{0.5}O_{3-\delta}$	Planar Planar Planar Planar	500 500 1000 1000	0.463 0.351 0.216 0.149	900 900 900 900	Air/He Air/CO_2 Air/He Air/CO_2	[173]
44	$Ce_{0.8}Gd_{0.2}O_{2-\delta}$ - $Pr_{0.6}Sr_{0.4}Co_{0.5}Fe_{0.4}Nb_{0.1}O_{3-\delta}$	Planar Planar Planar Planar	500 500 1000 1000	0.336 0.254 0.134 0.112	900 900 900 900	Air/He Air/CO_2 Air/He Air/CO_2	[173]
45	$Ce_{0.9}Pr_{0.1}O_{2-\delta}$ – $Mn_{1.5}Co_{1.5}O_{4-\delta}$	Planar Planar	300 300	0.358 0.276	1000 950	Air/CO_2 Air/CO_2	[174]

		Planar Planar	500 500	0.164 0.149	1000 1000	Air/He Air/CO_2	
46	$Ce_{0.9}Gd_{0.1}O_{2-\delta}$ – $Ba_{0.5}Sr_{0.5}Co_{0.8}Fe_{0.2}O_{3-\delta}$	Planar	500	0.5	950	Air/CO_2	[175]
47	$Ce_{0.9}Gd_{0.1}O_{2-\delta}$ – $NiFe_2O_4$	Planar Planar	500 500	0.19 0.16	950 950	Air/He Air/CO_2	[176]
48	$La_{0.6}Sr_{0.4}Co_{0.2}Fe_{0.8}O_{3-\delta}$ + $Ce_{0.9}Gd_{0.1}O_{2-\delta}$ – $NiFe_2O_4$	Planar	10 + 8	3.582	1000	Air/Ar	[177]
49	$Ce_{0.9}Gd_{0.1}O_{2-\delta}$ – Fe_2O_3	Planar	500	0.20	1000	Air/CO_2	[178]
50	$Ce_{0.9}Gd_{0.1}O_{2-\delta}$ – $MnFe_2O_4$	Planar Planar	1000 250	2.68 13.4	1000 1000	Air/Ar+5 % H_2 Air/Ar+10 % CH_4	[179]
51	$Ce_{0.8}Gd_{0.1}Pr_{0.1}O_{2-\delta}$ – $CoFe_2O_4$	Capillary Capillary Capillary Capillary	200 200 200 200	0.209 0.440 0.657 0.299	900 950 1000 950	Air/He Air/He Air/He Air/CO_2	[180]
52	$(ZrO_2)_{0.92}(Y_2O_3)_{0.08}$ – Pd $(ZrO_2)_{0.92}(Y_2O_3)_{0.08}$ – Pt $(ZrO_2)_{0.92}(Y_2O_3)_{0.08}$ – Boron doped $MgLaCrO_\lambda$ $(ZrO_2)_{0.92}(Y_2O_3)_{0.08}$ – $In_{0.9}Pr_{0.1}$	Planar Planar Planar Planar Planar Planar	800 800 800 800 300 250	2.1 1.8 0.4 2.3 5.5 6.1	1100 1100 1100 1100 1100 1100	Air/H_2 Air/H_2 Air/H_2 Air/H_2 Air/H_2 Air/H_2	[181]
53	$Zr_{0.8}Y_{0.2}O_{2-\delta}$ - $La_{0.8}Sr_{0.2}Cr_{0.5}Fe_{0.5}O_{3-\delta}$	Planar Planar Planar	120 120 120	0.045 0.131 0.896	900 900 900	Air/Ar Air/H_2 Air/CO	[182]
54	$(ZrO_2)_{0.92}(Y_2O_3)_{0.08}$ -$SrCo_{0.4}Fe_{0.6}O_{3-\delta}$	Planar Planar	1200 2000	0.597 0.269	750 850	0.21/0.001 0.21/0.001	[183]
55	$Zr_{0.84}Y_{0.16}O_{1.92}$ – $La_{0.8}Sr_{0.2}MnO_{3-\delta}$	Planar Capillary	150 160	0.190 0.210	900 950	0.21/0.002 Air/He	[184] [79]
56	$(ZrO_2)_{0.92}(Y_2O_3)_{0.08}$ -$La_{0.7}Sr_{0.3}MnO_{3-\delta}$	Planar Planar Planar	100 100 100	0.194 0.336 0.403	850 900 950	Air/He Air/He Air/He	[185]
57	$Zr_{0.84}Y_{0.16}O_{1.92}$ – $La_{0.8}Sr_{0.2}Cr_{0.5}Fe_{0.5}O_{3-\delta}$	Capillary Capillary	270 270	0.496 3.370	950 950	Air/He Air/CO	[186]
58	$Zr_{0.8}Y_{0.2}O_{1.9}$ – $La_{0.8}Sr_{0.2}CrO_{3-\delta}$	Tubular Tubular	1230 1230	0.0092 0.032	950 930	Air/He Air/He-CO (80-20 %)	[71]

59	$(ZrO_2)_{0.92}(Y_2O_3)_{0.08}$ – $La_{0.8}Sr_{0.2}CrO_{3-\delta}$	Planar Planar	115 115	0.910 1.120	750 850	Air/CO Air/CO	[187]
60	$Sc_{0.198}Ce_{0.012}Zr_{0.789}O_{1.90}$ – $(La_{0.8}Sr_{0.2})_{0.95}Cr_{0.5}Fe_{0.5}O_{3-\delta}$	Planar Planar Planar	20 200 300	2.640 0.552 0.396	900 900 900	Air/H_2 Air/H_2 Air/H_2	[188]
61	$Zr_{0.802}Sc_{0.18}Y_{0.018}O_{1.901}$-$(La_{0.8}Sr_{0.2})_{0.98}MnO_{3-\delta}$	Tubular	20-30	0.664	900	Air/H_2-CO	[189]
62	$(Y_2O_3)_{0.01}(Sc_2O_3)_{0.10}(ZrO_2)_{0.89}$ – $MnCo_2O_4$	Planar Planar Planar Planar Planar Planar Planar Planar Planar Planar	7 7 7 7 7 7 7 7 7 7	0.216 0.366 0.619 0.940 1.052 0.291 0.321 0.388 0.493 0.604	750 800 850 900 940 750 800 850 900 940	Air/N_2 Air/N_2 Air/N_2 Air/N_2 Air/N_2 Air/CO_2 Air/CO_2 Air/CO_2 Air/CO_2 Air/CO_2	[190]
63	$(Y_2O_3)_{0.01}(Sc_2O_3)_{0.10}(ZrO_2)_{0.89}$ – $Zn_{0.98}Al_{0.02}O_{1.01}$	Planar Planar	1000 8	0.246 0.119	925 925	Air/N_2 Air/N_2	[191]
64	$(Y_2O_3)_{0.01}(Sc_2O_3)_{0.10}(ZrO_2)_{0.89}$ – $LaCr_{0.85}Cu_{0.10}Ni_{0.05}O_{3-\delta}$	Planar Planar Planar Planar	1000 1000 110 110	0.198 0.183 0.762 0,743	950 950 950 950	Air/N_2 Air/CO_2 Air/N_2 Air/CO_2	This work
65	$(La_{0.9}Sr_{0.1})_{0.98}Ga_{0.8}Mg_{0.2}O_{3-\delta}$ – $La_2Ni_{0.8}Cu_{0.2}O_{4+\delta}$	Planar Planar	650 1000	0.027 0.017	900 900	0.21/0.013 0.21/0.013	[192]
66	$Bi_{1.5}Y_{0.3}Sm_{0.2}O_3$ – $La_{0.8}Sr_{0.2}MnO_{3-\delta}$	Capillary Capillary	290 290	0.39 0.013	850 650	Air/He Air/He	[193]
67	$La_{0.15}Sr_{0.85}Ga_{0.3}Fe_{0.7}O_{3-\delta}$ – $Ba_{0.5}Sr_{0.5}Fe_{0.2}Cr_{0.8}O_{3-\delta}$	Planar	1990	0.352	915	Air/He	[77]

References

[1] B.A. van Hassel, Oxygen transfer across composite oxygen transport membranes, Solid State Ionics. 174 (2004) 253–260. doi:10.1016/j.ssi.2004.07.034.

[2] H.J.M. Bouwmeester, Dense ceramic membranes for methane conversion, Catal. Today. 82 (2003) 141–150. doi:10.1016/S0920-5861(03)00222-0.

[3] S.J. Xu, W.J. Thomson, Oxygen permeation rates through ion-conducting perovskite membranes, Chem. Eng. Sci. 54 (1999) 3839–3850. doi:10.1016/S0009-2509(99)00015-9.

[4] P.J. Gellings, H.J.M. Bouwmeester, Ion and mixed conducting oxides as catalysts, Catal. Today. 12 (1992) 1–105. doi:10.1016/0920-5861(92)80046-P.

[5] H.J.M. Bouwmeester, A.J. Burggraaf, Dense ceramic membranes for oxygen separation, in: CRC Press (Ed.), CRC Handb. Solid State Electrochem., 1997.

[6] H.J.M. Bouwmeester, H. Kruidhof, A.J. Burggraaf, Importance of the surface exchange kinetics as rate limiting step in oxygen permeation through mixed-conducting oxides, Solid State Ionics. 72 (1994) 185–194.

[7] J.A. Lane, S.J. Benson, D. Waller, J.A. Kilner, Oxygen transport in $La_{0.6}Sr_{0.4}Co_{0.2}Fe_{0.8}O_{3-\delta}$, Solid State Ionics. 121 (1999) 201–208.

[8] Energy Information Administration, Annual Energy Review 2011, 2011. www.eia.gov/aer.

[9] M. Puig-Arnavat, S. Soprani, M. Søgaard, K. Engelbrecht, J. Ahrenfeldt, U.B. Henriksen, P.V. Hendriksen, Integration of mixed conducting membranes in an oxygen–steam biomass gasification process, RSC Adv. 3 (2013) 20843–20854. doi:10.1039/c3ra44509g.

[10] J.H. Joo, G.S. Park, C.Y. Yoo, J.H. Yu, Contribution of the surface exchange kinetics to the oxygen transport properties in $Gd_{0.1}Ce_{0.9}O_{2-\delta}$-$La_{0.6}Sr_{0.4}Co_{0.2}Fe_{0.8}O_{3-\delta}$ dual-phase membrane, Solid State Ionics. 253 (2013) 64–69. doi:10.1016/j.ssi.2013.08.038.

[11] J. Sirman, Chapter 6: The Evolution of Materials and Architecture for Oxygen Transport Membranes, in: Nonporous Inorg. Membr. Chem. Process., 2006: pp. 178–179.

[12] X. Dong, W. Jin, Mixed conducting ceramic membranes for high efficiency power generation with CO_2 capture, Curr. Opin. Chem. Eng. 1 (2012) 163–170. doi:10.1016/j.coche.2012.03.003.

[13] S. Baumann, J.M. Serra, M.P. Lobera, S. Escolástico, F. Schulze-Küppers, W.A. Meulenberg, Ultrahigh oxygen permeation flux through supported $Ba_{0.5}Sr_{0.5}Co_{0.8}Fe_{0.2}O_{3-\delta}$ membranes, J. Memb. Sci. 377 (2011) 198–205. doi:10.1016/j.memsci.2011.04.050.

[14] J. Gurauskis, Ø.F. Lohne, D.S. Lagergren, E.T. Wefring, K. Wiik, Oxygen permeation in symmetric and asymmetric $La_{0.2}Sr_{0.8}Fe_{0.8}Ta_{0.2}O_{3-\delta}$ membranes, J. Eur. Ceram. Soc. 36 (2016) 1427–1434. doi:10.1016/j.jeurceramsoc.2016.01.004.

[15] Z. Shao, W. Yang, Y. Cong, H. Dong, J. Tong, G. Xiong, Investigation of the permeation behavior and stability of a $Ba_{0.5}Sr_{0.5}Co_{0.8}Fe_{0.2}O_{3-\delta}$ oxygen membrane, J. Memb. Sci. 172 (2000) 177–188.

[16] Y. Teraoka, T. Nobunaga, N. Yamazoe, Effect of Cation Substitution on the Oxygen Semipermeability of Perovskite-type Oxides, Chem. Lett. (1988) 503–506.

[17] Z. Shao, G. Xiong, J. Tong, H. Dong, W. Yang, Ba effect in doped $Sr(Co_{0.8}Fe_{0.2})O_{3-\delta}$ on the phase structure and oxygen permeation properties of the dense ceramic membranes, Sep. Purif. Technol. 25 (2001) 419–429.

[18] J. Tong, W. Yang, R. Cai, B. Zhu, L. Lin, Novel and ideal zirconium-based dense membrane reactors for partial oxidation of methane to syngas, Catal. Letters. 78 (2002) 129–137.

[19] S. Liu, G.R. Gavalas, Oxygen selective ceramic hollow fiber membranes, J. Memb. Sci. 246 (2005) 103–108. doi:10.1016/j.memsci.2004.09.028.

[20] T. Nagai, W. Ito, T. Sakon, Relationship between cation substitution and stability of perovskite structure in $SrCoO_{3-\delta}$-based mixed conductors, Solid State Ionics. 177

(2007) 3433–3444. doi:10.1016/j.ssi.2006.10.022.

[21] P. Zeng, Z. Shao, S. Liu, P.Z. Xu, Influence of M cations on structural , thermal and electrical properties of new oxygen selective membranes based on $SrCo_{0.95}M_{0.05}O_{3-\delta}$ perovskite, Sep. Purif. Technol. 67 (2009) 304–311. doi:10.1016/j.seppur.2009.03.047.

[22] H. Luo, B. Tian, Y. Wei, H. Wang, Oxygen Permeability and Structural Stability of a Novel Tantalum-Doped Perovskite $BaCo_{0.7}Fe_{0.2}Ta_{0.1}O_{3-\delta}$, AIChE J. 56 (2010). doi:10.1002/aic.

[23] S. Gopalan, Using ceramic mixed ionic and electronic conductors for gas separation, J. Miner. Met. Mater. Soc. 54 (2002) 26–29. doi:10.1007/BF02701692.

[24] A.J. Jacobson, S. Kim, A. Medina, Y.L. Yang, A. Abeles, Dense oxide membranes for oxygen separation and methane conversion, Mater. Res. Soc. 497 (1998) 29–34. doi:https://doi.org/10.1557/PROC-497-29.

[25] A. Leo, S. Liu, J.C.D. da Costa, Development of mixed conducting membranes for clean coal energy delivery, Int. J. Greenh. Gas Control. 3 (2009) 357–367. doi:10.1016/j.ijggc.2008.11.003.

[26] W. Zhou, R. Ran, Z. Shao, Progress in understanding and development of $Ba_{0.5}Sr_{0.5}Co_{0.8}Fe_{0.2}O_{3-\delta}$-based cathodes for intermediate-temperature solid-oxide fuel cells: A review, J. Power Sources. 192 (2009) 231–246. doi:10.1016/j.jpowsour.2009.02.069.

[27] W. Yang, H. Wang, X. Zhu, L. Lin, Development and application of oxygen permeable membrane in selective oxidation of light alkanes, Top. Catal. 35 (2005) 155–167. doi:10.1007/s11244-005-3820-6.

[28] R. Kiebach, K. Engelbrecht, K. Kwok, S. Molin, M. Søgaard, P. Niehoff, F. Schulze-Küppers, R. Kriegel, J. Kluge, P.V. Hendriksen, Joining of ceramic $Ba_{0.5}Sr_{0.5}Co_{0.8}Fe_{0.2}O_3$ membranes for oxygen production to high temperature alloys, J. Memb. Sci. 506 (2016) 11–21. doi:10.1016/j.memsci.2016.01.050.

[29] P. Haworth, S. Smart, J. Glasscock, J.C. Diniz da Costa, High performance yttrium-

doped BSCF hollow fibre membranes, Sep. Purif. Technol. 94 (2012) 16–22. doi:10.1016/j.seppur.2012.04.005.

[30] M. Arnold, H. Wang, A. Feldhoff, Influence of CO_2 on the oxygen permeation performance and the microstructure of perovskite-type $(Ba_{0.5}Sr_{0.5})(Co_{0.8}Fe_{0.2})O_{3-\delta}$ membranes, J. Memb. Sci. 293 (2007) 44–52. doi:10.1016/j.memsci.2007.01.032.

[31] Z. Shao, W. Yang, Y. Cong, H. Dong, J. Tong, G. Xiong, Investigation of the permeation behavior and stability of a $Ba_{0.5}Sr_{0.5}Co_{0.8}Fe_{0.2}O_{(3-\delta)}$ oxygen membrane, J. Memb. Sci. 172 (2000) 177–188. doi:10.1016/S0376-7388(00)00337-9.

[32] L. Ge, W. Zhou, R. Ran, S. Liu, Z. Shao, W. Jin, N. Xu, Properties and performance of A-site deficient $(Ba_{0.5}Sr_{0.5})_{1-x}Co_{0.8}Fe_{0.2}O_{3-\delta}$ for oxygen permeating membrane, J. Memb. Sci. 306 (2007) 318–328. doi:10.1016/j.memsci.2007.09.004.

[33] Z. Taheri, K. Nazari, N. Seyed-Matin, A.A. Safekordi, B. Ghanbari, S. Zarrinpashne, R. Ahmadi, Comparison of oxygen permeation through some perovskite membranes synthesized with EDTNAD, React. Kinet. Mech. Catal. 100 (2010) 459–469. doi:10.1007/s11144-010-0158-2.

[34] F. Schulze-Küppers, S. Baumann, F. Tietz, H.J.M. Bouwmeester, W.A. Meulenberg, Towards the fabrication of $La_{0.98-x}Sr_xCo_{0.2}Fe_{0.8}O_{3-\delta}$ perovskite-type oxygen transport membranes, J. Eur. Ceram. Soc. 34 (2014) 3741–3748. doi:10.1016/j.jeurceramsoc.2014.06.012.

[35] X. Tan, Z. Wang, B. Meng, X. Meng, K. Li, Pilot-scale production of oxygen from air using perovskite hollow fibre membranes, J. Memb. Sci. 352 (2010) 189–196. doi:10.1016/j.memsci.2010.02.015.

[36] Y. Teraoka, H.-M. Zhang, S. Furukawa, N. Yamazoe, Oxygen permeation through perovskite-type oxides, Chem. Lett. (1985) 1743–1746.

[37] L. Qiu, T.H. Lee, L.M. Liu, Y.L. Yang, A.J. Jacobson, Oxygen permeation studies of $SrCo_{0.8}Fe_{0.2}O_{3-\delta}$, Solid State Ionics. 76 (1995) 321–329.

[38] S. Baumann, J.M. Serra, M.P. Lobera, S. Escolástico, F. Schulze-Küppers, W. a. Meulenberg, Ultrahigh oxygen permeation flux through supported

$Ba_{0.5}Sr_{0.5}Co_{0.8}Fe_{0.2}O_{3-\delta}$ membranes, J. Memb. Sci. 377 (2011) 198–205. doi:10.1016/j.memsci.2011.04.050.

[39] E. Bucher, A. Egger, G.B. Caraman, W. Sitte, Stability of the SOFC Cathode Material (Ba,Sr)(Co,Fe)$O_{3-\delta}$ in CO_2-Containing Atmospheres, J. Electrochem. Soc. 155 (2008) B1218. doi:10.1149/1.2981024.

[40] M. Pilar Lobera, S. Escolastico, J. Garcia-Fayos, J.M. Serra, Ethylene Production by ODHE in Catalytically Modified $Ba_{0.5}Sr_{0.5}Co_{0.8}Fe_{0.2}O_{3-\delta}$ Membrane Reactors, ChemSusChem. 5 (2012) 1587–1596. doi:10.1002/cssc.201100747.

[41] R. Kriegel, R. Kircheisen, J. Töpfer, Oxygen stoichiometry and expansion behavior of $Ba_{0.5}Sr_{0.5}Co_{0.8}Fe_{0.2}O_{3-\delta}$, Solid State Ionics. 181 (2010) 64–70. doi:10.1016/j.ssi.2009.11.012.

[42] S. Švarcová, K. Wiik, J. Tolchard, H.J.M. Bouwmeester, T. Grande, Structural instability of cubic perovskite $Ba_xSr_{1-x}Co_{1-y}Fe_yO_{3-\delta}$, Solid State Ionics. 178 (2008) 1787–1791. doi:10.1016/j.ssi.2007.11.031.

[43] A.S. Möbius, Charakterisierung perowskitischer Hochtemperaturmembranen zur Sauerstoffbereitstellung für fossil gefeuerte Kraftwerksprozesse, RWTH Aachen University, 2010.

[44] O. Ravkina, T. Klande, A. Feldhoff, Investigation of carbonates in oxygen-transporting membrane ceramics, J. Memb. Sci. 480 (2015) 31–38. doi:10.1016/j.memsci.2015.01.042.

[45] L.-W. Tai, M.M. Nasrallah, H.U. Anderson, D.M. Sparlin, S.R. Sehlin, Structure and electrical properties of $La_{1-x}Sr_xCo_{1-y}$, Fe_yO_3. Part 1 . The system La0.8Sr0.2Co1-yFeyO3, 76 (1995).

[46] J.W. Stevenson, T.R. Armstrong, R.D. Carneim, L.R. Pederson, W.J. Weber, Electrochemical Properties of Mixed Conducting Perovskites $La_{1-x}M_xCo_{1-y}Fe_yO_{3-\delta}$ (M = Sr, Ba, Ca), J. Electrochem. Soc. 143 (1996) 2722–2729. doi:10.1149/1.1837098.

[47] A. Petric, P. Huang, F. Tietz, Evaluation of La-Sr-Co-Fe-O perovskites for solid oxide fuel cells and gas separation membranes, Solid State Ionics. 135 (2000) 719–725.

doi:Proceedings Paper.

[48] H. Ullmann, N. Trofimenko, F. Tietz, D. Stöver, A. Ahmad-Khanlou, Correlation between thermal expansion and oxide ion transport in.pdf, Solid State Ionics. 138 (2000) 79–90.

[49] R.-R. Liu, S. Taniguchi, Y. Shiratori, K. Ito, K. Sasaki, Influence of SO_2 on the Long-term Durability of SOFC Cathodes, ECS Trans. 35 (2011) 2255–2260. doi:10.1149/1.3570221.

[50] D. Wang, J. Leng, Effect of SO_2 on Performance of Solid Oxide Fuel Cell Cathodes, Chem. Res. Chinese Univ. 28 (2012) 866–868.

[51] C. Lalanne, Synthèse et mise en forme de nouveaux matériaux de cathode pour piles ITSOFC: réalisation et tests de cellules, University of Bordeaux I, 2005.

[52] E. Boehm, Les nickelates $A_2MO_{4+\delta}$ nouveaux matériaux de cathode pour piles à combustible SOFC moyenne température, Unversity of Bordeaux I, 2002.

[53] M. Greenblatt, Ruddlesden-Popper properties $Ln_{n+1}Ni_nO_{3n+1}$ nickelates: structure and properties, Solid State Mater. Sci. 2 (1997) 174–183.

[54] A. Aguadero, M.J. Escudero, M. Pérez, J.A. Alonso, V. Pomjakushin, L. Daza, Effect of Sr content on the crystal structure and electrical properties of the system $La_{2-x}Sr_xNiO_{4+\delta}$ ($0 \leq x \leq 1$), Dalt. Trans. (2006) 4377–4383. doi:10.1039/B606316K.

[55] V.V. Kharton, A.A. Yaremchenko, A.L. Shaula, M.V. Patrakeev, E.N. Naumovich, D.I. Logvinovich, J.R. Frade, F.M.B. Marques, Transport properties and stability of Ni-containing mixed conductors with perovskite- and K_2NiF_4-type structure, J. Solid State Chem. 177 (2004) 26–37. doi:10.1016/S0022-4596(03)00261-5.

[56] E.N. Naumovich, V.V. Kharton, Atomic-scale insight into the oxygen ionic transport mechanisms in La_2NiO_4-based materials, J. Mol. Struct. THEOCHEM. 946 (2010) 57–64. doi:10.1016/j.theochem.2009.12.003.

[57] A.L. Shaula, E.N. Naumovich, A.P. Viskup, V. V. Pankov, A. V. Kovalevsky, V. V. Kharton, Oxygen transport in $La_2NiO_{4+\delta}$: Assessment of surface limitations and

multilayer membrane architectures, Solid State Ionics. 180 (2009) 812–816. doi:10.1016/j.ssi.2009.01.005.

[58] V. V Kharton, A.P. Viskup, E.N. Naumovich, F.M.B. Marques, Oxygen ion transport in La_2NiO_4 -based ceramics, J. Mater. Chem. 9 (1999) 2623–2629.

[59] D. ping Huang, Q. Xu, F. Zhang, W. Chen, H. xing Liu, J. Zhou, Synthesis and electrical conductivity of $La_2NiO_{4+\delta}$ derived from a polyaminocarboxylate complex precursor, Mater. Lett. 60 (2006) 1892–1895. doi:10.1016/j.matlet.2005.12.044.

[60] S.-Y. Jeon, M.-B. Choi, H.-N. Im, J.-H. Hwang, S.-J. Song, Oxygen ionic conductivity of $La_2NiO_{4+\delta}$ via interstitial oxygen defect, J. Phys. Chem. Solids. 73 (2012) 656–660. doi:10.1016/j.jpcs.2012.01.006.

[61] J.B. Smith, T. Norby, On the Steady-State Oxygen Permeation Through $La_2NiO_{4+\delta}$ Membranes, J. Electrochem. Soc. 153 (2006) A233 – A238. doi:10.1149/1.2138679.

[62] Y. Takeda, R. Kanno, M. Sakano, O. Yamamoto, M. Takeda, Y. Bando, H. Akinaga, K. Takita, J.B. Goodenough, Crystal chemistry and physical properties of La2-xSrxNiO4 (0<x<1.6), Mat. Res. Bull. 25 (1990) 293–306.

[63] V.V. Vashook, S.P. Tolochko, I.I. Yushkevich, L.V. Makhnach, I.F. Kononyuk, H. Altenburg, J. Hauck, H. Ullmann, Oxygen nonstoichiometry and electrical conductivity of the solid solutions $La_{2-x}Sr_xNiO_y$ ($0 \le x \le 0.5$), Solid State Ionics. 110 (1998) 245–253. doi:10.1016/S0167-2738(98)00134-9.

[64] K. Wu, S. Xie, G.S. Jiang, W. Liu, C.S. Chen, Oxygen permeation through $(Bi_2O_3)_{0.74}(SrO)_{0.26}$-Ag (40 % v/o) composite, J. Memb. Sci. 188 (2001) 189–193.

[65] J.W. ten Elshof, N.Q. Nguyen, M.W. den Otter, H.J.M. Bouwmeester, Oxygen Permeation Properties if Dense $Bi_{1.5}Er_{0.5}O_3$ - Ag Cermet Membranes, J. Electrochem. Soc. 144 (1997) 4361–4366.

[66] K. Kobayashi, T. Tsunoda, Oxygen permeation and electrical transport properties of 60 vol.% $Bi_{1.6}Y_{0.4}O_3$ and 40 vol.% Ag composite prepared by the sol-gel method, Solid State Ionics. 175 (2004) 405–408. doi:10.1016/j.ssi.2003.11.046.

[67] F.T. Akin, J.Y.S. Lin, Oxygen permeation through oxygen ionic or mixed-conducting ceramic membranes with chemical reactions, J. Memb. Sci. 231 (2004) 133–146. doi:10.1016/j.memsci.2003.11.012.

[68] J. Kim, Y.S. Lin, Synthesis and oxygen permeation properties of ceramic-metal dual-phase membranes, J. Memb. Sci. 167 (2000) 123–133.

[69] C.S. Chen, Ph.D Thesis, University of Twente, 1994.

[70] W. Li, T. Tian, F. Shi, Y. Wang, C. Chen, $Ce_{0.8}Sm_{0.2}O_{2-\delta}$-$La_{0.8}Sr_{0.2}MnO_{3-\delta}$ dual-phase composite hollow fiber membrane for oxygen separation, Ind. Eng. Chem. Res. 48 (2009) 5789–5793. doi:10.1016/j.memsci.2012.03.026.

[71] B. Wang, M. Zhan, D. Zhu, W. Liu, C. Chen, Oxygen permeation and stability of $Zr_{0.8}Y_{0.2}O_{0.9}$–$La_{0.8}Sr_{0.2}CrO_{3-\delta}$ dual-phase composite, J. Solid State Electrochem. 10 (2006) 625–628. doi:10.1007/s10008-006-0136-9.

[72] V. V. Kharton, A.V. Kovalevsky, A.P. Viskup, F.M. Figueiredo, A.A. Yaremchenko, E.N. Naumovich, F.M.B. Marques, Oxygen permeability of $Ce_{0.8}Gd_{0.2}O_{2-\delta}$-$La_{0.7}Sr_{0.3}MnO_{3-\delta}$ composite membranes, J. Electrochem. Soc. 147 (2000) 2814–2821. doi:10.1016/S1464-2859(00)88703-9.

[73] A.L. Shaula, V.V. Kharton, F.M.B. Marques, Phase interaction and oxygen transport in $La_{0.8}Sr_{0.2}Fe_{0.8}Co_{0.2}O_3$-$(La_{0.9}Sr_{0.1})_{0.98}Ga_{0.8}Mg_{0.2}O_3$ composites, J. Eur. Ceram. Soc. 24 (2004) 2631–2639. doi:10.1179/096797804225018633.

[74] V. V. Kharton, A.V. Kovalevsky, A.P. Viskup, A.L. Shaula, F.M. Figueiredo, E.N. Naumovich, F.M.B. Marques, Oxygen transport in $Ce_{0.8}Gd_{0.2}O_{2-\delta}$-based composite membranes, Solid State Ionics. 160 (2003) 247–258. doi:10.1016/S0167-2738(03)00183-8.

[75] Q. Li, X. Zhu, W. Yang, Single-step fabrication of asymmetric dual-phase composite membranes for oxygen separation, J. Memb. Sci. 325 (2008) 11–15. doi:10.1016/j.memsci.2008.08.002.

[76] X. Zhu, Q. Li, Y. Cong, W. Yang, Syngas generation in a membrane reactor with a highly stable ceramic composite membrane, Catal. Commun. 10 (2008) 309–312.

doi:10.1016/j.catcom.2008.09.014.

[77] H. Wang, W.S. Yang, Y. Cong, X. Zhu, Y.S. Lin, Structure and oxygen permeability of a dual-phase membrane, J. Memb. Sci. 224 (2003) 107–115. doi:10.1016/j.memsci.2003.07.003.

[78] J. Yi, Y. Zuo, W. Liu, L. Winnubst, C. Chen, Oxygen permeation through a $Ce_{0.8}Sm_{0.2}O_{2-\delta}$-$La_{0.8}Sr_{0.2}CrO_{3-\delta}$ dual-phase composite membrane, J. Memb. Sci. 280 (2006) 849–855. doi:10.1016/j.memsci.2006.03.011.

[79] W. Li, J.J. Liu, C.S. Chen, Hollow fiber membrane of yttrium-stabilized zirconia and strontium-doped lanthanum manganite dual-phase composite for oxygen separation, J. Memb. Sci. 340 (2009) 266–271. doi:10.1016/j.memsci.2009.05.052.

[80] D. Wang, Y. Guo, K. Liang, K. Tao, Crystal structure of zirconia by Rietveld refinement, Sci. China (Series A). 42 (1999) 80–86. doi:10.1007/BF02872053.

[81] H. Arashi, H. Naito, Oxygen permeability in ZrO_2-TiO_2-Y_2O_3 system, Solid Stat. 53-56 (1992) 431–435.

[82] Y. Nigara, Y. Kosaka, K. Kawamura, J. Mizusaki, M. Ishigame, Oxygen permeability in ZrO_2 -CeO_2 -MgO at high temperatures, Solid State Ionics. 86-88 (1996) 739–744.

[83] M.M. Hiroaki Yanagida, Kunihiko Koumoto, Kunihito Komoto, The Chemistry of Ceramics, 1996.

[84] X.J. Chen, K.A. Khor, S.H. Chan, L.G. Yu, Influence of microstructure on the ionic conductivity of yttria-stabilized zirconia electrolyte, Mater. Sci. Eng. A. 335 (2002) 246–252. doi:10.1016/S0921-5093(01)01935-9.

[85] V.V. Kharton, E.N. Naumovich, A.A. Vecher, Research on the electrochemistry of oxygen ion conductors in the former Soviet Union. I. ZrO_2 -based ceramic materials, J. Solid State Electrochem. 3 (1999) 61–81. doi:10.1007/s100080050131.

[86] J.W. Fergus, Electrolytes for solid oxide fuel cells, J. Power Sources. 162 (2006) 30–40. doi:10.1016/j.jpowsour.2006.06.062.

[87] J.B. Goodenough, Oxide-ion electrolytes, Annu. Rev. Mater. Res. 33 (2003) 91–128.

[88] S.J. Skinner, J.A. Kilner, Oxygen ion Conductors, Mater. Today. (2003) 30–37.

[89] T. Ishihara, N.M. Sammes, O. Yamamoto, Chapter 4: Electrolytes, in: High-Temperature Solid Oxide Fuel Cells Fundam. Des. Appl., 2003: pp. 83–117.

[90] J.W. Fergus, Materials Challenges for Solid Oxide Fuel Cells, J. Miner. Met. Mater. (2007) 56–62.

[91] O. Yamamoto, Solid oxide fuel cells: fundamental aspects and prospects, Electrochim. Acta. 45 (2000) 2423–2435. doi:10.1016/S0013-4686(00)00330-3.

[92] Y. Arachi, H. Sakai, O. Yamamoto, Y. Takeda, N. Imanishai, Electrical conductivity of the ZrO_2 – Ln_2O_3 (Ln = lanthanides) system, Solid State Ionics. 121 (1999) 133–139. doi:10.1016/S0167-2738(98)00540-2.

[93] S.P.S. Badwal, F.T. Ciacchi, D. Milosevic, Scandia–zirconia electrolytes for intermediate temperature solid oxide fuel cell operation, Solid State Ionics. 136-137 (2000) 91–99. doi:10.1016/S0167-2738(00)00356-8.

[94] T.H. Estell, S.N. Flengas, Electrical properties of solid oxide electrolytes, Chem. Rev. 70 (1970) 339–376.

[95] O. Yamamoto, Y. Arati, Y. Takeda, N. Imanishi, Y. Mizutani, M. Kawai, Y. Nakamura, Electrical-Conductivity of Stabilized Zirconia with Ytterbia and Scandia, Solid State Ionics. 79 (1995) 137–142. <Go to ISI>://A1995RL16900026.

[96] A. Weber, E. Ivers-Tiffée, Materials and concepts for solid oxide fuel cells (SOFCs) in stationary and mobile applications, J. Power Sources. 127 (2004) 273–283. doi:10.1016/j.jpowsour.2003.09.024.

[97] V.V. Kharton, F.M.B. Marques, A. Atkinson, Transport properties of solid oxide electrolyte ceramics: a brief review, Solid State Ionics. 174 (2004) 135–149. doi:10.1016/j.ssi.2004.06.015.

[98] V.G. Artemov, I.E. Kuritsyna, S.P. Lebedev, G.A. Komandin, P.O. Kapralov, I.E. Spektor, V.V Kharton, S.I. Bredikhin, A.A. Volkov, Analysis of electric properties of ZrO_2-Y_2O_3 single crystals using teraherz IR and impedance spectroscopy techniques,

Russ. J. Electrochem. 50 (2014) 690–693. doi:10.1134/S1023193514070039.

[99] S. Wang, T. Kobayashi, M. Dokiya, T. Hashimoto, Electrical and Ionic Conductivity of Gd-Doped Ceria, J. Electrochem. Soc. 147 (2000) 3606–3609. doi:10.1149/1.1393946.

[100] B.C.H. Steele, Appraisal of $Ce_{1-y}Gd_yO_{2-y/2}$ electrolytes for IT-SOFC operation at 500C, Solid State Ionics. 129 (2000) 95–110.

[101] M. Mogensen, N.M. Sammes, G.A. Tompsett, Physical, chemical and electrochemical properties of pure and doped ceria, Solid State Ionics. 129 (2000) 63–94. doi:Doi 10.1016/S0167-2738(99)00318-5.

[102] J.M. Ralph, A.C. Schoeler, M. Krumpelt, Materials for lower temperature solid oxide fuel cells, J. Mater. Sci. 36 (2001) 1161–1172.

[103] H. Inaba, H. Tagawa, Cera-based solid electrolytes, Solid State Ionics. 83 (1996) 1–16.

[104] E. Ivers-Tiffée, A. Weber, D. Herbstritt, Materials and technologies for SOFC-components, J. Eur. Ceram. Soc. 21 (2001) 1805–1811. doi:10.1016/S0955-2219(01)00120-0.

[105] X. Sha, Z. Lü, X. Huang, J. Miao, L. Jia, X. Xin, W. Su, Preparation and properties of rare earth co-doped $Ce_{0.8}Sm_{0.2-x}Y_xO_{1.9}$ electrolyte materials for SOFC, J. Alloys Compd. 424 (2006) 315–321. doi:10.1016/j.jallcom.2005.12.061.

[106] H. Yahiro, K. Eguchi, H. Arai, Electrical properties and reducibilities of ceria-rare earth oxide systems and their application to Solid Oxide Fuel Cell, Solid State Ionics. 36 (1989) 71–75.

[107] M. Balaguer, C. Solís, J.M. Serra, Structural−Transport Properties Relationships on $Ce_{1-x}Ln_xO_{2-\delta}$ System (Ln = Gd , La , Tb , Pr , Eu , Er , Yb , Nd) and Effect of Cobalt Addition, J. Phys. Chem. 116 (2012) 7975–7982.

[108] M. Mogensen, T. Lindegaard, U.R. Hansen, G. Mogensen, Physical Properties of Mixed Conductor Solid Oxide Fuel Cell Anodes of Doped CeO_2, J. Electrochem. Soc.

141 (1994) 2122–2128. doi:10.1149/1.2055072.

[109] Y. Lin, S. Fang, D. Su, K.S. Brinkman, F. Chen, Enhancing grain boundary ionic conductivity in mixed ionic–electronic conductors, Nat. Commun. 6 (2015) 6824. doi:10.1038/ncomms7824.

[110] H.J.B. P. J. Gellings, The CRC Handbook of Solid State Electrochemistry, 1997.

[111] Sukhvinder, P.S. Badwal, F.T. Ciacchi, Ceramic membranes for oxygen separation, Adv. Mater. 13 (2001) 993–996. doi:10.1016/S0958-2118(01)80295-0.

[112] A. Petric, H. Ling, Electrical conductivity and thermal expansion of spinels at elevated temperatures, J. Am. Ceram. Soc. 90 (2007) 1515–1520. doi:10.1111/j.1551-2916.2007.01522.x.

[113] T. Horita, Y. Xiong, H. Kishimoto, K. Yamaji, N. Sakai, M.E. Brito, H. Yokakawa, Oxide Scale Formation on Alloy Interconnects in CH4 Fuels for Solid Oxide Fuel Cells, Solid Oxide Fuel Cells IX. (2001) 603–610.

[114] H.U. Anderson, Review of p-type doped perovskite materials for SOFC and other applications, Solid State Ionics. 52 (1992) 33–41.

[115] J. Mizusaki, Nonstoichiometry, diffusion, and electrical properties of perovskite-type oxide electrode materials, Solid State Ionics. 52 (1992) 79–91.

[116] H. Yokokawa, N. Sakai, T. Kawada, M. Dokiya, Thermodynamic stabilities of perovskite oxides for electrodes and other electrochemical materials, Solid State Ionics. 52 (1992) 43–56.

[117] R.E. Williford, P. Singh, Engineered cathodes for high performance SOFCs, J. Power Sources. 128 (2004) 45–53.

[118] S. Gupta, M.K. Mahapatra, P. Singh, Lanthanum chromite based perovskites for oxygen transport membrane, Mater. Sci. Eng. R Reports. 90 (2015) 1–36. doi:10.1016/j.mser.2015.01.001.

[119] N. Sakai, H. Yokokawa, T. Horita, K. Yamaji, Lanthanum Chromite-Based Interconnects as Key Materials for SOFC Stack Development, Int. J. Appl. Ceram.

Technol. 1 (2004) 23–30. doi:10.1111/j.1744-7402.2004.tb00151.x.

[120] J.G.M. Furtado, R.N. Oliveira, Development of lanthanum chromites-based materials for solid oxide fuel cell interconnects, Rev. Matéria. 13 (2008) 147–153. doi:10.1016/j.ssi.2004.04.010.

[121] P. Singh, N.Q. Minh, Solid Oxide Fuel Cells: Technology Status, Int. J. Appl. Ceram. Technol. 1 (2004) 5–15. doi:10.1111/j.1744-7402.2004.tb00149.x.

[122] N. Xu, H. Zhao, W. Wei, X. Lu, W. Ding, F. Li, Dependence of critical radius of the cubic perovskite ABO_3 oxides on the radius of A- and B-site cations, Int. J. Hydrogen Energy. 35 (2010) 7295–7301.

[123] Z.G. Yang, J.W. Stevenson, P. Singh, Solid Oxide Fuel Cells, Adv. Mater. Process. 161 (2003) 34–37.

[124] J.W. Fergus, Lanthanum chromite-based materials for solid oxide fuel cell interconnects, Solid State Ionics. 171 (2004) 1–15.

[125] T. Horita, Chapter 15: $LaCrO_3$-based Perovskite for SOFC Interconnects, in: Perovskite Oxide Solid Oxide Fuel Cells, 2009: pp. 285–296.

[126] M. Mori, Y. Hiei, N.M. Sammes, Sintering behavior and mechanism of Sr-doped lanthanum chromites with A site excess composition in air, Solid State Ionics. 123 (1999) 103–111.

[127] M. Mori, Y. Hiei, N.M. Sammes, Sintering behavior of Ca- or Sr-doped $LaCrO_3$ perovskites including second phase of $AECrO_4$ (AE=Sr, Ca) in air, Solid State Ionics. 135 (2000) 743–748.

[128] L.A. Chick, J. Liu, J.W. Stevenson, T.R. Armstrong, D.E. McCready, G.D. Maupin, G.W. Coffey, C.A. Coyle, Phase Transitions and Transient Liquid-Phase Sintering in Calcium-Substituted Lanthanum Chromite, J. Am. Ceram. Soc. 80 (1997) 2109–2120. doi:10.1111/j.1151-2916.1997.tb03095.x.

[129] S. Simner, J. Hardy, J. Stevenson, T. Armstrong, Sintering of non-stoichiometric strontium doped lanthanum chromite, J. Mater. Sci. Lett. 19 (2000) 863–865.

doi:10.1023/A:1006733414271.

[130] S. Simner, J.S. Hardy, J.W. Stevenson, T.R. Armstrong, Sintering mechanisms in strontium doped lanthanum chromite, J. Mater. Sci. 34 (1999) 5721–5732. <Go to ISI>://000083227700005.

[131] J.D. Carter, M.M. Nasrallah, H.U. Anderson, Liquid phase behaviour in nonstoichiometric calcium-doped lanthanum chromites, J. Mater. Sci. 31 (1996) 157–163. doi:10.1007/BF00355140.

[132] V.V. Kharton, A.V. Kovalevsky, A.P. Viskup, F.M. Figueiredo, A.A. Yaremchenko, E.N. Naumovich, F.M.B. Marques, Oxygen Permeability of $Ce_{0.8}Gd_{0.2}O_{3-\delta}$-$La_{0.7}Sr_{0.3}MnO_{3-\delta}$ Composite Membranes, J. Electrochem. Soc. 147 (2000) 2814–2821.

[133] V.. Kharton, A.V. Kovalevsky, A.P. Viskup, A.L. Shaula, F.M. Figueiredo, E.N. Naumovich, F.M.B. Marques, Oxygen transport in $Ce_{0.8}Gd_{0.2}O_{2-\delta}$-based composite membranes, Solid State Ionics. 160 (2003) 247–258. doi:10.1016/S0167-2738(03)00183-8.

[134] J.H. Joo, K.S. Yun, J.H. Kim, Y. Lee, C.Y. Yoo, J.H. Yu, Substantial Oxygen Flux in Dual-Phase Membrane of Ceria and Pure Electronic Conductor by Tailoring the Surface, ACS Appl. Mater. Interfaces. 7 (2015) 14699–14707. doi:10.1021/acsami.5b03392.

[135] A.J. Samson, M. Søgaard, P. Vang Hendriksen, $(Ce,Gd)O_{2-\delta}$-based dual phase membranes for oxygen separation, J. Memb. Sci. 470 (2014) 178–188. doi:10.1016/j.memsci.2014.07.028.

[136] S. Cheng, H. Huang, S. Ovtar, S.B. Simonsen, M. Chen, W. Zhang, M. Søgaard, A. Kaiser, P.V. Hendriksen, C. Chen, High-Performance Microchanneled Asymmetric $Gd_{0.1}Ce_{0.9}O_{1.95-\delta}$-$La_{0.6}Sr_{0.4}Fe_{O3-\delta}$-Based Membranes for Oxygen Separation, ACS Appl. Mater. Interfaces. 8 (2016) 4548–4560. doi:10.1021/acsami.5b10714.

[137] K. Kobayashi, M. Nishioka, K. Sato, T. Inoue, S. Hamakawa, T. Tsunoda, Synthesis and oxygen permeation properties of 75 mol.% $Ce_{0.}75Nd_{0.25}O_{1.875}$–25 mol.% $Nd_{1.8}Ce_{0.2}CuO_4$ composite, J. Solid State Electrochem. 10 (2006) 629–634.

doi:10.1007/s10008-006-0137-8.

[138] H. Luo, T. Klande, Z. Cao, F. Liang, H. Wang, J. Caro, A CO_2-stable reduction-tolerant Nd-containing dual phase membrane for oxyfuel CO_2 capture, J. Mater. Chem. A. 2 (2014) 7780–7787. doi:10.1039/c3ta14870j.

[139] S. Guo, Z. Liu, J. Zhu, X. Jiang, Z. Song, W. Jin, Highly oxygen-permeable and CO_2-stable $Ce_{0.8}Sm_{0.2}O_{2-\delta}$-$SrCo_{0.9}Nb_{0.1}O_{3-\delta}$ dual-phase membrane for oxygen separation, Fuel Process. Technol. 154 (2016) 19–26. doi:10.1016/j.fuproc.2016.07.009.

[140] P. Wang, H. Cheng, Y. Wang, X. Lu, X. Zou, L. Luo, Investigation of Co–doped Dual $Ce_{0.8}Sm_{0.2}O_{2-\delta}$ –$Ba_{0.95}La_{0.05}Zr_{0.1}Fe_{0.9-x}Co_xO_{3-\delta}$ phase Oxygen Transport Membranes, MATEC Web Conf. 67 (2016) 1–6.

[141] J. Yi, Y. Zuo, W. Liu, L. Winnubst, C. Chen, Oxygen permeation through a $Ce_{0.8}Sm_{0.2}O_{2-\delta}$-$La_{0.}8Sr_{0.2}CrO_{3-\delta}$ dual-phase composite membrane, J. Memb. Sci. 280 (2006) 849–855. doi:10.1016/j.memsci.2006.03.011.

[142] H. Takamura, T. Kobayashi, T. Kasahara, A. Kamegawa, M. Okada, Oxygen permeation and methane reforming properties of ceria-based composite membranes, J. Alloys Compd. 408 (2006) 1084–1089. doi:10.1016/j.jallcom.2004.12.139.

[143] X. Zhu, W. Yang, Composite membrane based on ionic conductor and mixed conductor for oxygen permeation, AIChE J. 54 (2008) 665–672. doi:10.1002/aic.

[144] X. Zhu, Q. Li, Y. He, Y. Cong, W. Yang, Oxygen permeation and partial oxidation of methane in dual-phase membrane reactors, J. Memb. Sci. 360 (2010) 454–460. doi:10.1016/j.memsci.2010.05.044.

[145] Z. Cao, X. Zhu, W. Li, B. Xu, L. Yang, W. Yang, Asymmetric dual-phase membranes prepared via tape-casting and co-lamination for oxygen permeation, Mater. Lett. 147 (2015) 88–91. doi:10.1016/j.matlet.2015.02.033.

[146] T. Chen, H. Zhao, N. Xu, Y. Li, X. Lu, W. Ding, F. Li, Synthesis and oxygen permeation properties of a $Ce_{0.8}Sm_{0.2}O_{2-\delta}$–$LaBaCo_2O_{5+\delta}$ dual-phase composite membrane, J. Memb. Sci. 370 (2011) 158–165. doi:10.1016/j.memsci.2011.01.007.

[147] I. Kagomiya, T. Iijima, H. Takamura, Oxygen permeability of nanocrystalline $Ce_{0.8}Gd_{0.2}O_{1.9}$-$CoFe_2O_4$ mixed-conductive films, J. Memb. Sci. 286 (2006) 180–184. doi:10.1016/j.memsci.2006.09.032.

[148] Y. Lin, S. Fang, D. Su, K.S. Brinkman, F. Chen, Enhancing grain boundary ionic conductivity in mixed ionic–electronic conductors, Nat. Commun. 6 (2015) 6824. doi:10.1038/ncomms7824.

[149] B. Wang, J. Yi, L. Winnubst, C. Chen, Stability and oxygen permeation behavior of $Ce_{0.8}Sm_{0.2}O_{2-\delta}$–$La_{0.8}Sr_{0.2}CrO_{3-\delta}$ composite membrane under large oxygen partial pressure gradients, J. Memb. Sci. 286 (2006) 22–25. doi:10.1016/j.memsci.2006.06.009.

[150] W. Li, T. Tian, F. Shi, Y. Wang, C. Chen, $Ce_{0.8}Sm_{0.2}O_{2-\delta}$-$La_{0.8}Sr_{0.2}MnO_{3-\delta}$ Dual-Phase Composite Hollow Fiber Membrane for Oxygen Separation, Ind. Eng. Chem. Res. 48 (2009) 5789–5793. doi:10.1016/j.memsci.2012.03.026.

[151] X. Yin, L. Hong, Z. Liu, Oxygen permeation through the LSCO-80/CeO_2 asymmetric tubular membrane reactor, J. Memb. Sci. 268 (2006) 2–12. doi:10.1016/j.memsci.2005.06.005.

[152] M. Balaguer, J. García-Fayos, C. Solís, J.M. Serra, Fast Oxygen Separation Through SO_2 - and CO_2 -Stable Dual-Phase Membrane Based on $NiFe_2O_4$ –$Ce_{0.8}Tb_{0.2}O_{2-\delta}$, Chem. Mater. 25 (2013) 4986–4993. doi:10.1021/cm4034963.

[153] T. Chen, H. Zhao, Z. Xie, L. Feng, X. Lu, W. Ding, F. Li, Electrical conductivity and oxygen permeability of $Ce_{0.8}Sm_{0.2}O_{2-\delta}$–$PrBaCo_2O_{5+\delta}$ dual-phase composites, Int. J. Hydrogen Energy. 37 (2012) 5277–5285. doi:10.1016/j.ijhydene.2011.12.113.

[154] S. Cheng, M. Søgaard, L. Han, W. Zhang, M. Chen, a. Kaiser, P. V. Hendriksen, A novel CO_2 - and SO_2-tolerant dual phase composite membrane for oxygen separation, Chem. Commun. 51 (2015) 7140–7143. doi:10.1039/C5CC00001G.

[155] M.B. Choi, S.Y. Jeon, H.J. Hwang, J.Y. Park, S.J. Song, Composite of $Ce_{0.8}Gd_{0.2}O_{2-\delta}$ and $GdBaCo_2O_{5+\delta}$ as oxygen separation membranes, Solid State Ionics. 181 (2010) 1680–1684. doi:10.1016/j.ssi.2010.09.027.

[156] W. Fang, F. Steinbach, C. Chen, A. Feldhoff, An Approach To Enhance the CO_2 Tolerance of Fluorite-Perovskite Dual-Phase Oxygen-Transporting Membrane, Chem. Mater. 27 (2015) 7820–7826. doi:10.1021/acs.chemmater.5b03823.

[157] W. Fang, F. Liang, Z. Cao, F. Steinbach, A. Feldhoff, A mixed ionic and electronic conducting dual-phase membrane with high oxygen permeability, Angew. Chemie - Int. Ed. 54 (2015) 4847–4850. doi:10.1002/anie.201411963.

[158] J. Gurauskis, S. Ovtar, A. Kaiser, M. Søgaard, P.V. Hendriksen, Ceria based composite membranes for oxygen separation, ECS Trans. 64 (2014) 251–258. doi:10.1149/06402.

[159] S. Ovtar, J. Gurauskis, A. Bjørnetun Haugen, C. Chatzichristodoulou, A. Kaiser, P.V. Hendriksen, Oxygen transport properties of tubular $Ce_{0.9}Gd_{0.1}O_{1.95}$-$La_{0.6}Sr_{0.4}FeO_{3-\delta}$ composite asymmetric oxygen permeation membranes supported on magnesium oxide, J. Memb. Sci. 523 (2017) 576–587. doi:10.1016/j.memsci.2016.09.060.

[160] J.H. Joo, K.S. Yun, Y. Lee, J. Jung, C.Y. Yoo, J.H. Yu, Dramatically enhanced oxygen fluxes in fluorite-rich dual-phase membrane by surface modification, Chem. Mater. 26 (2014) 4387–4394. doi:10.1021/cm501240f.

[161] S. Fang, C. Chen, L. Winnubst, Effect of microstructure and catalyst coating on the oxygen permeability of a novel CO_2-resistant composite membrane, Solid State Ionics. 190 (2011) 46–52. doi:10.1016/j.ssi.2011.03.009.

[162] J. Zhou, X. Tang, D. He, C. Wu, Y. Zhang, W. Ding, Y. Jin, C. Sun, Oxygen permeability and CO_2-tolerance of $Ce_{0.9}Gd_{0.1}O_{2-\delta}$ – $SrCo_{0.8}Fe_{0.1}Nb_{0.1}O_{3-\delta}$ dual-phase membrane, J. Alloys Compd. 646 (2015) 204–210. doi:10.1016/j.jallcom.2015.06.116.

[163] Z. Zhang, W. Zhou, Y. Chen, D. Chen, J. Chen, S. Liu, W. Jin, Z. Shao, Novel Approach for Developing Dual-Phase Ceramic Membranes for Oxygen Separation through Beneficial Phase Reaction, ACS Appl. Mater. Interfaces. 7 (2015) 22918–22926. doi:10.1021/acsami.5b05812.

[164] E. Ruiz-Trejo, P. Boldrin, J.L. Medley-Hallam, J. Darr, A. Atkinson, N.P. Brandon, Partial oxidation of methane using silver/gadolinia-doped ceria composite

membranes, Chem. Eng. Sci. 127 (2015) 269–275. doi:10.1016/j.ces.2015.01.047.

[165] K.J. Yoon, O.A. Marina, Highly stable dual-phase $Y_{0.8}Ca_{0.2}Cr_{0.8}Co_{0.2}O_3$-$Sm_{0.2}Ce_{0.8}O_{1.9}$ ceramic composite membrane for oxygen separation, J. Memb. Sci. 499 (2016) 301–306. doi:10.1016/j.memsci.2015.10.064.

[166] K. Partovi, C.H. Rüscher, F. Steinbach, J. Caro, Enhanced oxygen permeability of novel Cu-containing CO_2-tolerant dual-phase membranes, J. Memb. Sci. 503 (2016) 158–165. doi:10.1016/j.memsci.2016.01.019.

[167] M. Ramasamy, S. Baumann, J. Palisaitis, F. Schulze-Küppers, M. Balaguer, D. Kim, W.A. Meulenberg, J. Mayer, R. Bhave, O. Guillon, M. Bram, Influence of Microstructure and Surface Activation of Dual-Phase Membrane $Ce_{0.8}Gd_{0.2}O_{2-\delta}$-$FeCo_2O_4$ on Oxygen Permeation, J. Am. Ceram. Soc. 99 (2016) 349–355. doi:10.1111/jace.13938.

[168] H. Li, Y. Liu, X. Zhu, Y. Cong, S. Xu, W. Xu, W. Yang, Oxygen permeation through Ca-contained dual-phase membranes for oxyfuel CO_2 capture, Sep. Purif. Technol. 114 (2013) 31–37. doi:10.1016/j.seppur.2013.04.021.

[169] H. Li, X. Zhu, Y. Liu, W. Wang, W. Yang, Comparative investigation of dual-phase membranes containing cobalt and iron-based mixed conducting perovskite for oxygen permeation, J. Memb. Sci. 462 (2014) 170–177. doi:10.1016/j.memsci.2014.03.047.

[170] X. Zhu, H. Liu, Y. Cong, W. Yang, Novel dual-phase membranes for CO_2 capture via an oxyfuel route, Chem. Commun. 48 (2012) 251. doi:10.1039/c1cc16631j.

[171] Z. Wang, W. Sun, Z. Zhu, T. Liu, W. Liu, A novel cobalt-free, CO_2-stable, and reduction-tolerant dual-phase oxygen-permeable membrane, ACS Appl. Mater. Interfaces. 5 (2013) 11038–11043. doi:10.1021/am403272z.

[172] H. Luo, H. Jiang, T. Klande, Z. Cao, Novel Cobalt-Free, Noble Metal-Free Oxygen-Permeable $40Pr_{0.6}Sr_{0.4}FeO_{3-\delta}$–$60Ce_{0.9}Pr_{0.1}O_{2-\delta}$ Dual-Phase Membrane, Chem. Mater. 24 (2012) 2148–2154. http://pubs.acs.org/doi/abs/10.1021/cm300710p.

[173] H. Cheng, P. Wang, H. Zhao, K. Li, X. Lu, Q. Xu, Synthesis, CO_2-tolerance and rate-determining step of Nb-doped $Ce_{0.8}Gd_{0.2}O_{2-\delta}$–$Pr_{0.6}Sr_{0.4}Co_{0.5}Fe_{0.5}O_{3-\delta}$ ceramic

membranes, Ceram. Int. 43 (2017) 6477–6486. doi:10.1016/j.ceramint.2017.02.068.

[174] H. Luo, H. Jiang, T. Klande, F. Liang, Z. Cao, H. Wang, J. Caro, Rapid glycine-nitrate combustion synthesis of the CO_2-stable dual phase membrane $40Mn_{1.5}Co_{1.5}O_{4-\delta}$–$60Ce_{0.9}Pr_{0.1}O_{2-\delta}$ for CO_2 capture via an oxy-fuel process, J. Memb. Sci. 423-424 (2012) 450–458. doi:10.1016/j.memsci.2012.08.046.

[175] J. Xue, Q. Liao, Y. Wei, Z. Li, H. Wang, A CO_2-tolerance oxygen permeable $60Ce_{0.9}Gd_{0.1}O_{2-\delta}$-$40Ba_{0.5}Sr_{0.5}Co_{0.8}Fe_{0.2}O_{3-\delta}$ dual phase membrane, J. Memb. Sci. 443 (2013) 124–130. doi:10.1016/j.memsci.2013.04.067.

[176] H. Luo, K. Efimov, H. Jiang, A. Feldhoff, H. Wang, J. Caro, CO_2-stable and cobalt-free dual-phase membrane for oxygen separation, Angew. Chemie - Int. Ed. 50 (2011) 759–763. doi:10.1002/anie.201003723.

[177] C. Gaudillere, J. Garcia-Fayos, M. Balaguer, J.M. Serra, Enhanced Oxygen Separation through Robust Freeze-Cast Bilayered Dual-Phase Membranes., ChemSusChem. 7 (2014) 2554–2561. doi:10.1002/cssc.201402324.

[178] H. Luo, H. Jiang, K. Efimov, F. Liang, H. Wang, J. Caro, CO_2-Tolerant Oxygen-Permeable Fe_2O_3-$Ce_{0.9}Gd_{0.1}O_{2-\delta}$ Dual Phase Membranes, Ind. Eng. Chem. Res. 50 (2011) 13508–13517. doi:10.1021/ie200517t.

[179] H. Takamura, K. Okumura, Y. Koshino, A. Kamegawa, M. Okada, Oxygen permeation properties of ceria-ferrite-based composites, in: J. Electroceramics, 2004: pp. 613–618. doi:10.1007/s10832-004-5167-y.

[180] X. Bi, X. Meng, P. Liu, N. Yang, Z. Zhu, R. Ran, S. Liu, A novel CO_2-resistant ceramic dual-phase hollow fiber membrane for oxygen separation, J. Memb. Sci. 522 (2017) 91–99. doi:10.1016/j.memsci.2016.09.008.

[181] T.J. Mazanec, T.L. Cable, J.G. Frye, Electrocatalytic Cells for Chemical-Reaction, Solid State Ionics. 53 (1992) 111–118. doi:10.1016/0167-2738(92)90372-V.

[182] W. Fang, Y. Zhang, J. Gao, C. Chen, Oxygen permeability of asymmetric membrane of functional $La_{0.8}Sr_{0.2}Cr_{0.5}Fe_{0.5}O_{3-\delta}$ (LSCrF)-$Zr_{0.8}Y_{0.2}O_{2-\delta}$ (YSZ) supported on porous YSZ, Ceram. Int. 40 (2014) 799–803. doi:10.1016/j.ceramint.2013.06.070. ~~PhD~~

~~student~~

[183] S. Lia, W. Jin, N. Xu, J. Shi, Mechanical strength, and oxygen and electronic transport properties of $SrCo_{0.4}Fe_{0.6}O_{3-\delta}$-YSZ membranes, J. Memb. Sci. 186 (2001) 195–204.

[184] W. He, H. Huang, J. fen Gao, L. Winnubst, C. sheng Chen, Phase-inversion tape casting and oxygen permeation properties of supported ceramic membranes, J. Memb. Sci. 452 (2014) 294–299. doi:10.1016/j.memsci.2013.09.063.

[185] K.S. Yun, C.Y. Yoo, S.G. Yoon, J.H. Yu, J.H. Joo, Chemically and thermo-mechanically stable LSM-YSZ segmented oxygen permeable ceramic membrane, J. Memb. Sci. 486 (2015) 222–228. doi:10.1016/j.memsci.2015.03.049.

[186] T. Liu, Y. Wang, R. Yuan, J. Gao, C. Chen, H.J.M. Bouwmeester, Enhancing the oxygen permeation rate of $Zr_{0.84}Y_{0.16}O_{1.92}$-$La_{0.8}Sr_{0.2}Cr_{0.5}Fe_{0.5}O_{3-\delta}$ dual-phase hollow fiber membrane by coating with Ce0.8Sm0.2O1.9 nanoparticles, ACS Appl. Mater. Interfaces. 5 (2013) 9454–9460.

[187] A.S. Yu, T.-S. Oh, R. Zhu, A. Gallegos, R.J. Gorte, J.M. Vohs, Surface modification of $La_{0.8}Sr_{0.2}CrO_{3-\delta}$–YSZ dual-phase membranes for syngas production, Faraday Discuss. 182 (2015) 213–225. doi:10.1039/C5FD00007F.

[188] Z. Dehaney-Steven, D. Papargyriou, J.T.S. Irvine, Flux investigations on composite $(La_{0.8}Sr_{0.2})_{0.95}Cr_{0.5}Fe_{0.5}O_{3-\delta}$-$Sc_{0.198}Ce_{0.012}Zr_{0.789}O_{1.90}$ oxygen transport membranes, Solid State Ionics. 288 (2016) 338–341. doi:10.1016/j.ssi.2016.01.017.

[189] S. Gupta, J.J. Adams, J.R. Wilson, E.G. Eddings, M.K. Mahapatra, P. Singh, Performance and post-test characterization of an OTM system in an experimental coal gasifier, Appl. Energy. 165 (2016) 72–80. doi:10.1016/j.apenergy.2015.12.077.

[190] S. Pirou, J. Gurauskis, V. Gil, M. Søgaard, P.V. Hendriksen, A. Kaiser, S. Ovtar, R. Kiebach, Oxygen permeation flux through 10Sc1YSZ-$MnCo_2O_4$ asymmetric membranes prepared by two-step sintering, Fuel Process. Technol. 152 (2016) 192–199. doi:10.1016/j.fuproc.2016.06.019.

[191] S. Pirou, J.M. Bermudez, P.V. Hendriksen, A. Kaiser, T. Ramirez, M. Millan, R. Kiebach, Stability and performance of robust dual-phase

$(ZrO_2)_{0.89}(Y_2O_3)_{0.01}(Sc_2O_3)_{0.10}$-$Al_{0.02}Zn_{0.98}O_{1.01}$ oxygen transport membranes, J. Memb. Sci. 543 (2017) 18–27. doi:10.1016/j.memsci.2017.08.044.

[192] A.L. Shaula, V. V. Kharton, F.M.B. Marques, A. V. Kovalevsky, A.P. Viskup, E.N. Naumovich, Oxygen permeability of mixed-conducting composite membranes: Effects of phase interaction, J. Solid State Electrochem. 10 (2006) 28–40. doi:10.1007/s10008-005-0650-1.

[193] C. Yang, Q. Xu, C. Liu, J. Liu, C. Chen, W. Liu, $Bi_{1.5}Y_{0.3}Sm_{0.2}O_3$-$La_{0.8}Sr_{0.2}MnO_{3-\delta}$ dual-phase composite hollow fiber membrane for oxygen separation, Mater. Lett. 65 (2011) 3365–3367. doi:10.1016/j.matlet.2011.07.062.

Chapter 3: Objectives and content of the thesis

The main objective of this thesis was to develop highly efficient and chemically stable oxygen transport membranes for direct integration in oxy-fuel combustion power plants, which entails that the permeating oxygen is swept and directly diluted using recirculated flue gas. To succeed, several challenges had to be studied and solved:

1) Identification of suitable materials: The manufacturing concept of stable and highly permeating oxygen transport membranes is based on the development of thin dense dual-phase membranes. These thin layers, applied on a porous support, open up the possibility of minimizing solid state diffusion barriers. The infiltration of nano-sized catalytic coatings in the porous support creates catalytic surface activation layers to overcome slow surface exchange/reaction kinetics. Materials fulfilling all the required proprieties for the development of these asymmetric membranes had to be identified. The required properties were, among others, the chemical, thermal and mechanical stability under realistic power plant conditions (applicable to all layers), high ionic and electronic conductivities (selective membrane layer), good mechanical strength (porous support), no reactivity between the materials (all layers), and compatible thermal expansion coefficients (all layers). As a result of an initial literature study, three dual-phase composites were studied in parallel as dense selective membrane: $(ZrO_2)_{0.89}(Y_2O_3)_{0.01}(Sc_2O_3)_{0.10}$-$MnCo_2O_4$ (**sub-chapters 5.1.** and **5.2.**), $(ZrO_2)_{0.89}(Y_2O_3)_{0.01}(Sc_2O_3)_{0.10}$-$Al_{0.0}2Zn_{0.98}O_{1.01}$ (**sub-chapter 5.3**.) and $(ZrO_2)_{0.89}(Y_2O_3)_{0.01}(Sc_2O_3)_{0.10}$-$LaCr_{0.85}Cu_{0.10}Ni_{0.05}O_{3-\delta}$ (**sub-chapters 5.4.** and **5.5.**). The porous support was, in all cases made of 3YSZ, while several catalytic porous backbone materials were studied depending on the dual-phase membrane used (8YSZ, 10ScYSZ-$MnCo_2O_4$, $Ce_{0.8}Tb_{0.2}O_{2-\delta}$ (CTO)-$NiFe_2O_4$ (NFO) and 10ScYSZ-$LaCr_{0.85}Cu_{0.10}Ni_{0.05}O_{3-\delta}$).
2) Development of planar asymmetric membranes: In practice, the approach entails the parallel development of all layers: stable porous supports, thin dense dual-phase membrane layers, porous catalytic backbones and meso-porous nano-particulate catalytic coatings. All layers were produced separately by tape-casting. The asymmetric membranes were assembled by lamination. Adapted co-sintering cycles

were used to achieve thin dense membrane layers supported on mechanically strong porous supports. Catalytic surface activation was performed by infiltrations of aqueous catalytic solutions into the porous backbones. During these steps, several issues were encountered (e.g. unfavorable shrinkage behavior between layers, instability of materials or diffusion of elements during sintering, unsuccessful catalyst infiltrations in the porous layers due to unsuitable pore size or pore connectivity, etc.) making the development of the membranes challenging.

3) Membrane testing: As proof of concept, the planar developed membranes were tested under idealized conditions (air (feed gas)/N_2 (sweep gas)) and under realistic power plant conditions (air (feed gas)/250 ppm of SO_2, 3 vol.% H_2O, 5 vol.% O_2 balanced by CO_2 (sweep gas)). Short tests (few days) were performed to obtain the performances of the membranes between 750 °C and 950 °C, while long-term tests (250 h-1700 h) were carried out at 850 °C to verify the stability of the membranes under harsh conditions (CO_2, or CO_2 + SO_2 + H_2O (sweep gas)).

This thesis consists of 6 chapters, which are briefly described below.

Chapter 1 gives a general introduction on oxygen transport membranes (OTMs) in the context of carbon capture and storage (CCS) and utilization (CCU).

Chapter 2 summarizes the background on oxygen transport membranes. The chapter explains the operating process of OTMs (**sub-chapter 2.1.**) and summarizes the transport mechanism of oxygen ions through the membranes (**sub-chapter 2.2.**). Additionally, an overview of the typical membrane geometries is presented (**sub-chapter 2.3.**) and a brief literature review on membrane materials (single + dual-phase membranes) is done (**sub-chapter 2.4.**).

Chapter 3 describes the objectives of the thesis and its content.

Chapter 4 presents the fabrication and characterization techniques used in this study. It gives a general description of the shaping techniques used: tape-casting, lamination, de-binding and sintering, and catalyst activation of porous structures (**sub-chapter 4.1.**). Microstructural and electrochemical characterization techniques performed on the raw materials and assembled membranes are presented (**sub-chapter 4.2.**). Finally, the

experimental set-ups used for oxygen permeation measurements and the corresponding calculations to obtain the oxygen flux permeating through the membranes are detailed (**sub-chapter 4.3.**).

Chapter 5 is the results and discussion part of this thesis. It deals with the development and characterizations of the oxygen transport membranes studied during the thesis. This chapter is based on four publications which are treated individually in separate sub-chapters (**sub-chapters 5.1.** to **5.4.**), and a section of unpublished results obtained on the development and tests of supported $(ZrO_2)_{0.89}(Y_2O_3)_{0.01}(Sc_2O_3)_{0.10}$-$LaCr_{0.85}Cu_{0.10}Ni_{0.05}O_{3-\delta}$ oxygen transport membranes (**sub-chapter 5.5.**). The contents of the sub-chapters are detailed below.

Sub-chapter 5.1. contains the manuscript "Oxygen permeation flux through 10Sc1YSZ-$MnCo_2O_4$ asymmetric membranes prepared by a two-step sintering" published in *Fuel Processing Technology* (2016). This manuscript describes the development and performances of thin (7 µm) $(Y_2O_3)_{0.01}(Sc_2O_3)_{0.10}(ZrO_2)_{0.89}$ – $MnCo_2O_4$ dual-phase membranes supported on zirconia porous structures. The composite membranes were prepared by tape-casting, lamination, and fired in a two-step sintering process, and then characterized with respect to sinterability, microstructure and oxygen transport properties.

Sub-chapter 5.2. presents the manuscript "Improving performance of oxygen transport membranes in simulated oxy-fuel power plant conditions by catalytic surface enhancement". This study investigates the stability of dual-phase oxygen transport membranes consisting of 70 vol.% $(Y_2O_3)_{0.01}(Sc_2O_3)_{0.10}(ZrO_2)_{0.89}$ and 30 vol.% $MnCo_2O_4$ and the influence of catalytic porous backbones on their performance in a simulated oxy-fuel power plant flue-gas atmosphere (SO_2, H_2O, CO_2). The stability of a 7 µm thick asymmetric membrane was evaluated by a long-term test (170 h) performed in simulated oxy-fuel power plant flue-gas (250 ppm SO_2 + 5 % O_2 + 3 % H_2O balanced in CO_2). Aiming to achieve a better understanding of oxygen surface reactions (especially in oxy-fuel conditions), five catalytic porous backbone materials—(i) $(Y_2O_3)_{0.08}(ZrO_2)_{0.92}$ (8YSZ), (ii) 8YSZ-MCO (40-60 vol.%), (iii) 10Sc1YSZ-MCO (40-60 vol.%), (iv) 10Sc1YSZ-MCO (70-30 vol.%), and (v) $Ce_{0.8}Tb_{0.2}O_{2-\delta}$ (CTO)-$NiFe_2O_4$ (NFO) (40-60 vol.%)—were prepared and characterized by electrochemical impedance spectroscopy (EIS). Finally, oxygen permeation measurements

were performed on 0.5 mm thick 10Sc1YSZ-MCO membranes coated with (i) 8YSZ, (ii) 10Sc1YSZ-MCO and (iii) CTO-NFO activated porous backbones to investigate the influence of the backbones on the performance of the membrane under clean conditions (sweep gas: Ar) and oxy-fuel conditions (sweep gas: SO_2 + CO_2 + Ar).

Sub-chapter 5.3. includes the manuscript "Stability and performance of robust dual-phase $(ZrO_2)_{0.89}(Y_2O_3)_{0.01}(Sc_2O_3)_{0.10}$-$Al_{0.02}Zn_{0.98}O_{1.01}$ oxygen transport membranes" published in the *Journal of Membrane Science* (2017). The study presents development and characterizations of 50 vol.% $Al_{0.02}Zn_{0.98}O_{1.01}$ and 50 vol.% $(ZrO_2)_{0.89}(Y_2O_3)_{0.01}(Sc_2O_3)_{0.10}$ dual phase composite oxygen transport membranes. The stability of the composite membrane in gas streams containing CO_2, SO_2 and H_2O was investigated in order to verify the applicability of the membrane in oxy-fuel power plant schemes involving direct exposure to flue gas. Additionally, long-term electrical conductivity measurements (900 h) and oxygen permeation tests were performed to demonstrate the potential of the composite material as oxygen transport membrane.

Sub-chapter 5.4. contains the manuscript "Performances and stability of $(ZrO_2)_{0.89}(Y_2O_3)_{0.01}(Sc_2O_3)_{0.10}$-$LaCr_{0.85}Cu_{0.10}Ni_{0.05}O_{3-\delta}$ oxygen transport membranes under conditions relevant for oxy-fuel combustion". This article presents the development and characterization of self-standing dual-phase oxygen transport membranes consisting of 70 vol.% of $(ZrO_2)_{0.89}(Y_2O_3)_{0.01}(Sc_2O_3)_{0.10}$ (10Sc1YSZ) and 30 vol.% of $LaCr_{0.85}Cu_{0.10}Ni_{0.05}O_{3-\delta}$ (LCCN). The stability of the composite membrane was studied in conditions relevant for oxy-fuel combustion (CO_2, SO_2, H_2O). X-ray diffraction (XRD), X-ray fluorescence (XRF), attenuated total reflection Fourier transform infrared spectroscopy (ATR-FTIR), Raman spectroscopy and scanning electronic microscopy with energy dispersive X-ray spectroscopy (SEM-EDX) were used to characterize the material after exposure to the gases. Oxygen permeation fluxes across 1000 µm thick and 110 µm thick self-supported 10Sc1YSZ-LCCN (70-30 vol.%) membranes were measured from 700 °C to 950 °C using air as the feed gas and N_2 or CO_2 as the sweep gas. Tests were performed to study the influence of (i) the thickness, (ii) the catalyst layer and (iii) the operation time, on the performances of the membrane.

Sub-chapter 5.5. presents a brief overview of unpublished results and the main challenges related to the development of supported thin $(ZrO_2)_{0.89}(Y_2O_3)_{0.01}(Sc_2O_3)_{0.10}$-$LaCr_{0.85}Cu_{0.10}Ni_{0.05}O_{3-\delta}$ oxygen transport membranes. Supported 10Sc1YSZ-LCCN membranes were developed using two architectures (symmetric and asymmetric supported membranes). After de-binding and sintering processes fully dense membrane layers were obtained however the porous support structures were too dense to allow ideal gases diffusion and ideal catalyst infiltrations. Despite the imperfect microstructure, a 10Sc1YSZ-LCCN (70-30 vol.%) symmetrical supported membrane was characterized by oxygen permeation measurement. Perfectible fluxes of 1.11 $mL_N\,cm^{-2}\,min^{-1}$ and 2.32 $mL_N\,cm^{-2}\,min^{-1}$ were obtained at 950 °C in air/N_2 and O_2/N_2, respectively.

Chapter 6 contains the conclusion and outlook.

Chapter 4: Fabrication and characterization of oxygen transport membranes

In this work, a fabrication process for planar, asymmetric dual-phase OTMs was developed. The composite membranes were prepared by tape-casting, lamination and co-firing. Porous supports, porous catalytic backbones and dense selective layers were developed separately by tape-casting. Lamination was used to join the green cast tapes into asymmetric multilayer membranes. Sintering cycles were optimized to achieve thin dense membrane layers supported on mechanically strong porous supports. The membranes were activated by infiltration of aqueous catalyst solutions into the porous backbone layers. Careful adjustment of processing parameters in each of these shaping techniques (tape-casting, lamination, sintering process, catalyst infiltrations) are required to establish a well-controlled fabrication process for defect free membranes.

On the margins of the membrane fabrication, microstructural and electrochemical characterizations are important and necessary steps to lead the material development and component manufacturing of electrochemical devices. During this study, microstructural and electrochemical characterization techniques were used to ensure that the properties of the selected materials and of the developed membranes were suitable to reach the targeted performance of the membranes.

In this chapter, details about the used shaping techniques: tape-casting, lamination, de-binding and sintering processes, and catalyst activation of porous structures; are described (**sub-chapter 4.1.**). Microstructural (X-ray diffraction [XRD], particle size distribution [PSD], specific surface area analysis [BET], scanning electron microscopy [SEM], density measurements, dilatometry) and electrochemical (electrical conductivity measurements, electrochemical impedance spectroscopy, oxygen permeation measurements) characterization techniques performed on the raw materials and assembled membranes are presented (**sub-chapter 4.2.**). Finally, the experimental set-ups used for oxygen permeation measurements and the corresponding calculations to obtain the oxygen flux permeating through the membranes are detailed (**sub-chapter 4.3.**).

4.1. Fabrication of oxygen transport membranes

Planar green ceramic structures can be developed via several shaping techniques such as printing, extrusion, coating, dry pressing, etc., which can be divided into three groups depending on the amount of solvent in the feedstock [1]: (i) wet forming techniques: techniques containing the largest amount of solvent where the use of slurries, slips or pastes are required (casting techniques, coating, printing), (ii) plastic forming techniques: techniques using high pressure to make the feedstock plastic and adopt the shape of the mould (extrusion, injection moulding, roll compaction), and (iii) dry forming techniques, techniques not using solvent (dry pressing, calendaring). Generally, the plastic and dry techniques are used to produce planar ceramic structures from 100 to 5000 µm thick. For the development of high-performance OTMs, a selective thin membrane layer should be produced (thickness range of 5-30 µm was aimed), which requires the use of a wet shaping technique such as flatbed screen printing, dip coating, soft lithography, slot-die-coating and tape-casting [2, 3]. Among these techniques, tape-casting presents the advantages of being a well-established and relatively simple technique with a low-implementation cost to produce planar ceramic sheets with a large area, good surface quality and controlled microstructures. Moreover, flat ceramic sheets with a wide range of possible porosities (from highly porous to completely dense) and sintered thicknesses (5 to 1500 µm) can be prepared from flexible and sizable green tapes. Considering these advantages, tape-casting was selected as fabrication method to develop the different planar layers of porous support, porous catalytic backbone, and dense dual-phase membrane layer.

4.1.1. Tape-casting

4.1.1.1. Tape-casting process

In tape-casting, the first step is the preparation of a uniform and homogeneous starting suspension (called slurry). The raw powders need to be mixed with some organic additives (dispersants, binders and plasticisers) in order to obtain a colloidal dispersion with high homogeneity and stability which can be shaped in a green tape with adequate strength and flexibility for further processing steps. The next sub-section (**4.1.1.2.**) gives more details on the slurry preparation process. When the slurry preparation is done, the suspension is poured into a tape-caster reservoir with a polymer carrier film underneath. As illustrated in

Figure 4. 1, the tape is formed when the slurry flows beneath the blade(s) of a doctor blade, forming a thin tape on the polymer carrier film. During this study, all tapes were prepared using a dual blade system. Such a system helps to control the hydrodynamic forces behind the casting blade. The thickness of the tape varies directly with the height of the gap between the blade(s) and the polymer carrier film, the speed of the carrier film and the drying shrinkage. It is important that the tape dries in a controlled atmosphere (ventilated chamber) in order to avoid defects formation during the drying step. When the tape is completely dry, it can finally be removed from the polymer carrier film and can be further processed. High control of each step in the process (slurry preparation, the casting process, the drying process) is very important to achieve a ceramic material with the required geometry and properties [4].

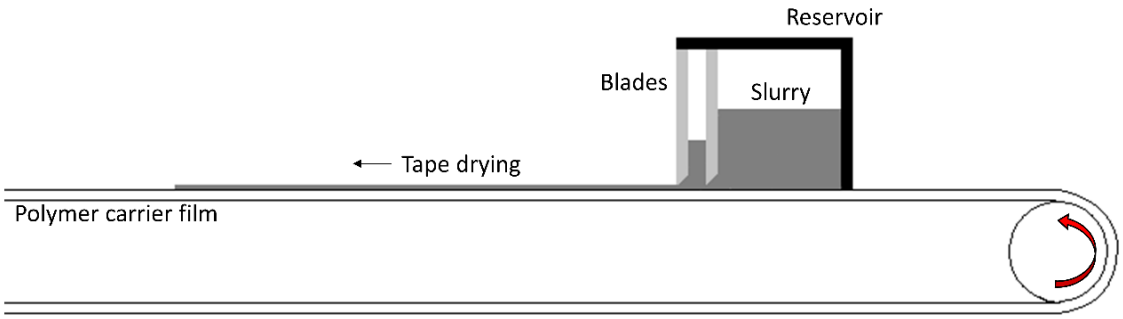

Figure 4. 1: Schematic of the tape-casting process.

4.1.1.2. Slurry preparation

In this section, the role of slurry components (powders, solvents, dispersants, binders and plasticisers) is explained, and more details are given on the overall slurry preparation. More details on specific formulations can be found in the articles included in **Chapter 5**. Moreover, Table 4. 1 gives an example of a slurry formulation used for the development of the different layers of $(ZrO_2)_{0.89}(Y_2O_3)_{0.01}(Sc_2O_3)_{0.10}$ (10Sc1YSZ) – $MnCo_2O_4$ (MCO) dual-phase asymmetric OTMs, presented in **sub-chapter 5.1.**.

Table 4. 1: Slurry formulation used for the development of the different layers of $(ZrO_2)_{0.89}(Y_2O_3)_{0.01}(Sc_2O_3)_{0.10}$ (10Sc1YSZ) – $MnCo_2O_4$ (MCO) dual-phase asymmetric OTMs (in vol.%).

OTM layers	Powders	Dispersant	Binder/plasticizer system	Solvent
Porous support	3YSZ + 20 vol.% Al_2O_3: 7.6 Graphite: 6.4 PMMA: 5.3	PVP: 1.6	PVB, Pycal: 47.9	Ethanol: 31.2
Activation layer	8YSZ: 4.8 PMMA: 12.3	PVP: 1.1	PVB, Pycal: 44.4	Ethanol: 37.4
Dense membrane	10Sc1YSZ-MCO (70-30 vol.%): 11.9	PVP: 2.4	PVB, Pycal: 37.9	Ethanol: 47.8

3YSZ: $(Y_2O_3)_{0.03}(ZrO_2)_{0.97}$
PMMA: Poly(methyl methacrylate) $(C_5O_2H_8)_n$
8YSZ: $(Y_2O_3)_{0.08}(ZrO_2)_{0.92}$
10Sc1YSZ-MCO: $(ZrO_2)_{0.89}(Y_2O_3)_{0.01}(Sc_2O_3)_{0.10}$ - $MnCo_2O_4$
PVP: Polyvinylpyrrolidone $(C_6H_9NO)_n$
PVB: Polyvinyl butyral $(C_8H_{14}O_2)_n$

- The powders

The powder is obviously the main ingredient of the slurry. Additives in the tape-casting process are only used to hold the powder particles together in order to produce a sintered layer with appropriate size, shape and properties. Afterwards, during the sintering step they are burnt. Therefore, it is crucial to characterize the powder in terms of average particle size distribution, surface area and purity before and during the slurry preparation.

The characterization of the surface area is essential because the total powder area is proportional to the amount of organic additives (dispersants, binders, plasticisers) that need to be added to the slurry to provide the proper dispersing or binding. The surface area of raw powders used for the development of the membranes was controlled by BET analysis (characterization technique detailed in **section 4.2.1.**) and was aimed to be approximately 10 $m^2 g^{-1}$. The particle size is also an important factor, and it is closely related to the surface area. Indeed, smaller is the particle size, higher is the surface area of the powder. Consequently, small particles need a higher concentration of organic additives compared to big particles. The particle size also affects significantly the shrinkage since small particles have a high surface energy that induces a high driving force leading to higher shrinkage during sintering. Therefore, using a wide range of particle sizes can affect the homogenous

sinterability of the tape. The final microstructure of a sintered green tape depends also on the shape and size distribution of the particles since the packing structure is directly related to them [5]. Submicron particle size powders (d_{90} < 1 µm, d_{50} < 0.3 µm) were used to develop the different membrane layers. For the preparation of porous tapes, it is especially important to selected pore-former materials considering the shape and size of their particles in order to obtain a tape with sufficient open-porosity (median particle sizes up to 7 µm were used for pore-former materials).

- The solvents

The main role of the solvent is to dissolve the organic additives added to the slurry (dispersants, binders and plasticisers), without reacting with the powders. During the drying step of the tape, it is important that the solvent evaporates quickly in order to avoid defect formation [4]. However, too fast drying leads to the formation of a skin at the top of the tape and can also induce defects like cracks [4]. The desired thickness of the tape can play a role in the selection of the solvent since thick tapes need more time to dry. Consequently, a solvent with a higher volatility can be used for the development of thick tapes. Several studies used a mixture of solvents to have a better control of the rheological properties and of the drying speed especially [6 – 11]. Thus, varying the ratio of two solvents which have different volatility properties allow keeping the same drying time while changing the thickness of the tape. Nevertheless, in order to avoid differential volatilization only azeotropic mixtures evaporating as a single liquid must be used [4]. The use of multiple solvents in slurry formulations allows for the increase of their ability to dissolve all the organic additives. The most widely applied organic solvents in tape-casting are alcohols, ketones and hydrocarbons. They exhibit low boiling point, high vapour pressure and low heat vaporization and therefore require less energy during drying.

- The dispersants

Dispersants are organic additives used to increase the homogeneity of the tapes by keeping particles apart, thanks to steric and/or electrostatic repulsions. Both mechanisms have been discussed in the literature [12, 13]. Acids absorbed on the surface of the particles and later dissociated create a charge on the particle surface, which confers the electrostatic repulsions inhibiting the agglomeration of particles. The steric repulsion mechanism consists

of long-chain polymers absorbed onto the particle surface that act as spacers between the particles of the raw materials [12]. A third mechanism, referred to electrosteric stabilization is a combination of both steric and electrostatic repulsion [13].

- The binders

Binders provide the network that maintains the entire chemical system together by creating long-chain polymers during drying. In tape-casting and the processing steps that follow, the binder must provide compatibility with the system in terms of solubility, slurry viscosity, green strength of tapes, burnout temperature and glass transition temperature (T_g) during firing [4, 14]. By the specific characteristics of the polymers used as binders (chemistry, molecular weight, chain length) the rheology of tape-casted slurries, green tape strength and debinding profile can be influenced [14]. Typically, in tape-casting cellulose derivates, polyvinyls and polyacrylates are used [14].

- The plasticisers

Plasticisers are added to the slurry to confer sufficient flexibility on the green tape by breaking the close alignment and bonding of the binder molecules and/or by avoiding frictions in between the polymer chains. Commonly, plasticisers can be classified into two groups, depending on their working mechanisms, to plasticize a green tapes:

(1) Type I plasticisers, called glass transition temperature (T_g) modifiers or binder solvents [15], are organic additives that soften the polymer chains between the particles, allowing more flexibility. They act by shortening the polymer chain lengths or by partially dissolving them. In fact, they have a very similar role to the solvents' but possess lower volatility. They can be considered as slow-drying solvents.

(2) Type II plasticisers allow avoiding frictions in between the polymer chains, which also lead to a higher flexibility of the green tapes. During the drying step, they can help to prevent cracking by decreasing the yield stress of the green bodies. Nevertheless, their mechanism has for consequence to decrease the strength of the tapes by reducing the van der Waals bonding between adjacent chains [16].

Slurries containing a too low amount of plasticisers will produce rigid and easily breakable green tapes while too high amounts of plasticiser will reduce the strength of the tape (too

much bonding of the binder molecules broken). Therefore, it is necessary to use the most advantageous ratio of plasticisers/binders in order to obtain the optimum flexibility and strength for the green tapes.
The most common plasticisers are phthalate (plasticisers type I: BBP, DBP, etc.) and glycol (plasticisers type II: glycerol, PEG, PPG, etc.) derivates.

- Slurry processing

The order in which all the components of the slurry are mixed is very important. The first step of the slurry preparation consists to efficiently deagglomerate the material(s) by milling the powder(s) with solvent(s) and dispersant(s). This dispersion step is essential to obtain homogeneous and high-quality surface tapes as well as uniform shrinkage during sintering. Several milling equipment can be used such as ball-mills or planetary mills. The dispersion time can vary from few hours to 72 h, depending on the agglomerates and the quantity of powder(s). During a second step, the plasticiser/binder system is added to the slurry. The slurry is mixed until the binder is completely dissolved (usually around 24 h) using a low milling speed to avoid degradation of the high molecular weight binder molecules. Before casting, the slurry is sieved to remove any coarse inhomogeneity and de-aired in a closed container under vacuum to remove dissolved gas in the slurry. Tape's viscosity is checked to ensure that the solvent loss is controlled and the viscosity is suitable for tape casting. If the viscosity is too high, solvent(s) can be added to the slurry. On the other hand, if the viscosity is too low, part of the solvent(s) can be evaporated by using a vacuum.

4.1.2. Lamination

Lamination is a frequently used technique to manufacture ceramic multilayer devices like OTMs [17 – 23]. The technique consists of joining the binder phases of two adjacent green tapes together. This can be done using heat, pressure or both. The most common process, the so-called thermo-compression lamination, combines elevated temperature (up to 70 °C) and pressure (up to 30 MPa) [1]. Temperature, pressure and dwell time are the three main parameters of this method [24].
More details on the lamination procedure used for the fabrication of each developed membrane can be found in **Chapter 5**.

4.1.3. De-binding and sintering

4.1.3.1. De-binding

The term de-binding refers to the removal of the binder(s) and the other organic additives (dispersant[s] and plasticiser[s]) from the green tapes. Several methods such as solvent de-binding [25 – 27] or catalytic de-binding [25] can be used. Nevertheless, the thermal decomposition (thermal de-binding) is by far the most used method for de-binding. In this case, the organics are removed as vapour by heating, with emission of carbon and carbon monoxide. The removal of the organics is physically controlled by heat transfer into the membranes and mass transport of the decomposition products out of the membranes. The de-binding process by thermal decomposition can be roughly divided into three steps: (1) initial heating of the binder until it softens at its T_g (around 100 °C), (2) removal of the molten binder by evaporation (temperature range 200 – 400 °C), and (3) further removal of the binder remaining in the tape at temperature above 400 °C. Thermal de-binding cycles are usually performed till a maximum temperature of 600 – 700 °C. The molecular weight and melting point of the organic additives present in the tapes have to be considered to determine the de-binding step. Temperature steps (dwell) and/or slow heating ramps (< 1 °C min^{-1}) are commonly used during the de-binding step to avoid the creation and propagation of defects while organic removal takes place. Thermogravimetric analyses can be performed on the tapes to determine precisely the temperatures at which organic additive removal occurs.

More specific details on the de-binding cycles used to develop the membranes can be found in **Chapter 5**.

4.1.3.2. Sintering

Sintering is the process to convert the dried, de-binded tape into a continuous polycrystalline body by heat treatment. Basically in this process, the powder particles are joined together into a mechanically stable ceramic body by a densification process. It is a crucial step in the development of OTMs, the properties of ceramic material being modified through sintering to give the product its final characteristics. The overall process can be divided into three main stages:

- During the *initial stage* the surface roughness is decreased and the particles start to adhere and grow together. This stage would begin as soon as some degree of atomic mobility is achieved and end when grain growth begins to occur. Almost no shrinkage is observable during the initial stage (typically 0 – 5 % [28]).

- During the *intermediate stage* further neck growth occurs and the cross-structural area of the pore phase decreases.

- During the *final stage* the remaining channel-like pores break down into isolated, closed pores. This stage begins when the body achieves 90 – 95 % of theoretical density. Difficulties are commonly encountered to remove the last few percent of porosity because of differential grain growth between large and small grains.

Figure 4. 2 presents the main stages of the sintering process.

It is commonly admitted that six different sintering mechanisms, illustrated in Figure 4. 3, are involved for the densification of a green body. They can be described as below:

1. surface diffusion: diffusion of atoms along the surface of a particle
2. lattice diffusion (from the surface): diffusion of atoms from the surface through the lattice
3. vapour transport: evaporation of atoms that condense on a different surface
4. grain boundary diffusion: diffusion of atoms along the grain boundary
5. lattice diffusion (from the grain boundary): diffusion of atoms from the grain boundary through the lattice
6. plastic flow: dislocation motion causes flow of matter

If all of them lead to bonding and growth of necks between particles, increasing therefore the strength of the body, only the mechanisms 4, 5, and 6 densify the ceramic material (densifying mechanisms). Indeed, the three first mechanisms produce microstructural changes without causing shrinkage (non-densifying mechanisms). They take atoms from the surface and rearrange them onto another surface or part of the same surface. On the other hand, the three last mechanisms remove material from the grain boundary/bulk regions to the surface of the pores, thereby eliminating porosity and increasing the density of the material. It is particularly important to distinguish between densifying and non-densifying mechanisms, considering the final microstructure which is desired (porous or dense samples). Several parameters can influence the competition that the sintering

involves between these two categories of mechanisms. For example, green body with large pores and small grains will lead to a porous microstructure, while higher temperatures and/or compact green bodies will promote dense final product [16].

The manufacturing of dense dual-phase membranes, possessing different sintering properties, supported on highly porous layers was an important challenge of this study. An adaptation of the sintering step (heating ramps, temperatures, atmospheres) was necessary for each different materials used. **Chapter 5**, which deals with the results and discussion of the study, will describe in every single case how the sintering step was handled.

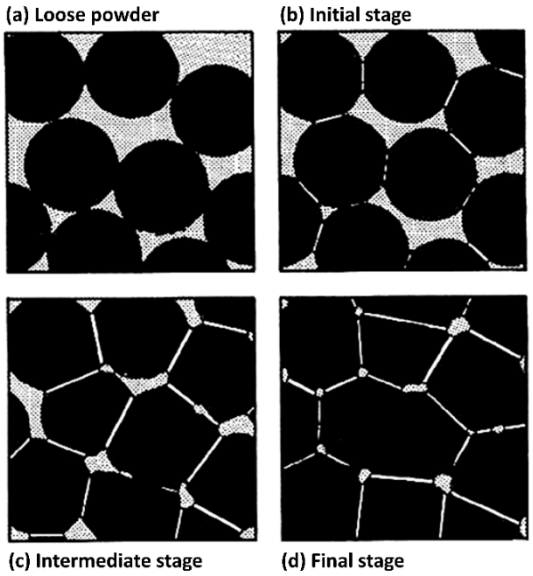

Figure 4. 2: Illustration of the main stages of the sintering process. (a) Loose powder before sintering, (b) initial stage, (c) intermediate stage and (d) final stage. Figure taken from [29].

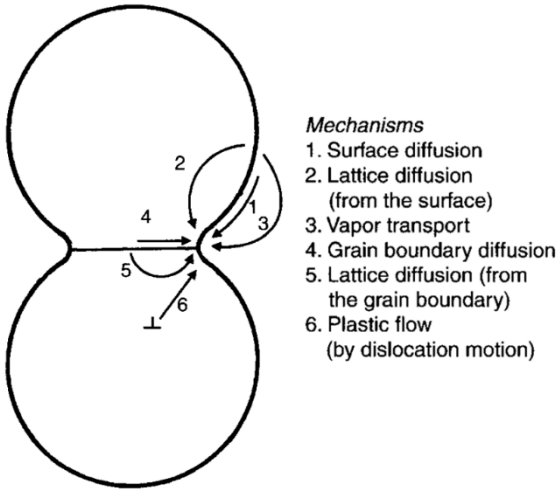

Figure 4. 3: Schematic representation of the sintering mechanisms for a system of two particles. Figure taken from [28].

4.1.4. Catalyst activation of porous structures

As explained in **section 2.2** dealing with the transport of oxygen through asymmetric membranes, the oxygen flux produced by a membrane is in direct proportion to its thickness. In the case of asymmetric membranes, the thin selective layer gives the advantage of minimizing the resistance arising from bulk diffusion. Consequently, additional mechanisms such as (i) catalytic surface exchange and (ii) gaseous transport become limiting factors of the oxygen separation [30]. Moreover, regarding dual-phase membranes, the existence of two phases gives an important influence of the grain boundary between them, since it can either promote or block the transport of ionic and electronic species across the membrane. Therefore, a large catalytic activity toward surface oxygen exchange is required. In order to improve the oxygen flux further on the surfaces, the surface exchange kinetics have to be enhanced on both sides of the dense membrane layer. It was demonstrated that very high catalytic activity can be prepared by infiltration of electro-catalytic materials into porous ionic conducting backbone structures [31, 32]. For example, Figueiredo *et al.* proved that an increase of the surface area of $CaTi_{0.8}Fe_{0.2}O_{3-\delta}$ membranes by screen-printing porous layers of the same material (covered on both sides and impregnated with a silver nitrate solution) leads to an enhancement of the oxygen permeation flux by a factor of 1.70 [33]. A recent study on thin $La_{0.8}Sr_{0.2}Cr_{0.5}Fe_{0.5}O_{3-\delta}$-$Zr_{0.84}Y_{0.16}O_{2-\delta}$ (LSCr-YSZ) dual-phase membranes also demonstrated that the application of activated porous structures (here LSCr-YSZ impregnated with mixed nitrate solutions of $Ni(NO_3)_2$, $Sm(NO_3)_3$ and $Ce(NO_3)_3$) around the selective membrane layer improve by one order of magnitude the oxygen permeability compared to a bare membrane [34].

More details on the development and the catalytic activation of the porous backbones can be found in **Chapter 5**.

4.2. Characterization of oxygen transport membranes

4.2.1. Characterization of raw powders

- X-Ray diffraction

X-ray diffraction (XRD) analyses were performed to determine the structure and crystallinity of in-house synthesized materials (e.g. $LaCr_{0.85}Cu_{0.10}Ni_{0.05}O_{3-\delta}$) and to control the stability of

the membranes after the sintering process and stability tests. When all peaks in the experimental diffraction patterns can be identified using inventoried references (JCPDS patterns), the phases are considered pure.

In this study, two different diffractometers were used:

- 10ScYSZ-MCO membranes (results presented **sub-chapter 5.2.**) were analysed using a PANalytical Cubix fast diffractometer equipped with a CuKα1 radiation (λ = 1.5406 Å) and a X'Celerator detector in Bragg−Brentano geometry. XRD patterns recorded in the 2Θ-range of 10-90° were analyzed using X'Pert Highscore Plus software.

- 10Sc1YSZ-AZO and 10Sc1YSZ-LCCN membranes (results presented **sub-chapter 5.3.** and **5.4.**) were analysed using a PANalytical diffractometer equipped with a Ni-filtered Cu Kα radiation (40 mA, 45 kV) over a 2Θ-range of 5-80º and a position-sensitive detector using a step size of 0.05º and a step time of 120 s. The XRD patterns were processed using the X'Pert Highscore Plus software to identify the species present in the samples.

- Particle size distribution analysis

The particle size distribution (PSD) of the raw materials was determined during the slurry preparation for tape-casting since this parameter as an important influence on the final microstructure of the membranes. A method based on laser diffraction was used for this purpose. Laser diffraction measures particle size distributions by measuring the angular variation in the intensity of light scattered as a laser beam passes through a dispersed particulate sample. Large particles scatter light at small angles relative to the laser beam and small particles scatter light at large angles. The angular scattering intensity data is then analysed to calculate the size of the particles responsible for creating the scattering pattern. The particle size is reported as a volume equivalent sphere diameter.

In this study, a Laser Diffraction Particle Size Analyzer LS 13 320 (Beckman Coulter, USA, Figure 4. 4) was used. The material particles were dispersed in ethanol.

Figure 4. 4: Laser Diffraction Particle Size Analyzer LS 13 320 from Beckman Coulter, USA.

- Specific surface area

The specific surface area corresponds to the surface area of the particles per unit of mass or volume of material. It is generally determined by the physical adsorption of gas molecules on a solid surface, as described by the Brunauer-Emmett-Teller (BET) theory [35]. The theory is based on three assumptions: (i) gas molecules are physically adsorbed on a solid in layers infinitely, (ii) there is no interaction between each adsorption layer and (iii) the Langmuir theory [36] can be applied to each layer. The amount of adsorbed gas is dependent on the equilibrium pressure (p) and the saturation pressure (p_0) at the temperature of adsorption. The specific surface area of the material can be calculated by measuring the values of p/p_0.

In this study, the specific surface area of raw powders was measured by gas adsorption measurements based on BET theory using Quantachrome Autosorb 1 (Quantachrome GmbH & Co. KG, Germany, Figure 4. 5). The powders were de-gassed in vacuum at 300 °C for 3 h prior to surface absorption with krypton gas.

Figure 4. 5: Quantachrome Autosorb 1 from Quantachrome GmbH & Co. KG, Germany.

4.2.2. Microstructural characterizations

- Microscopy

SEM was carried out to investigate the microstructure of the membranes during the development (post-sintering analysis, post-infiltration analysis [catalysts]) and after the tests (post-mortem analysis). During manufacturing, the density of the selective composite layer and the porosity of the surrounding layers (porous catalytic backbones and porous support) were especially examined. Particular attention was dedicated to the distribution of the ionic and electronic conducting phases into the dense composites, and to the interfaces between the layers composing the asymmetric membranes. After impregnation of catalytic solutions into the porous structures, the latter were carefully analysed in order to evaluate the success of the infiltrations in a qualitative or quantitative manner. Post-mortem analyses were performed to observe the impact of the testing conditions (temperature, atmosphere, and sealing material compatibility) on the microstructure of the membranes. The presence of impurities, formation of new phases or diffusion of chemical elements were verified using an energy dispersive X-ray spectroscopy (EDX) system.

Several microscopes were used in the different articles reported in **Chapter 5**. Each article specifies the microscope used and the motivations of the analysis.

- Density measurements

The density of thick symmetrical membranes (e.g. pellets) was determined by the Archimedes method. Archimedes' principle states that the weight of a displaced fluid is directly proportional to the volume of the displaced fluid. Consequently, by measuring the weight of the membrane in water and in air, it possible to calculate the weight of the displaced fluid (here water) and to deduce therefrom the density of the membrane. Note that only the open porosity (pores where the fluid can access) will be taken into account in the density calculation when using the Archimedes method.

A software developed in-house (called ThreshAlyzer) was used to estimate the porosity of the different layers of asymmetric membranes by analyzing the contrast between pores (black) and materials (white/grey), thanks to SEM images of membrane cross-sections. The error bar of such measurements is estimated at 2 %. Note that this technique gives the total porosity percentage (open and close porosity) but includes only a limited surface of the samples. To avoid obtaining local density values which may not be representative of the complete surface of the samples, three density measurements were realized at different spots and an averaged density value was calculated.

- Dilatometry

Dilatometry is a thermoanalytical technique used to measure the shrinkage or expansion of materials (solids, powders, pastes or liquids) under negligible load as a function of the temperature. The degree of expansion divided by the change in temperature is called "thermal expansion coefficient" (α). It can be expressed as:

$$\alpha = \frac{1}{L_0}\left(\frac{\Delta l}{\Delta T}\right)$$

where L_0 is the initial sample length, while Δl and ΔT correspond to the change in length and temperature, respectively.

One of the important material-related challenges that need to be overcome to manufacture multilayers asymmetric membranes is to ensure the mechanical integrity of samples by selecting materials having close thermal expansion coefficients. Dilatometry measurements were performed on the selected membrane materials to determine the shrinkage and

sintering activity of the different membrane layers (porous support, catalytic porous layer and dense membrane layer).

Several types of dilatometers exist, such as capacitance dilatometers, connecting rod (push rod) dilatometers, high-resolution laser dilatometers, and optical dilatometers. In this study, a connecting rod dilatometer (Netzsch 402 CD, Netzsch, Germany) using a linear variable displacement transducer (LVDT) to measure the dimensional change of the samples was used (results presented in **sub-chapter 5.1.**). As the sample length changed during the temperature program, the LVDT core is moved, and an output signal proportional to the displacement is recorded. The temperature program was controlled using a thermocouple located next to the sample.

4.2.3. Electrochemical characterizations

- Electrical conductivity measurements

The electrical conductivity (σ) of a material is a number describing how much the material conducts charged species like ions or electrons. Conductivity is measured in units of S m^{-1} and is defined as the inverse of the resistivity (ρ), as described by the following equation:

$$\sigma = \frac{1}{\rho} \quad (1)$$

Commonly, the electrical resistivity is measured experimentally and the electrical conductivity of the material is deducted using the equation (1). In this study, the four-point technique was used to obtain the electrical resistivity of $(ZrO_2)_{0.89}(Y_2O_3)_{0.01}(Sc_2O_3)_{0.10}$-$Al_{0.02}Zn_{0.98}O_{1.01}$ (10Sc1YSZ-AZO) composite and deduce its electrical conductivity.

The four-point measurement technique was performed on a rectangular bar sample (ca. 4×4×17 mm^3). The bars were made by uniaxial pressing of the 10Sc1YSZ-AZO (50-50 vol.%) composite powder under 1000 kg load, and subsequently sintering them in air at 1200 °C for 6 h (heating/cooling ramps: 1 °C/min). Pt-wires were attached to the sides of the bar, which were painted with Pt-paste and then heat treated at 1000 °C for 1 h (heating/cooling ramps: 1 °C/min) to ensure good electrical contact (as shown Figure 4. 6). The current was applied on the extremities of the bar (2 points) and a resulting voltage is measured across the inner part of the bar (2 other points). The four-point resistivity of the material is then:

$$\rho = \frac{Vwh}{Il} \qquad (2)$$

Where ρ = Resistivity in Ω m

V = Voltage measured across the sample in volts (V)

I = Current measured through the sample in amperes (A)

w = Width of the sample in meters (m)

h = Height of the sample in meters (m)

l = Distance between the voltage probes in meters (m)

Considering the equations 1 and 2, the electrical conductivity can be expressed:

$$\sigma = \frac{Il}{Vwh} \qquad (3)$$

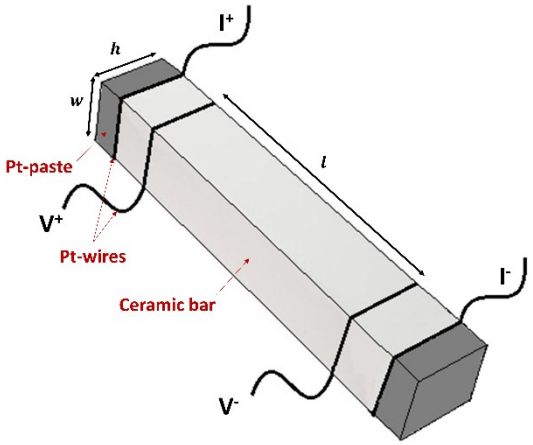

Figure 4. 6: Four-point configuration for electrical conductivity measurements.

Sub-chapter 5.3. of the thesis presents the results of electrical conductivity measurements performed on the 10Sc1YSZ-AZO (50-50 vol.%) dual phase membrane.

- Electrochemical impedance spectroscopy (EIS)

Electrochemical Impedance Spectroscopy (EIS) is a powerful technique to study electrochemical-systems. The technique can measure the dielectric and transport properties of materials and investigate mechanisms of electrochemical reactions. Electrochemical impedance is usually measured by applying an alternating (AC) potential to an electrochemical cell and then measuring the current through the cell. If a sinusoidal potential excitation is applied, the response to this potential will be an AC signal that can be analysed

as a sum of sinusoidal functions (Fournier series). The amplitude of the applied signal is usually small in order to ensure that the cell's response is pseudo-linear. In such case, the current response to a sinusoidal potential will be a sinusoidal at the same frequency but shifted in phase. The excitation voltage and the response current can be expressed by equations 4 and 5:

$$E(t) = E_0 \cdot \sin(\omega t) \quad (4)$$

$$I(t) = I_0 \cdot \sin(\omega t + \varphi) \quad (5)$$

The impedance response Z is calculated using the generalized Ohm's law:

$$Z(t) = \frac{E(t)}{I(t)} = \frac{E_0 \cdot \sin(\omega t)}{I_0 \cdot \sin(\omega t + \varphi)} = Z_0 \frac{\sin(\omega t)}{\sin(\omega t + \varphi)} \quad (6)$$

Where E_0 and I_0 are the peak amplitude of the AC potential and current, Z_0 is the impedance, ω is the angular frequency, t is the time and φ is the phase shift.

Knowing that most of electric components (i.e. capacitors or inductors) gives a response, which is not in phase with the stimulus, the impedance is usually represented as a vector expressed in a complex function. The potential and current responses can be described as:

$$E(t) = E_0 \cdot e^{(j\omega t)} \quad (7)$$

$$I(t) = I_0 \cdot e^{(j\omega t - \varphi)} \quad (8)$$

The impedance is then represented as:

$$Z = \frac{E(t)}{I(t)} = Z_0 \cdot e^{(j\varphi)} \quad (9)$$

In this thesis, EIS analyses were carried out to study the performance of different materials as catalytic porous backbones. Polarization resistances (Rp) were deducted from the measurements and compared to select the most suitable material for this function. **Sub-section 5.2.** presents the results of the EIS experiments performed.

4.3. Oxygen permeation measurements

In this study, oxygen permeation measurements were conducted using two models of the testing unit illustrated in Figure 4. 7. The testing units are referred to “DTU experimental set-up” and “UPV experimental set-up”. The majority of the tests were performed on the “DTU testing unit” nevertheless, several tests were also performed at the *Institute of Chemical Technology* (ITQ – Valencia, Spain) and, therefore, the two types of experimental set-ups used will be described below.

4.3.1. DTU experimental set-up

As described in Figure 4. 7.a, the membranes tested in the DTU testing unit type were placed between two alumina tubes, in the centre of a tube furnace. The temperature was monitored using thermocouples placed in direct contact with the membranes. Mass flow controllers (MFCs - Brooks) were used to control the inlet flow of the feed (high pO_2) and the sweep (low pO_2) gases. Various flow rates (in general from 0 to 9 L h^{-1}, depending on the MFCs) and nature of gases (i.e. air or O_2 as a feed gas, and Ar, N_2, CO_2 as a sweep gas) can be selected for the measurements. Tape-cast sodium aluminosilicate (NAS, Na_2O: 17.8 mol.%, Al_2O_3: 9.4 mol.% and SiO_2: 72.8 mol.% [37]) glass o-rings, with an inner diameter of 9 mm and glass transition temperature of 515 °C [38] were applied on both sides of the membranes to serve as sealing material between the alumina tubes and the membranes. The exterior surface of the membranes was also coated with NAS paste to ensure that oxygen cannot enter from the exterior compartment to the permeate side. Then the membranes were heated in air up to 940 °C and afterwards cooled to 750 °C to ensure a gas tight sealing. A gas chromatography (490 micro GC, Agilent, USA) was connected to the outlet of the permeate side to quantify any oxygen leaks into the permeate stream. Oxygen leaks could potentially enter the permeate side via pinholes or insufficient sealing at the membrane periphery. In-house built zirconia-based pO_2 sensors were used to determine the pO_2 of the inlet gas on the permeate side (before feeding to the membranes) and of the outlet gas (after passing over the membranes). The oxygen permeation flux was deduced based on the pO_2 difference between the inlet and the outlet of the gas flowing through the permeate side. The oxygen permeation flux through the membranes was calculated as:

$$J_{O_2} = \frac{pO_{2,permeate}^{out} \cdot \dot{n}^{out} - pO_{2,permeate}^{in} \cdot \dot{n}^{in}}{A} \quad (10)$$

where J_{O_2} is the oxygen permeation flux, $pO_{2,permeate}^{in}$ and $pO_{2,permeate}^{out}$ are respectively the oxygen partial pressures of the inlet and outlet gases, $\dot{n}^{in}$ and $\dot{n}^{out}$ are molar flow rates of inlet and outlet gases, respectively, and A is the effective area of the membrane. The Nernst equation (11) was used to calculate the oxygen partial pressure from the measured sensor voltage (V):

$$pO_2 = pO_{2,ref} . e^{\frac{4FV}{RT}} \quad (11)$$

where V is the open circuit voltage of the oxygen sensor, T is the temperature of the oxygen sensor, and $pO_{2,ref}$ is the oxygen partial pressure at the reference electrode which was maintained at 0.21 atm during the measurement.

Oxygen permeation measurements performed through $(Y_2O_3)_{0.01}(Sc_2O_3)_{0.10}(ZrO_2)_{0.89}$-$MnCo_2O_4$, $(Y_2O_3)_{0.01}(Sc_2O_3)_{0.10}(ZrO_2)_{0.89}$-$Al_{0.02}Zn_{0.98}O_{1.01}$ and $(Y_2O_3)_{0.01}(Sc_2O_3)_{0.10}(ZrO_2)_{0.89}$-$LaCr_{0.85}Cu_{0.10}Ni_{0.05}O_{3-\delta}$ composite membranes were conducted on DTU experimental set-ups. The results of these tests are presented in **sub-chapters 5.1.**, **5.3.,** 5**.4.** and **5.5.**.

4.3.2. UPV experimental set-up

The membrane-testing unit used at ITQ-UPV (Figure 4. 7.b) consists of a lab-scale quartz reactor. The membranes were sealed on one side (dense membrane layer side) to the quartz reactor using silver O-rings. At 850 °C, a sufficient weight load was applied to ensure a good sealing. The flow rate of gases (feed and sweep) was controlled by soap bubble flow meters. The permeate was analysed at steady state by online gas chromatography (CP-4900 Micro-GC, Varian, USA). The oxygen concentration was calculated from the O_2 signal area and its response factor previously calibrated. The total oxygen permeation was calculated as the product of the O_2 concentration ($\%O_{2,permeate}$) and the sweep flow ($\dot{n}^{out}$). The oxygen permeation flux (J_{O_2}) was then determined from the division of the total oxygen permeation by the effective area (A) of the membrane as:

$$J_{O_2} = \%O_{2,permeate} \cdot \frac{\dot{n}^{out}}{A} \quad (12)$$

To ensure gas-tightness the nitrogen concentration in the permeate gas was continuously controlled. Oxygen related to minor leaks was removed from J_{O_2} calculation by taking into account the presence of N_2 in the permeate stream. Therefore, the permeating oxygen ($\%O_{2,permeate}$) was calculated as:

$$\%O_{2,permeate} = \%O_{2,GC} - \left(\frac{0.21}{0.79} \cdot \%N_{2,GC}\right) \quad (13)$$

where $\%O_{2,GC}$ and $\%N_{2,GC}$ are the percentages of oxygen and nitrogen measured by the gas chromatography in the permeate, respectively.

Each test was repeated three times to minimize the analysis error. The experimental analytical error was below 0.5 %.

Oxygen permeation measurements performed through $(Y_2O_3)_{0.01}(Sc_2O_3)_{0.10}(ZrO_2)_{0.89}$-$MnCo_2O_4$ composite membrane were conducted on UPV testing units. The results of these tests are presented in the **sub-chapter 5.2.**.

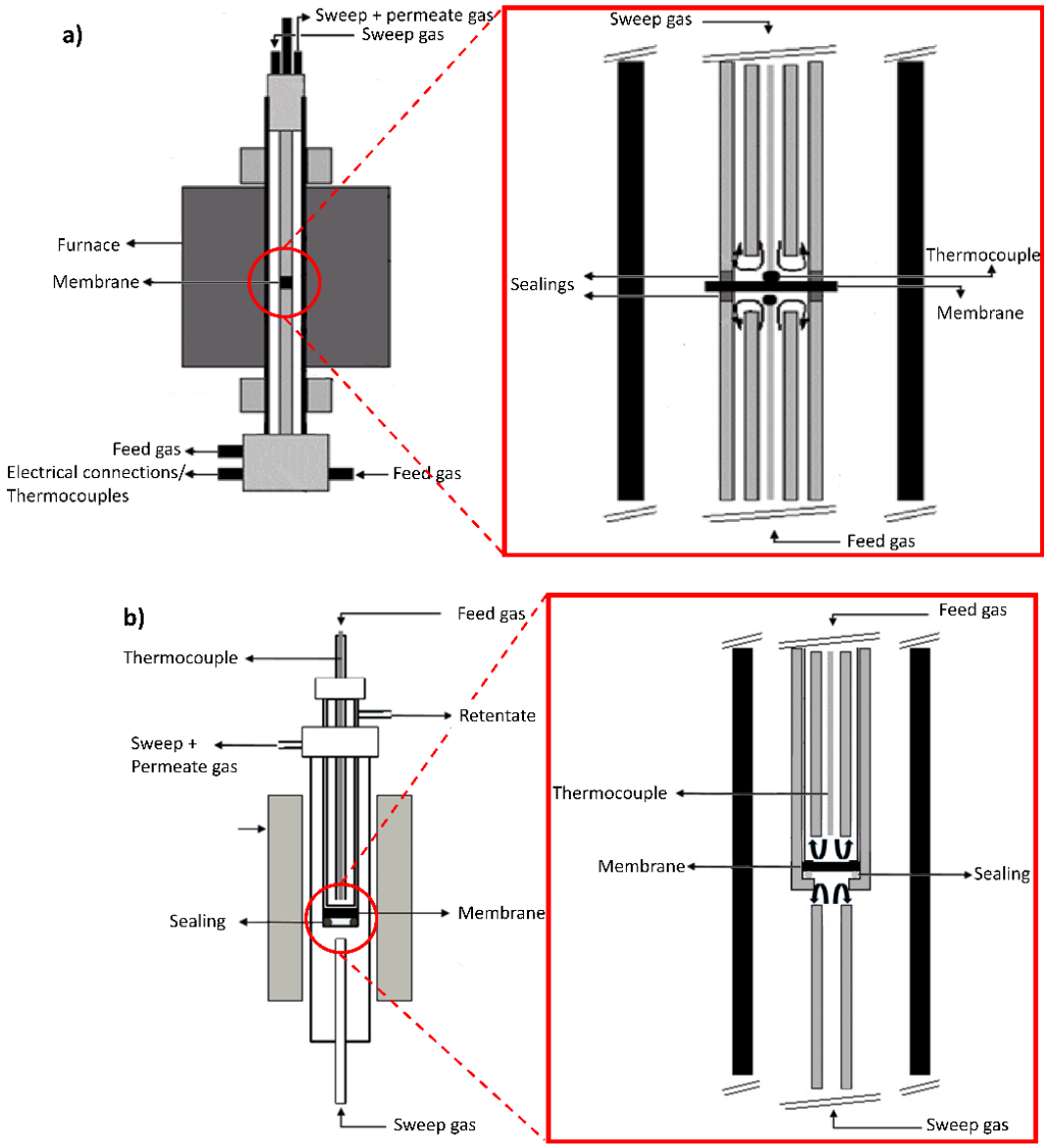

Figure 4. 7: Schematic illustration of the membrane testing units used for the oxygen permeation measurements presented in this thesis. (a) DTU testing unit, (b) UPV testing unit.

References

[1] J.S. Reed, Principles of Ceramics Processing, Second Edi, 1994.

[2] S.C. Singhal, K. Kendall, High Temperature Solid Oxide Fuel Cell: Fundamentals, Design and Applications., 2003.

[3] S. Ramousse, M. Menon, K. Brodersen, J. Knudsen, U. Rahbek, P.H. Larsen, Manufacturing of anode-supported SOFC's: Processing parameters and their influence, ECS Trans. 7 (2007) 317–327. doi:10.1149/1.2729107.

[4] R.E. Mistler, E.R. Twiname, Tape casting: theory and practice, Westerville: American Ceramic Society, 2000.

[5] F.V. Dimarcello, J.C. Williams, Preferred Organisation in Alumina Substrates, Am. Soc. Bull. 10 (1972) 309–314.

[6] G. Etchegoyen, T. Chartier, A. Julian, P. Del-Gallo, Microstructure and oxygen permeability of a $La_{0.6}Sr_{0.4}Fe_{0.9}Ga_{0.1}O_{3-\delta}$ membrane containing magnesia as dispersed second phase particles, J. Memb. Sci. 268 (2006) 86–95. doi:10.1016/j.memsci.2005.05.025.

[7] R. Bredesen, F. Mertins, T. Norby, Measurements of surface exchange kinetics and chemical diffusion in dense oxygen selective membranes, Catal. Today. 56 (2000) 315–324.

[8] N. Das, H.S. Maiti, Ceramic membrane by tape casting and sol-gel coating for microfiltration and ultrafiltration application, J. Phys. Chem. Solids. 70 (2009) 1395–1400. doi:10.1016/j.jpcs.2009.08.016.

[9] G. Etchegoyen, T. Chartier, P. Del-Gallo, An architectural approach to the oxygen permeability of a $La_{0.6}Sr_{0.4}Fe_{0.9}Ga_{0.1}O_{3-\delta}$ perovskite membrane, J. Eur. Ceram. Soc. 26 (2006) 2807–2815. doi:10.1016/j.jeurceramsoc.2005.06.025.

[10] H. Raeder, C. Simon, T. Chartier, H.L. Toftegaard, Tape Casting of Zirconia for Ion Conducting Membranes: A Study of Dispersants, J. Eur. Ceram. Soc. 13 (1994) 485–491.

[11] A. Julian, E. Juste, P.M. Geffroy, V. Coudert, S. Degot, P. Del Gallo, N. Richet, T.

Chartier, Elaboration of $La_{0.8}Sr_{0.2}Fe_{0.7}Ga_{0.3}O_{3-\delta}$ /$La_{0.8}M_{0.2}FeO_{3-\delta}$ (M = Ca, Sr and Ba) asymmetric membranes by tape-casting and co-firing, J. Memb. Sci. 333 (2009) 132–140. doi:10.1016/j.memsci.2009.02.002.

[12] R. Moreno, The role of slip additives in tape-casting technology. I: Solvents and dispersants, Am. Ceram. Soc. Bull. 71 (1992) 1521–1531.

[13] D. Shaw, Introduction to Colloid and Surface Chemistry 4th Edition, Butterworth-Heinemann, 1992.

[14] R. Moreno, The role of slip additives in tape casting technology. II: Binders and plasticizers, Am. Ceram. Soc. Bull. 71 (1992) 1647–1657.

[15] E.H. Immergut, H.F. Mark, Principles of Plasticization, in: Plast. Plast. Process., 1965: pp. 1–26. doi:10.1021/ba-1965-0048.

[16] M.N. Rahaman, Ceramic Processing, CRC Press, 2007.

[17] S. Pirou, J. Gurauskis, V. Gil, M. Søgaard, P.V. Hendriksen, A. Kaiser, S. Ovtar, R. Kiebach, Oxygen permeation flux through 10Sc1YSZ-$MnCo_2O_4$ asymmetric membranes prepared by two-step sintering, Fuel Process. Technol. 152 (2016) 192–199. doi:10.1016/j.fuproc.2016.06.019.

[18] Z. Dehaney-Steven, D. Papargyriou, J.T.S. Irvine, Flux investigations on composite $(La_{0.8}Sr_{0.2})_{0.95}Cr_{0.5}Fe_{0.5}O_{3-\delta}$-$Sc_{0.198}Ce_{0.012}Zr_{0.789}O_{1.90}$ oxygen transport membranes, Solid State Ionics. 288 (2016) 338–341. doi:10.1016/j.ssi.2016.01.017.

[19] A. Kaiser, S.P. Foghmoes, G. Pecanac, J. Malzbender, C. Chatzichristodoulou, J.A. Glasscock, D. Ramachandran, D.W. Ni, V. Esposito, M. Søgaard, P.V. Hendriksen, Design and optimization of porous ceramic supports for asymmetric ceria-based oxygen transport membranes, J. Memb. Sci. 513 (2016) 85–94. doi:10.1016/j.memsci.2016.04.016.

[20] A. Kaiser, S. Foghmoes, C. Chatzichristodoulou, M. Søgaard, J.A.A. Glasscock, H.L.L. Frandsen, P.V. Hendriksen, Evaluation of thin film ceria membranes for syngas membrane reactors —Preparation, characterization and testing, J. Memb. Sci. 378 (2011) 51–60. doi:10.1016/j.memsci.2010.12.012.

[21] Z. Cao, X. Zhu, W. Li, B. Xu, L. Yang, W. Yang, Asymmetric dual-phase membranes prepared via tape-casting and co-lamination for oxygen permeation, Mater. Lett. 147 (2015) 88–91. doi:10.1016/j.matlet.2015.02.033.

[22] L.L. Anderson, P.A. Armstrong, R.R. Broekhuis, M.F. Carolan, J. Chen, M.D. Hutcheon, C.A. Lewinsohn, C.F. Miller, J.M. Repasky, D.M. Taylor, C.M. Woods, Advances in ion transport membrane technology for oxygen and syngas production, Solid State Ionics. 288 (2016) 331–337. doi:10.1016/j.ssi.2015.11.010.

[23] S. Pirou, J.M. Bermudez, P.V. Hendriksen, A. Kaiser, T. Ramirez, M. Millan, R. Kiebach, Stability and performance of robust dual-phase $(ZrO_2)_{0.89}(Y_2O_3)_{0.01}(Sc_2O_3)_{0.10}$-$Al_{0.02}Zn_{0.98}O_{1.01}$ oxygen transport membranes, J. Memb. Sci. 543 (2017) 18–27. doi:10.1016/j.memsci.2017.08.044.

[24] S. Wang, D. Zhou, Z. Hou, Lamination of Green Ceramic Tapes by Applying Pressures Directly at Ambient Temperature, Mater. Manuf. Process. 29 (2014) 759–764. doi:10.1080/10426914.2014.901535.

[25] M. Salehi, Fabricating of Thin Planar and Tubular BSCF Oxygen Separation Membranes by Thermoplastic Processing, University of Fribourg, 2013.

[26] M. Salehi, E.M. Pfaff, A. Kaletsch, T. Graule, F. Clemens, B. Grobéty, Manufacturing of Tubular Dead-End Membranes by Continuous Thermoplastic Extrusion, Int. J. Appl. Ceram. Technol. 12 (2015) 13–18. doi:10.1111/ijac.12190.

[27] R.T. Cruz, S.R. Bragança, C.P. Bergmann, T. Graule, F. Clemens, Preparation of $Ba_{0.5}Sr_{0.5}Co_{0.8}Fe_{0.2}O_{3-\delta}$ (BSCF) feedstocks with different thermoplastic binders and their use in the production of thin tubular membranes by extrusion, Ceram. Int. 40 (2014) 7531–7538. doi:10.1016/j.ceramint.2013.12.014.

[28] L.C. De Jonghe, M.N. Rahaman, Chapter 4: Sintering of Ceramics, in: Handb. Adv. Ceram., 2003: pp. 187–264.

[29] T. Rivera, Synthesis and Thermoluminescent Characterization of Ceramics Materials, in: Adv. Ceram. - Synth. Charact. Process. Specif. Appl., 2011: pp. 127–164.

[30] P. Niehoff, S. Baumann, F. Schulze-Küppers, R.S. Bradley, I. Shapiro, W.A. Meulenberg, P.J. Withers, R. Vaßen, Oxygen transport through supported

$Ba_{0.5}Sr_{0.5}Co_{0.8}Fe_{0.2}O_{3-\delta}$ membranes, Sep. Purif. Technol. 121 (2014) 60–67. doi:10.1016/j.seppur.2013.07.002.

[31] A. Samson, M. Søgaard, R. Knibbe, N. Bonanos, High Performance Cathodes for Solid Oxide Fuel Cells Prepared by Infiltration of $La_{0.6}Sr_{0.4}CoO_{3-\delta}$ into Gd-Doped Ceria, J. Electrochem. Soc. 158 (2011) B650. doi:10.1149/1.3571249.

[32] S. Ovtar, J. Gurauskis, A. Bjørnetun Haugen, C. Chatzichristodoulou, A. Kaiser, P.V. Hendriksen, Oxygen transport properties of tubular $Ce_{0.9}Gd_{0.1}O_{1.95}$-$La_{0.6}Sr_{0.4}FeO_{3-\delta}$ composite asymmetric oxygen permeation membranes supported on magnesium oxide, J. Memb. Sci. 523 (2017) 576–587. doi:10.1016/j.memsci.2016.09.060.

[33] F.M. Figueiredo, V.V. Kharton, A.P. Viskup, J.R. Frade, Surface enhanced oxygen permeation in $CaTi_{1-x}Fe_xO_{3-\delta}$ ceramic membranes, J. Memb. Sci. 236 (2004) 73–80. doi:10.1016/j.memsci.2004.02.008.

[34] X. Liu, H. Wu, Z. He, J. Gao, X. Meng, T. Luo, C. Chen, Z. Zhan, Hebb-Wagner polarization assessment of enhanced oxygen permeability for surface modified oxygen transport membranes, Int. J. Hydrogen Energy. (2017) 1–7. doi:10.1016/j.ijhydene.2017.03.206.

[35] S. Brunauer, P.H. Emmett, E. Teller, Adsorption of Gases in Multimolecular Layers, J. Am. Chem. Soc. 60 (1938) 309–319. doi:10.1021/ja01269a023.

[36] I. Langmuir, The Adsorption of Gases on Plane Surfaces of Glass, Mica and Platinum, J. Am. Chem. Soc. 40 (1918) 1361–1403. doi:doi: 10.1021/ja02242a004.

[37] K.A. Nielsen, M. Solvang, S.B.L. Nielsen, A.R. Dinesen, D. Beeaff, P.H. Larsen, Glass composite seals for SOFC application, J. Eur. Ceram. Soc. 27 (2007) 1817–1822. doi:10.1016/j.jeurceramsoc.2006.05.046.

[38] A.J. Samson, M. Søgaard, P.V. Hendriksen, $(Ce,Gd)O_{2-\delta}$-based dual phase membranes for oxygen separation, J. Memb. Sci. 470 (2014) 178–188. doi:10.1016/j.memsci.2014.07.028.

Chapter 5: Results and discussions

During this PhD study, the three following composite materials: $(ZrO_2)_{0.89}(Y_2O_3)_{0.01}(Sc_2O_3)_{0.10}$-$MnCo_2O_4$ (**sub-chapters 5.1.** and **5.2.**), $(ZrO_2)_{0.89}(Y_2O_3)_{0.01}(Sc_2O_3)_{0.10}$-$Al_{0.02}Zn_{0.98}O_{1.01}$ (**sub-chapter 5.3**.) and $(ZrO_2)_{0.89}(Y_2O_3)_{0.01}(Sc_2O_3)_{0.10}$-$LaCr_{0.85}Cu_{0.10}Ni_{0.05}O_{3-\delta}$ (**sub-chapters 5.4.** and **5.5.**), were, in parallel, studied, developed, and successfully used to manufacture highly performing and chemically stable OTMs. This chapter presents four research articles related to their development and their characterizations as dual-phase OTMs for oxy-fuel combustion applications. These articles are treated individually in sub-chapters (**sub-chapters 5.1.** to **5.4.**) and have been published or are ready for publication in peer reviewed journals. One additional sub-chapter contains unpublished results obtained on the development and characterizations of supported $(ZrO_2)_{0.89}(Y_2O_3)_{0.01}(Sc_2O_3)_{0.10}$-$LaCr_{0.85}Cu_{0.10}Ni_{0.05}O_{3-\delta}$ oxygen transport membranes (**sub-chapter 5.5.**). At the beginning of each sub-chapter a brief introduction describes the content of the section and explains its contributions and significance to the problem statement addressed in this thesis.

5.1. Oxygen permeation flux through 10Sc1YSZ-$MnCo_2O_4$ asymmetric membranes prepared by two-step sintering

This sub-chapter contains the article “Oxygen permeation flux through 10Sc1YSZ-$MnCo_2O_4$ asymmetric membranes prepared by two-step sintering” published in Fuel Processing Technology (Fuel Process. Technol. 152 (2016) 192–199).

Prior to the study reported in this sub-chapter, 50 vol.% $(Y_2O_3)_{0.01}(Sc_2O_3)_{0.10}(ZrO_2)_{0.89}$ (10Sc1YSZ) – 50 vol.% $MnCo_2O_4$ composite disks were prepared by powder pressing and sintering processes and characterized in terms of oxygen transport properties. The oxygen permeation measurements through the 1 mm thick disk showed promising fluxes up to 0.34 $mL_N\ min^{-1}\ cm^{-2}$ (950 °C in air/N_2 gradient). The main objective of the study presented here was to decrease the thickness of this composite membrane in order to increase the oxygen permeation flux that was limited by the diffusion of oxide ions into the bulk material. This manuscript deals with the development and characterization of 7 μm thick 10Sc1YSZ-$MnCo_2O_4$ asymmetric membranes supported on YSZ porous supports. The composite membranes were prepared by tape-casting, lamination and fired in a two-step sintering process. Due to the decomposition of $MnCo_2O_4$ (by the formation of cobalt oxide above 1200 °C), the most challenging step of the asymmetric membrane preparation was the sintering process. The study shows how the two-step sintering method was successfully used to obtain a gastight membrane layer with the desired ratio of the ionic/electronic conductor that could not be obtained by conventional sintering. The oxygen permeation flux through a 7 μm 10Sc1YSZ-$MnCo_2O_4$ (70-30 vol.%) asymmetric membrane was studied from 750 to 940 °C under several atmospheres (air/pure oxygen as feed gases and N_2/CO_2 as sweep gases), and the long-term stability (1730 h) of the dual-phase membrane under pure CO_2 was investigated at 850 °C.

Oxygen permeation flux through 10Sc1YSZ-$MnCo_2O_4$ asymmetric membranes prepared by two-step sintering

*Stéven Pirou *[a], Jonas Gurauskis[a], Vanesa Gil[a], Martin Søgaard [a1], Peter Vang Hendriksen[a], Andreas Kaiser[a], Simona Ovtar[a], Ragnar Kiebach[a].*

[a] Department of Energy Conversion and Storage, Technical University of Denmark, Risø campus, Frederiksborgvej 399, DK-4000 Roskilde, Denmark

[1] Current address: Meneta Advanced Shims Technology A/S, Kirkegyden 52, DK-5270 Odense N, Denmark.

* Corresponding author: Tel: +45 93511217. E-mail address: stepir@dtu.dk.

Abstract

Asymmetric membranes based on a dual-phase composite consisting of $(Y_2O_3)_{0.01}(Sc_2O_3)_{0.10}(ZrO_2)_{0.89}$ (10Sc1YSZ) as ionic conductor and $MnCo_2O_4$ as electronic conductor were prepared and characterized with respect to sinterability, microstructure and oxygen transport properties. The composite membranes were prepared by tape casting, lamination and fired in a two-step sintering process. Microstructural analysis showed that a gastight thin membrane layer with the desired ratio of ionic/electronic conducting phases could be fabricated. Oxygen permeation fluxes across the 10Sc1YSZ-$MnCo_2O_4$ (70-30 vol.%) composite membrane were measured from 750 to 940 °C using air or pure oxygen as feed gases and N_2 or CO_2 as sweep gases. Fluxes up to 2.3 $ml_N\ min^{-1}cm^{-2}$ were obtained for the 7 micron thick membrane. A degradation test over 1730 hours showed an initial degradation of 21 % during the first 1100 hours after which stable performance was achieved. The observed degradation is attributed to coarsening of the infiltrated catalyst.

Keywords

Two-step sintering, Oxygen membranes, Composite membranes, Asymmetric membranes, Oxygen flux, CO_2 stability.

1. Introduction

To reduce global warming and adverse climate changes it is important to reduce anthropogenic CO_2. One possible approach to such emission reduction is to capture and sequester CO_2 from large point sources, e.g. fossil fuel power plants. Among the available technologies for Carbon Capture and Sequestration (CCS), oxy-fuel combustion is a promising option. This approach uses oxygen instead of air in the combustion process. By eliminating nitrogen from the oxidant gas stream, it is possible to produce a CO_2-enriched flue gas (90 – 95 % CO_2 in the dried flue gas) and the non-circulated part of the CO_2 can be compressed and stored [1]. The main energy demand for oxy-fuel process results from the oxygen production, which is today produced from cryogenic air separation units (ASUs), the only available technology for large-scale production. However, cryogenic air separation is a highly energy consuming and expensive process [2, 3], especially if small and medium scale combustion processes are considered. This energy demand could potentially be significantly lowered using thermally integrated separation modules based on ceramic oxygen transport membranes (OTM) [4, 5].

Typical oxygen transport membranes consist of a gastight mixed ionic and electronic conductor (MIEC), which allows oxygen diffusion through vacancies in the crystal lattice and simultaneous transport of electrons in the opposite direction. Membranes based on single phase MIEC materials can achieve high oxygen fluxes [6], but unfortunately most of flux wise promising membrane materials are not chemically stable under atmospheres containing CO_2, SO_2 and H_2O; conditions which are going to be encountered with membrane integration in power plants that are suitable for CCS. The materials having adequate chemical stability unfortunately typically do not provide sufficient oxygen transport. For example, compounds in the $Ba_{1-x}Sr_xCo_{1-y}Fe_yO_{3-\delta}$ (BSCF) and $La_{1-x}Sr_xCo_{1-y}Fe_yO_{3-\delta}$ (LSCF) series have attracted large interest due to their good electronic and ionic conductivity [7 – 11], however, their lack of chemical stability in the presence of CO_2 [12 – 17] (especially for the alkaline earth rich and cobalt rich compounds) clearly show the limitations of these compounds for oxy-fuel applications involving direct integration. Indeed, for materials containing La and alkaline earth metals the stability in CO_2 and SO_2 is low because of the potential formation of La/alkaline carbonates and sulphates. Carbonate formation at the surface of membrane reduces the surface exchange rate and consequently reduces the

oxide ion transport through the membrane. In contrast, ionic conductors like doped zirconia ($(ZrO_2)_{1-x}(Y_2O_3)_x$ (YSZ), $(ZrO_2)_{1-x}(Y_2O_3)_x(Sc_2O_3)_y$ (ScYSZ)) or doped ceria ($Ce_{1-x}Gd_xO_{2-\delta}$ (CGO), $Ce_{1-x}Sr_xO_{2-\delta}$ (CSO), $Ce_{1-x}Pr_xO_{2-\delta}$ (CPO)) have high chemical stability in CO_2 and at low oxygen partial pressure. Fluxes in membranes constructed from such materials is strongly limited by electronic conductivity [18, 19].

Dual-phase systems, where the membrane consists of a composite of a stable ionic conductor and a stable electronic conductor, can therefore be an alternative to the single phase system to ensure high oxygen flux and chemical stability at the same time.

Early reported dual-phase membranes were ceramic-metal (cermet) composites consisting of an oxygen ion-conducting oxide phase and an electron-conducting noble metal phase ($(ZrO_2)_{1-0.08}(Y_2O_3)_{0.08}$/Pt [20] and Bi_2O_3-Er_2O_3/Au [21]). The price of the membrane can strongly be decreased avoiding the noble metals by using only ceramic compounds ("cer/cer"). Such "cercer", e.g. composite membranes $NiFe_2O_4$ - $Ce_{0.9}Gd_{0.1}O_{1.95}$ (NFO-CGO10) [17] and $Ce_{0.8}Gd_{0.2}O_{1.9}$ - $MnFe_2O_4$ (CGO-MFO) [22] have indeed been shown to be stable in CO_2.

The thermodynamic driving force for oxygen transport through a MIEC membrane is the oxygen chemical potential gradient across the membrane, dictated by the imposed oxygen activities on the two sides of the membrane. The flux through the membrane is for the case of fast surface exchange given by the Wagner Equation (1):

$$J_{O_2} = \frac{RT}{16F^2L}\int_{pO_2^{permeate}}^{pO_2^{feed}} \frac{\sigma_e\sigma_i}{\sigma_e+\sigma_i}\,(pO_2)\; d\ln pO_2 \qquad (1)$$

where J_{O_2} is the oxygen permeation flux (mol m^{-2} s^{-1}), R is the gas constant, F is the Faraday constant, L is the membrane thickness, σ_e and σ_i are the electronic and the ionic conductivities, and pO_2^{feed} and $pO_2^{permeate}$ are the oxygen partial pressures at the high pressure side and low pressure side, respectively.

In order to obtain a high oxygen flux, the membrane should evidently (cf. Eq 1) be as thin as possible. Asymmetric membranes, which combine a relatively thick porous support (for mechanical stability) and a thin dense membrane layer, are a promising architecture to minimize the actual membrane thickness whilst ensuring mechanical robustness.

To manufacture dual-phase asymmetric membranes, the following material related challenges must be overcome: (i) a heat treatment which allows a proper co-sintering of all layers must be established, (ii) the two materials must be chemically compatible ensuring no (or very limited) reaction between the two phases, and finally (iii) the thermal expansion coefficients (TECs) between the membrane materials and the support must be very close to ensure mechanical integrity of the component.

Yttria stabilized zirconia (YSZ) has been studied as the ionic conductor in composite OTMs due to its high ionic conductivity, its thermodynamic stability in oxidizing and reducing atmospheres and its good mechanical strength [18]. The highest ionic conductivity for $(ZrO_2)_{1-x}(Y_2O_3)_x$ electrolytes is observed for x=0.08 (8YSZ) and is around 0.03 S cm^{-1} at 850 °C [23]. Further addition of Y_2O_3 will decrease the ionic conductivity due to enhanced association of the oxygen vacancies and dopant cations, which results in defect-complexes with low mobility [24]. Co-doping of scandium and yttrium in zirconia results in significant enhancement of the ionic conductivity as compared with 8YSZ. Artemov *et al.* reported that the ionic conductivity of $(Y_2O_3)_{0.01}(Sc_2O_3)_{0.10}(ZrO_2)_{0.89}$ (10Sc1YSZ) is higher than 0.12 S cm^{-1} at 850 °C [25]. Therefore, 10Sc1YSZ was chosen here as the ionic conductor for the dual-phase membrane.

Spinels containing manganese and cobalt are known to possess high electrical conductivity [26]. The electrical conductivity of $MnCo_2O_4$ is reported to be in the range of 60 – 100 S cm^{-1} at 800 – 900 °C [27, 28]. In addition, $MnCo_2O_4$ is much easier to sinter than many other spinel-type oxides, and has a thermal expansion coefficient (TEC) (9.7 ppm/K between room temperature and 1000 °C) [27] which is close to the TEC of 8YSZ (10.88 ppm/K [29] from room temperature to 1000 °C). These properties make it a promising candidate as the electronic conductor in a dual-phase system with 10Sc1YSZ (10Sc1YSZ-$MnCo_2O_4$). Yi *et al.* reported that the $MnCo_2O_4$ spinel starts to decompose by formation of cobalt oxide above 1200 °C [30], which is close to the required sintering temperature for the densification of YSZ. Therefore, it is expected to be difficult to fully densify a composite of $MnCo_2O_4$ and Sc1YSZ in an asymmetric membrane by conventional sintering.

Originally proposed by Chen and Wang, two-step sintering profiles allow producing nanostructured materials with high density at modest temperature, due to different grain growth and densification kinetics [31]. Indeed, with well-chosen two-step sintering profiles

the densification can proceed without grain growth. The suppression of the final-stage grain growth is achieved by exploiting the difference in kinetics between grain-boundary diffusion and grain-boundary migration. A typical two-step sintering profile consists of a first step with a fast heating rate (15 – 25 °C min^{-1}) to a peak temperature (without or with very short holding time (3 minutes maximum)) and, on a second step, the immediate cooling down to an isothermal plateau at a lower temperature. In the case of a composite membrane such a profile could allow a higher densification to achieve the desired microstructure in the composite membrane layer (and the porous support) while avoiding undesirable phase decompositions.

In this work we present how two-step sintering can be utilized to prepare planar asymmetric membranes consisting of a 10Sc1YSZ-$MnCo_2O_4$ composite. The membranes were manufactured by tape-casting, lamination and subsequently sintered in a two-step firing. First a sintering study is presented involving the laminated membranes heat treated at three different sintering profiles. This allowed manufacturing of fully dense membranes. Catalysts were applied at both surfaces and oxygen permeation measured under different atmospheres. Finally a durability test was conducted with CO_2 as sweep gas.

2. Experimental

2.1. Membrane preparation

As presented in Figure 5. 1, the asymmetric membranes consist of a 200 micron thick porous support (3YSZ + 20 vol.% of Al_2O_3) and a thin dense composite membrane layer (10Sc1YSZ-$MnCo_2O_4$, 7 µm) surrounded by two porous layers (8YSZ, 10 µm) that can be impregnated with a suitable catalyst. All layers were manufactured separately by tape casting. The YSZ (3YSZ and 8YSZ), 10Sc1YSZ and $MnCo_2O_4$ powders were purchased from Tosoh (Japan), Daiichi Kigenso Kagaku Kogyo Co. Ldt (Japan), and Marion Technologies (France), respectively. 3YSZ and 8YSZ powders were calcined for 2 h at 1100 °C and 900 °C, respectively prior to further processing. All materials were ball milled in ethanol to obtain particles within submicronic range. Three slurries were prepared and cast: (i) a slurry for the porous support layer containing 33 wt.% of pore formers in relation to the total solid content (Graphite (d_{v50}=7 µm) and PMMA (d_{v50}=1.8 µm) supplied by Graphit Kropfmühl AG (Germany) and Esprix Technologies (USA), respectively) (ii) a slurry for the

porous functional layers containing 33 wt.% of pore former (PMMA) and (iii) a slurry for the membrane layer free of pore former.

After drying, the green tapes were assembled by lamination at 135 °C and 30 mm diameter disks were cut out using a stamping tool.

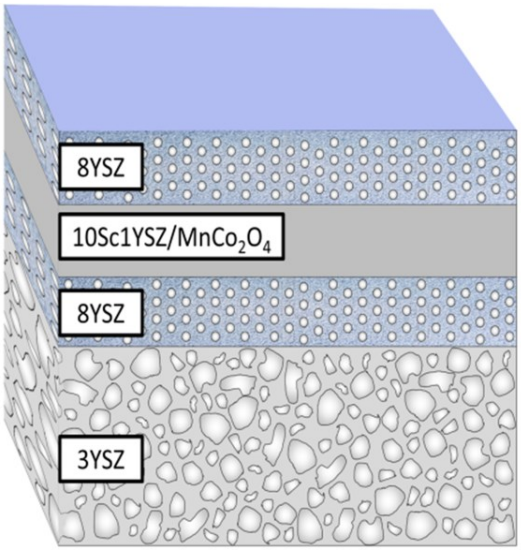

Figure 5. 1: Schematic structure of the 10Sc1YSZ-$MnCo_2O_4$ asymmetric membrane developed in this study, consisting of 4 layers from bottom to top: a porous 3YSZ support layer, a porous 8YSZ layer to be impregnated with a catalyst, the 10Sc1YSZ-$MnCo_2O_4$ membrane layer and a second porous 8YSZ for catalyst impregnation.

As is presented in Figure 5. 2, a sintering study was performed with following process parameters: (i) conventional sintering at 1250 °C for 6 h, (ii) conventional sintering at 1075 °C for 6 h (iii) two-step sintering, including a peak temperature of 1250 °C (3 min) and a dwell temperature of 1075 °C (6 h) (iv) two-step sintering at peak (3 min)/dwell (6 h) temperatures of 1225/1090 °C. Heating rates of 0.25 °C min^{-1} for the de-bindering and 1 °C min^{-1} for the sintering regime were used in all cycles. A holding time of 4 h at 600 °C was implemented in all sintering profiles to ensure complete removal of organic matter. A heating ramp of 25 °C min^{-1} was used for the peak of the two-step sintering profiles. A dwell period of six hours was employed in all four sintering cycles. Figure 5. 2 focuses on the last 30 hours of the sintering cycles since they distinguish the four sintering cycles. Table 5. 1 summarizes the complete sintering cycles used to optimize the microstructure of the 10Sc1YSZ-$MnCo_2O_4$ asymmetric membranes. The obtained samples were characterized and compared by: (i) SEM analysis (fracture cross-section) and (ii) EDX analysis (polished cross-section).

Table 5. 1: Overview table of the four different sintering cycles used to optimize the microstructure of the 10Sc1YSZ-$MnCo_2O_4$ asymmetric membranes.

Name (Code)	Heating rate step 1 (°C min^{-1})	Holding step 1	Heating rate step 2 (°C min^{-1})	Holding step 2	Heating rate step 3 (°C min^{-1})	Holding step 3	Cooling rate step 1 (°C min^{-1})	Holding step 4	Cooling rate step 2 (°C min^{-1})
Conventional sintering at 1250°C **(CS1250)**	0.25	600 °C / 4h	1	1250 °C / 6h	-	-	1.67	-	-
Conventional sintering at 1075°C **(CS1075)**	0.25	600 °C / 4h	1	1075 °C / 6h	-	-	1.67	-	-
Two-step sintering at 1250°C/1075°C **(TSS1250/1075)**	0.25	600 °C / 4h	1	1075 °C / 1min	25	1250 °C / 3min	25	1075 °C / 6h	1.67
Two-step sintering at 1225°C/1090°C **(TSS1225/1090)**	0.25	600 °C / 4h	1	1090 °C / 1min	25	1225 °C / 3min	25	1090 °C / 6h	1.67

After sintering, $Gd_{0.2}Ce_{0.8}O_{2-\delta}$ (GDC) and $LaNi_{0.6}Co_{0.4}O_{3-\delta}$ (LNC) aqueous solutions with concentration of 2.5 and 1.25 M were prepared by dissolving the corresponding nitrate solid solutions in water. The aqueous solutions were supplemented with a wetting agent (Triton X-100) and a complexing agent (Urea), and were infiltrated in both the porous YSZ layers to serve as oxygen oxidation/reduction catalysts. The samples were placed under vacuum to remove air and enhance the penetration of the solution into the porous support and the functional layers. This ensures an even distribution of the catalyst pre-cursor throughout the complete porous layers. The infiltrated samples were heat treated at 350 °C after each infiltration. The infiltration process was repeated 3 times for each aqueous solution, to ensure deposition of sufficient amounts catalyst in the porous layers. The impregnation procedure has been successfully applied in previous studies [32 – 34].

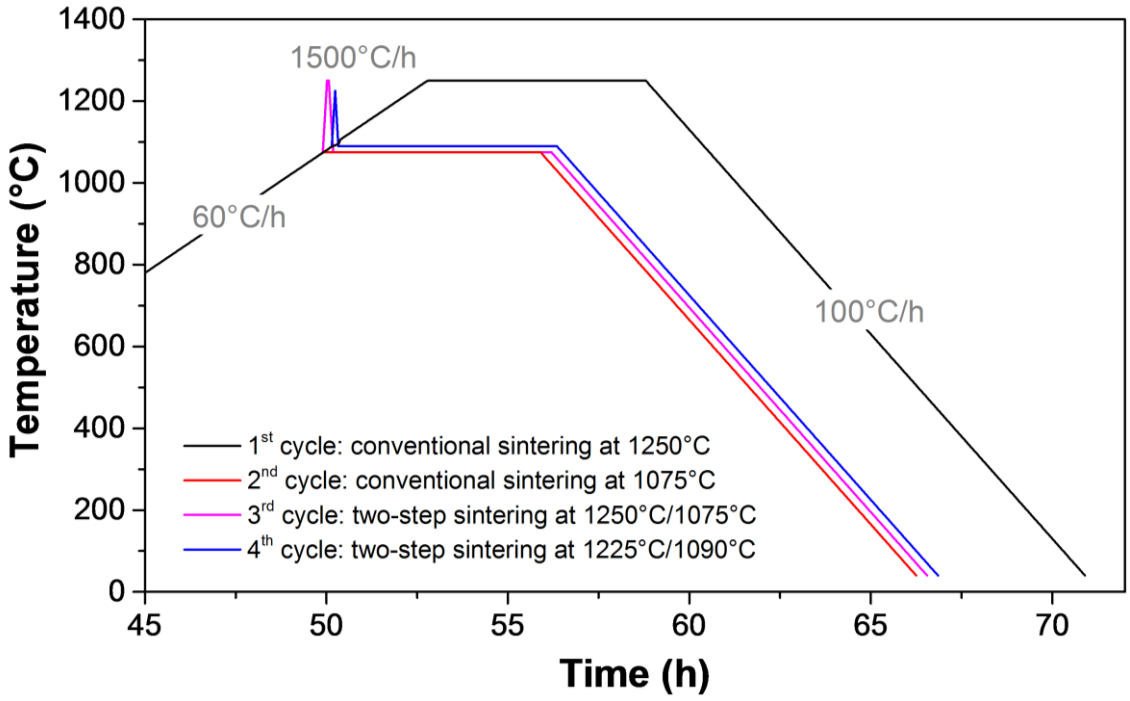

Figure 5. 2: Four different sintering cycles used to optimize the microstructure of the 10Sc1YSZ-$MnCo_2O_4$ asymmetric membranes: (i) conventional sintering at 1250 °C, (ii) conventional sintering at 1075 °C, (iii) two-step sintering at 1250 °C/1075 °C and (iv) two- step sintering at 1225 °C/1090 °C. The first 45 hours of the cycles are not shown since they are similar for the four different sintering cycles.

2.2. Membrane characterization

Contact dilatometry was used to determine the shrinkage and sintering activity of the porous support and the thin membrane layer materials. Rods (2 cm x 0.5 cm x 0.5 cm) of 3YSZ + 20 vol.% Al_2O_3 + 30 vol.% graphite and 10ScYSZ/$MnCo_2O_4$ (70/30 vol.%) powder mixtures were prepared by uniaxial pressing. Dilatometry on the dense bars was carried out on a Netzsch 402 CD differential dilatometer. The bar of the porous support material was pre-calcined at 1000 °C in order to avoid the destruction of the sample by the holder pressure of the dilatometer. The heating rate was 1 °C min^{-1} from 1000 °C to 1400 °C. The 10ScYSZ/$MnCo_2O_4$ (70/30 vol.%) bar, was heated at 0.5 °C min^{-1} from room temperature to 600 °C, then 1 °C min^{-1} from 600 °C to 1250 °C. All tests were performed in air.

The microstructure of the asymmetric membranes, and in particular the integrity of the thin film 10Sc1YSZ-$MnCo_2O_4$ layer, was investigated on fractured and polished cross-sections by scanning electron microscopy (SEM) using a Hitachi TM3000 equipped with a Bruker energy dispersive X-ray spectroscopy (EDX) system and a FE-SEM Zeiss Supra 35 electron microscope.

2.3. Oxygen permeation tests

Oxygen permeation measurements were conducted in an oxygen membrane rig built at Risø DTU as described by Samson [35]. It consists of two alumina tubes that contact the membrane from the top and from the bottom. The gases are introduced to the interior of the test house to vicinity of sample and onto both sides of the membrane via smaller diameter alumina tubes inserted within the large, outer alumina tubes. The membrane is placed in the middle of a height adjustable tube furnace. Tape cast sodium aluminosilicate (NAS, Na_2O: 17.8 mol.%, Al_2O_3: 9.4 mol.% and SiO_2: 72.8 mol.% [36]) glass rings, with an inner diameter of 9 mm, and a glass transition temperature of 515 °C [35] were used as sealing material between the alumina tubes and the membrane. The side walls of the samples were also coated with NAS paste to ensure that no oxygen enters from the sweep gas compartment to the membrane. To ensure a gas tight sealing, the membrane was heated in air up to 940 °C and afterwards cooled to 750 °C. A gas chromatograph was connected to the outlet of the permeate side to quantify oxygen leak into the permeate stream (oxygen that enters the permeate compartment via pinholes or insufficient sealing at the membrane periphery). From a quantification of the leak the uncertainty of the measured permeation flux is less than 5 %, mainly originated from the uncertainty of the area of the tested membrane. During the test, air or pure O_2 with a flow of 100 $ml_N\ min^{-1}$ was fed to the feed side, while various flows of N_2 or CO_2 varying from 20 $ml_N\ min^{-1}$ to 150 $ml_N\ min^{-1}$ were fed to the permeate side. The membrane was assembled with the porous support on the feed side. The inlet flow of each gas was controlled and monitored by a mass flow controller (Brooks), while the outlet flow was determined by a mass flow meter (Bronkhorst). In the experiments reported here the flow out was equal to the flow in within 3 %. In-house built zirconia-based pO_2 sensors were used to determine the pO_2 of the inlet gas on the permeate side (before feeding to the membrane) and of the outlet gas (after passing over the membrane). Net oxygen permeation flux was deduced from the pO_2 difference between inlet and outlet, as given by:

$$J_{O_2} = \frac{pO_{2,permeate}^{out} \cdot \dot{n}^{out} - pO_{2,permeate}^{in} \cdot \dot{n}^{in}}{A} \qquad (2)$$

where J_{O_2} is the oxygen permeation flux, $pO_{2,permeate}^{in}$ and $pO_{2,permeate}^{out}$ are respectively the oxygen partial pressures of the inlet and outlet gases, $\dot{n}^{in}$ and $\dot{n}^{out}$ are molar flow rates of inlet and outlet gases, respectively, and A is the net area of the permeate side of the

membrane. The Nernst equation (3) is used to calculate the oxygen partial pressure from the measured sensor voltage (V):

$$V = \frac{R\,T}{4\,F} \ln \frac{pO_2}{pO_{2,ref}} \qquad (3)$$

where V is the open circuit voltage of the oxygen sensor, T is the temperature of the oxygen sensor and $pO_{2,ref}$ is the oxygen partial pressure at the reference electrode which was maintained at 0.21 atm during the measurement.

3. Results and Discussion

3.1. The effect of the sintering profile on the microstructure of 10Sc1YSZ-$MnCo_2O_4$ composite membranes

Simple percolation theory, assuming 6 nearest neighboring grains would predict a minimum of 33.3 vol.% of an electron conductive phase to form a continuous matrix in a composite system with random distribution of the phases. However, best consistence between the calculated and measured conductivity has in several systems been reported to be achieved with a slightly higher number of nearest neighboring grains [37, 38]. Percolation is thus expected to be achievable below the 33 %. In order to achieve the highest effective total conductivity in the membrane, a volume ratio between the ionic conductor (10Sc1YSZ) and electronic conductor ($MnCo_2O_4$) of 70:30 vol.% was chosen, reflecting that the ionic conductivity σ_{ionic} (0.12 S cm^{-1} at 850 °C) [25] is five hundred time lower than the electronic conductivity $\sigma_{electric}$ (60 S cm^{-1} at 800 °C) [27] and hence that one should use as much of the ionic conductor as possible while still maintaning percolation in the electronically conducting phase.

A critical step in the manufacturing of multi-layered membrane structures containing different ceramic materials is the optimization of the co-sintering process. In co-sintering, a good match of the shrinkage and strain rate of the different layers needs to be achieved in order to avoid the development of excessive stresses during sintering which can lead to mechanical failures [39]. For OTM applications, the thin membrane layer needs to be fully dense, while the support has to be sufficiently porous (usually 25 – 40 % of porosity, depending on support thickness and microstructure) to assure sufficient permeability for gas supply and distribution.

Conventional sintering at 1250 °C for 6 h in air (CS1250) did not result in a suitable microstructure for OTM use. Figure 5. 3 presents the SEM/EDX analysis of the polished cross-section of the asymmetric membrane after conventional sintering. As shown in Figure 5. 3.a, the thin membrane layer is around 5 µm thick and completely densified. Nevertheless, the elemental maps of manganese and cobalt display that both elements which should be concentrated in the dense membrane layer are evenly distributed through all other layers. The manganese and cobalt mobility is too high at the chosen firing conditions. For this reason, a two-step sintering method (see pink and blue curves in Figure 5. 2 corresponding to TSS1250/1075 and TSS1225/1090 in Table 5. 1) was subsequently attempted in order to fully densify the 10Sc1YSZ-$MnCo_2O_4$ dual-phase membrane while at the same time; (i) avoiding excessive Co and Mn diffusions and (ii) ensuring a sufficient mechanical strength of the YSZ/Al_2O_3 support structure.

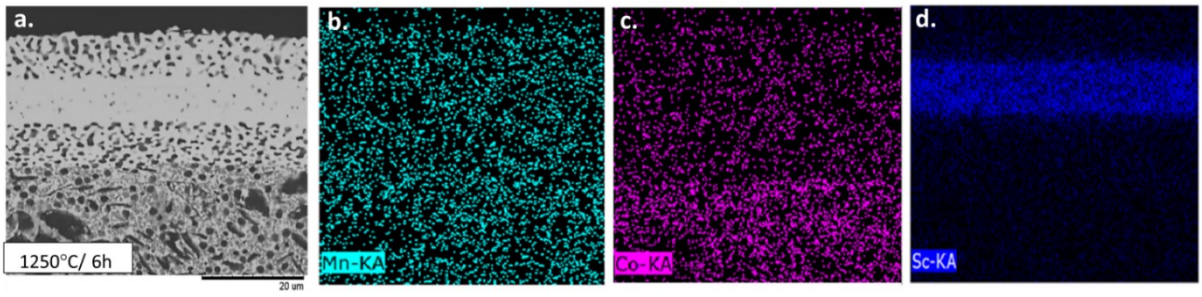

Figure 5. 3: Polished cross-section of an asymmetric membrane after a conventional sintering at 1250 °C/6 h (CS1250) (a) SEM picture (b, c, d) EDX maps of Co, Mn and Sc elements.

To elucidate the ideal sintering temperatures and optimize the sintering profile, separate dilatometry measurements were performed on the support and the membrane layer materials. The results of the dilatometry measurements are shown in Figure 5. 4. The temperatures where densification occurs most rapidly are approximately 1200 °C and 1025 °C for the support and the thin membrane layer, respectively. In order to optimize the sintering, these two temperatures were chosen as the targeted dwell temperatures in the two stage sintering profiles. A temperature point close to the maximum shrinkage domain of the porous support was defined as a peak temperature for the short term sintering step. Sintering the membrane structure to this peak temperature should increase the density of the thin membrane layer and should ensure a good mechanical strength of the support. A temperature point close to the maximum densification of the thin membrane layer was selected for the second step dwell period. Such a sintering profile allows the membrane to

sinter at relatively low temperature, and avoid the loss of $MnCo_2O_4$ experienced during conventional 6 h sintering at 1250 °C (CS1250).

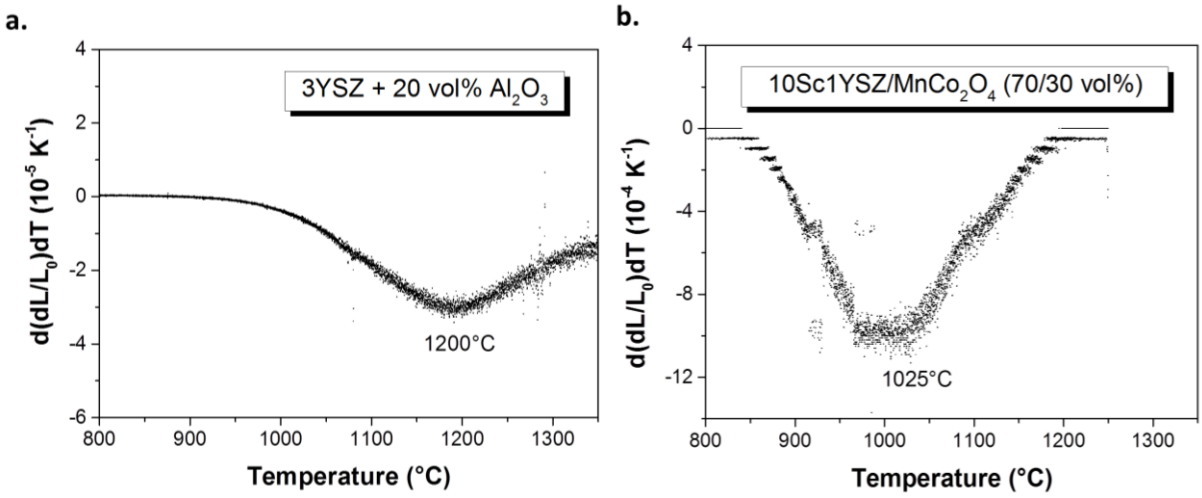

Figure 5. 4: Dilatometry curves, showing the shrinkage rate as function of sintering temperature for the porous support (a) and the thin membrane layer (b). Heating rate: 1 °C min^{-1}.

Figure 5. 5 presents the SEM images of a fracture cross-sections and the elemental maps of Mn, Co and Sc obtained by EDX of membranes sintered using the sintering profiles described in Table 5. 1 (TSS1250/1075, TSS1225/1090 and CS1075). Both membranes sintered using the two-step sintering method have fully dense membrane layers (Figures 5. 5. 5.a and 5. 5.e). Their porosities were evaluated to be less than 1 vol.% by using a phase distribution analysis software. In comparison, the membrane which was conventionally sintered at 1075 °C (CS1075) has a high porosity of 18 vol.%. Based on EDX results, the ratio of 10Sc1YSZ to $MnCo_2O_4$ in the thin membrane layer is about 75:25 vol.% (grains size: $d_{50\text{-}ScYSZ}$=1.01 µm and $d_{50\text{-}MCO}$=0.46 µm) in the case that the sintering profile (i) was used (TSS1250/1075, Figures 5. 5.b, 5, 5.c, 5. 5.d), while the same ratio is about 70:30 vol.% (grains size: $d_{50\text{-}ScYSZ}$=0.97 µm and $d_{50\text{-}MCO}$=0.51 µm) when the sintering profiles TSS1225/1090 (Figures 5. 5.f, 5. 5.g, 5. 5.h) or CS1075 (Figures 5. 5.j, 5. 5.k, 5. 5.l) were applied. These SEM/EDX results clearly show that the two-step sintering profiles allow on the densification of the 10Sc1YSZ-$MnCo_2O_4$ membrane layer without the loss of $MnCo_2O_4$ observed for the CS1075 one step profile.

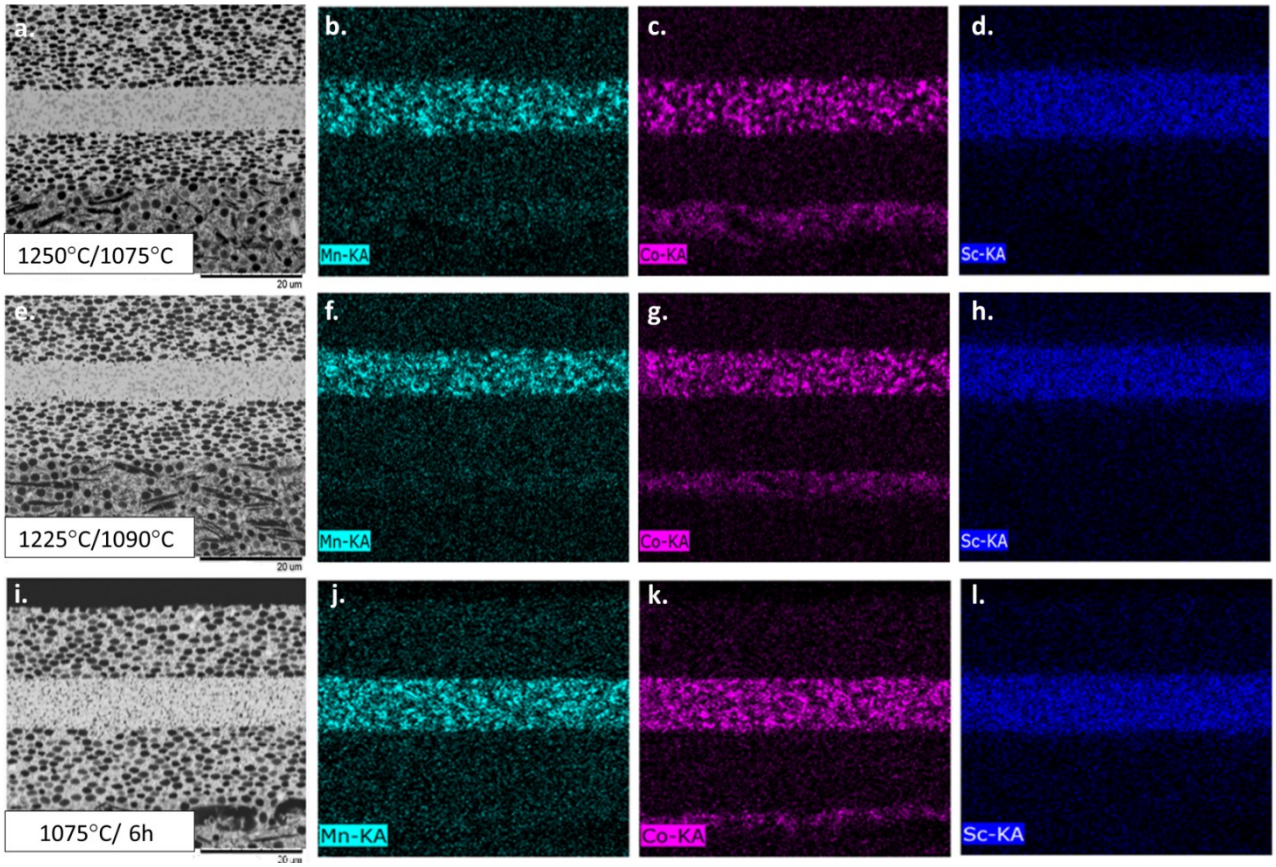

Figure 5. 5: SEM images and EDX maps (Mn, Co and Sc elements) of polished cross-sections of 10ScYSZ/$MnCo_2O_4$ asymmetric membranes TSS1250/1075 (a, b, c, d) TSS1225/1090 (e, f, g, h) and CS1075 (i, j, k, l).

3.2. Oxygen flux measurements on asymmetric dual-phase 10Sc1YSZ-$MnCo_2O_4$ membranes

The performance of the 10Sc1YSZ-$MnCo_2O_4$ (70-30 vol.%) asymmetric membranes on the 3YSZ support obtained by two-step sintering (TSS1225/1090) was evaluated carrying out oxygen permeation measurements, as described in Section 2.3.

Figure 5. 6 displays the oxygen permeation flux as a function of the ratio between the oxygen partial pressures of the feed and permeate sides ($\ln(pO_2^{feed}/pO_2^{permeate})$) using N_2 and CO_2 as sweep gases, and pure oxygen as a feed gas. The flux scales in direct proportion to the driving force across the membrane. The highest fluxes in O_2/N_2 and O_2/CO_2 were measured at 940 °C and correspond to 2.28 $ml_N\ cm^{-2}\ min^{-1}$ and 1.91 $ml_N\ cm^{-2}\ min^{-1}$, respectively. When air was used instead of pure oxygen as a feed gas, the fluxes decrease to 1.41 $ml_N\ cm^{-2}\ min^{-1}$ and 0.81 $ml_N\ cm^{-2}\ min^{-1}$, in N_2 and CO_2 respectively. Table 5. 2 lists the values of oxygen permeation in different atmosphere at different temperatures. At temperature above

900 °C, the oxygen permeation flux measured using CO_2 as the sweep gas is lower than that measured in N_2 at equivalent driving force. Several other studies of OTMs present lower performances in CO_2 when compared to N_2/He sweep [40 – 45]. The phenomenon has been suggested to be a consequence of suppressed oxygen surface exchange rate due to the chemisorption of CO_2 on the surface possibly blocking some oxygen vacancies [42, 45].

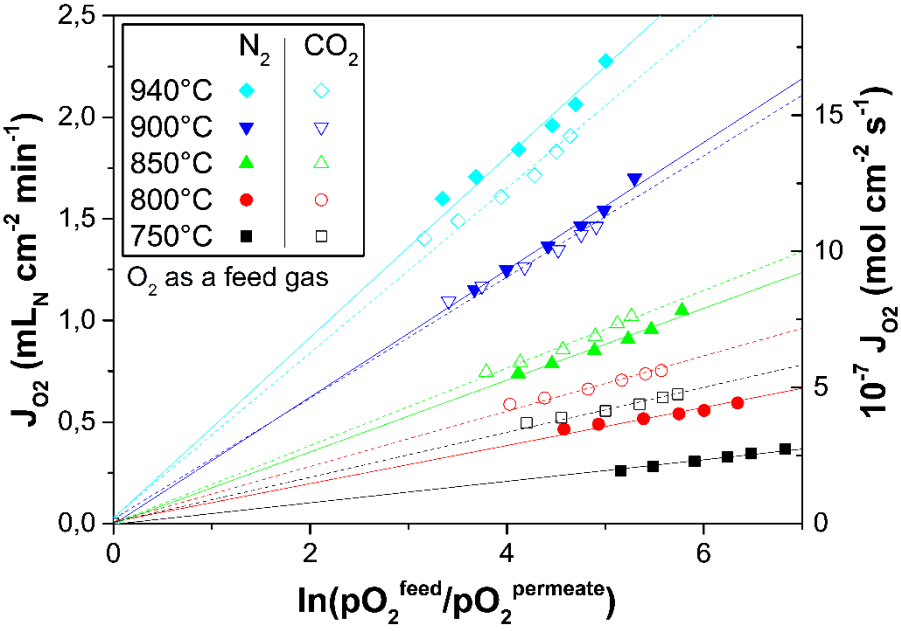

Figure 5. 6: Oxygen permeation flux of 10Sc1YSZ-$MnCo_2O_4$ (70-30 vol.%) membrane as a function of the natural logarithm ratio between the oxygen partial pressure of the feed and the permeate side using N_2 and CO_2 as a sweep gases and pure oxygen as a feed gas. The lines are a linear fit to the results.

Table 5. 2: Oxygen permeation fluxes ($ml_N\ cm^{-2}\ min^{-1}$) and driving force values through 10Sc1YSZ-$MnCo_2O_4$ (70-30 vol.%) asymmetric membrane as a function of the temperature and the used atmosphere.

Temperature (°C)	Atmosphere			
	Air/N_2	Air/CO_2	O_2/N_2	O_2/CO_2
	Oxygen permeation fluxes ($ml_N\ cm^{-2}\ min^{-1}$) / $\ln(pO_2^{feed}/pO_2^{permeate})$			
750	0.29 / 5.496	0.39 / 4.660	0.37 / 6.824	0.64 / 5.737
800	0.49 / 4.975	0.43 / 4.571	0.59 / 6.344	0.75 / 5.569
850	0.83 / 4.447	0.52 / 4.384	1.05 / 5.778	1.02 / 5.266
900	1.26 / 4.036	0.66 / 4.136	1.70 / 5.296	1.46 / 4.907
940	1.41 / 3.920	0.81 / 3.978	2.28 / 5.004	1.91 / 4.642

When the permeation flux is limited not only by bulk diffusion but also by surface-exchange kinetics, the oxygen-permeation flux can, in a simple approximate description, be characterized by a modified Wagner equation (4) [46]:

$$J_{O_2} = -\frac{1}{1+(\frac{2L_c}{L})}\frac{RT}{16F^2L}\int_{pO_2^{permeate}}^{pO_2^{feed}}\frac{\sigma_{el}\sigma_{ion}}{\sigma_{el}+\sigma_{ion}}\,(pO_2)d\ln pO_2 \qquad (4)$$

where L_c (= D_a/K_s) is the characteristic membrane thickness, D_a is the ambi-polar diffusion coefficient and K_s is the surface-exchange coefficient. When the membrane thickness (L) is much smaller than L_c, the oxygen permeation is mainly limited by the surface-exchange kinetics, while for L $\gg L_c$ the bulk diffusion is the main rate limiting factor. Since $\sigma_{el} \gg \sigma_{ion}$ for 10Sc1YSZ-$MnCo_2O_4$ (70-30 vol.%) [25, 27], the mixed conductivity term in the integrand in Eq. (5) becomes:

$$J_{O_2} = -\frac{1}{1+(\frac{2L_c}{L})}\frac{RT}{16F^2L}\int_{pO_2^{permeate}}^{pO_2^{feed}}\sigma_{ion}\,(pO_2)d\ln pO_2 \qquad (5)$$

An approximate characteristic membrane thickness (L_c) was calculated from the O_2/N_2 experiments in comparing measured fluxes with the ones calculated from Equation 5 using known conductivity values for the zirconia treating L_c as a fitting parameter. For the calculations, we considered that: $\sigma_{ion,10Sc1YSZ} \gg \sigma_{ion,MnCo_2O_4}$, and approximated that $\sigma_{ion} = x * \sigma_{ion,10Sc1YSZ}$, where x is the volume percentage of 10Sc1YSZ in the composite membrane. The ionic conductivities of 10Sc1YSZ from 750 to 940 °C were taken from the study by Irvine *et al.* [47]. The driving force ln($pO_2^{feed}/pO_2^{permeate}$) was fixed at 5 for the calculations.

Figure 5. 7 presents the thus obtained L_c values as a function of the temperature and a comparison with the actual membrane thickness (L). For the complete investigated temperature range L_c is much larger than L (10 to 20 times) which strongly indicates that surface-exchange kinetics is a main rate limiting factor for the oxygen permeation. In case of gas concentration polarization on the permeate side, the driving force will be overestimated which will result by a larger value of L_c. Calculations were performed at 950 °C by using a lower driving force than assumed in order to show that even with gas concentration polarization effect L_c is significantly larger than L. Nevertheless, it is important to mention that in principal the ionic and electronic conductivities of the two phases in the

membrane could deviate from the known materials values. For example, a modification of the microstructure, such as agglomeration of the phases could limit the percolation and therefore affect the conductivities. Also the ionic conductivity in the zirconia could in principle be reduced relative to that of the pure material due to interdiffusion of Mn, Co from the spinel. Moreover, the performed calculations do not consider a potential support limitation. A model developed by Niehoff *et al.* [48] introducing a surface correction factor for the calculation of L_c could be used to get more accurate results.

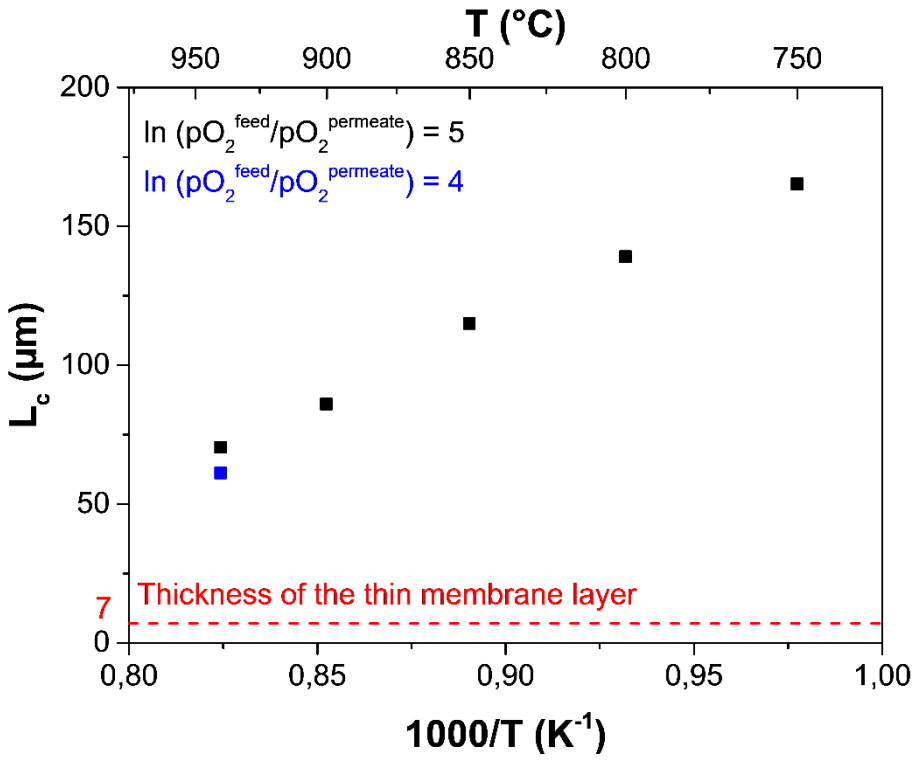

Figure 5. 7: The characteristic membrane thicknesses (L_c) as a function of temperature, for oxygen permeation fluxes obtained in O_2/N_2 with ln($pO_2^{feed}/pO_2^{permeate}$) = 5 (black) and 4 (blue).

In order to investigate the chemical and thermal long-term stability of the dual-phase membrane, the oxygen flux was measured for a continuous period of 1730 h with CO_2 as sweep gas and air as feed gas at 850 °C. Figure 5. 8 presents the evolution of the oxygen flux through the membrane as a function of the time (black line). The blue line represents the first derivative of the oxygen flux as a function of the time. For the first 1100 h the flux decreases while after it stays constant for the last 600 h of the experiment. Figure 5. 9 shows SEM images of the very fine GDC and LNC particles infiltrated onto the functional membrane layer as oxygen oxidation/reduction catalysts. Before the oxygen permeation test, individual GDC/LNC particles are in the range of 20 – 50 nm (Figure 5. 9.a), while after 1730 h of

testing in CO_2, they are in the range of 120-200 nm (Figure 5. 9.b). The particles thus clearly grow during the membrane operation. This coarsening causes a decrease in the surface area of the oxygen oxidation/reduction catalysts, therefore leading to surface exchange limitations. It is most likely the reason for the declining flux over the first 1100 hours.

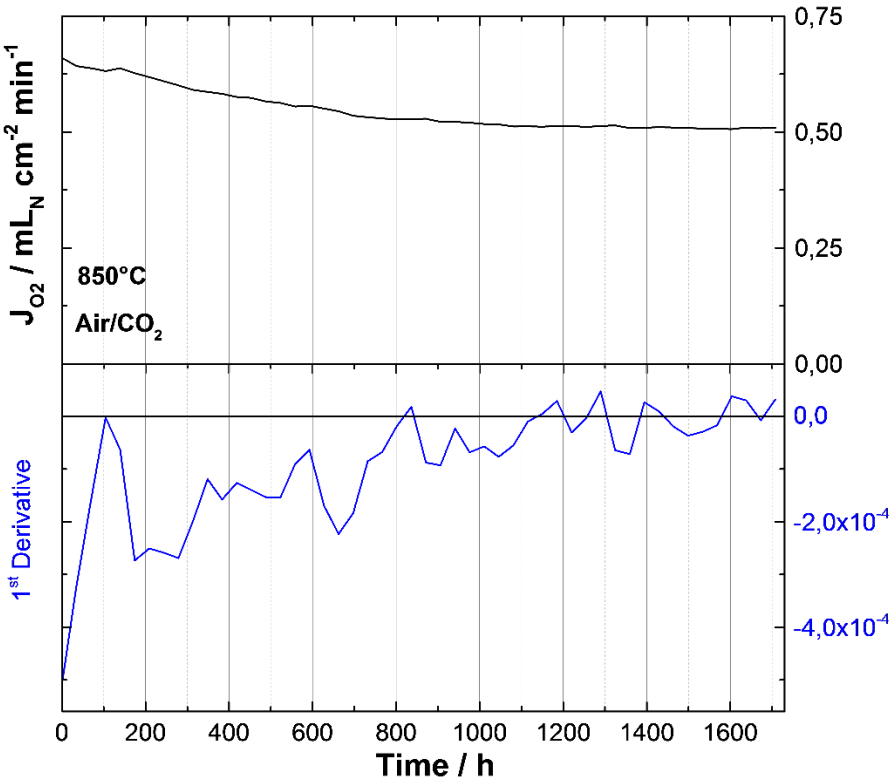

Figure 5. 8: Oxygen permeation flux through 10Sc1YSZ-$MnCo_2O_4$ (70-30 vol.%) composite membranes as a function of the time at 850 °C, with constant flow of air as a feed gas and 112 ml_N min^{-1} of CO_2 as a sweep gas.

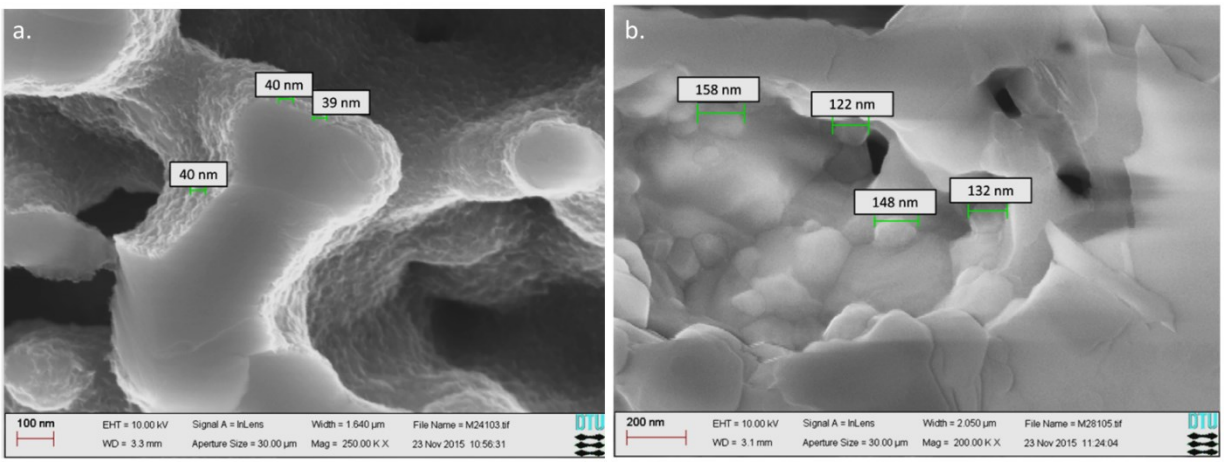

Figure 5. 9: SEM pictures of the GDC and LNC particles present onto the functional membrane layers prior to (a) and after (b) 1730 h of test in CO_2.

4. Conclusions

Dual-phase asymmetric 10Sc1YSZ-$MnCo_2O_4$ membranes were successfully prepared by tape casting, lamination and a two-step sintering process. The microstructure of the asymmetric membranes developed with different sintering cycles was studied and showed the advantages of the two-step sintering method to obtain a gastight membrane layer with the desired ratio of the ionic/electronic conductor. Such microstructures could not be obtained by conventional sintering. The oxygen permeation flux through a 7 μm 10Sc1YSZ-$MnCo_2O_4$ (70-30 vol.%) asymmetric membrane was studied from 750 to 940 °C under several atmospheres (air/pure oxygen as feed gases and N_2/CO_2 as sweep gases). An oxygen flux of 2.23 $ml_N\ min^{-1}cm^{-2}$ can be achieved at 940 °C in O_2/N_2 atmospheres. A chemical and thermal stability test under CO_2 (as sweep gas) was performed over 1730 h and showed initial degradation during 1100 h, after which stable performance was observed during the remaining 630 h of test. The observed degradation is attributed to coarsening of the infiltrated catalyst phase. The 10Sc1YSZ-$MnCo_2O_4$ (70-30 vol.%) asymmetric membrane itself seems stable in CO_2 atmosphere and is thus a good candidate for use in industrial applications where the contact with CO_2 is required, for example for the use in oxy-coal fired power plants for Carbon Capture and Sequestration (CCS). Further improvement of the surface catalyst layers is needed to reach the full potential of these membranes.

Acknowledgments

The financial support from EU through the “Graded Membranes for Energy Efficient New Generation Carbon Capture Process (GREEN-CC)” project (Grant agreement no. 608524) is gratefully acknowledged. Karen Brodersen and Søren Preben Vagn Foghmoes are acknowledged by the authors for helping with tape-casting, and Henrik Paulsen for assisting in the preparation of the samples for SEM/EDX analysis.

References

[1] H. Stadler, F. Beggel, M. Habermehl, B. Persigehl, R. Kneer, M. Modigell, et al., Oxyfuel coal combustion by efficient integration of oxygen transport membranes, Int. J. Greenh. Gas Control. 5 (2011) 7–15. doi:10.1016/j.ijggc.2010.03.004.

[2] S.M. Hashim, A.R. Mohamed, S. Bhatia, Current status of ceramic-based membranes for oxygen separation from air, Adv. Colloid Interface Sci. 160 (2010) 88–100. doi:10.1016/j.cis.2010.07.007.

[3] S. Smart, C.X.C. Lin, L. Ding, K. Thambimuthu, J.C. Diniz da Costa, Ceramic membranes for gas processing in coal gasification, Energy Environ. Sci. 3 (2010) 268–278. doi:10.1039/b924327e.

[4] M. Czyperek, P. Zapp, H.J.M. Bouwmeester, M. Modigell, K. Ebert, I. Voigt, et al., Gas separation membranes for zero-emission fossil power plants: MEM-BRAIN, J. Memb. Sci. 359 (2010) 149–159. doi:10.1016/j.memsci.2010.04.012.

[5] S.S. Hashim, A.R. Mohamed, S. Bhatia, Oxygen separation from air using ceramic-based membrane technology for sustainable fuel production and power generation, Renew. Sustain. Energy Rev. 15 (2011) 1284–1293. doi:10.1016/j.rser.2010.10.002.

[6] J. Gurauskis, Ø. F. Lohne, D. S. Lagergren, E. T. Wefring, K. Wiik, Oxygen permeation in symmetric and asymmetric $La_{0.2}Sr_{0.8}Fe_{0.8}Ta_{0.2}O_{3-\delta}$ membranes, J. Eur. Ceram. Soc. Submitted. In progress.

[7] S. Baumann, J.M. Serra, M.P. Lobera, S. Escolástico, F. Schulze-Küppers, W.A. Meulenberg, Ultrahigh oxygen permeation flux through supported $Ba_{0.5}Sr_{0.5}Co_{0.8}Fe_{0.2}O_{3-\delta}$ membranes, J. Memb. Sci. 377 (2011) 198–205. doi:10.1016/j.memsci.2011.04.050.

[8] E. Perry Murray, M.J. Sever, S.A. Barnett, Electrochemical performance of $(La,Sr)(Co,Fe)O_3$-$(Ce,Gd)O_3$ composite cathodes, Solid State Ionics. 148 (2002) 27–34. doi:10.1016/S0167-2738(02)00102-9.

[9] A. Esquirol, J. Kilner, N. Brandon, Oxygen transport in $La_{0.6}Sr_{0.4}Co_{0.2}Fe_{0.8}O_{3-\delta}$-$Ce_{0.8}Ge_{0.2}O_{2-x}$ composite cathode for IT-SOFCs, Solid State Ionics. 175 (2004) 63–67. doi:10.1016/j.ssi.2004.09.013.

[10] P. Haworth, S. Smart, J. Glasscock, J.C. Diniz da Costa, High performance yttrium-doped BSCF hollow fibre membranes, Sep. Purif. Technol. 94 (2012) 16–22. doi:10.1016/j.seppur.2012.04.005.

[11] J. Sunarso, S. Baumann, J.M. Serra, W.A. Meulenberg, S. Liu, Y.S. Lin, et al., Mixed ionic-electronic conducting (MIEC) ceramic-based membranes for oxygen separation, J. Memb. Sci. 320 (2008) 13–41. doi:10.1016/j.memsci.2008.03.074.

[12] E. Bucher, A. Egger, G.B. Caraman, W. Sitte, Stability of the SOFC Cathode Material (Ba,Sr)(Co,Fe)$O_{3-\delta}$ in CO_2-Containing Atmospheres, J. Electrochem. Soc. 155 (2008) B1218. doi:10.1149/1.2981024.

[13] H. Luo, H. Jiang, K. Efimov, J. Caro, H. Wang, Influence of the preparation methods on the microstructure and oxygen permeability of a CO_2-stable dual phase membrane, AIChE J. 57 (2011) 2738–2745. doi:10.1002/aic.12488.

[14] M. Pilar Lobera, S. Escolastico, J. Garcia-Fayos, J.M. Serra, Ethylene Production by ODHE in Catalytically Modified $Ba_{0.5}Sr_{0.5}Co_{0.8}Fe_{0.2}O_{3-\delta}$ Membrane Reactors, ChemSusChem. 5 (2012) 1587–1596. doi:10.1002/cssc.201100747.

[15] S.J. Benson, D. Waller, J.A. Kilner, Degradation of $La_{0.6}Sr_{0.4}Fe_{0.8}Co_{0.2}O_{3-\delta}$ in Carbon Dioxide and, J. Electrochem. Soc. 146 (2000) 1305–1309.

[16] M. Schulz, R. Kriegel, A. Kämpfer, Assessment of CO_2 stability and oxygen flux of oxygen permeable membranes, J. Memb. Sci. 378 (2011) 10–17. doi:10.1016/j.memsci.2011.02.037.

[17] H. Luo, K. Efimov, H. Jiang, A. Feldhoff, H. Wang, J. Caro, CO_2-stable and cobalt-free dual-phase membrane for oxygen separation, Angew. Chemie - Int. Ed. 50 (2011) 759–763. doi:10.1002/anie.201003723.

[18] M.M. Hiroaki Yanagida, Kunihiko Koumoto, Kunihito Komoto, The Chemistry of Ceramics, 1996.

[19] T. Kawada, J. Suzuki, M. Sase, A. Kaimai, K. Yashiro, Y. Nigara, et al., Determination of Oxygen Vacancy Concentration in a Thin Film of $La_{0.6}Sr_{0.4}CoO_{3-\delta}$ by an Electrochemical Method, J. Electrochem. Soc. 149 (2002) E252. doi:10.1149/1.1479728.

[20] T.J. Mazanec, T.L. Cable, J.G. Frye, Electrocatalytic Cells for Chemical-Reaction, Solid State Ionics. 53 (1992) 111–118. doi:10.1016/0167-2738(92)90372-V.

[21] C.S. Chen, A.J. Burggraaf, Stabilized bismuth oxide ± noble metal mixed conducting composites as high temperature oxygen separation membranes, J. Appl. Electrochem. 29 (1999) 355–360.

[22] H. Takamura, K. Okumura, Y. Koshino, A. Kamegawa, M. Okada, Oxygen permeation properties of ceria-ferrite-based composites, in: J. Electroceramics, 2004: pp. 613–618. doi:10.1007/s10832-004-5167-y.

[23] X.J. Chen, K.A. Khor, S.H. Chan, L.G. Yu, Influence of microstructure on the ionic conductivity of yttria-stabilized zirconia electrolyte, Mater. Sci. Eng. A. 335 (2002) 246–252. doi:10.1016/S0921-5093(01)01935-9.

[24] V.V. Kharton, E.N. Naumovich, A.A. Vecher, Research on the electrochemistry of oxygen ion conductors in the former Soviet Union. I. ZrO_2-based ceramic materials, J. Solid State Electrochem. 3 (1999) 61–81. doi:10.1007/s100080050131.

[25] V.G. Artemov, I.E. Kuritsyna, S.P. Lebedev, G.A. Komandin, P.O. Kapralov, I.E. Spektor, et al., Analysis of electric properties of ZrO_2-Y_2O_3 single crystals using teraherz IR and impedance spectroscopy techniques, Russ. J. Electrochem. 50 (2014) 690–693. doi:10.1134/S1023193514070039.

[26] E. Rios, J.-L. Gautier, G. Poillerat, P. Chartier, Mixed valency spinel oxides of transition metals and electrocatalysis: case of the $Mn_xCo_{3-x}O_4$ system, Electrochim. Acta. 44 (1998) 1491–1497. doi:10.1016/S0013-4686(98)00272-2.

[27] A. Petric, H. Ling, Electrical conductivity and thermal expansion of spinels at elevated temperatures, J. Am. Ceram. Soc. 90 (2007) 1515–1520. doi:10.1111/j.1551-2916.2007.01522.x.

[28] M.Y. Yoon, E.J. Lee, R.H. Song, H.J. Hwang, Preparation and properties of a $MnCo_2O_4$ for ceramic interconnect of solid oxide fuel cell via glycine nitrate process, Met. Mater. Int. 17 (2011) 1039–1043. doi:10.1007/s12540-011-6025-5.

[29] H.L. Frandsen, T. Ramos, A. Faes, M. Pihlatie, K. Brodersen, Optimization of the strength of SOFC anode supports, J. Eur. Ceram. Soc. 32 (2012) 1041–1052. doi:10.1016/j.jeurceramsoc.2011.11.015.

[30] E.J. Yi, M.Y. Yoon, J.W. Moon, H.J. Hwang, Fabrication of a $MnCo_2O_4$/gadolinia-doped Ceria (GDC) dual-phase composite membrane for oxygen separation, J. Korean Ceram. Soc. 47 (2010) 199–204. doi:10.4191/KCERS.2010.47.2.199.

[31] I. Chen, X. Wang, Sintering dense nanocrystalline ceramics without final-stage grain growth, Nature. 404 (2000) 168–71. doi:10.1038/35004548.

[32] R. Kiebach, C. Knöfel, F. Bozza, T. Klemensø, C. Chatzichristodoulou, Infiltration of ionic-, electronic- and mixed-conducting nano particles into $La_{0.75}Sr_{0.25}MnO_3$–$Y_{0.16}Zr_{0.84}O_2$ cathodes – A comparative study of performance enhancement and stability at different temperatures, J. Power Sources. 228 (2013) 170–177. doi:10.1016/j.jpowsour.2012.11.070.

[33] T. Klemensø, C. Chatzichristodoulou, J. Nielsen, F. Bozza, K. Thydén, R. Kiebach, et al., Characterization of impregnated GDC nano structures and their functionality in LSM based cathodes, Solid State Ionics. 224 (2012) 21–31. doi:10.1016/j.ssi.2012.07.011.

[34] V. Gil; K. Kammer Hansen, High performance infiltrated backbones for cathode-supported SOFC's, ECS Trans. 64 (2014) 41–51. doi:10.1149/06402.0041ecst.

[35] A.J. Samson, M. Søgaard, P. Vang Hendriksen, (Ce,Gd)$O_{2-\delta}$-based dual phase membranes for oxygen separation, J. Memb. Sci. 470 (2014) 178–188. doi:10.1016/j.memsci.2014.07.028.

[36] K.A. Nielsen, M. Solvang, S.B.L. Nielsen, A.R. Dinesen, D. Beeaff, P.H. Larsen, Glass composite seals for SOFC application, J. Eur. Ceram. Soc. 27 (2007) 1817–1822. doi:10.1016/j.jeurceramsoc.2006.05.046.

[37] S.K. Bhattacharya, A.C.D. Chaklader, Review on Metal-Filled Plastics. Part 1. Electrical Conductivity, Polym. Plast. Technol. Eng. 19 (1982) 21–51. doi:10.1080/03602558208067726.

[38] Z. Wu, Modelling of ambipolar transport properties of composite mixed ionic-electronic conductors. Solid State Ionics 1996;93:65–84. doi:10.1016/S0167-2738(96)00521-8.

[39] G. Pećanac, S. Foghmoes, M. Lipińska-Chwałek, S. Baumann, T. Beck, J. Malzbender, Strength degradation and failure limits of dense and porous ceramic membrane materials, J. Eur. Ceram. Soc. 33 (2013) 2689–2698. doi:10.1016/j.jeurceramsoc.2013.04.018.

[40] W. Li, T. Tian, F. Shi, Y. Wang, C. Chen, for Oxygen Separation, Ind. Eng. Chem. Res. 48 (2009) 5789–5793. doi:10.1016/j.memsci.2012.03.026.

[41] K. Zhang, L. Liu, Z. Shao, R. Xu, J. Diniz da Costa, S. Wang, et al., Robust ion-transporting ceramic membrane with an internal short circuit for oxygen production, J. Mater. Chem. A. 1 (2013) 9150–9156. doi:10.1039/c3ta11427a.

[42] X. Tan, N. Liu, B. Meng, J. Sunarso, K. Zhang, S. Liu, Oxygen permeation behavior of $La_{0.6}Sr_{0.4}Co_{0.8}Fe_{0.2}O_3$ hollow fibre membranes with highly concentrated CO_2 exposure, J. Memb. Sci. 389 (2012) 216–222. doi:10.1016/j.memsci.2011.10.032.

[43] V. Esposito, M. Søgaard, P.V. Hendriksen, Chemical stability of $La_{0.6}Sr_{0.4}CoO_{3-\delta}$ in oxygen permeation applications under exposure to N_2 and CO_2, Solid State Ionics. 227 (2012) 46–56. doi:10.1016/j.ssi.2012.08.015.

[44] H. Luo, H. Jiang, K. Efimov, F. Liang, H. Wang, J. Caro, CO_2-Tolerant Oxygen-Permeable Fe_2O_3-$Ce_{0.9}Gd_{0.1}O_{2-\delta}$ Dual Phase Membranes, Ind. Eng. Chem. Res. 50

(2011) 13508–13517. doi:10.1021/ie200517t.

[45] J.M. Serra, J. Garcia-Fayos, S. Baumann, F. Schulze-Küppers, W.A. Meulenberg, Oxygen permeation through tape-cast asymmetric all-$La_{0.6}Sr_{0.4}Co_{0.2}Fe_{0.8}O_{3-\delta}$ membranes, J. Memb. Sci. 447 (2013) 297–305. doi:10.1016/j.memsci.2013.07.030.

[46] H.J.B. P. J. Gellings, The CRC Handbook of Solid State Electrochemistry, 1997.

[47] J.T.S. Irvine, J.W.L. Dobson, T. Politova, S.G. Martin, A. Shenouda, Co-doping of scandia-zirconia electrolytes for SOFCs., Faraday Discuss. 134 (2007) 41–49; discussion 103–118, 415–419. doi:10.1039/b604441g.

[48] P. Niehoff, S. Baumann, F. Schulze-Küppers, R.S. Bradley, I. Shapiro, W.A. Meulenberg, Oxygen transport through supported $Ba_{0.5}Sr_{0.5}Co_{0.8}Fe_{0.2}O_{3-\delta}$, Separation and Purification Technology 121 (2014) 60–67, doi: 10.1016/j.seppur.2013.07.002

5.2. Improving the performance of oxygen transport membranes in simulated oxy-fuel power plant conditions by catalytic surface enhancement

This sub-chapter contains the manuscript “Improving the performance of oxygen transport membranes in simulated oxy-fuel power plant conditions by catalytic surface enhancement”, which is ready for submission.

Conclusions drawn from the previous study (“Oxygen permeation flux through 10Sc1YSZ-$MnCo_2O_4$ asymmetric membranes prepared by two-step sintering”) pointed-out two important challenges to solve to bring 10Sc1YSZ-$MnCo_2O_4$ membranes closer to commercialization: (i) further improvement of the surface catalyst layers is needed to reach the full potential of this dual-phase membrane and (ii) the oxygen permeation of the membrane must be measured in conditions relevant for industrial applications.

This article investigates the influence of different catalytic porous activation layers on the performance of 10Sc1YSZ-$MnCo_2O_4$ dual-phase membranes in conditions relevant for oxy-fuel combustion. The stability of the 7 µm thick membranes was evaluated by a long-term test (170 h) performed at 850 °C in simulated oxy-fuel combustion flue-gas conditions (250 ppm of SO_2, 3 vol.% H_2O, 5 vol.% O_2 balanced by CO_2). The analyses of the exposed membrane by X-ray diffraction (XRD), scanning electron microscopy (SEM) and Raman spectroscopy revealed excellent stability. Aiming to achieve a better understanding of the oxygen surface reactions (especially in oxy-fuel conditions), five catalytic porous backbone materials; (i) $(Y_2O_3)_{0.08}(ZrO_2)_{0.92}$ (8YSZ), (ii) 8YSZ-MCO (40-60 vol.%), (iii) 10Sc1YSZ-MCO (40-60 vol.%), (iv) 10Sc1YSZ-MCO (70-30 vol.%), and (v) $Ce_{0.8}Tb_{0.2}O_{2-\delta}$ (CTO)-$NiFe_2O_4$ (NFO) (40-60 vol.%) were prepared and characterized by electrochemical impedance spectroscopy (EIS). Finally, oxygen permeation measurements were performed on 10Sc1YSZ-MCO membranes coated with (i) 8YSZ, (ii) 10Sc1YSZ-MCO and (iii) CTO-NFO activated porous backbones to investigate the influence of the backbones on the oxygen permeability of the membrane under clean conditions (sweep gas: Ar) and oxy-fuel conditions (sweep gas: SO_2 + CO_2 + Ar).

Improving the performance of oxygen transport membranes in simulated oxy-fuel power plant conditions by catalytic surface enhancement

Stéven Pirou[a], Julio García-Fayos[b], María Balaguer[b], Ragnar Kiebach[a], José M. Serra[b]*

[a] Department of Energy Conversion and Storage, Technical University of Denmark, Risø campus, Frederiksborgvej 399, DK-4000 Roskilde, Denmark

[b] Instituto de Tecnología Química (Universitat Politècnica de València – Consejo Superior de Investigaciones Científicas), Av. Naranjos s/n, E-46022 Valencia, Spain

E-Mail addresses: stepir@dtu.dk, jugarfa@itq.upv.es, mabara@upvnet.upv.es, woki@dtu.dk, jmserra@itq.upv.es

[*] Corresponding author

Abstract

The stability of dual-phase oxygen transport membranes consisting of 70 vol.% $(Y_2O_3)_{0.01}(Sc_2O_3)_{0.10}(ZrO_2)_{0.89}$ and 30 vol.% $MnCo_2O_4$ (10Sc1YSZ-MCO (70-30 vol.%)) was investigated. Additionally, the influence of catalytic porous backbones on the performance in simulated oxy-fuel power plant flue-gas (250 ppm SO_2, H_2O, balance CO_2) was studied. The chemical stability of the dual-phase membrane was investigated by X-ray diffraction (XRD), Raman spectroscopy and scanning electron microscopy (SEM). The tests performed before and after the exposure to the simulated flue gas showed excellent chemical stability. Electrochemical impedance spectroscopy (EIS) measurements were performed on activated and non-activated porous catalytic backbones made of: (i) 8YSZ, (ii) 8YSZ-MCO (40-60 vol.%), (iii) 10Sc1YSZ-MCO (40-60 vol.%), (iv) 10Sc1YSZ-MCO (70-30 vol.%), and (v) $Ce_{0.8}Tb_{0.2}O_{2-\delta}$ (CTO) - $NiFe_2O_4$ (NFO) (40-60 vol.%) to achieve a better understanding of the oxygen surface reactions (especially in SO_2 and CO_2 containing atmospheres). The lowest polarization resistances (R_p) were found for 10Sc1YSZ-MCO (40-60 vol.%) and CTO-NFO (40-60 vol.%) porous backbones. Oxygen permeation tests realized on 10Sc1YSZ-MCO membranes demonstrated that the catalytic porous backbones can significantly influence the oxygen permeation flux of the membranes, and improvements of up to 50 % were achieved. Both EIS and oxygen permeation measurements showed a significant influence of SO_2 on the oxygen oxidation/reduction reactions (increase of R_p, decrease of oxygen permeation fluxes) due to SO_2 adsorption and blocking of active sites for the oxygen

reactions. Nevertheless, no microstructural degradation was found after SO_2 exposure and initial R_p values/oxygen permeation fluxes could be recovered in most cases.

Keywords

Oxygen transport membrane, Dual-phase membrane, Catalytic backbone, SO_2 stability, Oxy-fuel combustion

1. Introduction

The reduction of CO_2 emissions from power plants is currently an important challenge for the society. This mission can be achieved by introducing gas separation techniques to capture and store CO_2 from large point sources like fossil fuel power plants, steel plants or cement kilns. Among the available technologies for Carbon Capture and Storage (CCS), oxy-fuel combustion is a promising option. This approach uses pure oxygen to combust the fossil fuel, resulting in flue-gases consisting mainly of CO_2 (90 – 95 %) and steam [1, 2].Typically, cryogenic air separation units (ASUs) are used to produce the required oxygen. While this technique is mature, the process is particularly expensive and consumes a considerable amount of energy [3, 4]. Ceramic oxygen transport membranes (OTMs) that supply the oxygen needed for the combustion process may, when thermally integrated, operate more efficiently, using less energy [5 – 7].

ÓTMs are typically formed by Mixed Ionic Electronic Conductors (MIEC), which allow oxygen diffusion through vacancies in the crystal lattice and simultaneous transport of electrons in the opposite direction. The membranes are fully dense which results in a high selectivity in the separation. An oxygen partial pressure differential between an oxidizing gas (air at 0.21 atm) and reducing gas (recirculated flue gas at $pO_2 \approx 10^{-2}$ atm [8]) exists across the membrane, providing a driving force for the oxygen separation allowing oxygen ion transport from the high oxygen partial pressure side to the low oxygen partial pressure side. Membranes based on single MIEC materials can achieve high oxygen fluxes [9 – 19], however most of the promising materials are not chemically stable under atmosphere containing CO_2 and SO_2 [12, 20 – 26], which is particularly required for oxy-fuel combustion applications. Dual-phase composites consisting of separated ionic and electronic conductor phases are a promising alternative approach to ensure high oxygen flux and chemical stability in realistic power plant conditions.

Dual-phase membranes consisting of a thin (7 µm) dense layer made of 70 vol.% of $(Y_2O_3)_{0.01}(Sc_2O_3)_{0.10}(ZrO_2)_{0.89}$ (10Sc1YSZ) as ionic conductor and 30 vol.% of $MnCo_2O_4$ (MCO) as electronic conductor, supported on a $(Y_2O_3)_{0.03}(ZrO_2)_{0.97}$ (3YSZ) porous support, were developed and tested in a previous study [27]. The study showed the excellent stability of the asymmetric membrane in CO_2 containing atmosphere and oxygen permeation fluxes

as high as 1.41 $ml_N\ min^{-1}\ cm^{-2}$ and 2.23 $ml_N\ min^{-1}\ cm^{-2}$ obtained at 940 °C in air/N_2 and O_2/N_2 atmospheres, respectively.

Assuming that the oxygen flux produced by the membrane is in direct proportion with its thickness, thin asymmetric membranes are advantageous to minimize the resistance arising from bulk diffusion. In this case, other mechanisms such as catalytic surface exchange and gaseous transport become limiting factors of the oxygen separation as reported in literature [27]. Consequently, further improvement of the catalytic activity at the surface is required. In order to enhance the surface exchange kinetics, electro-catalytic materials (referred as *catalytic porous backbones* throughout this study) can be applied on both sides of the membrane [28].

The present article studies the stability of 10Sc1YSZ-MCO dual-phase membranes and the influence of the catalytic porous backbones on the oxygen permeation under conditions relevant for oxy-fuel combustion. The stability of a 7 µm thick asymmetric membrane was evaluated by a 170 h long test performed in simulated oxy-fuel power plant flue-gas (250 ppm SO_2 + 5 % O_2 + 3 % H_2O balanced in CO_2 [8]). Several characterization techniques (X-ray diffraction (XRD), Raman spectroscopy and scanning electron microscopy (SEM)) were used to verify the possible utilization of the membrane for direct application in oxy-fuel power plants. To further improve the membrane performance, five catalytic porous backbone materials; (i) $(Y_2O_3)_{0.08}(ZrO_2)_{0.92}$ (8YSZ), (ii) 8YSZ-MCO (40-60 vol.%), (iii) 10Sc1YSZ-MCO (40-60 vol.%), (iv) 10Sc1YSZ-MCO (70-30 vol.%), and (v) $Ce_{0.8}Tb_{0.2}O_{2-\delta}$ (CTO)-$NiFe_2O_4$ (NFO) (40-60 vol.%) were prepared, and characterized by electrochemical impedance spectroscopy (EIS). The impact of the catalytic activation of the backbones (infiltration of electro-catalytic solutions) on the efficiency of the oxygen separation was investigated and the oxygen permeation was measured in simulated oxy-fuel conditions (sweep gas: SO_2 + CO_2 + Ar).

2. Experimental

2.1. Preparation of porous backbone materials

Five screen-printable inks made of (i) 8YSZ, (ii) 8YSZ-MCO (40-60 vol.%), (iii) 10Sc1YSZ-MCO (40-60 vol.%), (iv) 10Sc1YSZ-MCO (70-30 vol.%), and (v) CTO-NFO (40-60 vol.%) were prepared by milling the powders with a 6 wt.% ethylcellulose-terpineol solution in a 1:1

weight ratio by using a triple roll mill. The 8YSZ powder used to prepare the ink (i) was purchased from Tosoh (Japan). The composite powders (ii), (iii), and (iv) were prepared by milling 8YSZ (Tosoh, Japan), MCO (Marion Technologies, France) and 10Sc1YSZ (Daiichi Kigenso Kagaku Kogyo Co. Ltd, Japan) commercial powders in ethanol using zirconia balls for 24 h. CTO-NFO (40-60 vol.%) was prepared by one pot Pechini method as described by Garcia-Fayos *et al.* in a previous study [29].

2.2. Membranes fabrication

Thin (7 µm) asymmetric supported membranes made of 70 vol.% of 10Sc1YSZ and 30 vol.% of MCO were prepared to study the thermochemical stability of the membrane under oxy-fuel power plants conditions. More robust membranes of 0.5 mm thick able to support higher pressure were required for oxygen permeation tests. This section describes the fabrication processes of these two membrane architectures.

2.2.1. Thick symmetric membrane

The ionic (10Sc1YSZ, Daiichi Kigenso Kagaku Kogyo Co. Ltd, Japan) and electronic ($MnCo_2O_4$, Marion Technologies, France) conductors were blended in a 70-30 vol.% ratio to form the 10Sc1YSZ-MCO composite material. The particle size of the powders was adjusted to the submicron range by 24 h of ball-milling in ethanol. After drying, the composite powder was uniaxially pressed on a 26 mm diameter steel die (50 MPa) to form green disks. The disks were sintered at 1250 °C for 6 h in air, and afterwards polished down to 0.5 mm by using SiC polishing papers. In-house made inks of (i) 8YSZ, (ii) 10Sc1YSZ-MCO (70-30 vol.%) and (iii) CTO-NFO (40-60 vol.%) were screen-printed on both sides of the membranes to serve as catalytic porous backbones. To obtain similar porosity for all catalytic porous backbones and therefore be able to compare their performances while neglecting the gas diffusion parameter, the coated membranes were calcined at different temperatures and the porosity of the backbones was checked by SEM. Thus, the 8YSZ porous backbone was formed at 1150 °C, CTO-NFO at 1100 °C, while 10Sc1YSZ-MCO were treated at 975 °C (2 h in air). To overcome slow surface exchange/reaction kinetics, the backbones were activated by infiltration of a 2 M precursor solution of Ce-Pr catalyst (molar ratio 1:1) prepared by dilution of Ce and Pr nitrates in ethanol/water. Figure 5. 10 presents schematic illustrations of the thick symmetrical membranes tested.

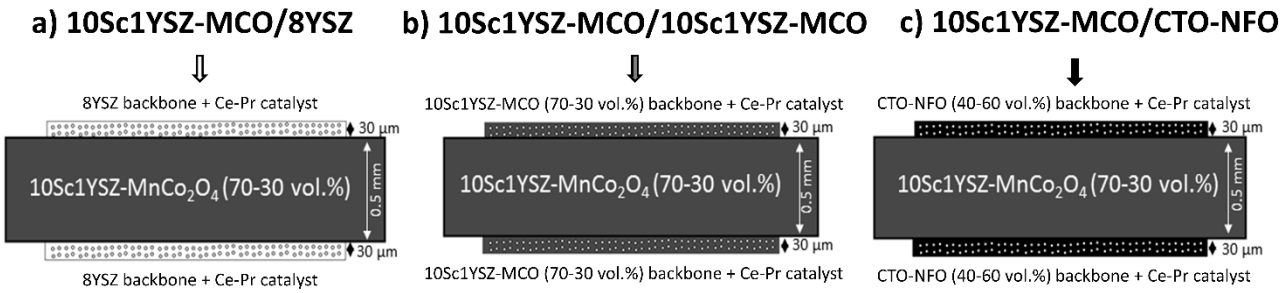

Figure 5. 10: Schematic illustrations of the 0.5 mm thick 10Sc1YSZ-MCO symmetrical membranes prepared for oxygen permeation measurements. Each membrane was coated with a different backbone material: a) 8YSZ, b) 10Sc1YSZ-MCO and c) CTO-NFO.

2.2.2. Thin asymmetric membrane

As presented Figure 5. 11, the asymmetric membrane consists of a three distinct layers: a 300 µm thick porous support (3YSZ + 20 vol.% of Al_2O_3), a 10 µm thick porous 8YSZ inter-layer and a thin (7 µm) 10Sc1YSZ-MCO dense layer (post sintering thicknesses). All layers were manufactured separately by tape-casting. Then, the green tapes were assembled by lamination at 135 °C and disks were cut out using a stamping tool. A two-step sintering including a peak temperature at 1225 °C (3 min) and a dwell temperature of 1090 °C (6 h) was used to develop the asymmetric membranes. The complete manufacturing procedure of the 10Sc1YS-MCO asymmetric membranes was detailed in a previous study [27].

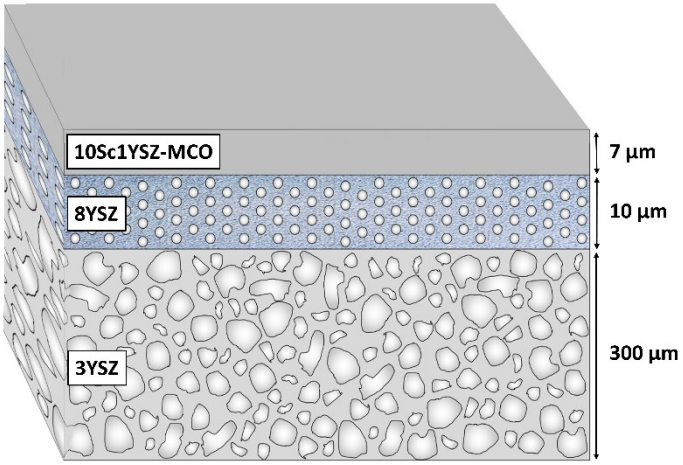

Figure 5. 11: Schematic illustration of the thin asymmetric 10Sc1YSZ-MCO membrane used for the long-term stability test in oxy-fuel conditions.

2.3. Characterization

2.3.1. Thermochemical stability test and material characterization

The thermochemical stability of a 7 µm thin asymmetric membrane was studied in a quartz horizontal testing unit. The testing unit was installed in an oven and heated up to 850 °C in wet N_2 (3 % H_2O). When the temperature was reached, the gas composition was switched to a gaseous mixture containing 250 ppm of SO_2 and 5 % of O_2 balanced in CO_2. The gaseous mixture was provided by a pre-mixed gas cylinder (Linde). Wet gas conditions (3 % H_2O) were supplied by bubbling the gas stream through water at room temperature. The asymmetric membrane was in direct contact with the gas mixture flowing at 10 $ml_N\ min^{-1}$ for 170 h. After the exposure of the membrane to the gas atmosphere, the testing unit was cooled down in wet N_2 by natural convection (20 – 25 °C min^{-1}).

To compare the microstructure of the tested asymmetric membrane with a similar untested membrane, X-ray diffraction (XRD), Raman spectroscopy and scanning electron microscopy with energy-dispersive X-ray spectroscopy (SEM-EDX) analyses were performed.

The XRD measurements were carried out using a PANalytical Cubix fast diffractometer, using CuKα1 radiation (λ = 1.5406 Å) and a X'Celerator detector in Bragg−Brentano geometry. XRD patterns recorded in the 2θ range from 10° to 90° were analyzed using X'Pert Highscore Plus software.

SEM-EDX analyses were performed using a ZEISS Ultra55 field emission scanning electron microscope.

Raman spectra were measured with a Renishaw inVia Raman spectrometer equipped with a Leica DMLM microscope and a 514-nm Ar+ ion laser as an excitation source. A x50 objective of 8-mm optical length was used to focus the depolarized laser beam on a spot of about 3 µm in diameter. The Raman scattering was collected with a charged coupled device (CCD) array detector.

2.3.2. Electrochemical Impedance Spectroscopy

Electrochemical Impedance Spectroscopy (EIS) measurements were performed on 1 mm thick fully dense $Ce_{0.8}Gd_{0.2}O_{2-\delta}$ (GDC) electrolytes coated on both sides by the studied backbone materials: (i) 8YSZ, (ii) 8YSZ-MCO (40-60 vol.%), (iii) 10Sc1YSZ-MCO (40-60

vol.%), (iv) 10Sc1YSZ-MCO (70-30 vol.%), and (v) CTO-NFO (40-60 vol.%). As stated in the section 2.2.1., to obtain similar porosity for all catalytic layers the coated GDC electrolytes were calcined at different temperatures. The performance of the backbones was investigated with and without infiltrations of a homemade catalytic solution of Ce and Pr nitrates (excepting 8YSZ, only tested with catalyst infiltrations). The same amount of catalyst was infiltrated in each backbone. The infiltrated backbones were treated at 850 °C for 2 h in air. Finally, a top gold mesh was painted on the surfaces of all samples in order to ensure proper current collection during the EIS measurements.

The symmetrical cells were tested by means of electrochemical impedance spectroscopy in a two-point configuration. Input signal was 0 V DC – 20 mV AC amplitude in the 0.01 – $3 \cdot 10^5$ Hz frequency range. This signal was generated by a Solartron 1470E and a 1455A FRA module equipment. EIS measurements were performed at 850 °C, under several atmospheres ((i) 21 % O_2 in N_2, (ii) 5 % O_2 in N_2, (iii) 5 % O_2 in CO_2 and (iv) 250 ppm SO_2 + 5 % O_2 in CO_2). In all the cases, the total gas flow remained constant (100 ml·min^{-1}). Zview™ 2 fitting programme was employed to analyse the impedance spectra.

2.3.3. Oxygen permeation tests

Oxygen permeation studies were carried out in a lab-scale quartz reactor (Figure 5. 12). Synthetic air (21 vol.%, O_2) was fed with a flow rate of 100 mL_N min^{-1}, while argon, CO_2 and SO_2 mixtures were used as sweep gases on the permeate side in a 4-end mode configuration with a flow rate of 150 mL_N min^{-1}. The flow rates were controlled by mass flow controllers. Both streams were fed at atmospheric pressure. The temperature was measured by a thermocouple attached to the membrane. A PID controller maintained the temperature within 2 °C of the set point. Gas-tight sealing was achieved using O-rings with tailored alloys for sealing at 850 °C. The permeate was analyzed at steady state by online gas chromatography using a micro-GC Varian CP-4900 equipped with Molsieve5A, Pora-Plot-Q glass capillary, and CP-Sil modules. Oxygen concentration was calculated from the O_2 signal area and its response factor previously calibrated. The total oxygen permeation was calculated as the product of the O_2 concentration ($\%O_{2,permeate}$) and the sweep flow ($\dot{n}^{sweep}$). The oxygen permeation flux (J_{O_2}) was then determined from the division of the total oxygen permeation by the effective area (A) of the membrane as:

$$J_{O_2} = \%O_{2,permeate} \cdot \frac{\dot{n}^{sweep}}{A} \quad (1)$$

To ensure leak free conditions the nitrogen concentration in the permeate gas was continuously controlled. Oxygen related to minor leaks was removed from J_{O_2} calculation by taking into account the presence of N_2 in the permeate stream. Therefore, the permeating oxygen ($\%O_{2,permeate}$) was calculated as:

$$\%O_{2,permeate} = \%O_{2,GC} - \left(\frac{0.21}{0.79} \cdot \%N_{2,GC}\right) \quad (2)$$

where $\%O_{2,GC}$ and $\%N_{2,GC}$ are the percentages of oxygen and nitrogen measured by the gas chromatography in the permeate, respectively.

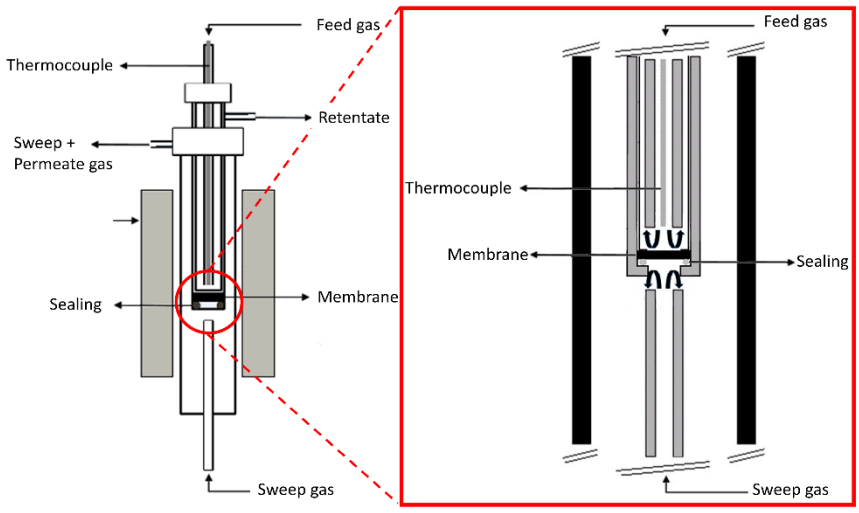

Figure 5. 12: Schematic illustration of the lab-scale quartz reactor used for the oxygen permeation tests.

3. Results and discussion

3.1. Thermochemical stability in oxy-fuel conditions

To investigate the applicability of the membrane in oxy-fuel power plants, the effects of a gas stream containing CO_2, SO_2 and H_2O on the membrane were studied.

In this section, post mortem analyses (XRD, Raman spectroscopy and SEM) of a membrane exposed to a continuous flow of simulated oxy-fuel power plant flue-gas (250 ppm of SO_2, 5 % of O_2, 3 % of H_2O balanced with CO_2) during 170 h at 850 °C are presented and compared to an untested sample.

Figure 5. 13 shows the XRD diffractograms of the treated and untreated 10Sc1YSZ-MCO membranes. Both diffractograms are comparable, additional diffraction peaks related to the formation of new crystalline phases could not be observed, and all observed peaks belong to 10Sc1YSZ [30 – 32] or $MnCo_2O_4$ (JCPDS card No. 23-1237).

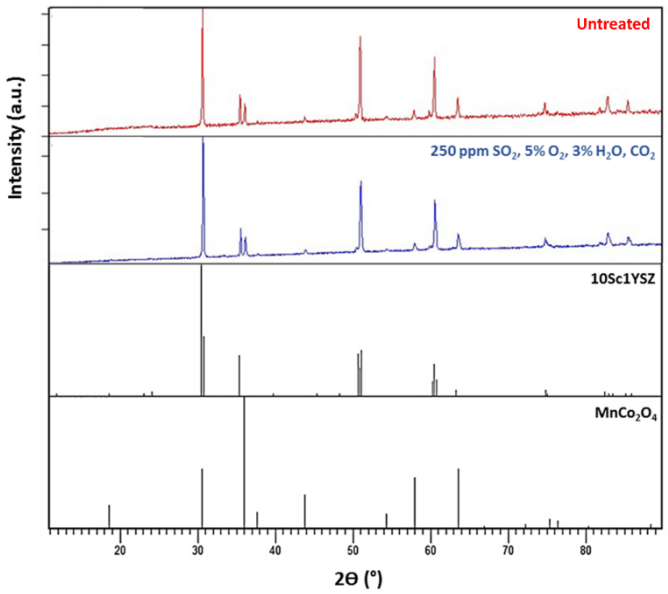

Figure 5. 13: XRD diffractograms of treated and untreated 10Sc1YSZ-MCO membranes and XRD patterns of 10Sc1YSZ and $MnCo_2O_4$.

Knowing that it is difficult/not possible to detect very low amounts of crystalline phases or non-crystalline phases with XRD analysis, additional Raman spectroscopy was performed (Figure 5. 14). This technique is well suited for the detection of small amount of carbonates or sulfates, however no additional peaks were found in the spectra of the treated membrane, suggesting that the exposure to the different gases did not create any new phases.

Figure 5. 15 shows SEM images of the cross-sections of treated and untreated membranes. No evidence of interface reactions or cracks in the dense membrane layer during the long-term exposure was found. The 10Sc1YSZ-MCO layer remains fully dense and well attached to the porous supporting layers. Neither carbon nor sulfur were detected by EDX analysis, thus discarding the presence of carbonates or sulfates in the treated membrane.

Overall, the combined analyses confirmed the stability of the composite material and the membrane assembly at 850 °C under conditions relevant for oxy-fuel combustion.

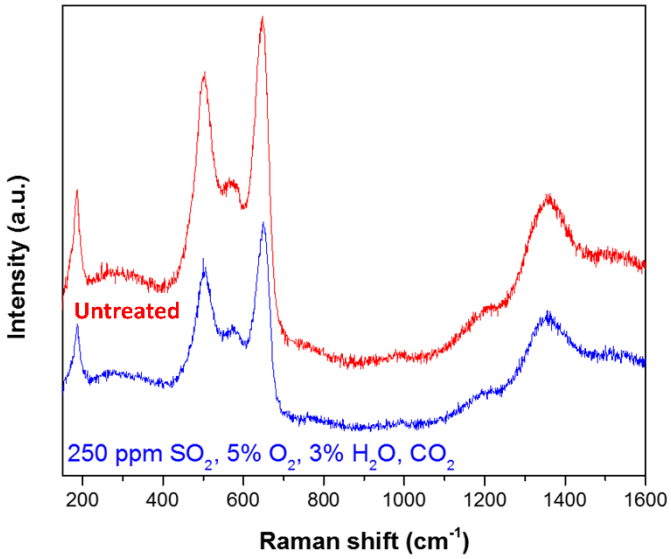

Figure 5. 14: Raman spectra of the fresh and the treated 10Sc1YSZ-MCO membranes.

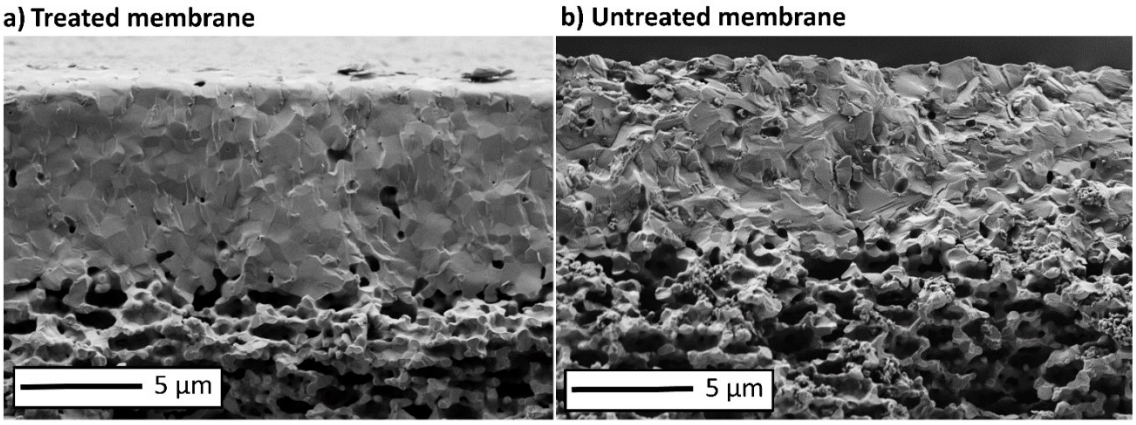

Figure 5. 15: SEM images of cross-sections of 10Sc1YSZ-MCO asymmetric membranes exposed to a continuous flow of CO_2 with 250 ppm of SO_2, 5 % of O_2, and 3 % of H_2O during 170 h (a) and unexposed (b).

3.2. Characterization of catalytic porous backbones by electrochemical impedance spectroscopy

EIS measurements were performed on dense $Ce_{0.8}Gd_{0.2}O_{2-\delta}$ symmetrical cells and results were processed to obtain the resistances associated to the porous backbones. Only the contributions in the negative imaginary part were taken into account to calculate these resistances. The values were corrected by the area of the porous backbones and the resulting values were divided by two, since both surfaces of the cells were coated. The final numbers correspond to the polarization resistance (R_p) of the porous backbones. R_p can

give an idea of the conductivity of every catalytic system (the lower the R_p, the higher the conductivity of the porous backbone). In this section the R_p of the different catalytic porous backbones are compared. The influence of the ionic conductivity, the electronic conductivity, the catalytic activation and harsh atmosphere conditions (SO_2, CO_2 and H_2O) on the R_p are discussed.

Electrical and ionic conductivities of the relevant materials are summarized in Table 5. 3.

Figure 5. 16 and Figure 5. 17 present the R_p of the porous backbones with and without catalyst infiltrations. Due to a lack of an electronic conducting phase, the 8YSZ porous backbones cannot efficiently catalyze the oxygen oxidation/reduction reactions. Consequently, cells coated with 8YSZ backbones were only tested with Ce-Pr catalyst infiltrations (Figure 5. 17).

Table 5. 3: Electrical and ionic conductivities (S cm^{-1}) of materials used to prepare the porous backbones.

	Material	Electrical conductivity at 800 °C in air	Ionic conductivity at 800 °C (except where noted) in air	Ref.
Ionic conducting materials	$(Y_2O_3)_{0.08}(ZrO_2)_{0.92}$ (8YSZ)		0.030 (850 °C)	[33]
	$(Y_2O_3)_{0.01}(Sc_2O_3)_{0.10}(ZrO_2)_{0.89}$ (10Sc1YSZ)		0.072 (840 °C)	[34]
	$Ce_{0.8}Tb_{0.2}O_{2-\delta}$ (CTO)		0.035	[35]
Electronic conducting materials	$MnCo_2O_4$ (MCO)	60		[36]
	$NiFe_2O_4$ (NFO)	0.26		[36]

3.2.1. Influence of the ionic conductivity, electronic conductivity, and the catalyst activation on the polarization resistances

The influence of the ionic conductivity on the ability of the backbones to transport oxygen can be evaluated by comparing the R_p of 8YSZ-MCO (40-60 vol.%) and 10Sc1YSZ-MCO (40-60 vol.%) composites. Indeed, with 0.072 S cm^{-1} at 840 °C, [34] 10Sc1YSZ presents 2 times higher ionic conductivity than 8YSZ (0.030 S cm^{-1} at 850 °C [33]). The experiments showed that the ionic conductivity of the porous backbones significantly influences the R_p, especially when the backbones are not infiltrated. Thus, the 10Sc1YSZ-MCO (40-60 vol.%)

porous backbone presents R_p values approximately 8 times lower than the 8YSZ-MCO (40-60 vol.%) porous backbone (Figure 5. 16). Similar conclusions can be drawn for the activated porous backbones (Figure 5. 17), even though the difference between the 8YSZ-MCO (40-60 vol.%) and the 10Sc1YSZ-MCO (40-60 vol.%) porous backbone is not as pronounced (2 times lower).

The influence of the electronic conductivity on the R_p can be noticed by varying the content of electronic conducting phase in the composite. In this study, the ratio of ionic/electronic conductors of the 10Sc1YSZ-MCO composite was varied. The increase of MCO resulted in a significant decrease in R_p for both activated and non-activated backbones. As expected, the highest R_p among the activated backbones was obtained for the 8YSZ backbone. The 10Sc1YSZ-MCO (70-30 vol.%) composite presents the second highest R_p of the tested backbones. As shown in the Bode plot (Figure 5. 18.a), processes contributing to the high frequencies part of the spectra are mainly responsible for the large R_p value. These processes are related to the transport of species through the 10Sc1YSZ-MCO/Ce-doped material interface [37], which could indicate that a lack of electronic conductivity limits the performance of this backbone. When the content of the electronic conducting phase was increased from 30 % to 60 %, lower Z'' values were obtained (Figures 5. 18.a and 5. 18.b) resulting to 3 to 7 times lower R_p, underlining the conclusion drawn above.

The infiltration of nano-particulate Ce and Pr catalysts into the porous catalytic backbones increases the catalytic surface area for oxygen oxidation/reduction reactions and therefore improves the ability of the backbones to incorporate and transport oxygen. Consequently, in every studied atmospheres activated porous catalytic backbones present lower R_p than non-activated backbones. The largest improvement was observed for the two backbones having the lowest ionic conductivity (8YSZ-MCO (40-60 vol.%) and CTO-NFO (40-60 vol.%)), see ionic conductivities Table 5. 3).

To resume, EIS measurements showed that the material serving as porous catalytic backbone should preferably have a good ionic conductivity and a good electronic conductivity. To illustrate this importance, Figure 5. 19 presents the reaction mechanism of the oxygen reduction reaction (ORR) taking place in the porous catalytic backbone at the high pO_2 side (feed side). Two cases are distinguished: (i) a membrane coated with a porous backbone made of a composite of a good ionic conductor and a good electronic conductor

(e.g. 10Sc1YSZ-MCO, CTO-NFO) and (ii) a membrane coated with a porous backbone made of a single ionic conducting phase (e.g. 8YSZ). As described by the Equation 3, the ORR requires oxygen gas (O_2) and electrons (e^-) to form oxide ions (O^{2-}). Once the oxygen ions are formed, a percolating ionic conducting phase is required to lead them to the membrane and therefore allow the oxygen permeation. Consequently, a good mix of ionic and electronic conducting phases is beneficial to increase the number of triple phase boundary. Figure 5. 19 illustrates the difference of area available for the ORR if a mixed ionic and electronic conductive (MIEC) material or a purely ionic conductive material is used as porous catalytic backbone. For the MIEC material, the area for the ORR is extended along the entire surface of the backbone, while for a purely ionic conducting material only the interface of the porous backbone and the dense membrane layer is suitable for the reaction. The oxygen oxidation reaction (OOR) reforming the gas after the permeation of the oxide ions through the membrane requires also the triple phase boundary zones and could have been taken as an example in the same way as the ORR. In this sense, the composites having the most beneficial mixed of ionic and electronic conductivity (10Sc1YSZ-MCO (40-60 vol.%) and CTO-NFO (40-60 vol.%)) are therefore the two most suitable porous catalytic backbones among the tested candidates to transport oxygen.

Oxygen reduction reaction: $O_2 + 4e^- = 2O^{2-}$ (3)

3.2.2. Influence of oxy-fuel conditions on the polarization resistances

As described in section 2.3.2., EIS measurements were performed at 850 °C under clean and oxy-fuel combustion conditions. A strong influence of SO_2 on the oxygen oxidation/reduction reactions was observed. As shown by Figure 5. 18, SO_2 enlarges the magnitude of resistive processes appearing at low frequencies, probably due to SO_2 adsorption and blocking of active sites for the oxygen reactions [29]. Depending on the materials, the R_p of activated backbones are 2.5 to 10 times larger in contact to SO_2 than in air, and 2.5 to 6 times larger for non-activated backbones. Nevertheless, the material structure of the backbones was not irreversibly altered upon sulfur exposure and most of the initial R_p values were recovered after a short time in clean atmosphere (5 % O_2 in N_2).

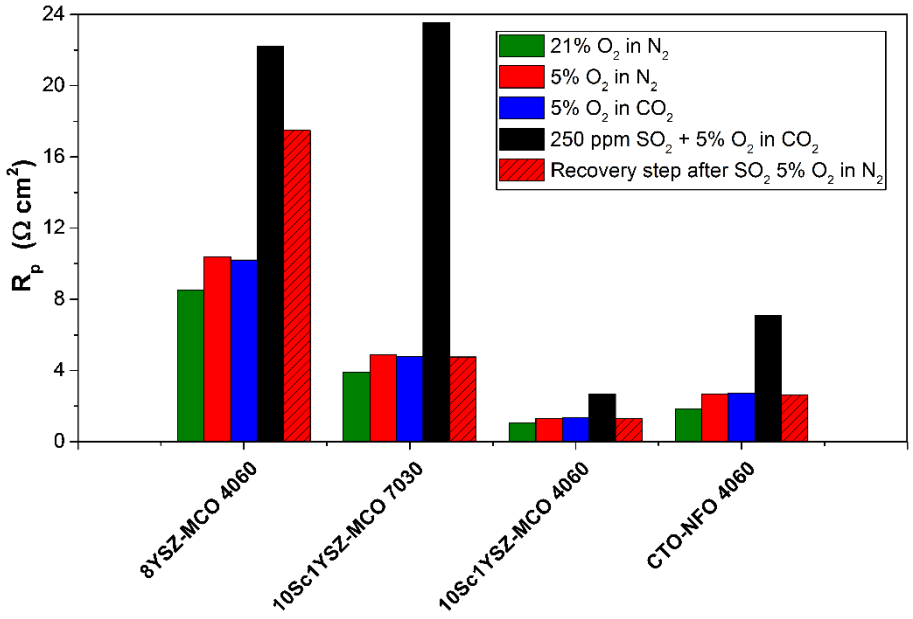

Figure 5. 16: Representation of the polarization resistances associated to 8YSZ-MCO (40-60 vol.%), 10Sc1YSZ-MCO (70-30 vol.%), 10Sc1YSZ-MCO (40-60 vol.%) and CTO-NFO (40-60 vol.%) non-infiltrated porous backbones.

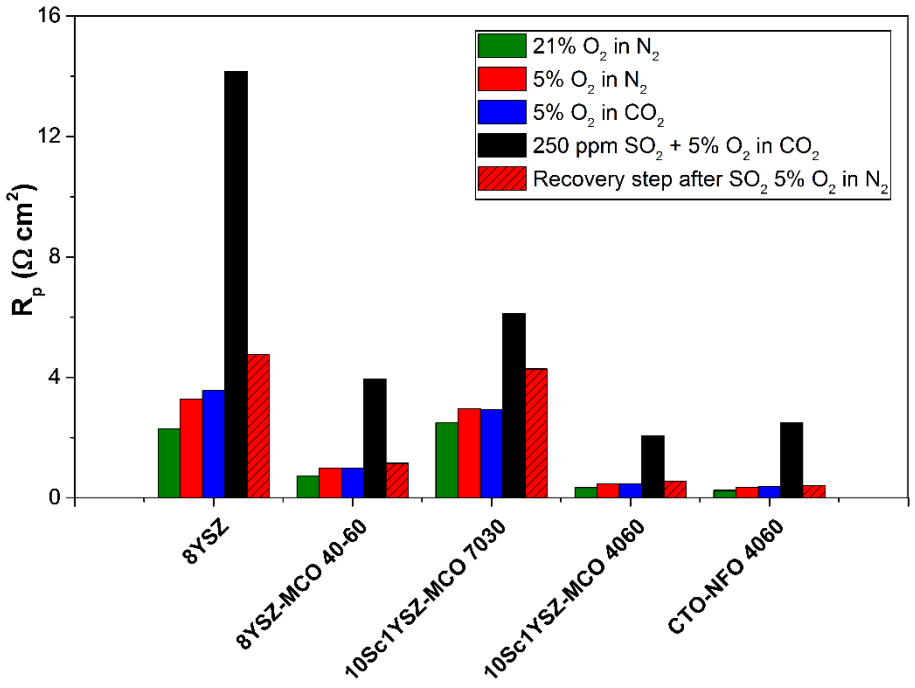

Figure 5. 17: Representation of the polarization resistances associated to 8YSZ-MCO (40-60 vol.%), 10Sc1YSZ-MCO (70-30 vol.%), 10Sc1YSZ-MCO (40-60 vol.%) and CTO-NFO (40-60 vol.%) porous backbones infiltrated by a Ce-Pr nitrates based catalytic solution.

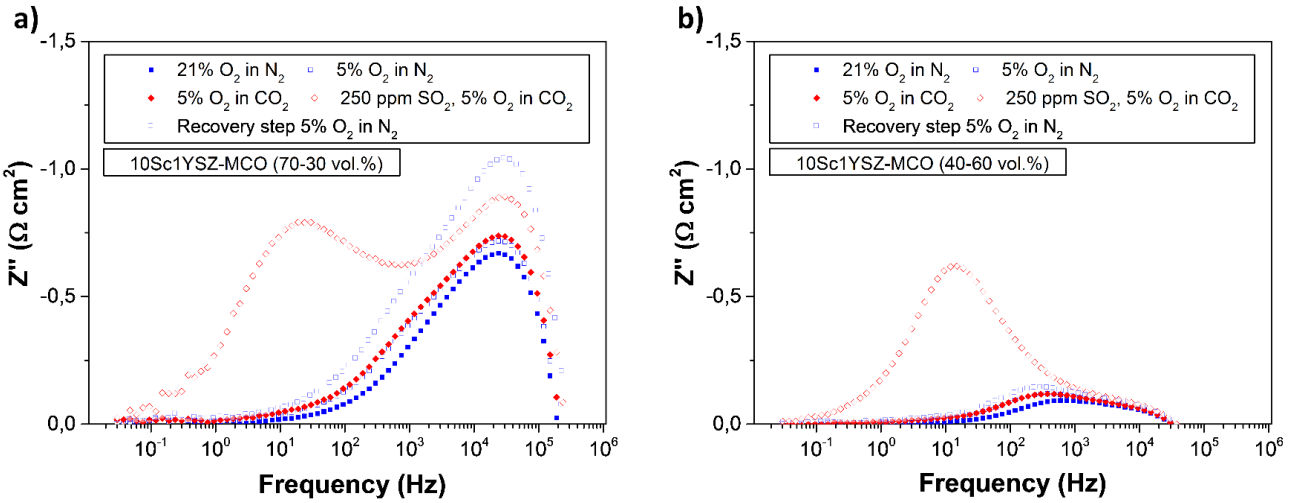

Figure 5. 18: Bode plots for the 10Sc1YSZ-MCO (70-30 vol.%) porous backbone (a) and the 10Sc1YSZ-MCO (40-60 vol.%) porous backbone (b) infiltrated by a Ce-Pr nitrates based catalytic solution. Measurements were performed at 850 °C under different atmospheres.

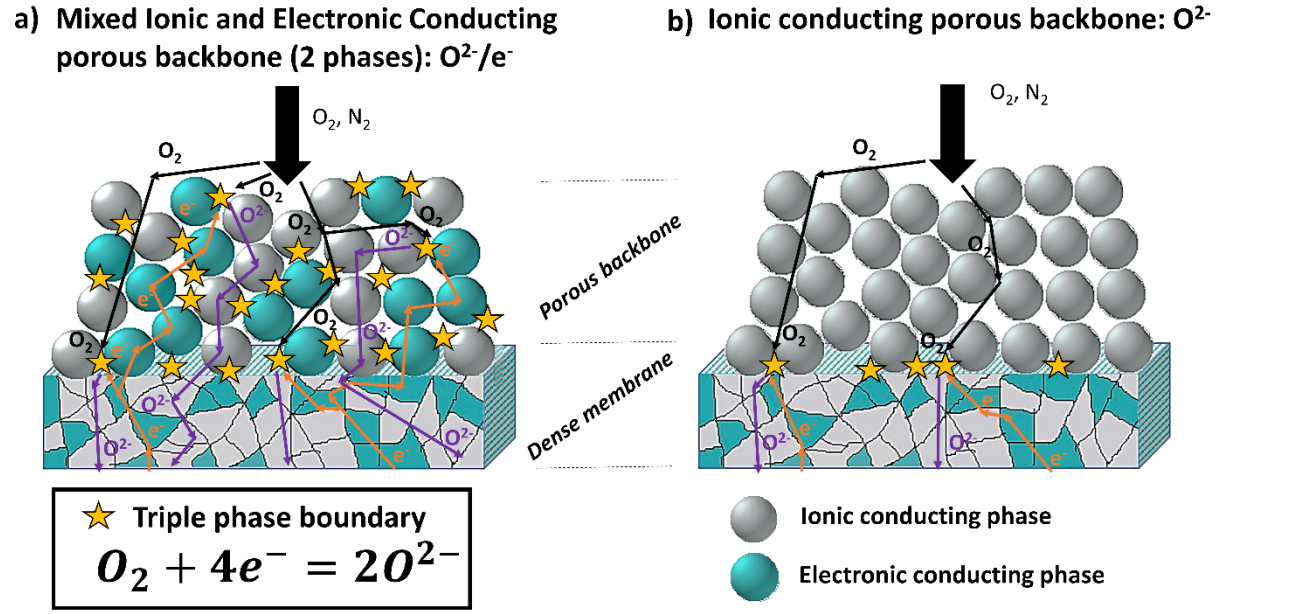

Figure 5. 19: Schematic illustrations of the mechanism of the oxygen reduction reaction considering two cases: a membrane coated with a composite porous backbone made of a good ionic and a good electronic conductor (a), and a membrane coated with a purely ionic conducting porous backbone (single-phase) (b).

3.3. Oxygen permeation tests

Figure 5. 20 shows the oxygen permeation flux through 10Sc1YSZ-MCO symmetrical membranes coated with different porous backbones (Figure 5. 20.a: 8YSZ, 5. 20.b: 10Sc1YSZ-MCO (70-30 vol.%) and 5. 20.c: CTO-NFO (40-60 vol.%)). The tests were performed at 850 °C using different sweep gases. They were sequenced as: (i) test in Ar (150 ml_N min^{-1}, 2 h, black symbols), (ii) test in 70 % Ar + 30 % CO_2 (150 ml_N min^{-1}, 12 h, red

symbols), (iii) test in 70 % Ar + 30 % CO_2 + 250 ppm of SO_2 (150 ml_N min^{-1}, 12 h, blue symbols) and (iv) recovery step in Ar (150 ml_N min^{-1}, black symbols). Air was used as a feed gas for the complete duration of the tests and fed at 100 ml_N min^{-1}.

In clean conditions (sweep gas: Ar, phase (i)) the membrane with CTO-NFO backbones presents the highest oxygen permeation flux (0.28 ml_N min^{-1} cm^{-2}), while the one coated with 8YSZ porous backbones has the lowest performance (0.19 ml_N min^{-1} cm^{-2}). The results observed during phase (i) are in accordance with the results of the EIS measurements: the backbone having the lowest polarization resistance (CTO-NFO) presents the highest oxygen permeation flux. The three membranes displayed a stable flux in 30 % CO_2 (phase (ii)). Nevertheless, when the sweep gas was switched from 30 % CO_2 to 250 ppm SO_2 in 70 % Ar + 30 % CO_2, the oxygen permeation fluxes dropped around 0.12 ml_N min^{-1} cm^{-2} no matters the catalytic backbone coated. The loss of permeation can be ascribed to the fact the SO_2 affects oxygen permeation due to competitive adsorption phenomena on the membrane surfaces [29]. Despite this drop, the oxygen permeation flux is still acceptable when compared with the dramatic oxygen permeation degradations of state-of-the-art oxygen membranes when exposed to sulfur and carbon dioxide containing environments [25, 26, 38, 39]. For example, BSCF membranes show very high oxygen permeability when He is used as a sweep gas (2.76 mL_N cm^{-2} min^{-1} at 900 °C), but the oxygen flux drops near zero when changing the sweep gas to pure CO_2 [25]. Significant degradations of the oxygen permeability were also observed with LSCF membranes exposed to SO_2. Gao *et al.* reported an oxygen permeability drop of 80 % after exposure to SO_2 [26]. Finally, when returning to clean conditions (phase (iv)), oxygen permeation flux can be recovered reflecting thus the stability of the materials. Only the membrane coated with the CTO-NFO porous catalytic backbones do not recover the initial oxygen permeability (65 % recovery). This result could be due to a delamination of the porous catalytic backbones due to the different material used in the membrane and the backbone.

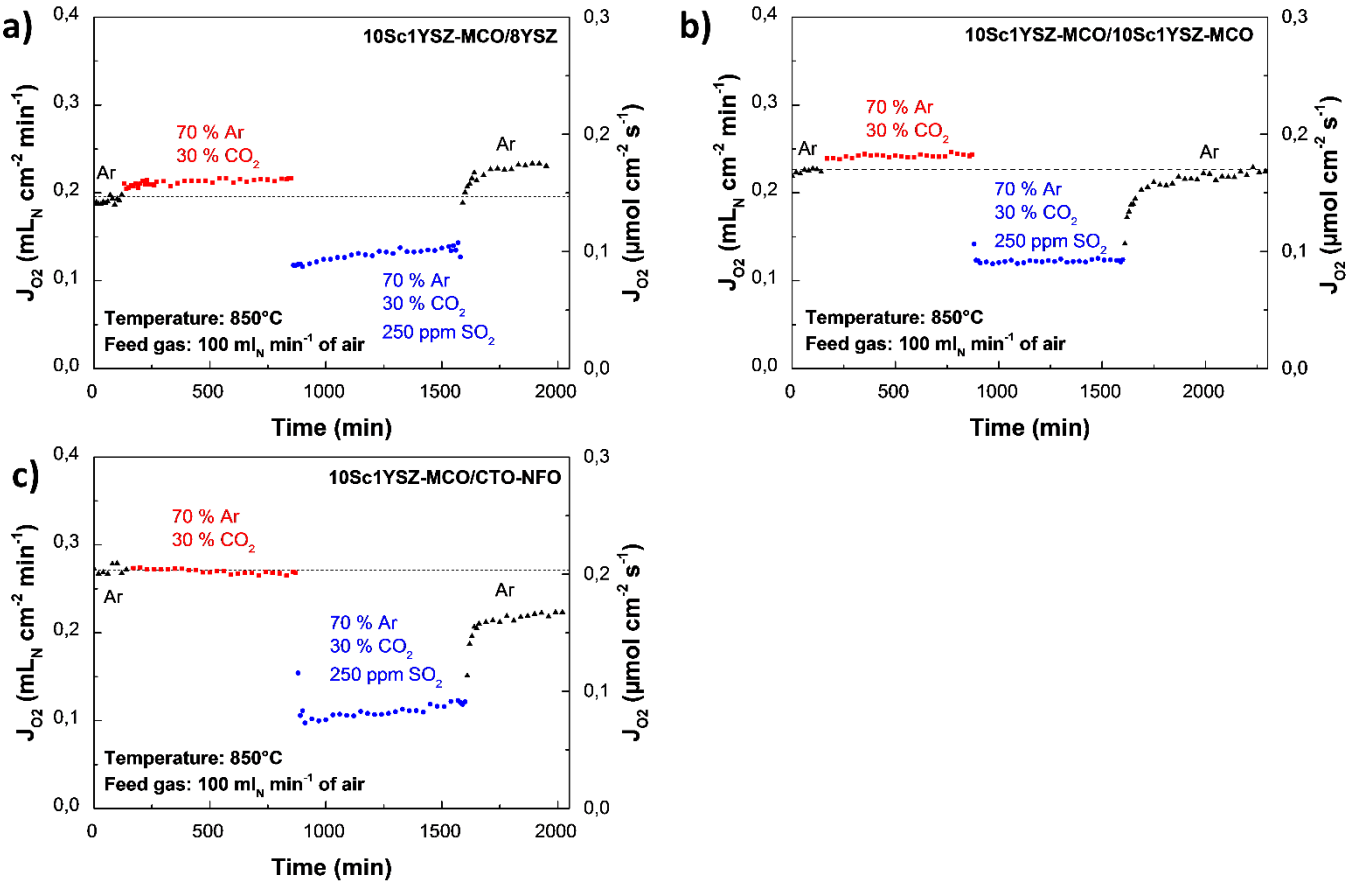

Figure 5. 20: Oxygen permeation flux of 0.5 mm thick 10Sc1YSZ-MCO (70-30 vol.%) membranes as a function of the time. The membranes were coated with 8YSZ (a), 10Sc1YSZ-MCO (70-30 vol.%) (b), and CTO-NFO (40-60 vol.%) (c) porous catalytic backbones which were infiltrated by a Ce-Pr catalytic solution. The tests were performed in 4 different sweep gas atmosphere: (i) Ar, (ii) 70 % Ar + 30 % CO_2, (iii) 70 % Ar + 30 % CO_2 + 250 ppm SO_2 and (iv) Ar (recovery step).

Conclusion

The stability of a 7 µm thick 10Sc1YSZ-MCO (70-30 vol.%) dual-phase membrane was studied in simulated oxy-fuel combustion conditions (250 ppm SO_2, 3 % H_2O, 5 % O_2 balanced with CO_2). The results of the tests underlined the excellent stability of the membrane in SO_2 and CO_2 containing atmospheres. To achieve a better understanding of the oxygen surface reactions (especially in SO_2 and CO_2 containing atmospheres), electrochemical impedance spectroscopy (EIS) measurements were performed on porous catalytic backbones consisting of: (i) 8YSZ, (ii) 8YSZ-MCO (40-60 vol.%), (iii) 10Sc1YSZ-MCO (40-60 vol.%), (iv) 10Sc1YSZ-MCO (70-30 vol.%), and (v) $Ce_{0.8}Tb_{0.2}O_{2-\delta}$ (CTO) - $NiFe_2O_4$ (NFO) (40-60 vol.%). The lowest polarization resistances (R_p) were acquired with 10Sc1YSZ-MCO (40-60 vol.%) and CTO-NFO (40-60 vol.%) porous backbones, demonstrating the importance of a mixed ionic and electronic conductivity in the catalytic

porous backbones. Oxygen permeation tests were realized on 10Sc1YSZ-MCO membranes coated with different porous backbones ((i) 8YSZ, (ii) 10Sc1YSZ-MCO (70-30 vol.%) and (iii) CTO-NFO (40-60 vol.%)) which were infiltrated with Ce and Pr nano-particulate catalysts. The CTO-NFO activated backbone increased the oxygen permeation flux about 50 % (0.28 $mL_N\ cm^{-2}\ min^{-1}$, 850 °C, air/Ar) compared to the membrane with 8YSZ activated backbone (0.19 $mL_N\ cm^{-2}\ min^{-1}$, 850 °C, air/Ar). A significant influence of SO_2 on the oxygen oxidation/reduction reactions was observed, and R_p and oxygen permeability of the samples exposed to 250 ppm of SO_2 were significantly affected. Nevertheless, no microstructural degradation was found after SO_2 exposure and initial R_p/oxygen permeation fluxes could be recovered in most of the cases.

References

[1] H. Stadler, F. Beggel, M. Habermehl, B. Persigehl, R. Kneer, M. Modigell, P. Jeschke, Oxyfuel coal combustion by efficient integration of oxygen transport membranes, Int. J. Greenh. Gas Control. 5 (2011) 7–15. doi:10.1016/j.ijggc.2010.03.004.

[2] H. Stadler, F. Beggel, M. Habermehl, B. Persigehl, R. Kneer, M. Modigell, P. Jeschke, Oxyfuel coal combustion by efficient integration of oxygen transport membranes, Int. J. Greenh. Gas Control. 5 (2011) 7–15. doi:10.1016/j.ijggc.2010.03.004.

[3] S.M. Hashim, A.R. Mohamed, S. Bhatia, Current status of ceramic-based membranes for oxygen separation from air, Adv. Colloid Interface Sci. 160 (2010) 88–100. doi:10.1016/j.cis.2010.07.007.

[4] S. Smart, C.X.C. Lin, L. Ding, K. Thambimuthu, J.C. Diniz da Costa, Ceramic membranes for gas processing in coal gasification, Energy Environ. Sci. 3 (2010) 268–278. doi:10.1039/b924327e.

[5] M. Czyperek, P. Zapp, H.J.M. Bouwmeester, M. Modigell, K. Ebert, I. Voigt, W.A. Meulenberg, L. Singheiser, D. Stöver, Gas separation membranes for zero-emission fossil power plants: MEM-BRAIN, J. Memb. Sci. 359 (2010) 149–159. doi:10.1016/j.memsci.2010.04.012.

[6] S.S. Hashim, A.R. Mohamed, S. Bhatia, Oxygen separation from air using ceramic-based membrane technology for sustainable fuel production and power generation, Renew. Sustain. Energy Rev. 15 (2011) 1284–1293. doi:10.1016/j.rser.2010.10.002.

[7] M. Puig-Arnavat, S. Soprani, M. Søgaard, K. Engelbrecht, J. Ahrenfeldt, U.B. Henriksen, P.V. Hendriksen, Integration of mixed conducting membranes in an oxygen–steam biomass gasification process, RSC Adv. 3 (2013) 20843–20854. doi:10.1039/c3ra44509g.

[8] E.S. Rubin, A.B. Rao, M.B. Berkenpas, Technical Documentation : Oxygen-based Combustion Systems (Oxyfuels) with Carbon Capture and Storage (CCS), 2007.

[9] P. Haworth, S. Smart, J. Glasscock, J.C. Diniz da Costa, High performance yttrium-doped BSCF hollow fibre membranes, Sep. Purif. Technol. 94 (2012) 16–22. doi:10.1016/j.seppur.2012.04.005.

[10] R. Kiebach, K. Engelbrecht, K. Kwok, S. Molin, M. Søgaard, P. Niehoff, F. Schulze-Küppers, R. Kriegel, J. Kluge, P.V. Hendriksen, Joining of ceramic $Ba_{0.5}Sr_{0.5}Co_{0.8}Fe_{0.2}O_3$ membranes for oxygen production to high temperature alloys, J. Memb. Sci. 506 (2016) 11–21. doi:10.1016/j.memsci.2016.01.050.

[11] S. Baumann, J.M. Serra, M.P. Lobera, S. Escolástico, F. Schulze-Küppers, W.A. Meulenberg, Ultrahigh oxygen permeation flux through supported $Ba_{0.5}Sr_{0.5}Co_{0.8}Fe_{0.2}O_{3-\delta}$ membranes, J. Memb. Sci. 377 (2011) 198–205. doi:10.1016/j.memsci.2011.04.050.

[12] M. Arnold, H. Wang, A. Feldhoff, Influence of CO_2 on the oxygen permeation performance and the microstructure of perovskite-type $(Ba_{0.5}Sr_{0.5})(Co_{0.8}Fe_{0.2})O_{3-\delta}$ membranes, J. Memb. Sci. 293 (2007) 44–52. doi:10.1016/j.memsci.2007.01.032.

[13] Z. Shao, W. Yang, Y. Cong, H. Dong, J. Tong, G. Xiong, Investigation of the permeation behavior and stability of a $Ba_{0.5}Sr_{0.5}Co_{0.8}Fe_{0.2}O_{(3-\delta)}$ oxygen membrane, J. Memb. Sci. 172 (2000) 177–188. doi:10.1016/S0376-7388(00)00337-9.

[14] L. Ge, W. Zhou, R. Ran, S. Liu, Z. Shao, W. Jin, N. Xu, Properties and performance of A-site deficient $(Ba_{0.5}Sr_{0.5})_{1-x}Co_{0.8}Fe_{0.2}O_{3-\delta}$ for oxygen permeating membrane, J. Memb. Sci. 306 (2007) 318–328. doi:10.1016/j.memsci.2007.09.004.

[15] Z. Taheri, K. Nazari, N. Seyed-Matin, A.A. Safekordi, B. Ghanbari, S. Zarrinpashne, R. Ahmadi, Comparison of oxygen permeation through some perovskite membranes synthesized with EDTNAD, React. Kinet. Mech. Catal. 100 (2010) 459–469. doi:10.1007/s11144-010-0158-2.

[16] F. Schulze-Küppers, S. Baumann, F. Tietz, H.J.M. Bouwmeester, W.A. Meulenberg, Towards the fabrication of $La_{0.98-x}Sr_xCo_{0.2}Fe_{0.8}O_{3-\delta}$ perovskite-type oxygen transport membranes, J. Eur. Ceram. Soc. 34 (2014) 3741–3748. doi:10.1016/j.jeurceramsoc.2014.06.012.

[17] X. Tan, Z. Wang, B. Meng, X. Meng, K. Li, Pilot-scale production of oxygen from air using perovskite hollow fibre membranes, J. Memb. Sci. 352 (2010) 189–196. doi:10.1016/j.memsci.2010.02.015.

[18] J. Gurauskis, Ø.F. Lohne, D.S. Lagergren, E.T. Wefring, K. Wiik, Oxygen permeation

in symmetric and asymmetric $La_{0.2}Sr_{0.8}Fe_{0.8}Ta_{0.2}O_{3-\delta}$ membranes, J. Eur. Ceram. Soc. 36 (2016) 1427–1434. doi:10.1016/j.jeurceramsoc.2016.01.004.

[19] M.P. Lobera, M. Balaguer, J. García-Fayos, J.M. Serra, Catalytic Oxide-Ion Conducting Materials for Surface Activation of $Ba_{0.5}Sr_{0.5}Co_{0.8}Fe_{0.2}O_{3-\delta}$ Membranes, ChemistrySelect. 2 (2017) 2949–2955. doi:10.1002/slct.201700530.

[20] E. Bucher, A. Egger, G.B. Caraman, W. Sitte, Stability of the SOFC Cathode Material (Ba,Sr)(Co,Fe)$O_{3-\delta}$ in CO_2-Containing Atmospheres, J. Electrochem. Soc. 155 (2008) B1218. doi:10.1149/1.2981024.

[21] X. Tan, N. Liu, B. Meng, J. Sunarso, K. Zhang, S. Liu, Oxygen permeation behavior of $La_{0.6}Sr_{0.4}Co_{0.8}Fe_{0.2}O_3$ hollow fibre membranes with highly concentrated CO_2 exposure, J. Memb. Sci. 389 (2012) 216–222. doi:10.1016/j.memsci.2011.10.032.

[22] M. Pilar Lobera, S. Escolastico, J. Garcia-Fayos, J.M. Serra, Ethylene Production by ODHE in Catalytically Modified $Ba_{0.5}Sr_{0.5}Co_{0.8}Fe_{0.2}O_{3-\delta}$ Membrane Reactors, ChemSusChem. 5 (2012) 1587–1596. doi:10.1002/cssc.201100747.

[23] S.J. Benson, D. Waller, J.A. Kilner, Degradation of $La_{0.6}Sr_{0.4}Fe_{0.8}Co_{0.2}O_{3-\delta}$ in Carbon Dioxide and Water Atmospheres, J. Electrochem. Soc. 146 (2000) 1305–1309.

[24] M. Schulz, R. Kriegel, A. Kämpfer, Assessment of CO_2 stability and oxygen flux of oxygen permeable membranes, J. Memb. Sci. 378 (2011) 10–17. doi:10.1016/j.memsci.2011.02.037.

[25] S. Engels, T. Markus, M. Modigell, L. Singheiser, Oxygen permeation and stability investigations on MIEC membrane materials under operating conditions for power plant processes, J. Memb. Sci. 370 (2011) 58–69. doi:10.1016/j.memsci.2010.12.021.

[26] J. Gao, L. Li, Z. Yin, J. Zhang, S. Lu, X. Tan, Poisoning effect of SO_2 on the oxygen permeation behavior of $La_{0.6}Sr_{0.4}Co_{0.2}Fe_{0.8}O_{3-\delta}$ perovskite hollow fiber membranes, J. Memb. Sci. 455 (2014) 341–348. doi:10.1016/j.memsci.2013.12.073.

[27] S. Pirou, J. Gurauskis, V. Gil, M. Søgaard, P.V. Hendriksen, A. Kaiser, S. Ovtar, R. Kiebach, Oxygen permeation flux through 10Sc1YSZ-$MnCo_2O_4$ asymmetric membranes prepared by two-step sintering, Fuel Process. Technol. 152 (2016) 192–199. doi:10.1016/j.fuproc.2016.06.019.

[28] A. Samson, M. Søgaard, R. Knibbe, N. Bonanos, High Performance Cathodes for Solid Oxide Fuel Cells Prepared by Infiltration of $La_{0.6}Sr_{0.4}CoO_{3-\delta}$ into Gd-Doped Ceria, J. Electrochem. Soc. 158 (2011) B650. doi:10.1149/1.3571249.

[29] J. Garcia-Fayos, M. Balaguer, J.M. Serra, Dual-Phase Oxygen Transport Membranes for Stable Operation in Environments Containing Carbon Dioxide and Sulfur Dioxide, ChemSusChem. 8 (2015) 4242–4249. doi:10.1002/cssc.201500951.

[30] S. Pirou, J.M. Bermudez, P.V. Hendriksen, A. Kaiser, T. Ramirez, M. Millan, R. Kiebach, Stability and performance of robust dual-phase $(ZrO_2)_{0.89}(Y_2O_3)_{0.01}(Sc_2O_3)_{0.10}$-$Al_{0.02}Zn_{0.98}O_{1.01}$ oxygen transport membranes, J. Memb. Sci. 543 (2017) 18–27. doi:10.1016/j.memsci.2017.08.044.

[31] I. Kuritsyna, V. Sinitsyn, A. Melnikov, Y. Fedotov, E. Tsipis, A. Viskup, S. Bredikhin, V. Kharton, Oxygen exchange, thermochemical expansion and cathodic behavior of perovskite-like $Sr_{0.7}Ce_{0.3}MnO_{3-\delta}$, Solid State Ionics. 262 (2014) 349–353. doi:10.1016/j.ssi.2013.11.013.

[32] T.M. McCoy, Extension of the master sintering curve for constant heating rate modeling, Georgia Institute of Technology, 2008.

[33] X.J. Chen, K.A. Khor, S.H. Chan, L.G. Yu, Influence of microstructure on the ionic conductivity of yttria-stabilized zirconia electrolyte, Mater. Sci. Eng. A. 335 (2002) 246–252. doi:10.1016/S0921-5093(01)01935-9.

[34] J.T.S. Irvine, J.W.L. Dobson, T. Politova, S.G. Martin, A. Shenouda, Co-doping of scandia-zirconia electrolytes for SOFCs., Faraday Discuss. 134 (2007) 41–49; discussion 103–118, 415–419. doi:10.1039/b604441g.

[35] M. Balaguer, C. Solís, J.M. Serra, Study of the transport properties of the mixed ionic electronic conductor $Ce_{1-x}Tb_xO_{2-\delta}$ + Co (x = 0.1, 0.2) and evaluation as oxygen-transport membrane, Chem. Mater. 23 (2011) 2333–2343. doi:10.1021/cm103581w.

[36] A. Petric, H. Ling, Electrical conductivity and thermal expansion of spinels at elevated temperatures, J. Am. Ceram. Soc. 90 (2007) 1515–1520. doi:10.1111/j.1551-2916.2007.01522.x.

[37] L. Navarrete, M. Balaguer, V.B. Vert, J.M. Serra, Tailoring Electrocatalytic Properties

of Solid Oxide Fuel Cell Composite Cathodes Based on $(La_{0.8}Sr_{0.2})_{0.95}MnO_{3+\delta}$ and Doped Cerias $Ce_{1-x}Ln_xO_{2-\delta}$ (Ln=Gd, La, Er, Pr, Tb and x=0.1-0.2), Fuel Cells. 17 (2017) 100–107. doi:10.1002/fuce.201600133.

[38] Y. Alqaheem, A. Thursfield, G. Zhang, I.S. Metcalfe, The impact of sulfur contamination on the performance of $La_{0.6}Sr_{0.4}Co_{0.2}Fe_{0.8}O_{3-\delta}$ oxygen transport membranes, Solid State Ionics. 262 (2014) 262–265. doi:10.1016/j.ssi.2014.01.011.

[39] A. Waindich, A. Möbius, M. Müller, Corrosion of $Ba_{1-x}Sr_xCo_{1-y}Fe_yO_{3-\delta}$ and $La_{0.3}Ba_{0.7}Co_{0.2}Fe_{0.8}O_{3-\delta}$ materials for oxygen separating membranes under Oxycoal conditions, J. Memb. Sci. 337 (2009) 182–187. doi:10.1016/j.memsci.2009.03.041.

5.3. Stability and performance of robust dual-phase $(ZrO_2)_{0.89}(Y_2O_3)_{0.01}(Sc_2O_3)_{0.10}$-$Al_{0.02}Zn_{0.98}O_{1.01}$ oxygen transport membranes

This sub-chapter contains the manuscript "Stability and performance of robust dual-phase $(ZrO_2)_{0.89}(Y_2O_3)_{0.01}(Sc_2O_3)_{0.10}$-$Al_{0.02}Zn_{0.98}O_{1.01}$ oxygen transport membranes" published in the Journal of Membrane Science (J. Memb. Sci. 543 (2017) 18–27).

In parallel to the work carried out on 10Sc1YSZ-$MnCo_2O_4$ membranes, the development of 10Sc1YSZ-$Al_{0.02}Zn_{0.98}O_{1.01}$ (AZO) dual-phase membranes was considered to overcome, in particular, problems related to the decomposition of $MnCo_2O_4$ requiring the use of a two-step sintering process. AZO, which presents the advantages of: (i) having a high electronic conductivity (σ_{AZO}= 164 S cm^{-1} at 820 °C), (ii) being chemically stable in both CO_2 and SO_2 atmospheres, and (iii) being a non-toxic, abundant and inexpensive material, could be a promising candidate as the electronic conducting phase for dual-phase OTMs.

In order to evaluate the possible application of 50 vol.% 10Sc1YSZ - 50 vol.% AZO dual-phase membranes in relevant oxy-fuel power plant conditions, the stability of the composite material was investigated in different atmospheres, including CO_2, SO_2 and H_2O. Dual-phase membranes were prepared both in the form of thick self-standing membranes (1 mm) and thin asymmetric membranes (8 μm). The effect of different oxygen partial pressure on the microstructure of the membrane material during sintering and during oxygen permeation tests was investigated. Finally, the performance of the membranes was evaluated by a long-term electrical conductivity measurement under CO_2 and by oxygen permeation tests.

Stability and performance of robust dual-phase $(ZrO_2)_{0.89}(Y_2O_3)_{0.01}(Sc_2O_3)_{0.10}$-$Al_{0.02}Zn_{0.98}O_{1.01}$ oxygen transport membranes

Stéven Pirou[a], Jose M. Bermudez[b], Peter Vang Hendriksen[a], Andreas Kaiser[a], Tomás Ramirez Reina[b1], Marcos Millan[b], Ragnar Kiebach[a].*

[a] Department o Energy Conversion and Storage, Technical University of Denmark, Risø campus, Frederiksborgvej 399, DK-4000 Roskilde, Denmark

[b] Department of Chemical Engineering, Imperial College London, South Kensington Campus, London SW7 2AZ, United Kingdom

* corresponding author

E-Mail addresses: stepir@dtu.dk, j.bermudez-menendez@imperial.ac.uk, pvhe@dtu.dk, akai@dtu.dk, t.ramirezreina@surrey.ac.uk, marcos.millan@imperial.ac.uk, woki@dtu.dk

[1] T.R.Reina present address: Department of Chemical & Process Engineering, University of Surrey, Guildford, GU2 7HX, United Kingdom

Abstract

Dual-phase composite oxygen transport membranes consisting of 50 vol.% $Al_{0.02}Zn_{0.98}O_{1.01}$ and 50 vol.% $(ZrO_2)_{0.89}(Y_2O_3)_{0.01}(Sc_2O_3)_{0.10}$ were successfully developed and tested. The applicability of the membrane in oxy-fuel power plants schemes involving direct exposure to flue gas was evaluated by exposing the membrane to gas streams containing CO_2, SO_2, H_2O and investigating possible reactions between the membrane material and these gases. The analyses of the exposed composites by x-ray diffraction (XRD), x-ray fluorescence (XRF), attenuated total reflection Fourier transform infrared spectroscopy (ATR-FTIR), and Raman spectroscopy revealed excellent stability. Additionally, an electrical conductivity measurement over 900 h confirmed that the composite is stable under prolonged exposure to CO_2. However, an instability of the dual-phase membrane under oxygen partial pressures below pO_2 ~10^{-4} atm. was found. Oxygen permeation tests on a 1 mm thick self-standing membrane resulted in an oxygen flux of 0.33 $mL_N\ min^{-1}\ cm^{-2}$ at 925 °C in air/N_2. Stability tests in CO_2 with 3 vol.% O_2 demonstrated the potential for the use of 10Sc1YSZ-AZO dual-phase membranes in oxy-combustion processes involving direct exposure to flue gas.

Keywords

Oxygen transport membrane, Composite membrane, CO_2 stability, SO_2 tolerance, Oxy-fuel combustion.

1. Introduction

Oxygen transport membranes (OTMs) are a promising technology for producing pure oxygen or supplying oxygen to some oxidation process at both small and large scale. Especially high temperature processes, such as biomass gasification, oxy-fired cement production, or oxy-fuel combustion where some (waste) heat can be made available for air preheating, are interesting application areas. Here, OTMs can provide oxygen at a lower energy consumption than with conventional oxygen production from cryogenic distillation or vacuum pressure swing adsorption, if the OTMs are used in small to medium units and in thermally integrated separation modules [1 – 3].

Typical OTMs are dense membranes made from mixed ionic electronic conductors (MIECs), which enable oxygen diffusion through vacancies in the crystal lattice and simultaneous transport of electrons in the opposite direction. An oxygen partial pressure difference between the gas atmosphere on the feed and the permeate side provides the driving force for the transport of oxygen ions across the membrane. The flux through the membrane is given by the Wagner Equation (1) for the case of fast surface exchange:

$$J_{O_2} = \frac{RT}{16F^2L}\int_{pO_{2,feed}}^{pO_{2,permeate}} \frac{\sigma_e\sigma_i}{\sigma_e+\sigma_i}\,(pO_2)\,dln\,pO_2 \quad (1)$$

where J_{O_2} is the oxygen permeation flux (mol m^{-2} s^{-1}), R is the gas constant (J mol^{-1} K^{-1}), T is the absolute temperature (K), F is the Faraday constant (C mol^{-1}), L is the membrane thickness (m), σ_e and σ_i are the electronic and the ionic conductivities (S m^{-1}), and $pO_{2,permeate}$ and $pO_{2,feed}$ are the oxygen partial pressures at the high pressure and low pressure sides (Pa), respectively.

In recent years, a significant number of publications have been dedicated to membranes based on single-phase MIEC materials, such as $Ba_{1-x}Sr_xCo_{1-y}Fe_yO_{3-\delta}$ (BSCF) and $La_{1-x}Sr_xCo_{1-y}Fe_yO_{3-\delta}$ (LSCF) [4 – 12]. Their good electronic and ionic conductivities allow high oxygen fluxes. However, most of the promising MIEC materials are not chemically stable under atmospheres containing CO_2 and SO_2, which is required when using OTMs in "direct integration mode" in biomass gasification, cement production or oxy-combustion based coal fired power plant processes targeting carbon capture. "Direct integration mode" signifies process schemes, where the membranes are exposed directly to a flue gas (or

pyrolysis gas) on the permeate side of the membrane. Such direct integration is beneficial for process economy and efficiency but places stringent requirements on the materials, specifically stability in CO_2 and SO_2 which are inevitable constituents/impurities arising from the calcination of limestone, and the combustion of sulphur-containing coal or biomass.

The composition of the flue gas in an oxy-fuel power plant can vary depending on several parameters: oxygen purity, fuel composition and the extent of "false air intrusion". Therefore, the conditions the membrane is exposed to can vary from case to case. A representative composition would be; CO_2 (80 – 90 mol.%), N_2 (8 – 10 mol.%), H_2O (2 – 3 mol.%), O_2 (2 – 3 mol.%) and SO_2 (200 – 500 ppm) [13]. Some of these gases (mainly CO_2 and SO_2) will react quickly with most alkaline-earth doped perovskite based materials (common OTMs materials) leading to reduced permeability due to the formation of alkaline earth carbonates and sulphates such as $(Ba_xSr_{1-x})CO_3$ and $SrSO_4$ [7, 14 – 19]. Composite materials of a stable ionic and a stable electronic conductor (in a dual-phase membrane) can be an interesting alternative to overcome the stability limitations of single-phase membrane materials in CO_2 and SO_2.

Yttria stabilized zirconia ($(ZrO_2)_{1-x}(Y_2O_3)_x$ (YSZ)) is a well-known strong and stable ionic conductor [20 – 22] which is used in many high temperature applications, such as in SOFC [23 – 25], and λ-sensors [26 – 28]. We propose here to develop a stable dual-phase membrane based on 10Sc1YSZ as the ionic conductor, because co-doping zirconia with scandium and yttrium ($(ZrO_2)_{1-(x+y)}(Y_2O_3)_x(Sc_2O_3)_y$ (ScYSZ)) significantly increases the ionic conductivity at an operation temperature of 850 °C (the ionic conductivity of $(ZrO_2)_{0.92}(Y_2O_3)_{0.08}$ (8YSZ) is 0.03 S cm^{-1} at 850 °C [29] whereas the ionic conductivity for $(ZrO_2)_{0.89}(Y_2O_3)_{0.01}(Sc_2O_3)_{0.10}$ (10Sc1YSZ) is 0.12 S cm^{-1} [30]).

Doped zinc oxide has recently been proposed as an electronic conductor for use in OTMs [31]. There are several reasons for this : (i) The conductivity of ZnO can by doping with small amounts of trivalent elements like Al, Ga or In be raised to more than 100 S/cm (at 820 °C, $\sigma_{Zn_{0.98}Al_{0.02}O}$ = 164 S cm^{-1} while σ_{ZnO} = 0.016 S cm^{-1}) [32 – 38]; (ii) ZnO is chemically stable in both CO_2 and SO_2 atmospheres [31]; and (iii) ZnO is non-toxic, abundant and inexpensive. Accordingly, $Al_{0.02}Zn_{0.98}O_{1.01}$ (AZO) was chosen here as the electronic conductor for the developed dual-phase membrane.

In order to evaluate the possible application of 10Sc1YSZ-AZO membranes in power plant relevant conditions, the stability of the 10Sc1YSZ-AZO composite was studied in different atmospheres, including CO_2, SO_2 and H_2O. Analytical techniques such as X-ray diffraction (XRD), X-ray fluorescence (XRF), attenuated total reflection Fourier transform infrared spectroscopy (ATR-FTIR), and Raman spectroscopy were used to characterize the material after exposure to the gases. Dual-phase membranes were prepared both in the form of thick self-standing membranes (i) and thin asymmetric membranes (ii). The effect of different oxygen partial pressure on the microstructure of the membrane material during sintering and during oxygen permeation tests was investigated. Finally, the performance of the membrane was evaluated by a long-term electrical conductivity measurement under CO_2 and by oxygen permeation tests.

2. Experimental

2.1. Thermochemical stability and characterization of 10Sc1YSZ-AZO composites

2.1.1. Thermochemical stability tests

The thermochemical stability of the 10Sc1YSZ-AZO composite was tested in a quartz up-flow vertical testing unit (Figure 5. 21). This unit consists of a liner containing a porous sample holder to enable an even distribution of gas. The testing unit is fitted inside an oven, capable of operation up to 1200 °C. The temperature is controlled by means of a thermocouple placed within the bed of material.

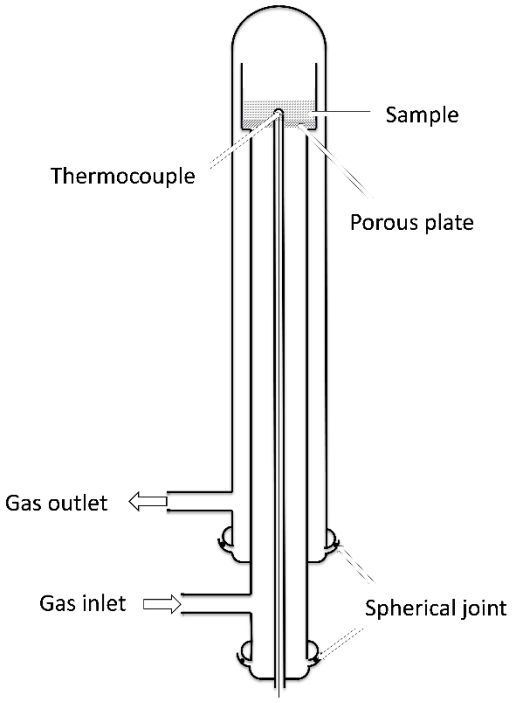

Figure 5. 21: Scheme of the testing unit used for the thermochemical stability tests of the 10Sc1YSZ-AZO samples.

To ensure a large contact area between the gases and the composites, loose powders were used instead of sintered components. For each run, 1 g of fresh 10Sc1YSZ-AZO powder was placed on the sample holder. Then, the testing unit was heated up to 850 °C in atmospheric air. At 850 °C, the gas composition was switched to the desired mixture of CO_2, SO_2 and H_2O to assess the effect of these gases on the stability of the 10Sc1YSZ-AZO. Reference experiments in air and CO_2 were also performed. Different concentrations of CO_2 and SO_2 were provided using two gas cylinders, one with CO_2 (purity 99.8 vol.%) and the other with 2000 ppm of SO_2 in CO_2. Steam was added using an evaporator fed by a syringe pump, which enabled the amount of water to be controlled. The powders were exposed to the different mixtures of $CO_2/SO_2/H_2O$ at a total gas flow rate of 0.25 L_N min^{-1} for 8 hours at atmospheric pressure. The gas compositions used in the different tests are summarized in Table 5. 4. The concentrations of gases in the mixtures were adjusted using rotameters. For safety reasons, the outlet gases were cooled down to room temperature to remove steam. Afterwards, the dry flue gases passed through a series of two saturated NaOH solutions to remove SO_2. After the exposure of the powders to the gas atmosphere, the testing unit was cooled down in the same gas atmosphere to avoid possible decomposition (by oxidation) of the species formed during the treatments and thus recover the material for characterization.

Table 5. 4: Gas compositions in thermochemical stability tests performed on 10Sc1YSZ-AZO powder at 850 °C for 8 hours. A gas flowrate of 0.25 L_N min^{-1} at atmospheric pressure was used.

Test	CO_2 (vol.%) (1)	SO_2 (ppm v/v) (1)	H_2O (vol.%) (2)
Reference(3)	0	0	0
CO_2	100	0	0
500SO_2	Balance	500	0
100SO_2 10H_2O	Balance	100	10
500SO_2 10H_2O	Balance	500	10
2000SO_2 10H_2O	Balance	2000	10
500SO_2 30H_2O	Balance	500	30

(1) Dry basis; (2) Percentage of the total flow, including steam; (3) Performed in air

2.1.2. Material characterization

Before and after the high temperature gas exposure treatment, the powder samples were characterized by a series of analytical techniques to detect any reactions of the powder materials with the different gases.

X-ray diffraction (XRD) patterns were obtained using a PANalytical diffractometer equipped with a Ni-filtered Cu Kα radiation (40 mA, 45 kV) over a 2Θ-range of 5-80º and a position-sensitive detector using a step size of 0.05º and a step time of 120 s. The XRD patterns were processed using the X'Pert Highscore Plus software to identify the species present in the samples.

X-ray fluorescence (XRF) was performed to determine the chemical composition of the fresh and treated samples, using a PANalytical Epsilon3XLE X-ray fluorescence spectrophotometer with a 50 kV silver anode tube as source of radiation.

A Perkin Elmer FTIR 100 spectrometer was used to perform attenuated total reflection Fourier transform infrared spectroscopy (ATR-FTIR). Background-subtracted spectra were collected at room temperature and the spectra were baseline-corrected using Spectrum 10™ software.

Raman spectra were collected on a Renishaw InVia Raman spectrometer equipped with a charge-coupled device and a Leica microscope. A 785-nm HPNIR diode laser with

maximum power of 300 mW was used as an excitation source. A 1200 mm^{-1} grating was used for all measurements, providing a spectral resolution of ± 1 cm^{-1}. The laser spot was focused on the sample surface using a long working distance 50×. The laser beam spot size was around 1.28 µm.

2.2. Membrane manufacturing

Thick (1 mm) self-standing symmetric membranes and thin (8 µm) asymmetric supported membranes of 10Sc1YSZ-AZO were prepared (see sections 2.2.1 and 2.2.2) to study the stability of the composite material as a function of the oxygen partial pressure and for oxygen permeation tests.

2.2.1. Thick symmetric membranes

The 10Sc1YSZ and AZO powders were purchased from Daiichi Kigenso Kagaku Kogyo Co. Ldt (Japan) and Nanostructured & Amorphous Material, Inc (USA), respectively. The ionic and electronic conductors were blended in an equal volume ratio to form the 10Sc1YSZ-AZO composite material. The particles size of the powders were adjusted to the submicron range using ball-milling. Subsequently, 15 mm diameter membranes were formed using a uniaxial press (1000 kg load). The membrane disks were sintered at 1200 °C for 6 hours under different oxygen partial pressures: 0.21 bar (air) and 10^{-5} bar (N_2). After sintering, the sample disks were polished down to 1 mm and an in-house prepared ink of $(La_{0.80}Sr_{0.20})MnO_{3-\delta}$ – $(Y_2O_3)_{0.08}(ZrO_2)_{0.92}$ (LSM-YSZ (50-50 vol.%)) was screen-printed on both sides of the membrane to serve as oxygen oxidation/reduction catalyst. Finally, the membrane was heated to 980 °C for 2 hours in air in order to dry the printed catalyst and make it adhere to the membrane surface.

2.2.2. Thin asymmetric membranes

Post sintering, the asymmetric membranes consist of a 200 µm thick porous support (3YSZ + 20 vol.% of Al_2O_3) and a thin dense composite membrane layer (10Sc1YSZ/AZO, 8 µm) surrounded by two porous layers (8YSZ, 10 µm) which subsequently can be impregnated with a suitable catalyst. All layers were manufactured separately by tape-casting. The YSZ (3YSZ and 8YSZ) powders were purchased from Tosoh (Japan) and were calcined for 2 h at 1100 °C and 900 °C, respectively prior to further processing. All materials were ball milled

in ethanol to obtain particles in submicronic range (d_{v50} < 1 µm). From these powders three slurries were prepared and used for tape-casting: (i) a slurry for the porous support layer containing 33 wt.% of pore formers in relation to the total solid content (Graphite (d_{v50} = 7 µm) and poly(methyl methacrylate) (PMMA) (d_{v50} = 1.8 µm) supplied by Graphit Kropfmühl AG (Germany) and Esprix Technologies (USA), respectively) (ii) a slurry for the porous functional layers containing 33 wt.% of pore former (PMMA) and (iii) a slurry for the dense membrane layer free of pore former. The three slurries were prepared using the same organic additives: ethanol (solvent), polyvinylpyrrolidone (PVP, dispersant), polyvinyl butyral (PVB, binder) and polyoxyethylene aryl ether (Pycal 94, plasticiser). After drying, the green tapes were assembled by lamination at 135 °C and 30 mm diameter disks were cut out using a stamping tool. The asymmetric membranes were sintered at 1200 °C for 6 h in different atmospheres in order to study the stability of the thin 10Sc1YSZ-AZO film under various oxygen partial pressures. After sintering, $Gd_{0.2}Ce_{0.8}O_{2-\delta}$ (GDC) and $LaNi_{0.6}Co_{0.4}O_{3-\delta}$ (LNC) aqueous solutions with concentration of 2.5 and 1.25 M were prepared and infiltrated into the YSZ porous layers. The impregnation procedure has been described in detail in a previous study [39].

2.3. Characterization of 10Sc1YSZ-AZO-membranes

10Sc1YSZ-AZO membranes were sintered in different atmospheres in order to study the influence of the oxygen partial pressure on the microstructure of the membranes during the sintering step. The microstructure of the membranes was investigated on polished cross-sections by SEM using a Hitachi TM3000 operated at 15 kV.

Electrical conductivity measurements were performed on a bar (1.7 cm x 0.4 cm x 0.4 cm) of 10Sc1YSZ-AZO (50-50 vol.%) prepared by isostatic pressing. The bar was sintered at 1200 °C for 6 h in air prior to the conductivity measurements. The 10Sc1YSZ-AZO bar was heated at 1 °C min^{-1} from room temperature to 850 °C and conductivity measured successively in air (24 h), in CO_2 (890 h) and again in air (24 h), to study the impact of the CO_2 on the electrical conductivity of the dual-phase material. The flow of gas was maintained at 100 mL_N min^{-1} by using mass flow controllers (Brooks). An in-house built zirconia-based pO_2 sensor was used to determine the pO_2 in the gases. Current was applied via two strips of platinum and the resulting potential was measured between two point probes. The four

terminal resistance, R_{ABCD}, was defined by the Ohm's law. Subsequently the electrical conductivity σ, expressed in units of S cm^{-1}, was calculated as below:

$$\sigma = \frac{l}{a \cdot R_{ABCD}} \quad (2)$$

where a is the cross sectional area of the rod (cm^2) and l is the distance between the potential probes (cm).

Oxygen permeation measurements were conducted in a membrane test rig described previously in [40]. Two permeation tests were performed to evaluate the performances of both the thick self-standing and the thin asymmetric membranes. Two additional tests were done to investigate the stability of the membrane at low oxygen partial pressures. As schematically shown in Figure 5. 22, the membranes were placed in the middle zone of a height adjustable tube furnace, between two alumina tubes. Thermocouples were placed in direct contact with the membrane, inside the alumina tube, in order to monitor the temperature. Tape-cast sodium aluminosilicate (NAS, Na_2O: 17.8 mol.%, Al_2O_3: 9.4 mol.% and SiO_2: 72.8 mol.% [41]) glass rings, with an inner diameter of 9 mm, and a glass transition temperature of 515 °C [40] were used as sealing material between the alumina tubes and the membrane. The exterior surface of the samples were also coated with NAS paste to ensure that oxygen cannot enter from the sweep gas compartment to the membrane. To ensure a gas tight sealing, the membrane was heated in air up to 940 °C and afterwards cooled to 750 °C. A gas chromatograph was connected to the outlet of the permeate side to quantify any oxygen leaks into the permeate stream (oxygen that enters the permeate compartment via pinholes or insufficient sealing at the membrane periphery). To evaluate the performance of the thick self-standing and thin asymmetric membranes, air (100 mL_N min^{-1}) and N_2 (150 mL_N min^{-1}) were fed to the feed and the permeate side of the membrane, respectively. The inlet flow of each gas was controlled and monitored by a mass flow controller (Brooks). In-house built zirconia-based pO_2 sensors were used to determine the pO_2 of the inlet gas on the permeate side (before feeding to the membranes) and of the outlet gas (after passing over the membranes). Oxygen permeation flux was deduced based on the pO_2 variations between the inlet and the outlet of the gas flowing through the permeate side. The oxygen permeation flux through the membranes was calculated as:

$$J_{O_2} = \frac{pO_{2,permeate}^{out} \cdot \dot{n}^{out} - pO_{2,permeate}^{in} \cdot \dot{n}^{in}}{A} \quad (3)$$

where J_{O_2} is the oxygen permeation flux, $pO_{2,permeate}^{in}$ and $pO_{2,permeate}^{out}$ are respectively the oxygen partial pressures of the inlet and outlet gases of the permeate side, $\dot{n}^{in}$ and $\dot{n}^{out}$ are molar flow rates of inlet and outlet gases, respectively, and A is the net area of the permeate side of the membrane. The Nernst equation (4) is used to calculate the oxygen partial pressure from the measured sensor voltage (V):

$$pO_2 = pO_{2,ref}.e^{\frac{4FV}{RT}} \quad (4)$$

where V is the open circuit voltage of the oxygen sensor, T is the temperature of the oxygen sensor and $pO_{2,ref}$ is the oxygen partial pressure at the reference electrode which was maintained at 0.21 atm during the measurement.

The stability study of the membrane under low pO_2 atmospheres was carried out on two self-standing membranes of 1 mm thickness at 850 °C. During the first test, a continuous flow of 150 mL_N min^{-1} of pure CO_2 was fed to the permeate side, while the second membrane was tested in CO_2 + 3 vol.% of O_2. Both tests were performed using a constant flow of 100 mL_N min^{-1} of air as a feed gas. After 200 h, the microstructures of the membranes were analyzed by scanning electron microscopy and compared to a similar fresh membrane.

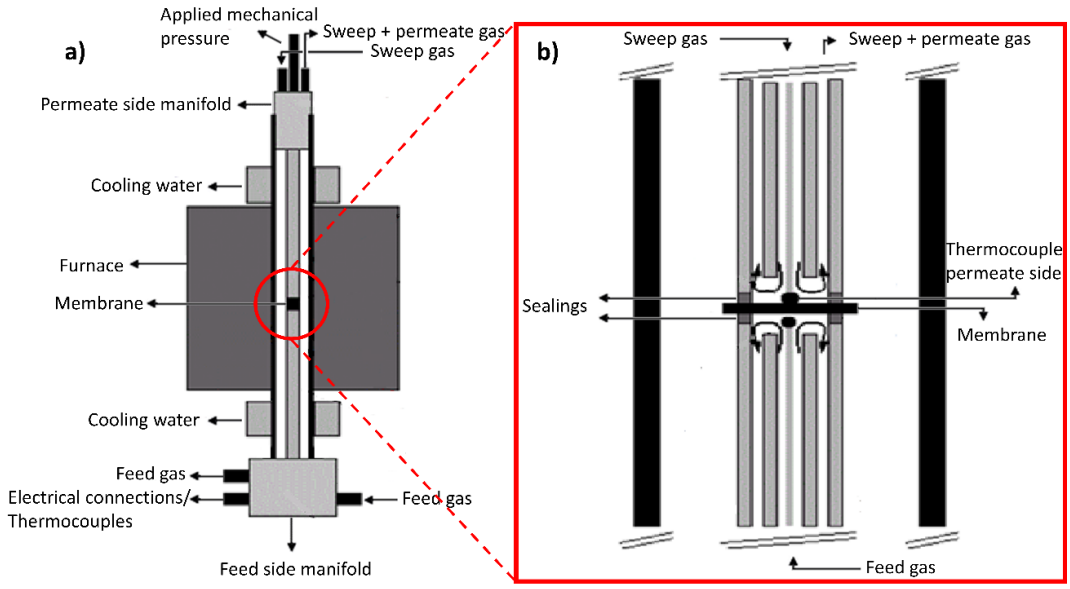

Figure 5. 22: Schematic illustration of: a) the entire membrane test rig used for oxygen permeation measurements, including membrane, furnace, gas supply, manifolds and b) a zoom into the area with gas compartments, sealings and active membrane.

3. Results and discussion

3.1. Stability studies

3.1.1. Chemical stability of 10Sc1YSZ-AZO composite material under relevant flue gas conditions in power plants

Here, the effects of exposure to different impurities in oxy-combustion flue gases, CO_2, SO_2 and H_2O, on the stability of 10Sc1YSZ-AZO powder are presented. In the experiments involving exposure to SO_2, the total amount of sulphur put in contact with the samples was 0.02 g for the experiment using 100 ppm of SO_2, 0.08 g for the experiments with 500 ppm of SO_2, and finally 0.32 g for the experiment using 2000 ppm of SO_2. The relative large quantities of sulphur used in these experiments should improve the detection of any reaction products (sulphates) within the detection limits of the analytical tests.

Figure 5. 23 shows results of the XRD characterization before and after exposure of the composite material to CO_2 and SO_2. The powder diffractograms of the fresh and the treated samples of 10Sc1YSZ-AZO are identical and additional peaks related to the formation of new crystalline phases could not be observed within the detection limits. The diffractograms of the fresh and treated samples plotted in Figure 5. 23 correspond to a combination of Sc and Y doped ZrO_2 and $Al_{0.02}Zn_{0.98}O_2$ peaks.

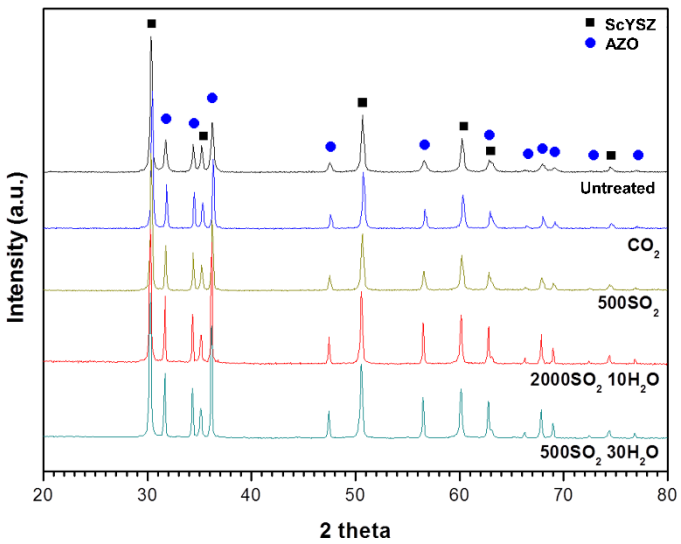

Figure 5. 23: Powder XRD patterns of 10Sc1YSZ-AZO after treatment in different atmospheres (from top to bottom): untreated (black), in pure CO_2 (blue), in a mixture of 500 ppm of SO_2 in CO_2 (yellow), in a mixture of 2000 ppm of SO_2 in CO_2 and 10 % of steam (red) and in a mixture of 500 ppm of SO_2 in CO_2 and 30 % of steam (cyan).

However, very low amounts of crystalline phases or non-crystalline phases are difficult to detect with powder X-ray diffraction. Therefore, additional characterization by Raman and ATR-FTIR was performed to further exclude any formation of small amounts of secondary phases after exposure to the gases. Figure 5. 24 shows the ATR-FTIR and Raman spectra of the same samples investigated previously by XRD (Figure 5. 23). Both techniques are well suited for detection of small amounts of carbonates or sulphates. Any presence of carbonates would be detectable by sharp signals in the range of 850-900 cm^{-1} or broad peaks in the range of 1400-1600 cm^{-1} [42 – 44]. Sulphates would give rise to signals in the range from 950 to 1250 cm^{-1} [42, 43, 45] or in the range of 200-800 cm^{-1} and/or between 900 and 1400 cm^{-1} in the Raman spectra. However, it is noteworthy that no new peaks are observed in these ranges when comparing ATR-FTIR and Raman spectra of the samples before and after treatment. The ATR-FTIR and Raman spectra of untreated and treated samples are identical.

With the aim of discarding any possible incorporation of sulphur or carbon during the treatments, also XRF and elemental analysis were performed on the fresh and treated samples. Neither carbon nor sulphur were detected by any of these techniques. It should be noted that the detection limit of these techniques are in the range of a few ppm (if instead alkaline earth containing cobaltite perovskite type materials are investigated after similar exposures with the same characterization techniques significant amounts of both sulphates and carbonates are detected [46]).

XRD, XRF, ATR-FTIR, and Raman were used to investigate the chemical stability of 10Sc1YSZ-AZO composite material after exposure to gasses characteristic of power plant flue gases. None of the techniques showed presence of any secondary non-desired phases in the treated samples. Accordingly, the analyses prove the excellent stability of the 10Sc1YSZ-AZO composite in the tested environments, indicating that this composite is, in terms of stability, a good candidate for use in OTMs applied in oxy-combustion processes.

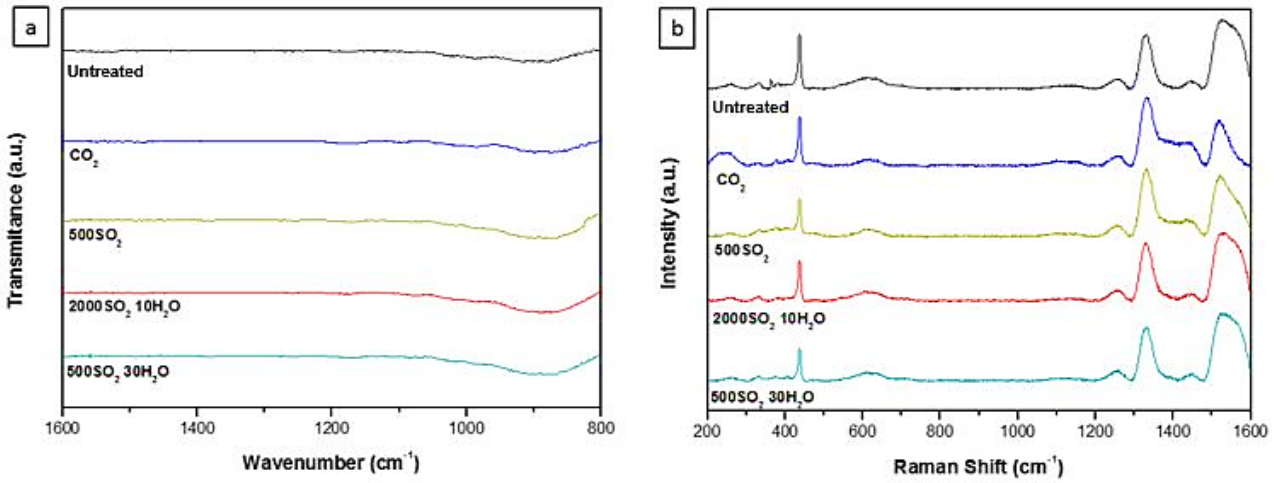

Figure 5. 24: a) ATR-FTIR spectra; and b) Raman spectra of the 10Sc1YSZ-AZO fresh (black), treated with pure CO_2 (blue), with 500 ppm of SO_2 in CO_2 (yellow), with 2000 ppm of SO_2 in CO_2 and 10 % of steam (red) and with 500 ppm of SO_2 in CO_2 and 30 % of steam (cyan).

3.1.2. Effect of the oxygen partial pressure on the microstructure of 10Sc1YSZ-AZO dual-phase membranes

The effect of the oxyge partial pressure (pO_2) on the microstructure of 10Sc1YSZ-AZO dual-phase membranes during sintering was studied on thick self-standing (1 mm) and thin supported membranes (8 µm).

Figure 5. 25 presents the polished cross-section of 1 mm thick 10Sc1YSZ-AZO membranes after conventional sintering at 1200 °C for 6 h in N_2 (Figure 5. 25.a) and in air (Figure 5. 25.b). The SEM analysis reveals that the membrane sintered in air is completely dense, while the membrane sintered in N_2 is porous on the first 30 µm of each side. The EDX analysis clearly shows the absence of the AZO phase on the sides, while the remaining porous backbone consists of 10Sc1YSZ phase (Figure 5. 25.c). Clearly, a significant amount of AZO is lost when sintering the composite in nitrogen. The microstructure after sintering in N_2 would only be applicable as a membrane if a suitable catalyst is subsequently impregnated into the porous all zirconia structures at the two surfaces. Applying a catalyst on top the membrane surface would not work, as there is no electronic percolation all the way to the sample surfaces. These results are in accordance with results from Bérardan *et al.* [47] which also indicated that AZO was more volatilized during a sintering at high temperature in nitrogen than in air.

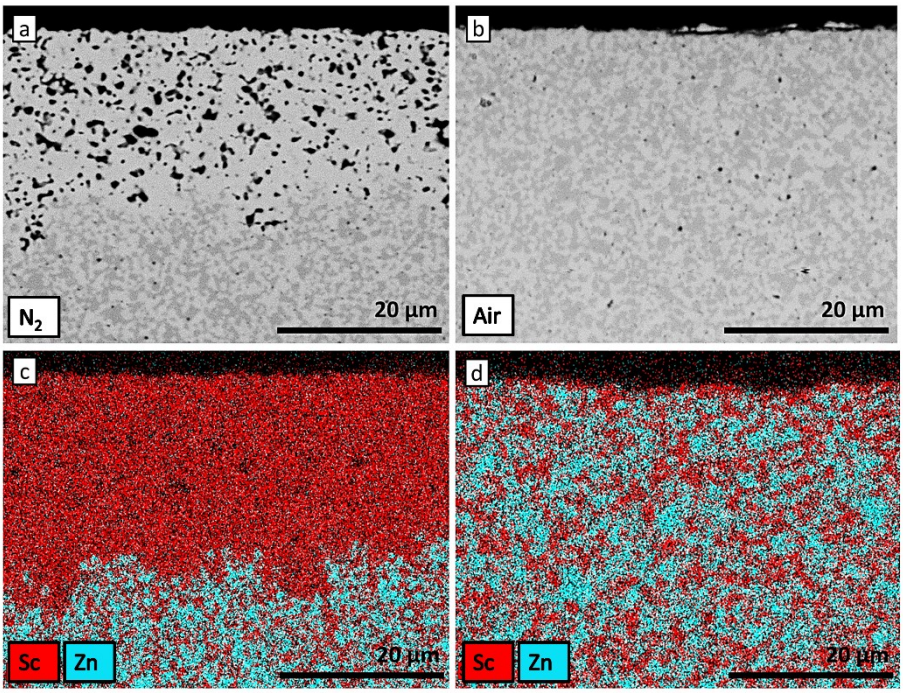

Figure 5. 25: SEM images (top) and EDX maps (bottom) of the elements Sc (red) and Zn (blue) of polished cross-sections of 10Sc1YSZ-AZO membranes, sintered at 1200 °C in N_2 (a, c) and in air (b, d).

Figure 5. 26 presents the cross-sections of symmetric membranes composed of a 8 µm thin 10Sc1YSZ-AZO composite layer and a 200 µm 3YSZ support that were sintered at 1200 °C for 6 hours in 3 different atmospheres: (i) N_2, (ii) air and (iii) O_2. Significant alterations of the microstructure in the 10Sc1YSZ-AZO membrane layer can be observed depending on the oxygen partial pressure during the sintering. The membrane sintered in N_2 appears highly porous due to the loose of the zinc oxide phase (Figure 5. 26.a), while under higher oxygen partial pressure atmospheres (air or pure O_2) the composite layer is dense and the desired ratio of ionic/electronic conductor is maintained (Figure 5. 26.b and 5. 26.c).

To summarize, the study on the membranes microstructure stability shows that the development of 10Sc1YSZ-AZO composite membranes is challenging because of the high volatility of the AZO phase in low oxygen partial pressure atmospheres. When using thick self-standing membranes, this problem can easily be circumvented by removing the 10Sc1YSZ porous phase on both sides of the membranes by polishing. The same issue cannot be so simply solved with thin asymmetric membranes. Therefore, for the development of asymmetric membrane, sintering has to be performed under sufficiently high oxygen partial pressure in order to keep the AZO phase in the composite. This is not easily achieved as even when applying pure oxygen during sintering a thin dense layer without

much ZnO forms at the interfaces between the dense layer and the infiltration layers (see Figure 5. 26.b and 5. 26.c). This layer will hamper membrane performance, as there is no electronic percolation through this layer.

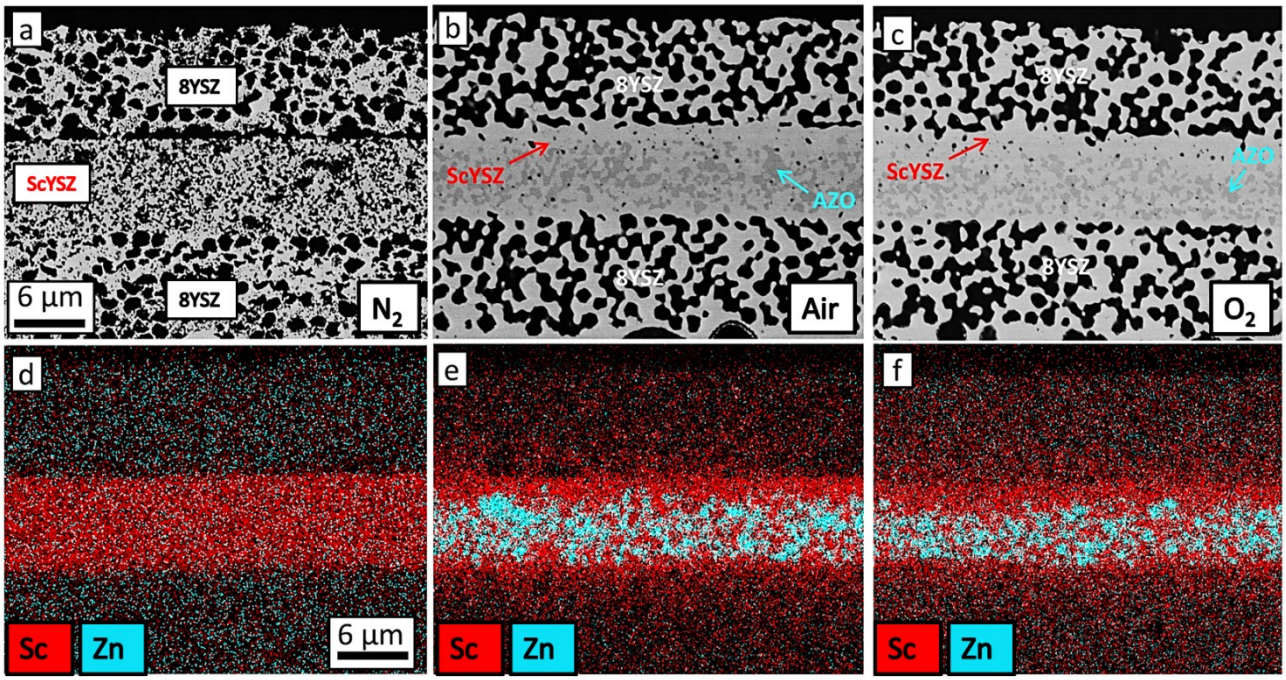

Figure 5. 26: SEM images and EDX maps (Sc and Zn elements) of 10Sc1YSZ-AZO (50-50 vol.%) thin asymmetric membranes sintered at 1200 °C in N_2 (a, d), air (b, e) and pure oxygen (c, f).

3.2. Electrical conductivity measurements

As briefly introduced in section 2.3, a long-term electrical conductivity test was performed on a 10Sc1YSZ-AZO composite bar at 850 °C in CO_2 in order to investigate the influence of a prolonged exposure to CO_2 on the electrical conductivity of the dual-phase material. Figure 5. 27 presents the electrical conductivity of the composite material and the oxygen partial pressure realized during the test as a function of time. Initially air was fed to the furnace and after 24 h, the feed was changed to CO_2. After 890 h in CO_2 air was again applied for 24 h. Overall, the electrical conductivity did not decrease during the 900 h of testing. The conductivity increases by a factor of 10 when switching from air to CO_2 showing the expected increase of the electrical conductivity of AZO by lowering the pO_2 [47, 48]. The first and last 24 h of the test, performed in air, gave similar values of conductivity (4 % of derivation), thus indicating that the initial electrical conductivity of the composite material (in air) can be recovered. In other words, changes in the conductivity of the samples were not observed when switching back to air atmosphere after treatment in CO_2 and any changes in

conductivity are due to the defect-chemistry of AZO (that responds reversibly to pO_2 changes) and not to effects of microstructural changes.

The cross-sections of the 10Sc1YSZ-AZO composite bar after the electrical conductivity measurement are shown in Figure 5. 28. Figure 5. 28.a displays the microstructure of a sample section where the platinum paste was applied locally as a current collector covering the sample surface, while Figure 5. 28.b shows a section not covered by the platinum. The comparison of the two images clearly shows that the Pt layer supresses the volatilization of the AZO. Consequently, the current feed probes applied during conductivity measurements seems to have worked well, i.e. contact is not lost here despite the tendency of the sample to lose AZO. The effective conductivity of the bar would be expected to drop a little over time as clearly the top ~ 4 µm of sample have become depleted in the electronic conductor. However, as the depleted layer constitutes only a small fraction of the cross section the effect of the depletion is not observed over the period in CO_2. After returning to air, indeed a small reduction in the sample conductance is observed which could in part be due to loss of AZO. The conductivity measurements presented in Figure 5. 27 show that the exposure to CO_2 (and associated reduction in oxygen activity) itself increases the sample conductivity. XRD patterns, ATR-FTIR and Raman spectra, in Figures 5. 23 and 5. 24 show that CO_2 does not react or directly contributes to the destabilization of AZO. Nevertheless, the loss of AZO in the dual-phase material (Figure 5. 28.b) over time will lead to a decrease of the conductivity because of the loss of the electrical conducting phase. It is important to note here that the conductivity test was performed in much lower oxygen partial pressure ($pO_2 \approx 2.10^{-4}$ bar) than at realistic conditions of the envisioned application areas ($pO_2 \approx 3.10^{-2}$ bar [13]). It is essential to distinguish between the effect of the CO_2 and the effect of the low oxygen partial pressure, when discussing the stability of the composite. This is further investigated and discussed below in section 3.3.2.

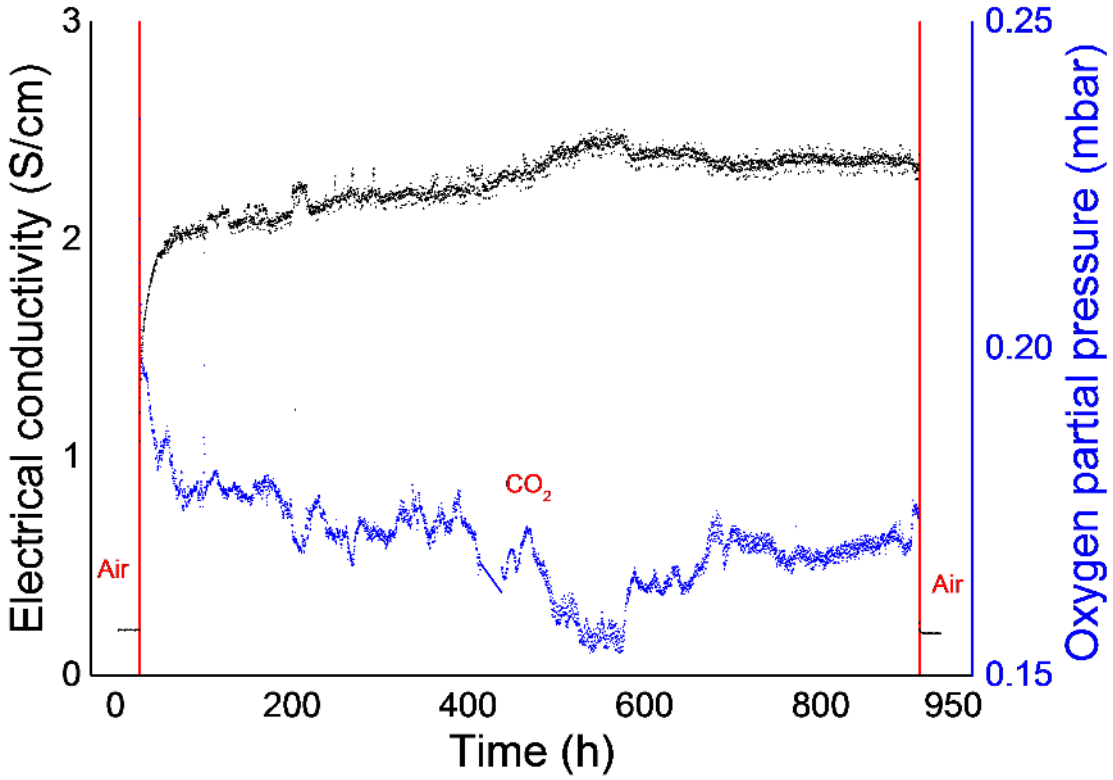

Figure 5. 27: Electrical conductivity of a 10Sc1YSZ-AZO bar (black curve) and oxygen partial pressure in the platform test (blue curve) as a function of the time. The test was performed at 850 °C in air (first and last 24 h) and in CO_2. The dotted line represents the initial value of the electrical conductivity in air.

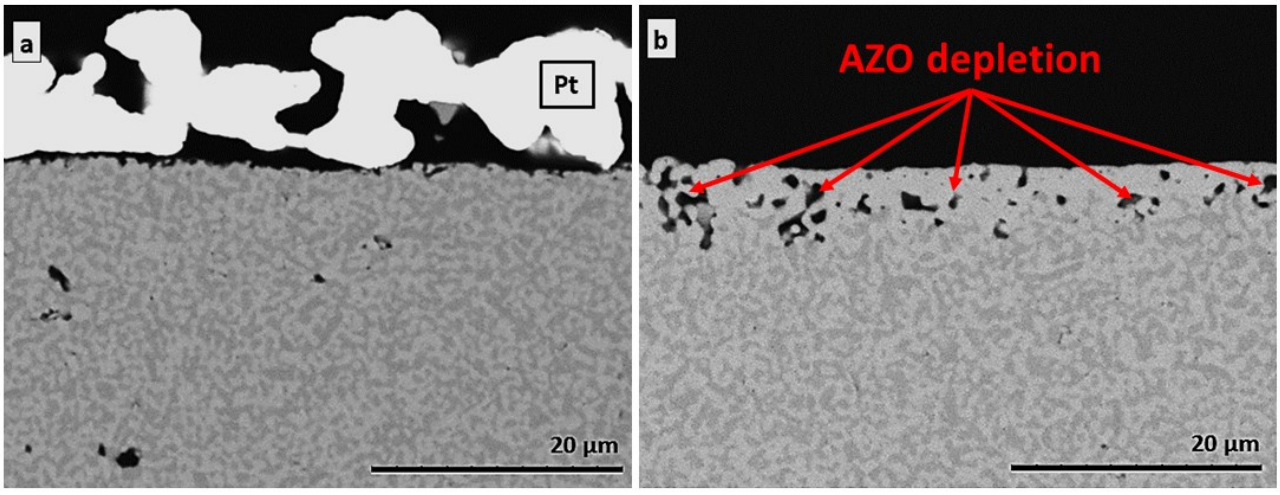

Figure 5. 28: SEM images of polished cross-sections of the 10Sc1YSZ-AZO bar after the electrical conductivity measurement with (a) and without (b) Pt current collector.

3.3. Oxygen permeation measurements

3.3.1. Performances of thick self-standing and thin supported membranes

The performance of a 1 mm thick 10Sc1YSZ-AZO self-standing membrane and an 8 µm thick 10Sc1YSZ-AZO supported membrane was evaluated carrying out oxygen permeation measurements, as described in Section 2.3.

Figure 5. 29 presents the oxygen permeation fluxes of the two membranes with different thicknesses as a function of temperature when using N_2 as sweep gas, and air as a feed gas. Based on the Wagner equation (1), described in section 1, the oxygen flux should scale inversely with membrane thickness. Interestingly, the opposite was found here: the 1 mm thick membrane shows a higher oxygen flux than the thin asymmetric membrane. As shown in Figure 5. 29, at 925 °C the oxygen flux through the 1 mm thick membrane corresponds to 0.33 $mL_N\ min^{-1}\ cm^{-2}$, while only a flow of 0.16 $mL_N\ min^{-1}\ cm^{-2}$ was measured across the thin supported membrane. Clearly, the performance of the asymmetric membrane is drastically lower than anticipated. The oxygen permeation flux through the self-standing membrane is mainly limited by the bulk diffusion. Indeed, the proximity of activation energy values of the membrane (69.1 kJ mol^{-1}) and 10Sc1YSZ (62.7 kJ mol^{-1} at 850 °C [49]) attests that the conductivity of the ionic phase is limiting the performance of the self-standing membrane. Considering that and knowing that the asymmetric membrane is approximately a hundred times thinner than the self-standing membrane, a significant increase of the oxygen permeation flux would be expected when using the thin asymmetric membrane. A likely explanation for the low performance is a lack of percolation in the electronic phase across the dense 10Sc1YSZ-AZO composite layer. The SEM micrographs of the cross sections (Figure 5. 26.b) shows clear signs that the outer parts of the dense membrane layer are completely depleted in AZO and would behave effectively as an electrolyte hampering the oxygen permeation flux.

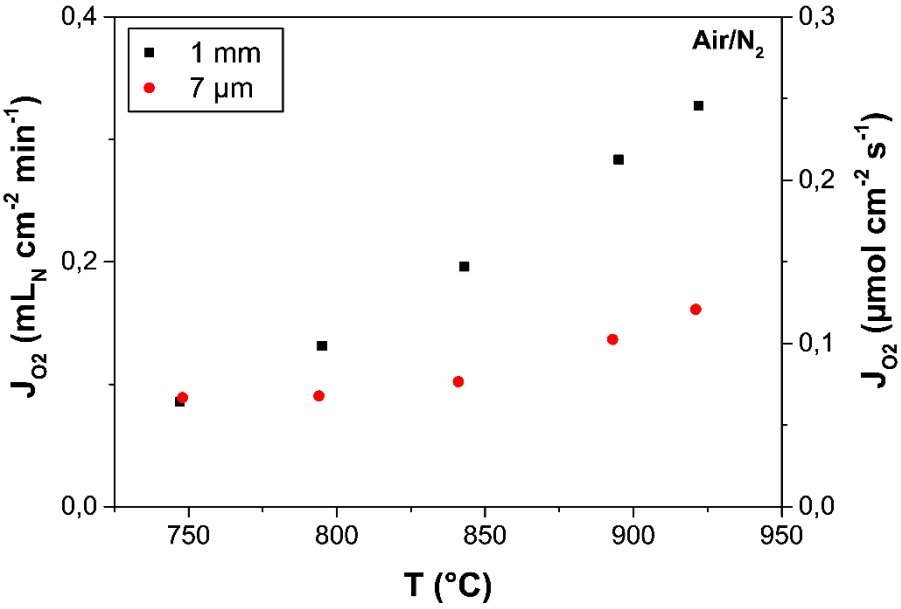

Figure 5. 29: Oxygen permeation fluxes of 10Sc1YSZ-AZO membranes as a function of the temperature using air as a feed gas and N_2 as a sweep gas.

3.3.2. Long-term stability tests in CO_2

To further investigate the influence of the pO_2 on the microstructural degradation of the membrane and to confirm that the observed instability of AZO is due to the mildly reducing atmosphere (pO_2 < 10^{-4} bar) and not of the presence of CO_2, the stability of 1 mm thick self-standing membranes was investigated under different pO_2 conditions on the permeate side. One membrane was tested under an air/CO_2 gradient while the other test was conducted between air and CO_2 + 3 vol.% of O_2. It should be emphasized that the pO_2 conditions of the second test resembles realistic conditions for an application of the OTMs in oxy-fuel power plants [13], and are therefore considered the more relevant. After 200 h of exposure, the microstructure of the tested membranes was compared to a fresh membrane. Results are presented in Figure 5. 30. The polished cross-section of a fresh membrane is displayed in Figure 5. 30.a, the membrane tested with pure CO_2 on the permeate side is presented in Figure 5. 30.b and finally the membrane tested in CO_2 + 3 vol.% O_2 is reproduced in Figure 5. 30.c. As expected, from both the long term conductivity test and the studies of the sintering in various gasses, a significant loss of AZO is observed for the membrane exposed to pure CO_2 after 200 hours due to the instability of the AZO phase in low pO_2 atmosphere (pO_2 ≈ 2.10^{-4} bar). The first 10 µm on the permeate side appear highly porous. However, the microstructure of the second long term tested membrane is practically identical to the fresh

one, demonstrating that no AZO is lost under exposure to CO_2 with 3 vol.% of O_2 at the permeate side . This experiment proves that the 10Sc1YSZ-AZO dual-phase membranes is applicable under oxy-fuel conditions (high CO_2 activity) as long as the oxygen activity at the permeate side is maintained at ~ 2 – 3 %. For the case of a low pO_2 ~10^{-4} atm. the membrane would, if in the form of a thin film, most likely not be applicable due to the observed loss of material.

A previous study from Cheng *et al.* reported on the use of AZO in a composite oxygen membrane in combination with CGO [31]. A stable flux through a 1 mm thick membrane over ~500 hours in a gradient between air and CO_2 was also found elucidating material robustness towards CO_2. However, the conducted thick membrane experiment [31] “masks” problems related to material loss under low pO_2 as discussed here for AZO/zirconia composites due to the large material reservoir. Given the material loss rates observed here, it is unlikely that any thin film (L ~ 10 – 20 µm) composite membrane realization involving AZO would perform reliably under long term operation (thousands of hours) if the pO_2 on the permeate side is lower than 10^{-4} bar. If pO_2 on the permeate side is on the order of 10^{-2} bar material loss seems tolerable (c.f. Figure 5. 30.c).

Practical application of the investigated composite would require the flux can be increased substantially above the values reported in Figure 5. 29. The obvious approach, as also adopted here, would be to reduce the membrane thickness. Whereas a thin film component strong enough for test could obviously be manufactured, it presented no gain in oxygen transport (see section 3.3.1.). This, as discussed (section 3.3.1.) is most likely due to thin “all electrolyte” skin layers that form during firing of the component due to loss of AZO from the surface of the composite. Hence, it is related to the high vapor phase of the ZnO and its limited stability under reducing conditions. Countering measures must be developed to prevent this surface depletion if the full potential of ZnO as a cheap electronic conductor in composite oxygen membranes should be realized. A stabilization of the zinc oxide phase could be achieved by decreasing the sintering temperature, for example by using a dopant element as a sintering aid. The utilization of a protective porous layer with a high AZO content covering the dense membrane would help to prevent the depletion of the zinc oxide phase and seems a feasible route to reduce the problem.

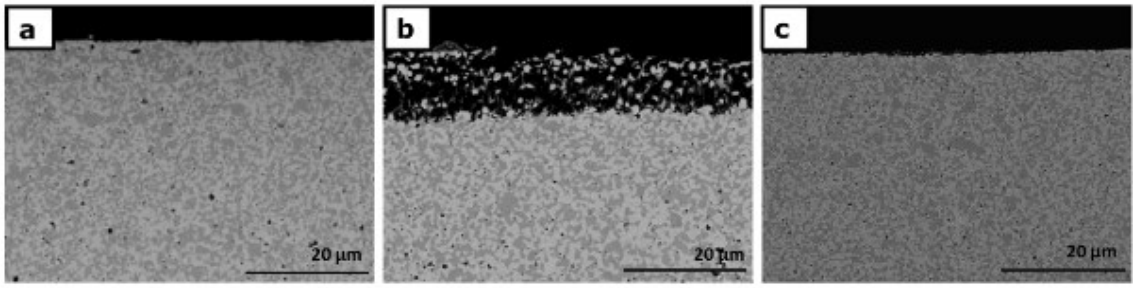

Figure 5. 30: SEM images of the polish cross-sections of 1 mm thick self-standing 10Sc1YSZ-AZO membranes. (a) fresh membrane, (b) tested in air/CO_2 atmosphere, and (c) tested in air/CO_2 + 3 vol.% O_2 atmosphere.

4. Conclusions

The stability of the dual-phase composite membranes consisting of 50 vol.% $Al_{0.02}Zn_{0.98}O_{1.01}$ (AZO) and 50 vol.% $(ZrO_2)_{0.89}(Y_2O_3)_{0.01}(Sc_2O_3)_{0.10}$ (10Sc1YSZ) was studied in simulated oxy-fuel power plant flue gas atmospheres (CO_2, SO_2, H_2O) using several characterization techniques (XRD, XRF, ATR-FTIR, and Raman spectroscopy). The tests underlined the excellent stability of the materials under application relevant atmospheres. 10Sc1YSZ-AZO is concluded to be a promising material combination for OTMs integrated in oxy-fuel power plants where oxygen activity on the permeate side is above 2.10^{-4} atm. The material is not suitable for use in gasification applications or other applications where the oxygen content on the permeate side is below 100 ppm. In addition the low stability of the zinc oxides phase under very mildly reducing atmosphere makes the fabrication of thin and high performance asymmetric membranes complicated (due to formation of all electrolyte “skin layers”). Clearly thick self-standing membranes show too limited performances to be commercialized and further R&D is required to realize thin and highly performing 10Sc1YSZ-AZO asymmetric membranes, where performance is not limited by lack of electronic percolation, as was the case for the here tested asymmetric membranes.

Acknowledgments

The financial support from EU through the “Graded Membranes for Energy Efficient New Generation Carbon Capture Process (GREEN-CC)” project (Grant agreement no. 608524) is gratefully acknowledged. Henrik Paulsen is acknowledged by the authors for helping with the preparation of the samples for SEM-EDX analysis.

References

[1] S.S. Hashim, A.R. Mohamed, S. Bhatia, Oxygen separation from air using ceramic-based membrane technology for sustainable fuel production and power generation, Renew. Sustain. Energy Rev. 15 (2011) 1284–1293. doi:10.1016/j.rser.2010.10.002.

[2] M. Puig-Arnavat, S. Soprani, M. Søgaard, K. Engelbrecht, J. Ahrenfeldt, U.B. Henriksen, P.V. Hendriksen, Integration of mixed conducting membranes in an oxygen–steam biomass gasification process, RSC Adv. 3 (2013) 20843–20854. doi:10.1039/c3ra44509g.

[3] M. Czyperek, P. Zapp, H.J.M. Bouwmeester, M. Modigell, K. Ebert, I. Voigt, W.A. Meulenberg, L. Singheiser, D. Stöver, Gas separation membranes for zero-emission fossil power plants: MEM-BRAIN, J. Memb. Sci. 359 (2010) 149–159. doi:10.1016/j.memsci.2010.04.012.

[4] R. Kiebach, K. Engelbrecht, K. Kwok, S. Molin, M. Søgaard, P. Niehoff, F. Schulze-Küppers, R. Kriegel, J. Kluge, P.V. Hendriksen, Joining of ceramic $Ba_{0.5}Sr_{0.5}Co_{0.8}Fe_{0.2}O_3$ membranes for oxygen production to high temperature alloys, J. Memb. Sci. 506 (2016) 11–21. doi:10.1016/j.memsci.2016.01.050.

[5] S. Baumann, J.M. Serra, M.P. Lobera, S. Escolástico, F. Schulze-Küppers, W.A. Meulenberg, Ultrahigh oxygen permeation flux through supported $Ba_{0.5}Sr_{0.5}Co_{0.}8Fe_{0.2}O_{3-\delta}$ membranes, J. Memb. Sci. 377 (2011) 198–205. doi:10.1016/j.memsci.2011.04.050.

[6] P. Haworth, S. Smart, J. Glasscock, J.C. Diniz da Costa, High performance yttrium-doped BSCF hollow fibre membranes, Sep. Purif. Technol. 94 (2012) 16–22. doi:10.1016/j.seppur.2012.04.005.

[7] M. Arnold, H. Wang, A. Feldhoff, Influence of CO_2 on the oxygen permeation performance and the microstructure of perovskite-type $(Ba_{0.5}Sr_{0.5})(Co_{0.8}Fe_{0.2})O_{3-\delta}$ membranes, J. Memb. Sci. 293 (2007) 44–52. doi:10.1016/j.memsci.2007.01.032.

[8] Z. Shao, W. Yang, Y. Cong, H. Dong, J. Tong, G. Xiong, Investigation of the permeation behavior and stability of a $Ba_{0.5}Sr_{0.5}Co_{0.8}Fe_{0.2}O_{(3-\delta)}$ oxygen membrane, J. Memb. Sci. 172 (2000) 177–188. doi:10.1016/S0376-7388(00)00337-9.

[9] L. Ge, W. Zhou, R. Ran, S. Liu, Z. Shao, W. Jin, N. Xu, Properties and performance of A-site deficient $(Ba_{0.5}Sr_{0.5})_{1-x}Co_{0.8}Fe_{0.2}O_{3-\delta}$ for oxygen permeating membrane, J. Memb. Sci. 306 (2007) 318–328. doi:10.1016/j.memsci.2007.09.004.

[10] Z. Taheri, K. Nazari, N. Seyed-Matin, A.A. Safekordi, B. Ghanbari, S. Zarrinpashne, R. Ahmadi, Comparison of oxygen permeation through some perovskite membranes synthesized with EDTNAD, React. Kinet. Mech. Catal. 100 (2010) 459–469. doi:10.1007/s11144-010-0158-2.

[11] F. Schulze-Küppers, S. Baumann, F. Tietz, H.J.M. Bouwmeester, W.A. Meulenberg, Towards the fabrication of $La_{0.98-x}Sr_xCo_{0.2}Fe_{0.8}O_{3-\delta}$ perovskite-type oxygen transport membranes, J. Eur. Ceram. Soc. 34 (2014) 3741–3748. doi:10.1016/j.jeurceramsoc.2014.06.012.

[12] X. Tan, Z. Wang, B. Meng, X. Meng, K. Li, Pilot-scale production of oxygen from air using perovskite hollow fibre membranes, J. Memb. Sci. 352 (2010) 189–196. doi:10.1016/j.memsci.2010.02.015.

[13] E.S. Rubin, A.B. Rao, M.B. Berkenpas, Technical Documentation : Oxygen-based Combustion Systems (Oxyfuels) with Carbon Capture and Storage (CCS), 2007.

[14] X. Tan, N. Liu, B. Meng, J. Sunarso, K. Zhang, S. Liu, Oxygen permeation behavior of $La_{0.6}Sr_{0.4}Co_{0.8}Fe_{0.2}O_3$ hollow fibre membranes with highly concentrated CO_2 exposure, J. Memb. Sci. 389 (2012) 216–222. doi:10.1016/j.memsci.2011.10.032.

[15] S. Engels, T. Markus, M. Modigell, L. Singheiser, Oxygen permeation and stability investigations on MIEC membrane materials under operating conditions for power plant processes, J. Memb. Sci. 370 (2011) 58–69. doi:10.1016/j.memsci.2010.12.021.

[16] J. Gao, L. Li, Z. Yin, J. Zhang, S. Lu, X. Tan, Poisoning effect of SO_2 on the oxygen permeation behavior of $La_{0.6}Sr_{0.4}Co_{0.2}Fe_{0.8}O_{3-\delta}$ perovskite hollow fiber membranes, J. Memb. Sci. 455 (2014) 341–348. doi:10.1016/j.memsci.2013.12.073.

[17] E. Bucher, A. Egger, G.B. Caraman, W. Sitte, Stability of the SOFC Cathode Material $(Ba,Sr)(Co,Fe)O_{3-\delta}$ in CO_2-Containing Atmospheres, J. Electrochem. Soc. 155 (2008) B1218. doi:10.1149/1.2981024.

[18] S.J. Benson, D. Waller, J.A. Kilner, Degradation of $La_{0.6}Sr_{0.4}Fe_{0.8}Co_{0.2}O_{3-\delta}$ in Carbon

Dioxide and Water Atmospheres, J. Electrochem. Soc. 146 (2000) 1305–1309.

[19] M. Schulz, R. Kriegel, A. Kämpfer, Assessment of CO_2 stability and oxygen flux of oxygen permeable membranes, J. Memb. Sci. 378 (2011) 10–17. doi:10.1016/j.memsci.2011.02.037.

[20] S. Lia, W. Jin, N. Xu, J. Shi, Mechanical strength, and oxygen and electronic transport properties of $SrCo_{0.4}Fe_{0.6}O_{3-\delta}$ -YSZ membranes, J. Memb. Sci. 186 (2001) 195–204.

[21] B. Wang, M. Zhan, D. Zhu, W. Liu, C. Chen, Oxygen permeation and stability of $Zr_{0.8}Y_{0.2}O_{0.9}$–$La_{0.8}Sr_{0.2}CrO_{3-\delta}$ dual-phase composite, J. Solid State Electrochem. 10 (2006) 625–628. doi:10.1007/s10008-006-0136-9.

[22] M.M. Hiroaki Yanagida, Kunihiko Koumoto, Kunihito Komoto, The Chemistry of Ceramics, 1996.

[23] M. Han, X. Tang, H. Yin, S. Peng, Fabrication, microstructure and properties of a YSZ electrolyte for SOFCs, J. Power Sources. 165 (2007) 757–763. doi:10.1016/j.jpowsour.2006.11.054.

[24] C.-J. Li, C.-X. Li, X.-J. Ning, Performance of YSZ electrolyte layer deposited by atmospheric plasma spraying for cermet-supported tubular SOFC, Vacuum. 73 (2004) 699–703. doi:10.1016/j.vacuum.2003.12.096.

[25] S.P. Simner, J.P. Shelton, M.D. Anderson, J.W. Stevenson, Interaction between La(Sr)FeO_3 SOFC cathode and YSZ electrolyte, Solid State Ionics. 161 (2003) 11–18. doi:10.1016/S0167-2738(03)00158-9.

[26] J.-H. Lee, B.-K. Kim, K.-L. Lee, H.-I. Kim, K.-W. Han, A new catalyst monitoring sensor for gasoline engine using YSZ-Al_2O_3 as solid electrolyte and gas diffusion barrier, Sensors Actuators, B Chem. 59 (1999) 9–15.

[27] S. Fischer, R. Pohle, B. Farber, R. Proch, J. Kaniuk, M. Fleischer, R. Moos, Method for detection of NOx in exhaust gases by pulsed discharge measurements using standard zirconia-based lambda sensors, Sensors Actuators, B Chem. 147 (2010) 780–785. doi:10.1016/j.snb.2010.03.092.

[28] R. Ramamoorthy, P.K. Dutta, S.A. Akbar, Oxygen sensors: Materials, methods,

designs and applications, J. Mater. Sci. 38 (2003) 4271–4282. doi:10.1023/A:1026370729205.

[29] X.J. Chen, K.A. Khor, S.H. Chan, L.G. Yu, Influence of microstructure on the ionic conductivity of yttria-stabilized zirconia electrolyte, Mater. Sci. Eng. A. 335 (2002) 246–252. doi:10.1016/S0921-5093(01)01935-9.

[30] V.G. Artemov, I.E. Kuritsyna, S.P. Lebedev, G.A. Komandin, P.O. Kapralov, I.E. Spektor, V.V Kharton, S.I. Bredikhin, A.A. Volkov, Analysis of electric properties of ZrO_2-Y_2O_3 single crystals using teraherz IR and impedance spectroscopy techniques, Russ. J. Electrochem. 50 (2014) 690–693. doi:10.1134/S1023193514070039.

[31] S. Cheng, M. Søgaard, L. Han, W. Zhang, M. Chen, A. Kaiser, P.V. Hendriksen, A novel CO_2- and SO_2-tolerant dual phase composite membrane for oxygen separation, Chem. Commun. 51 (2015) 7140–7143. doi:10.1039/C5CC00001G.

[32] L. Han, D. V. Christensen, A. Bhowmik, S.B. Simonsen, L.T. Hung, E. Abdellahi, Y.Z. Chen, N. V. Nong, S. Linderoth, N. Pryds, Scandium-doped zinc cadmium oxide as a new stable n-type oxide thermoelectric material, J. Mater. Chem. A. 4 (2016) 12221–12231. doi:10.1039/C6TA03126A.

[33] L. Han, N. Van Nong, L.T. Hung, T. Holgate, N. Pryds, M. Ohtaki, S. Linderoth, The influence of α- and γ-Al_2O_3 phases on the thermoelectric properties of Al-doped ZnO, J. Alloys Compd. 555 (2013) 291–296. doi:10.1016/j.jallcom.2012.12.091.

[34] L. Han, L.T. Hung, N. Van Nong, N. Pryds, S. Linderoth, The influence of spark plasma sintering temperature on the microstructure and thermoelectric properties of Al,Ga dual-doped ZnO, J. Electron. Mater. 42 (2013) 1573–1581. doi:10.1007/s11664-012-2325-x.

[35] P.H. Miller, The Electrical Conductivity of Zinc Oxide, Phys. Rev. 60 (1941) 890–895. doi:10.1103/PhysRev.60.890.

[36] S.Y. Kuo, W.C. Chen, F.I. Lai, C.P. Cheng, H.C. Kuo, S.C. Wang, W.F. Hsieh, Effects of doping concentration and annealing temperature on properties of highly-oriented Al-doped ZnO films, J. Cryst. Growth. 287 (2006) 78–84. doi:10.1016/j.jcrysgro.2005.10.047.

[37] V. Fathollahi, M.M. Amini, Sol–gel preparation of highly oriented gallium-doped zinc oxide thin films, Mater. Lett. 50 (2001) 235–239. doi:10.1016/S0167-577X(01)00231-2.

[38] T. Minami, Transparent conducting oxide semiconductors for transparent electrodes, Semicond. Sci. Technol. 20 S35 Semicond. Sci. Technol. 20 (2005) 35–44. doi:10.1088/0268-1242/20/4/004.

[39] S. Pirou, J. Gurauskis, V. Gil, M. Søgaard, P.V. Hendriksen, A. Kaiser, S. Ovtar, R. Kiebach, Oxygen permeation flux through 10Sc1YSZ-$MnCo_2O_4$ asymmetric membranes prepared by two-step sintering, Fuel Process. Technol. 152 (2016) 192–199. doi:10.1016/j.fuproc.2016.06.019.

[40] A.J. Samson, M. Søgaard, P. Vang Hendriksen, $(Ce,Gd)O_{2-\delta}$-based dual phase membranes for oxygen separation, J. Memb. Sci. 470 (2014) 178–188. doi:10.1016/j.memsci.2014.07.028.

[41] K.A. Nielsen, M. Solvang, S.B.L. Nielsen, A.R. Dinesen, D. Beeaff, P.H. Larsen, Glass composite seals for SOFC application, J. Eur. Ceram. Soc. 27 (2007) 1817–1822. doi:10.1016/j.jeurceramsoc.2006.05.046.

[42] K. Nakamoto, Infared and Raman Spectra of Inorganic and Coordination Compounds: Part A: Theory and Applications in Inorganic Chemistry, Sixth Edition, 2008. doi:10.1002/9780470405840.

[43] E. Turianicová, A. Obut, A. Zorkovská, P. Baláž, M. Matik, J. Briančin, The effects of LiOH and NaOH on the carbonation of $SrSO_4$ by dry high-energy milling, Miner. Eng. 49 (2013) 98–102. doi:10.1016/j.mineng.2013.05.017.

[44] M.E. Böttcher, P. Gehlken, Á. Fernández-González, M. Prieto, Characterization of synthetic $BaCO_3$ - $SrCO_3$ (witherite-strontianite) solid-solutions by Fourier transform infrared spectroscopy, Eur. J. Miner. 9 (1997) 519–528. doi:10.1127/ejm/9/3/0519.

[45] A. Periasamy, S. Muruganand, M. Palaniswamy, Vibrational studies of Na_2SO_4, K_2SO_4, $NaHSO_4$ and $KHSO_4$ crystals, J. Chem. 2 (2009) 981–989.

[46] J.M. Bermudez, J. García-Fayos, T.R. Reina, G. Reed, M. Milan, J.M. Serra, Thermochemical stability of $NiFe_2O_4$-$Ce_{0.8}Tb_{0.2}O_{2-\delta}$ under real conditions for its

application in 4-end module oxygen transport membranes for oxycombustion, in: 14th Int. Conf. Inorg. Membr., Atlanta (USA), 2016.

[47] D. Bérardan, C. Byl, N. Dragoe, Influence of the preparation conditions on the thermoelectric properties of Al-doped ZnO, J. Am. Ceram. Soc. 93 (2010) 2352–2358. doi:10.1111/j.1551-2916.2010.03751.x.

[48] A. Janotti, C. Van de Walle, Fundamentals of zinc oxide as a semiconductor, Reports Prog. Phys. 72 (2009) 126501. doi:10.1088/0034-4885/72/12/126501.

[49] J.T.S. Irvine, J.W.L. Dobson, T. Politova, S.G. Martín, A. Shenouda, Co-doping of scandia-zirconia electrolytes for SOFCs., Faraday Discuss. 134 (2007) 41–49; discussion 103–118, 415–419. doi:10.1039/b604441g.

5.4. Performance and stability of $(ZrO_2)_{0.89}(Y_2O_3)_{0.01}(Sc_2O_3)_{0.10}$-$LaCr_{0.85}Cu_{0.10}Ni_{0.05}O_{3-\delta}$ oxygen transport membranes under conditions relevant for oxy-fuel combustion

This sub-chapter contains the manuscript "Performance and stability of $(ZrO_2)_{0.89}(Y_2O_3)_{0.01}(Sc_2O_3)_{0.10}$-$LaCr_{0.85}Cu_{0.10}Ni_{0.05}O_{3-\delta}$ oxygen transport membranes under conditions relevant for oxy-fuel combustion", which is ready for submission.

The low stability of the zinc oxide phase under very mildly reducing atmospheres making the fabrication of thin and highly performing asymmetric membranes complicated resulted in the re-openning of the question: what is the most suitable material for use as an electronic conducting phase in dual-phase OTMs directly integrated into oxy-fuel combustion power plants?

Lanthanum chromite based materials fulfil many of the requirements that an electronic conducting phase of OTMs directly integrated to oxy-fuel combustion power plants must have. Among them, lanthanum chromite exhibits excellent stability under stringent conditions such as highly reducing (even if not absolutely necessary or required for oxy-fuel combustion applications) atmospheres at elevated temperatures. Also, electrical conductivity of lanthanum chromite based materials can be rather high when doped by transition metals such as Cu or Ni.

In this study, the stability of 10Sc1YSZ-LCCN (70-30 vol.%) composite material was investigated under conditions relevant for oxy-fuel combustion (CO_2, SO_2, H_2O). Analytical techniques such as X-ray diffraction (XRD), X-ray fluorescence (XRF), attenuated total reflection Fourier transform infrared spectroscopy (ATR-FTIR), Raman spectroscopy and scanning electron microscopy with energy dispersive X-ray spectroscopy (SEM-EDX) were used to characterize the material after exposure to the gases. Oxygen permeation fluxes across 1000 µm thick and 110 µm thick self-supported 10Sc1YSZ-LCCN (70-30 vol.%) membranes were measured from 700 °C to 950 °C using air as the feed gas and N_2 or CO_2 as the sweep gas. Tests were performed to study the influence of (i) the thickness, (ii) the catalyst layer and (iii) the operation time, on the performances of the membrane.

Performance and stability of $(ZrO_2)_{0.89}(Y_2O_3)_{0.01}(Sc_2O_3)_{0.10}$-$LaCr_{0.85}Cu_{0.10}Ni_{0.05}O_{3-\delta}$ oxygen transport membranes under conditions relevant for oxy-fuel combustion

Stéven Pirou[a], Jose Bermudez Menendez[b], Beom Tak Na[c], Ji Haeng Yu[c], Peter Vang Hendriksen[a], Andreas Kaiser[a], Tomás Ramirez Reina[b1], Marcos Millan[b], Ragnar Kiebach[a].

[a] Department of Energy Conversion and Storage, Technical University of Denmark, Risø campus, Frederiksborgvej 399, DK-4000 Roskilde, Denmark

[b] Department of Chemical Engineering, Imperial College London, South Kensington Campus, London SW7 2AZ, United Kingdom

[c] Separation and Conversion Materials Laboratory, Korea Institute of Energy Research, 152 Gajeong-ro, Daejeon 34129, Republic of Korea

[1] T.R.Reina present address: Department of Chemical & Process Engineering, University of Surrey, Guildford, GU2 7HX, United Kingdom

E-Mail addresses: stepir@dtu.dk, j.bermudez-menendez@imperial.ac.uk, beomtakna@gmail.com, jhyu@kier.re.kr, pvhe@dtu.dk, akai@dtu.dk, t.ramirezreina@surrey.ac.uk, marcos.millan@imperial.ac.uk, woki@dtu.dk

Abstract

Dual-phase oxygen transport membranes consisting of 70 vol.% $(ZrO_2)_{0.89}(Y_2O_3)_{0.01}(Sc_2O_3)_{0.10}$ (10Sc1YSZ) and 30 vol.% $LaCr_{0.85}Cu_{0.10}Ni_{0.05}O_{3-\delta}$ (LCCN) were successfully developed and tested. The stability of the composite membrane was studied in simulated oxy-fuel power plant flue-gas conditions (CO_2, SO_2, H_2O). The analyses of the exposed composites by X-ray diffraction (XRD), X-ray fluorescence (XRF), attenuated total reflection Fourier transform infrared spectroscopy (ATR-FTIR) and Raman spectroscopy revealed excellent stability. Oxygen permeation fluxes across 1000 µm thick and 110 µm thick self-supported 10Sc1YSZ-LCCN (70-30 vol.%) membranes were measured from 700 °C to 950 °C using air as the feed gas and N_2 or CO_2 as the sweep gas. The 110 µm thick membrane, prepared by tape-casting and lamination processes, showed oxygen fluxes up to 1.02 $mL_N\ cm^{-2}\ min^{-1}$ (950 °C, air/N_2). Both membranes demonstrated

stable performances over long-term stability tests (250-300 h) performed at 850 °C using pure CO_2 as the sweep gas.

Keywords

Oxygen transport membrane, Dual-phase membrane, CO_2 stability, SO_2 tolerance, Oxy-fuel combustion

1. Introduction

Now and in the coming decades, one of the most important challenges for our society is to reduce greenhouse gas emissions, responsible for global warming. The dominating sources of anthropogenic CO_2 emission are use of fossil fuel in the energy and transport sector and industrial production of cement iron and steel [1]. To reduce these emissions, Carbon Capture and Utilization (CCU) or Storage (CCS) are important concepts currently under development. There are three fundamentally different approaches to carbon capture from point sources: pre-combustion separation, post-combustion separation and oxy-fuel combustion. In the latter one uses pure oxygen to combust the fossil fuel, resulting in flue-gases consisting mainly of CO_2 (90 – 95 %) and steam. The CO_2 can then be captured much more easily than when air is used in the combustion process resulting in a flue gas lean in CO_2 (10 – 14 % in dried gas) [2]. The oxygen required for the oxy-fuel process can be produced by several methods all of which require energy. Producing the oxygen locally via *oxygen transport membranes* (OTMs) that are both thermally and chemically integrated in the oxy-fuel process results in the lowest overall efficiency losses [3, 4]

OTMs are typically made of Mixed Ionic Electronic Conductors (MIEC). Such materials allow simultaneous transport of oxygen (via oxygen vacancies in the crystal lattice) and electrons. The membranes are fully dense which results in very high selectivity in the separation. An oxygen partial pressure differential between an oxidizing gas (air at 0.21 atm) and a reducing gas (recirculated flue gas at $pO_2 \approx 10^{-2}$ atm [5]) exists across the membrane and serves as the driving force for the oxygen transport. To reduce cost and maximize efficiency it is beneficial to directly integrate the OTMs in the oxy-fuel process, which entails that the membranes are exposed directly to recirculated flue-gases at the permeate side of the membrane. This imposes very stringent requirements to the membrane materials, specifically requiring chemical stability in CO_2, SO_2 and H_2O which are inevitable constituents/impurities arising from the combustion of fossil fuels**.** In literature, the OTMs materials achieving the highest oxygen fluxes are based on single-phase MIEC materials**,** such as $Ba_{1-x}Sr_xCo_{1-y}Fe_yO_{3-\delta}$ (BSCF) and $La_{1-x}Sr_xCo_{1-y}Fe_yO_{3-\delta}$ (LSCF) [6 – 15]. However, most of these materials, which show good transport properties, are not chemically stable in atmospheres containing CO_2 and SO_2 [9, 16 – 22] and are, therefore, not suitable for direct integration in oxy-fuel combustion power plants. Membranes prepared from two

thermodynamically very stable materials; one of which is an ionic conductor and one an electronic conductor is an interesting alternative to overcome the stability limitations of single-phase membrane materials in CO_2 and SO_2.

In this study, dual-phase membranes consisting of 70 vol.% $(Y_2O_3)_{0.01}(Sc_2O_3)_{0.10}(ZrO_2)_{0.89}$ and 30 vol.% $LaCr_{0.85}Cu_{0.10}Ni_{0.05}O_{3-\delta}$ (10Sc1YSZ-LCCN (70-30 vol.%)) were prepared and tested with respect to chemical stability and oxygen transport properties under conditions simulating direct integration in oxy-fuel combustion power plants.

Yttria-stabilized zirconia ($(ZrO_2)_{1-x}(Y_2O_3)_x$ (YSZ)) has previously been studied as the ionic conductor in composite OTMs due to its high ionic conductivity, its high stability at high temperature in both oxidizing and reducing atmospheres, and its good mechanical properties [23 – 25]. The highest ionic conductivity for $(ZrO_2)_{1-x}(Y_2O_3)_x$ electrolytes is observed for x= 0.08 (8YSZ). At 850 °C the conductivity is 0.03 $S.cm^{-1}$ [26]. However, higher ionic conductivity can be reached by co-doping of scandium and yttrium in zirconia. At 850 °C Artemov *et al.* reported an ionic conductivity of 0.12 $S.cm^{-1}$ for $(Y_2O_3)_{0.01}(Sc_2O_3)_{0.10}(ZrO_2)_{0.89}$ (10Sc1YSZ) [27]. Moreover, a recent study has demonstrated excellent stability of 10Sc1YSZ under CO_2, SO_2 and H_2O containing atmospheres [28].

Lanthanum chromite is a very stable compound, which has been studied as ceramic interconnect material in solid oxide fuel cells [29 – 33]. It is a fair p-type electronic conductor [33 – 36], it is chemically compatible with zirconia, and is therefore a candidate for the electronic conductor in a dual-phase membrane designed for integration into oxy-fuel combustion power plants. The conductivity of pure lanthanum chromite is rather low (0.96 S cm^{-1} at 800 °C in air, [37]) but it can be increased through doping. The substitution of Cr with aliovalent transition metals like Cu or Ni is expected to increase the electronic conductivity as also reported in a few studies [38 – 40].

The stability of the 10Sc1YSZ-LCCN was investigated on loose powder under simulated oxy-fuel combustion conditions (CO_2, SO_2, H_2O). Analytical techniques such as X-ray diffraction (XRD), X-ray fluorescence (XRF), attenuated total reflection Fourier transform infrared spectroscopy (ATR-FTIR), Raman spectroscopy and scanning electronic microscopy with energy dispersive X-ray spectroscopy (SEM-EDX) were used to characterize the material after exposure to the gases. The performance of the composite for transporting oxygen was evaluated by oxygen permeation measurements. The influence of

(i) the membrane thickness, (ii) catalyst activation layers on the membrane surface, and (iii) operation time on the oxygen permeation flux through the membranes was investigated.

2. Experimental

2.1. Thermochemical stability and characterization of 10Sc1YSZ-LCCN composite

2.1.1. Thermochemical stability tests

The thermochemical stability of 10Sc1YSZ-LCCN (70-30 vol.%) powder in the presence of CO_2, SO_2 and H_2O was tested at 850 °C in an up-flow vertical testing unit. Loose powders were used to maximize the contact area between the composite and the gases. The unit is based on a quartz tube equipped with a liner with a porous sample holder which facilitates an even distribution of the gas. A detailed description can be found elsewhere [28]. For each run, 1 g of fresh 10Sc1YSZ-LCCN (70-30 vol.%) powder that was placed on the holder. A thermocouple was located within the bed of material to monitor the temperature. Once the sample was loaded, the testing unit was introduced in an oven and heated up to 850 °C under a stationary air atmosphere. At 850 °C, the gas composition was switched to the different mixtures of CO_2/SO_2/H_2O, according to the compositions shown in Table 5. 5. This table also shows the total amount of sulfur seen by the samples in each of the experiments where SO_2 was supplied. The quantity of sulfur in contact with the sample was intentionally used in excess in order to easily detect possible reactions between SO_2 and the membrane materials during the analyses. Blank runs under air atmosphere and CO_2 were also performed. Two gas cylinders were used for preparing the gas mixtures, one with CO_2 (purity > 99.8 %) and one with a mixture of 2000 ppm of SO_2 balanced with CO_2. An evaporator, fed by a syringe pump to control the amount of water added, was used to generate the steam in the experiments performed under humid conditions. The experiments were performed at atmospheric pressure using a gas flow rate of 0.25 L_N min^{-1} during 8 h. The exhaust gases were cooled down to room temperature to remove steam before passing through two saturated NaOH solutions with the aim of removing SO_2 prior to their disposal. Once the experiment was finished, the testing unit was quenched under the reaction atmosphere with the objective of avoiding the presence of oxygen which would lead to the decomposition of

species formed during the treatments. Finally, the treated material was recovered for characterization.

Table 5. 5: Gas compositions used in the thermochemical stability tests performed on 10Sc1YSZ-LCCN (70-30 vol.%) powder. Tests were performed for 8 h at 850 °C and atmospheric pressure using a gas flow rate of 0.25 L_N min^{-1}.

Test	CO_2 (vol.%) (1)	SO_2 (ppm v/v) (1)	H_2O (vol.%) (2)	pO_2 (atm)	Total sulfur (g) (3)
Blank(4)	0	0	0	0.21	0
CO_2	100	0	0	$<5\cdot10^{-6}$	0
500SO_2	Balance	500	0	$<5\cdot10^{-6}$	0.0
500SO_2 10H_2O	Balance	500	10	$<5\cdot10^{-6}$	0.08
2000SO_2 10H_2O	Balance	2000	10	$<5\cdot10^{-6}$	0.32
500SO_2 30H_2O	Balance	500	30	$<5\cdot10^{-6}$	0.08

(1) Dry basis; (2) Percentage of the total flow, including steam; (3) Total sulfur seen by the sample in the treatment; (4) Performed in air

2.1.2. Material characterization

Before and after the gas exposure treatment, the 10Sc1YSZ-LCCN (70-30 vol.%) powders were characterized by a series of analytical techniques to detect and identify changes induced by the exposure.

X-ray diffraction (XRD) patterns were obtained in a PANalytical diffractometer equipped with a Ni-filtered Cu Kα radiation (40 mA, 45 kV) over a 2Θ-range of 5 to 80º and a position-sensitive detector using a step size of 0.05º and a step time of 120 s. The patterns were processed with the aim of identifying the species present in the samples, using the software X'Pert Highscore Plus.

X-ray fluorescence (XRF) and elemental analysis were performed to determine the chemical composition of the samples. XRF spectra were obtained in a PANalytical Epsilon3XLE X-ray fluorescence spectrophotometer with a 50 kV silver anode tube as source of radiation. Elemental analysis was performed in an Elementar Vario Microcube, using a combustion chamber that works up to 1800 °C. The gases leaving the combustion chamber are

absorbed in a trapping column and are then desorbed following a temperature program to be detected using a thermal conductivity detector.

Attenuated total reflection Fourier transform infrared spectroscopy (ATR-FTIR) analyses was performed using a Perkin Elmer FTIR 100 spectrometer. Spectra were collected at room temperature and baseline-corrected using the Spectrum 10™ software.

A Renishaw InVia Raman spectrometer equipped with a charge-coupled device and a Leica microscope was used for collecting Raman spectra. A 785 nm HPNIR diode laser with maximum power of 300 mW was used as an excitation source. A 1200 mm^{-1} grating was utilised for all measurements, providing a spectral resolution of +/- 1 cm^{-1}. The laser spot was focused on the sample surface using a long working distance 50x. The laser beam spot size was around 1.28 µm.

A JEOL JSM6400 operated at 20 kV equipped with energy dispersive X-ray spectroscopy (EDX) and a wavelength dispersive X-ray spectroscopy (WDS) systems was used for the microstructural/chemical characterization (SEM with EDX and WDS).

2.2. Membrane preparation

Thick (1000 µm) and thin (110 µm) self-supported membranes made of 70 vol.% $(Y_2O_3)_{0.01}(Sc_2O_3)_{0.10}(ZrO_2)_{0.89}$ - 30 vol.% $LaCr_{0.85}Cu_{0.10}Ni_{0.05}O_{3-\delta}$ (10Sc1YSZ-LCCN (70-30 vol.%)) were prepared using two different procedures as described below.

2.2.1. Thick membrane

The $LaCr_{0.85}Cu_{0.10}Ni_{0.05}O_{3-\delta}$ (LCCN) powder was prepared in-house via a nitrate-glycine synthesis [41] using a stoichiometric amount of nitrate precursors ($La(NO_3)_3 \cdot 6H_2O$, $Cr(NO_3)_3 \cdot 9H_2O$, $Cu(NO_3)_2 \cdot 6H_2O$ and $Ni(NO_3)_2 \cdot 6H_2O$) and glycine powder. Subsequently, the powder was calcined at 1200 °C for 3 h in air (heating/cooling ramp = 100 °C h^{-1}). The 10Sc1YSZ powder was purchased from Tosoh Daiichi Kigenso Kagaku Kogyo Co. Ldt (Japan). The ionic and electronic conductors were mixed in a 70/30 volume ratio to form the 10Sc1YSZ-LCCN (70-30 vol.%) composite material. A small amount (3 vol.%) of NiO (Alfa Aesar, United States), was mixed with the composite material to serve as sintering aid during the membrane preparation. The particles size of the powders were adjusted to the submicron range (d_{v50}<1 µm) using ball-milling in ethanol. After drying, a 15 mm diameter

membrane was formed using a uniaxial press (1000 kg load). The membrane was sintered at 1400 °C for 6 h in air. After sintering, the membrane was polished down to 1000 µm thick and an in-house prepared ink of $(Y_2O_3)_{0.08}(ZrO_2)_{0.92}$ - $(La_{0.80}Sr_{0.20})MnO_{3-\delta}$ (8YSZ-LSM (50-50 vol.%)) was screen-printed on both sides of the membrane to serve as oxygen oxidation/reduction catalyst. Finally, the membrane was heated to 980 °C for 2 h in air in order to dry the printed catalyst and make it adhere to the membrane surface.

2.2.2. Thin membrane

110 µm thick membranes were developed by a tape-casting and lamination process. Tape-casting presents the advantage of being a well-established and relatively simple technique with a low implementation cost to obtain planar ceramic sheets with a large area, good surface quality and controlled microstructures. The $LaCr_{0.85}Cu_{0.10}Ni_{0.05}O_{3-\delta}$ powder used for the preparation of the 110 µm thick membranes was purchased from Cerpotech (Norway). 10Sc1YSZ, LCCN and NiO powders were mixed by ball-milling for 48 h with appropriate amounts of solvents (ethanol, acetate) and organic additives (dioctyl phthalate, PVB-76, BYK-103) to form the required slurry for tape-casting. The slurry was cast using a doctor blade gap of 300 µm. After drying, the green tape was cut and multiple layers of tape were laminated at 70 °C under a pressure of 40 MPa in by a warm isostatic press (WIP) to obtain the desired thickness of membrane. Subsequently, 25 mm diameter disks were cut out using a laser cutter (LTT, Taiwan) and sintered using a two-step process including a peak temperature of 1500 °C (3 min) and a dwell temperature of 1450 °C (3 h). Heating ramps of 60 °C h^{-1} and 300 °C h^{-1} were used from room temperature to 1200 °C and from 1200 °C to 1500 °C, respectively. Cooling ramps of 300 °C h^{-1} and 180 °C h^{-1} were applied from 1500 °C to 1450 °C, and from 1450 °C to room temperature. As for the 1000 µm thick membrane, 8YSZ-LSM (50-50 vol.%) was applied on both sides of the membrane and dried using a heat treatment at 980 °C for 2 h in air.

2.3. Oxygen flux measurements

Oxygen permeation measurements were carried out in a membrane test rig described elsewhere [28]. Air was used on the feed side with a flow rate of 200 mL_N min^{-1}, while N_2 or CO_2 was fed as a sweep gas on the permeate side using various flow rates in the range from 20 mL_N min^{-1} to 200 mL_N min^{-1}. Inlet gases were individually controlled and monitored

by mass flow controllers (Brooks), while the outlet flow of the permeate side was determined by a mass flow meter (Bronkhorst). Thermocouples were placed in direct contact with the membrane in order to monitor the temperature. The membranes were sealed between two alumina tubes using tape-cast aluminosilicate glass rings (NAS, Na_2O: 17.8 mol.%, Al_2O_3: 9.4 mol.% and SiO_2: 72.8 mol.% [42]), with an inner diameter of 9 mm, an outer diameter of 14 mm. The glass transition temperature of the applied glass is 515 °C [43]. The exterior surface of the samples was also coated with NAS paste to ensure that there are no gas leaks from the surrounding atmosphere into the sweep chamber. The sealing procedure was completed prior to the measurements by heating the membranes to 950 °C in air for 1 h before cooling down to 750 °C to conduct the flux measurements. No gas was fed during the sealing procedure and slow heating/cooling ramps were used (30 °C h^{-1}). A gas chromatograph was connected to the outlet of the permeate side to quantify any oxygen leaks into the permeate stream (oxygen (and nitrogen) that enters the permeate compartment via pinholes or insufficient sealing at the membrane periphery). Zirconia-based pO_2 sensors built in-house were used to determine the pO_2 of the inlet gas on the permeate side (before feeding to the membranes) and of the outlet gas (after passing over the membrane). The oxygen permeation flux was deduced from the pO_2 difference between the inlet and the outlet of the gas flowing on the permeate side:

$$J_{O_2} = \frac{pO_{2,permeate}^{out} \cdot \dot{n}^{out} - pO_{2,permeate}^{in} \cdot \dot{n}^{in}}{A} \quad (1)$$

where J_{O_2} is the oxygen permeation flux, $pO_{2,permeate}^{in}$ and $pO_{2,permeate}^{out}$ are respectively the oxygen partial pressures in the inlet and outlet gases on the permeate side, $\dot{n}^{in}$ and $\dot{n}^{out}$ are molar flow rates of inlet and outlet gases, respectively, and A is the net area of the permeate side of the membrane. The Nernst equation (2) was used to calculate the oxygen partial pressure from the measured sensor voltage (V):

$$pO_2 = pO_{2,ref} . e^{\frac{4FV}{RT}} \quad (2)$$

where V is the open-circuit voltage of the oxygen sensor, $pO_{2,ref}$ is the oxygen partial pressure at the reference electrode (maintained at 0.21 atm during the measurements), and T is the temperature of the oxygen sensor.

3. Results and discussion

3.1. Chemical stability of 10Sc1YSZ-LCCN under conditions relevant for oxy-fuel combustion

Figure 5. 31 shows results of the XRD characterization of the composite material before and after exposure to different concentrations of impurity gases. The XRD patterns of the untreated sample show a combination of Sc and Y doped ZrO_2 and $LaCr_{0.85}Cu_{0.1}Ni_{0.05}O_{3-\delta}$ peaks. The XRD patterns of the treated samples are comparable; no additional peaks or changes in intensity were found, indicating that no new crystalline phases, within the detection limits (< 2 %) of the technique, are formed.

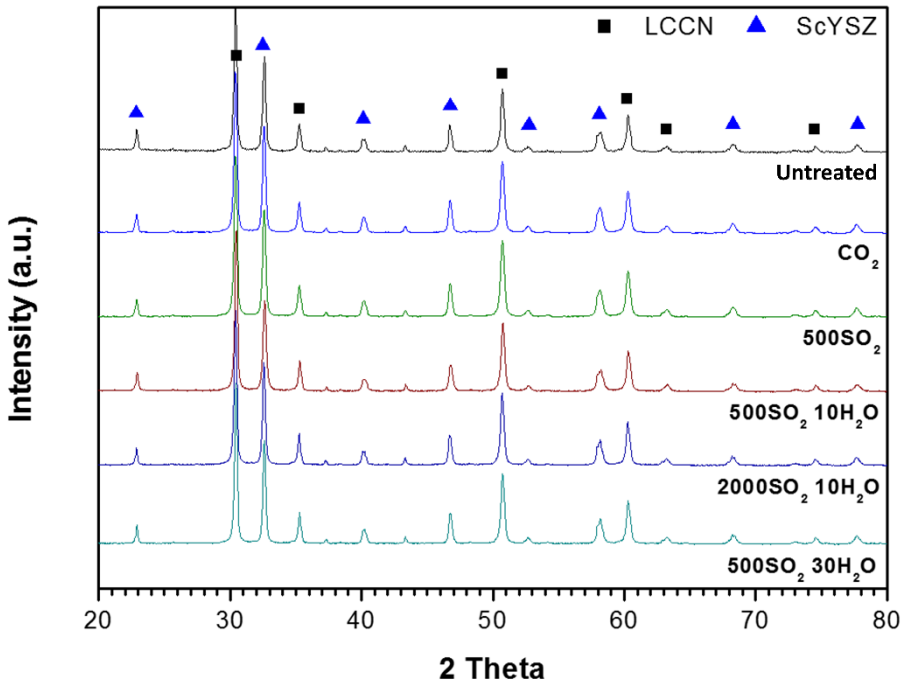

Figure 5. 31: XRD patterns of the 10Sc1YSZ-LCCN (70-30 vol.%) fresh (black), treated with pure CO_2 (blue), treated with 500 ppm of SO_2 in CO_2 (green), treated with 500 ppm of SO_2 in CO_2 and 10 % of steam (brown), treated with 2000 ppm of SO_2 in CO_2 and 10 % of steam (dark blue), and treated with 500 ppm of SO_2 in CO_2 and 30 % of steam (cyan).

However, X-ray diffraction is not sensitive to small amounts of second phases and is not able to detect non-crystalline species. For this reason, complementary characterization needed to be done before concluding that no new phases have formed on exposure. Raman and ATR-FTIR spectroscopies were used for this purpose. Figure 5. 32 shows the ATR-FTIR and Raman spectra of treated and untreated samples. In the case of the FTIR, the spectrum of the untreated sample is almost flat. After the treatments, the shape of the

spectra does not vary, conserving the flat profile. The presence of new species in form of carbonates can be excluded due to the absence of signals in the range of 850-900 cm^{-1} and/or 1400-1600 cm^{-1} [44 – 46]. Also no newly formed sulfates, which would have led to signals in the range from 900-1300 cm^{-1}, were found [44, 47 – 49]. Raman spectra of the treated samples did not show any additional signals when compared to the spectrum of the untreated 10Sc1YSZ-LCCN (70-30 vol.%), further indicating that neither carbonates (recognizable by signals in the range of 100-300 cm^{-1} and 1000-1100 cm^{-1}) nor sulfates (recognizable by signals in the range of 900-1000 cm^{-1}) [50 – 55] have formed.

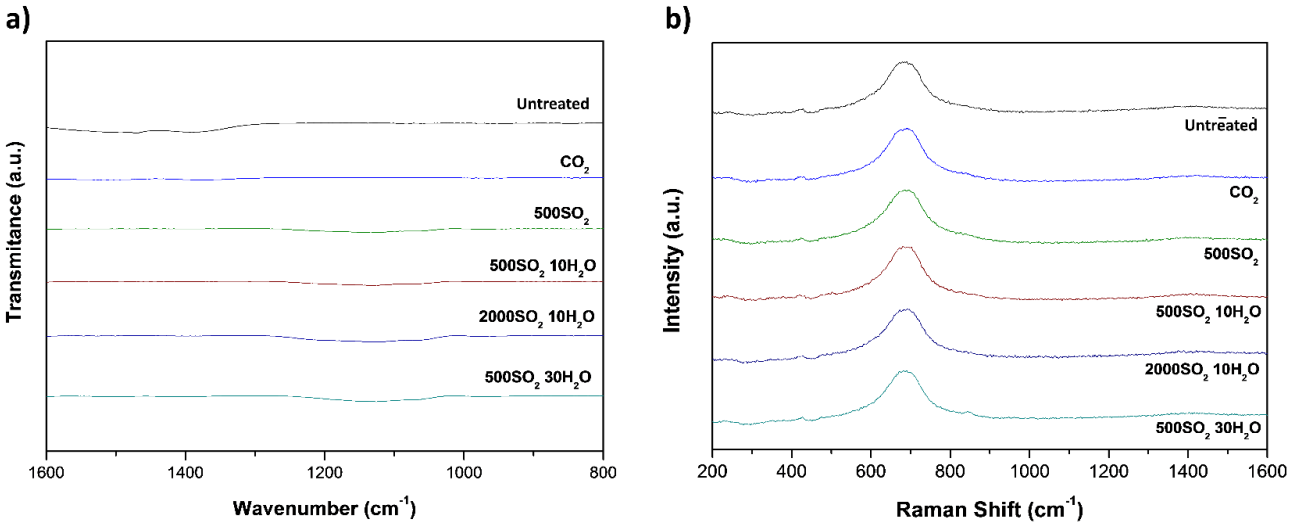

Figure 5. 32: a) ATR-FTIR spectra; and b) Raman spectra of the 10Sc1YSZ-LCCN (70-30 vol.%) fresh (black), treated with pure CO_2 (blue), treated with 500 ppm of SO_2 in CO_2 (green), treated with 500 ppm of SO_2 in CO_2 and 10 % of steam (brown), treated with 2000 ppm of SO_2 in CO_2 and 10 % of steam (dark blue) and treated with 500 ppm of SO_2 in CO_2 and 30 % of steam (cyan).

XRF and elemental analysis were performed to confirm the absence of carbon and sulfur in the samples, thus discarding the incorporation of these elements in other species that could not be detected by XRD or vibrational spectroscopy. Neither Carbon nor Sulfur was detected by any of these techniques. Finally, SEM-WDS analyses were performed on the sample treated with the higher concentration of SO_2 in the gas (Supplementary Material (Figure 5. 38)). It can be seen that the signal of sulfur is even lower than the signal corresponding to the background of Zr, thus discarding the presence of sulfur in the treated sample.

The chemical characterization performed for the treated and untreated samples confirmed the absence of secondary phases in the samples post-treatment, proving the excellent stability of this composite in the tested environments. These results suggest that 10Sc1YSZ-

LCCN (70-30 vol.%) in terms of stability is a good candidate for use in OTMs to be directly integrated in an oxy-fuel combustion processes.

3.2. Membrane microstructure

Figure 5. 33 shows SEM images of cross-sections of 1000 µm thick membranes (Figures 5. 33.a, 5. 33.c and 5. 33.e) and 110 µm thick membranes (Figures 5. 33.b, 5. 33.d and 5. 33.f) before and after the permeation tests. Figures 5. 33.a and 5. 33.b present the microstructures of the membranes before that 8YSZ-LSM (50-50 vol.%) was coated on both sides of the membranes to serve as oxygen oxidation/reduction catalyst, while Figures 5. 33.c, 5. 33.d, 5. 33.e and 5. 33.f display the microstructures of the membranes after tests. No degradation of the microstructures was observed. The brightest phase in the SEM images corresponds to LCCN, while 10Sc1YSZ appears slightly darker and NiO can be assigned to the darkest one. The porosity of the membranes was determined by image analysis and corresponds to 2 vol.% and 6.5 vol.% for the 1000 µm thick and the 110 µm thick membranes, respectively. The closed pores of the 110 µm thick membrane have an average diameter of approximately 3 µm. The difference in porosity between the 1000 µm thick membrane and the 110 µm thick membrane results from the different shaping techniques used. A higher densification was obtained for the1000 µm thick membranes (conventional sintering 1400 °C for 6 h) because the membranes were prepared by powder pressing, a method that results in a very high green density. On the other hand, tape-cast membranes have a significantly lower green density due to organic additives, and require higher temperatures to be sintered. In addition, $LaCrO_3$-based materials have poor sinterability due to volatilization of chromium vapor species above 1000 °C creating pores on the sides of the membranes [40, 56 – 58]. As a result, conventional sintering could not be used to obtain gastight 110 µm thick membranes while at the same time avoiding the chromium volatilization. The two-step sintering process used (peak temperature 1500 °C (3 min), dwell temperature 1450 °C (3 h)), helped to maximize the densification of the 10Sc1YSZ-LCCN membranes while keeping the chromium content in the LCCN phase.

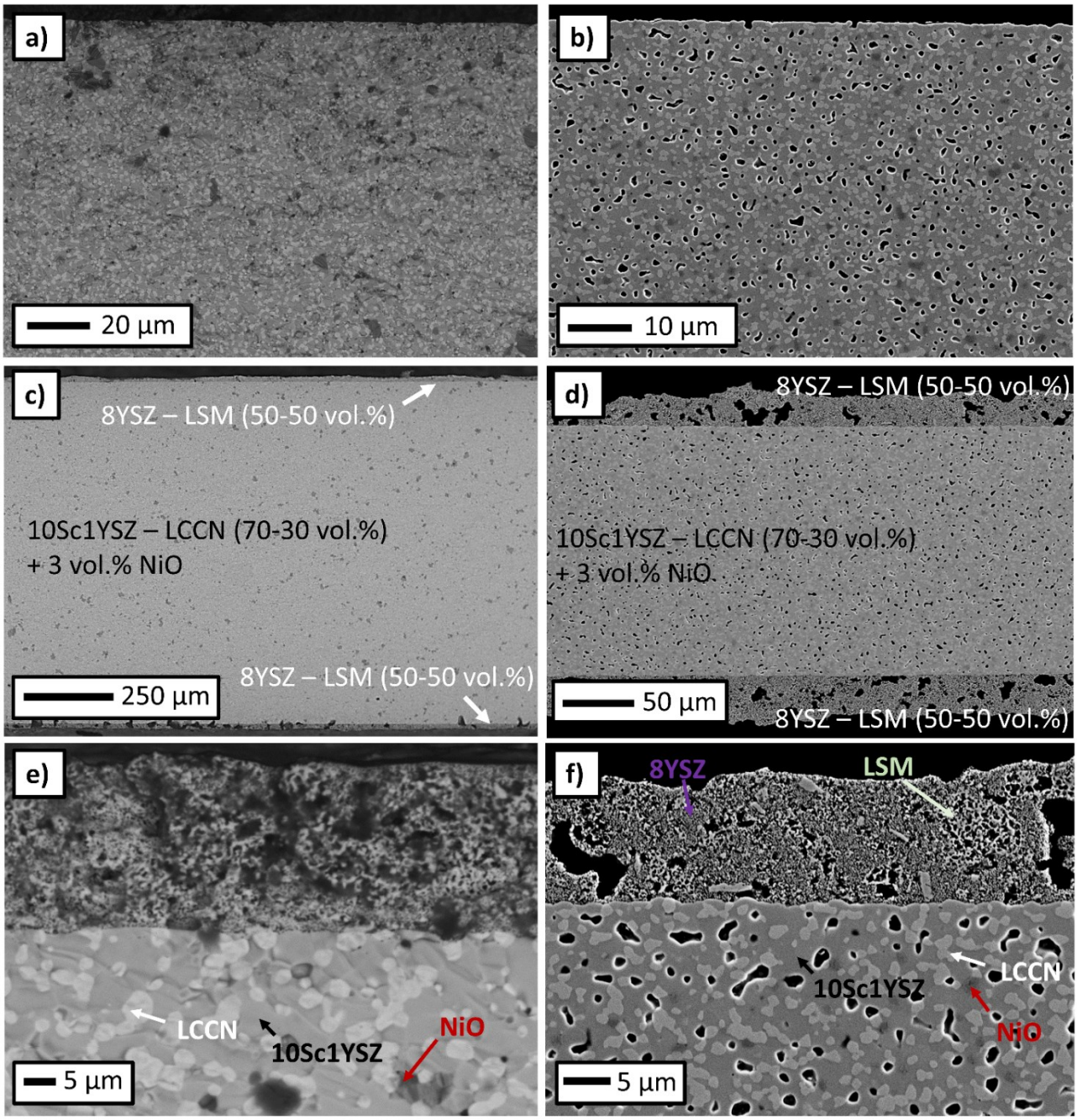

Figure 5. 33: SEM pictures of the polished cross-sections of 1000 µm thick (a, c, e) and 110 µm thick (b, d, f) 10Sc1YSZ-LCCN membranes. Figures a and b show the microstructures of the membranes before oxygen permeation tests while Figures c, d, e and f are post-mortem SEM pictures.

3.3. Oxygen permeation

This section shows how the membrane thickness (section 3.3.1.), the catalytic activation layers (section 3.3.2.) and the exposure time in CO_2 (section 3.3.3.) influence the oxygen permeation flux of the 10Sc1YSZ-LCCN membranes.

3.3.1. Influence of the membrane thickness on the oxygen permeation flux

Figure 3. 34 presents the oxygen permeation fluxes through the 1000 µm thick (black symbols) and the 110 µm thick (red symbols) membranes in the temperature range of 700-950 °C. The membranes were coated on both sides with 8YSZ-LSM (50-50 vol.%) porous activation layers to enhance the rate of the oxygen exchange reactions (oxidation/reduction) taking place at the surfaces. The figure reports oxygen permeation fluxes obtained using 200 $mL_N\ min^{-1}$ of air as the feed gas, and the same flow of N_2 (solid symbols) or CO_2 (empty symbols) as sweep gas. The highest performances were obtained in air/N_2 at 950 °C, and fluxes of 0.27 $mL_N\ cm^{-2}\ min^{-1}$ and 1.02 $mL_N\ cm^{-2}\ min^{-1}$ were recorded for the 1000 µm thick and the 110 µm thick membranes, respectively. Slightly lower oxygen fluxes were measured in CO_2 compared to N_2 sweep. Comparable results were reported in other studies [17, 59 – 64] where it was suggested that this phenomenon is a consequence of suppressed oxygen surface exchange rate due to the chemisorption of CO_2 on the surface possibly blocking some oxygen vacancies [17, 63]. As predicted by the Wagner equation (supplementary material: Figure 5. 39 and Section S 1), the thinner membrane (110 µm thick) showed a higher performance in the complete temperature range studied. However, it performs only 2 to 4 times better than the 1000 µm thick membrane, while the ratio of their thicknesses is about 9. These results indicate that the oxygen permeation through the 110 µm thick membrane is not exclusively limited by the diffusion of the oxide ions in the bulk.

Figure 5. 35 shows the oxygen permeation fluxes through the two membranes in the temperature range of 700 – 950 °C for different N_2 flow rates (sweep gas). The results indicate Arrhenius behavior although the activation energy (E_a) for the oxygen transport changed as a function of the temperature in the case of the 110 µm thick membrane (Figure 5. 35.a), which suggests that the rate-limiting step changes with temperature.

The surface exchange kinetics possess a higher activation energy than solid-state diffusion, resulting in higher apparent activation energy in the low-temperature region. For temperatures below 900 °C, the activation energy of the oxygen transport was estimated to be 89.8 – 94.7 $kJ\ mol^{-1}$. These values suggest that surface exchange kinetics are the main limiting factor of the oxygen permeation. Another hypothesis could be that the oxygen flux is limited by the (bulk) diffusion in the 8YSZ-LSM catalytic layers. One indication for this theory could be that the E_a values obtained are in close agreement with the activation energy

associated with the oxygen vacancy diffusion in 8YSZ-LSM (50-50 vol.%) porous active layers, which was reported to be 92 kJ mol^{-1} when the composite was sintered at 980 °C [65]. The values also correspond to the activation energy of oxide ion conduction in 8YSZ stated in the literature (from 85 kJ mol^{-1} to 99 kJ mol^{-1} [66 – 68]). On the other hand, for temperatures above 900 °C, the activation energy of the oxygen transport was evaluated between 51.1 and 60.5 kJ mol^{-1}. These values are in good accordance with the activation energy of the ionic conductivity of 10Sc1YSZ published by Irvine (62.7 kJ mol^{-1} in the temperature range 700 – 950 °C [69]). Figure 5. 35.b shows the Arrhenius plot of the 1000 µm thick membrane presenting a single range of activation energy (51.1 – 53.5 kJ mol^{-1}) from 700 °C to 950 °C. As expected, the diffusion of the oxide ions through the bulk of the membrane is the rate limiting-step in the entire temperature range investigated. The nature of the processes limiting the oxygen permeation flux at these temperatures (700 – 950 °C) does not seem to be significantly influenced by the sweep gas flow rate, since no important variation in E_a is observed. To summarize; in the complete temperature range studied the oxygen permeation of the thickest membrane (1000 µm) is limited by the bulk diffusion in the 10Sc1YSZ-LCCN membrane while for the thinner membrane (110 µm) the oxygen permeation is mainly limited by the surface exchange kinetics or bulk diffusion into the catalytic activation layers at low temperatures (T < 900 °C) and by the bulk diffusion in the membrane at high temperatures (T > 900 °C).

Accordingly, to further improve the oxygen permeation through 10Sc1YSZ-LCCN membranes, it is necessary to both decrease the bulk limitation and improve the surface exchange kinetics. The development of thin asymmetric membranes which combine a relatively thick porous support (300 – 1000 µm for mechanical stability) and a thin dense membrane layer (10 – 30 µm) may be an ideal solution to circumvent bulk diffusion limitations [8]. To overcome surface exchange kinetics limitations one could further infiltrate a suitable nano-particulate catalysts in the support layers of the asymmetric membranes. This technique has been successfully applied in previous studies [70 – 72].

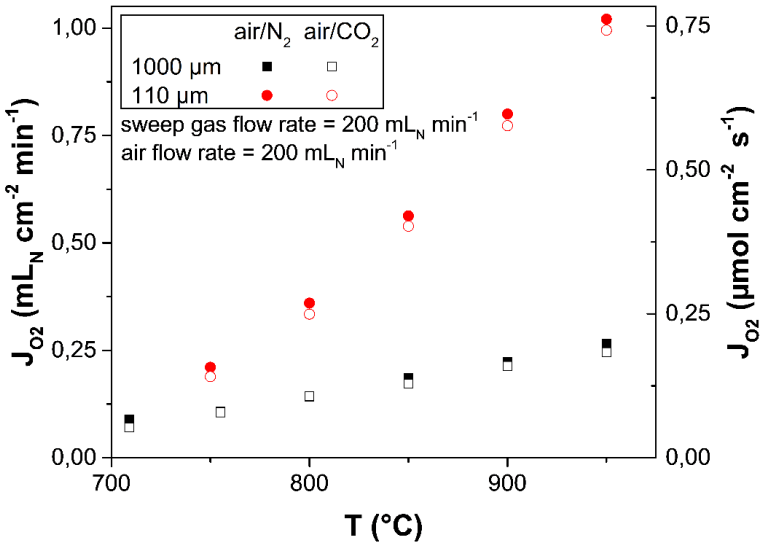

Figure 5. 34: Oxygen permeation fluxes through 1000 µm thick (black symbols) and the 110 µm thick (red symbols) 10Sc1YSZ-LCCN (70-30 vol.%) membranes in the temperature range of 700-950 °C. N_2 (solid symbols) and CO_2 (empty symbols) were used as sweep gases, while air was flowed as feed gas.

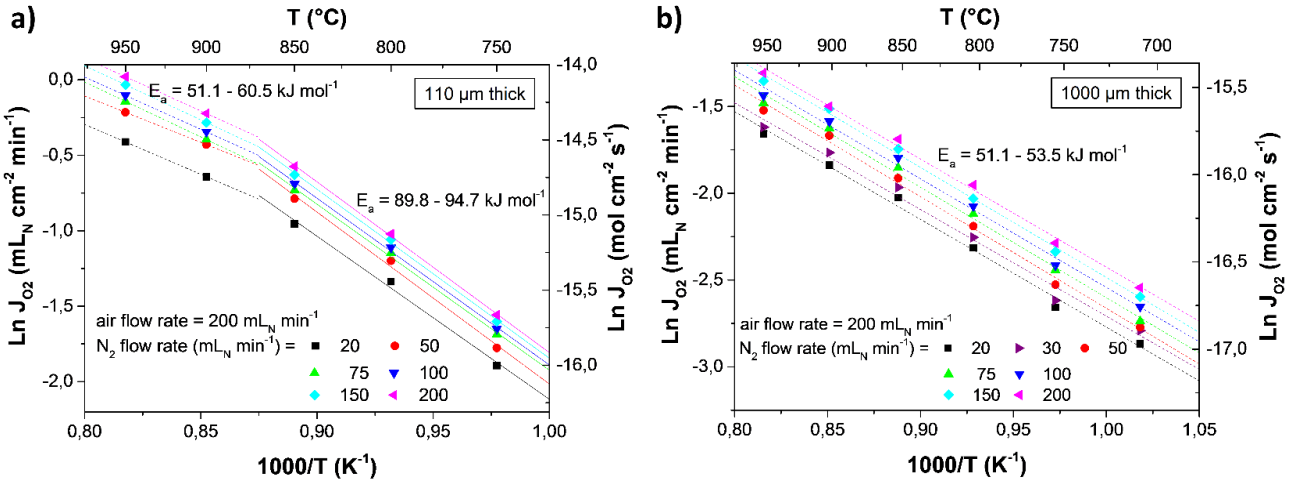

Figure 5. 35: Temperature dependence of the oxygen permeation flux through the 110 µm thick (a) and 1000 µm thick (b) 10Sc1YSZ-LCCN (70-30 vol.%) membranes coated with 8YSZ-LSM porous activation layers on both sides. 200 mL_N min^{-1} of air and 20-200 mL_N min^{-1} of N_2 were used as the feed and the sweep gases, respectively.

3.3.2. Influence of catalyst activation layers on the oxygen permeation flux

As mentioned in section 2.2., a 15 µm thick catalytic layer made of 8YSZ-LSM (50-50 vol.%) was deposited on both sides of the 110 µm dense 10Sc1YSZ-LCCN dual-phase membrane in order to enhance oxygen permeation. Figure 5. 36 illustrates the effect of the activation layers comparing the measured fluxes with and without these layers. Applying these layers results in a significant improvement of the oxygen flux. The improvement is notably higher at low temperatures (J_{O2} multiplied by 6 at 750 – 800 °C, Figure 5. 36.a). The inferior

performance of the bare membranes confirms that in these the surface exchange kinetics are limiting performance below 900 °C. At 950 °C the oxygen flux is increased by a factor of 3 with respect to the bare membrane. The lower improvement observed at higher temperatures reflects the relatively lower influences of the surface exchange at high temperature. Figure 5. 36.b compares the E_a values for the oxygen transport through the bare membrane (black) and the "activated" membrane (red). In the complete temperature range, the bare membrane presents higher activation energy than the activated membrane. This observation gives some support to the hypothesis that the activated membrane could be limited by bulk diffusion in the 8YSZ-LSM layers at low temperatures (T < 900 °C), while oxygen permeation of the bare membrane is unsurprisingly limited by surface exchange kinetics. However, the difference in activation energy could also reflect that for the bare membrane (chromite/YSZ) the incorporation reaction occurs via a different mechanisms than is the case for the activated membrane where oxygen exchange takes place at the LSM/YSZ triple phases.

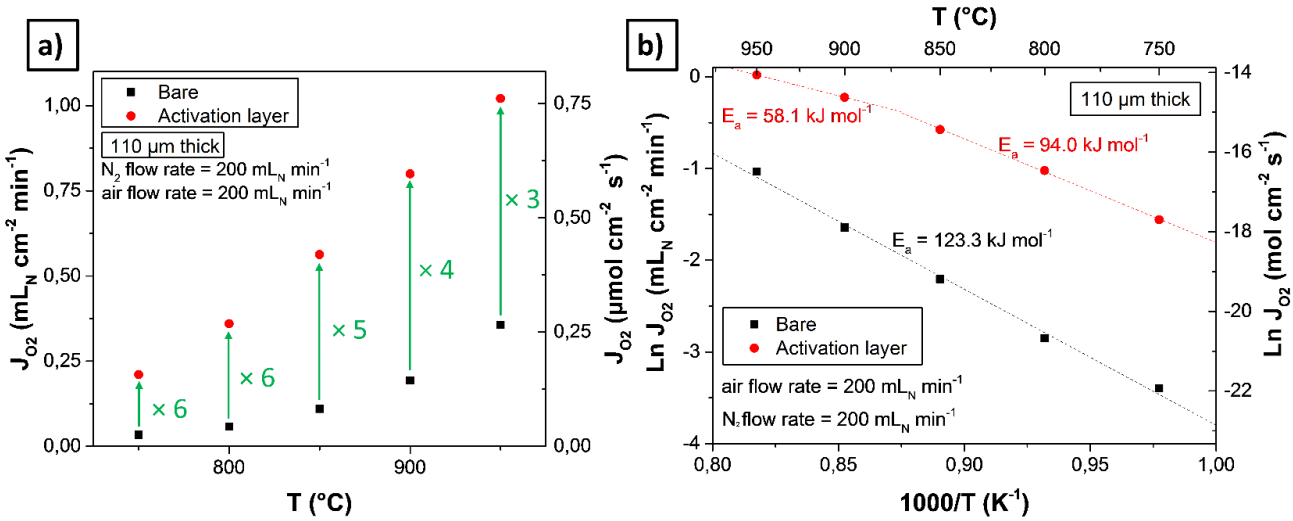

Figure 5. 36: Effect of the catalytic activation layers: Oxygen permeation flux through a 110 µm thick bare 10Sc1YSZ-LCCN membrane (black) and a 110 µm thick 10Sc1YSZ-LCCN membrane coated with 8YSZ-LSM (50-50 vol.%) activation layers on both sides (red) as a function of the temperature. 200 mL_N min^{-1} of air and 200 mL_N min^{-1} of N_2 were used as the feed and the sweep gases, respectively.

The improvement in flux falls below the expectation given by the thickness ratio between the thick and the thin sample (which would be expected **if** both membranes were bulk limited). Moreover, the flux of the thin coated membrane falls somewhat below the maximum achievable as calculated from the conductivity of zirconia, which is around 4 mL_N cm^{-2} min^{-1} at 950 °C under the pO_2 pressures here applied (see supplementary material). These two

considerations indicate that despite coating the membrane surfaces with a porous LSM/YSZ layer the losses at the surface are not negligible and that it can be possible to increase the flux further by developing a better coating.

3.3.3. Long-term stability in CO_2

To investigate the chemical and thermal long-term stability of the 10Sc1YSZ-LCCN membranes, the oxygen permeation through the 1000 µm thick membrane and the 110 µm thick membrane was measured at 850 °C, using 200 $mL_N\ min^{-1}$ of pure CO_2 as the sweep gas for 300 and 250 hours, respectively. Figure 5. 37 presents the evolution of the oxygen permeation flux for the 1000 µm thick membrane (black) and the 110 µm thick membrane (red) as a function of time. The dotted lines represent the first derivative of the oxygen flux as a function of the time. During the experiment, the oxygen permeation fluxes through the 1000 µm thick membrane and the 110 µm thick membrane decreased by 7.6 % and 6.4 %, respectively. The major part of the degradation takes place over the first 100 h of the tests (6.3 % and 6.0 % for the 1000 µm thick membrane and the 110 µm thick membrane, respectively). This degradation could be due to the initial surface oxygen desorption and the readjustment of the lattice structure of the membrane under the oxygen gradient [73]. In the remaining time the performance of the membranes was stable (0.3 to 1.3 % of degradation), thus confirming the results of the stability tests performed on 10Sc1YSZ-LCCN powder (section 3.1).

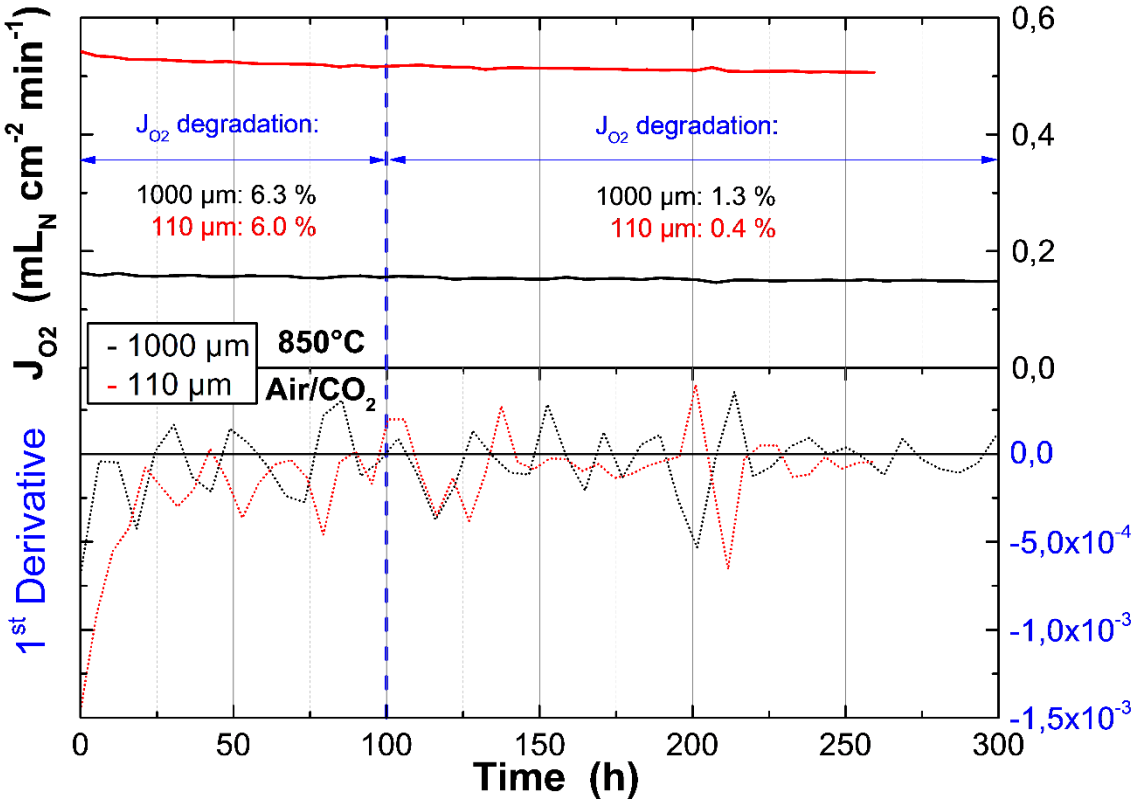

Figure 5. 37: Oxygen permeation flux through 1000 µm thick (black) and 110 µm thick (red) 10Sc1YSZ-LCCN (70-30 vol.%) membranes as a function of the time at 850 °C, with constant flows of air (feed gas, 200 mL_N min^{-1}) and CO_2 (sweep gas, 200 mL_N min^{-1}).

4. Conclusion

The stability of the dual-phase membranes made of 70 vol.% of $(ZrO_2)_{0.89}(Y_2O_3)_{0.01}(Sc_2O_3)_{0.10}$ (10Sc1YSZ) and 30 vol.% of $LaCr_{0.85}Cu_{0.10}Ni_{0.05}O_{3-\delta}$ (10Sc1YSZ-LCCN) was studied in conditions relevant to oxy-fuel combustion (CO_2, SO_2, H_2O) using several characterization techniques (XRD, XRF, ATR-FTIR and Raman spectroscopy). The tests underlined the excellent stability of the composite under application relevant atmospheres making 10Sc1YSZ-LCCN a promising dual-phase material for directly integrated OTM applications. Long-term stability tests (250 – 300 h) were performed under CO_2 (as sweep gas) and confirmed that 10Sc1YSZ-LCCN membranes produce a stable oxygen flux in CO_2 atmosphere. Oxygen permeation fluxes up to 0.27 mL_N cm^{-2} min^{-1} and 1.02 mL_N cm^{-2} min^{-1} (950 °C, air/N_2) were obtained for a thick (1000 µm) and a thin (110 µm) self-standing 10Sc1YSZ-LCCN membranes, respectively. These promising results may be further improved by the development of thin catalyst-impregnated asymmetric membranes which could be an ideal solution to overcome the main rate-limiting factors of the oxygen

permeation of the developed membranes (bulk diffusion limitations and surface exchange kinetics limitations).

SUPPLEMENTARY MATERIAL

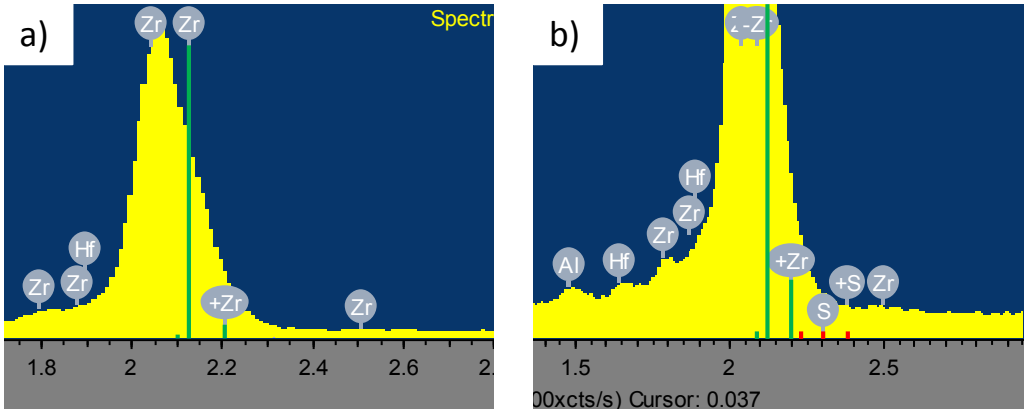

Figure 5. 38: EDX/WDS spectra of the: a) fresh 10Sc1YSZ-LCCN (70-30 vol.%); b) 10Sc1YSZ-LCCN (70-30 vol.%) treated with 2000 ppm of SO_2 in CO_2 and 10 % of steam. The results of the WDS are overlaying the EDX spectra (with a different scale). The green lines represent the signal (central line) and backgrounds (lateral lines) corresponding to Zr while the red signals represent signal and backgrounds of S.

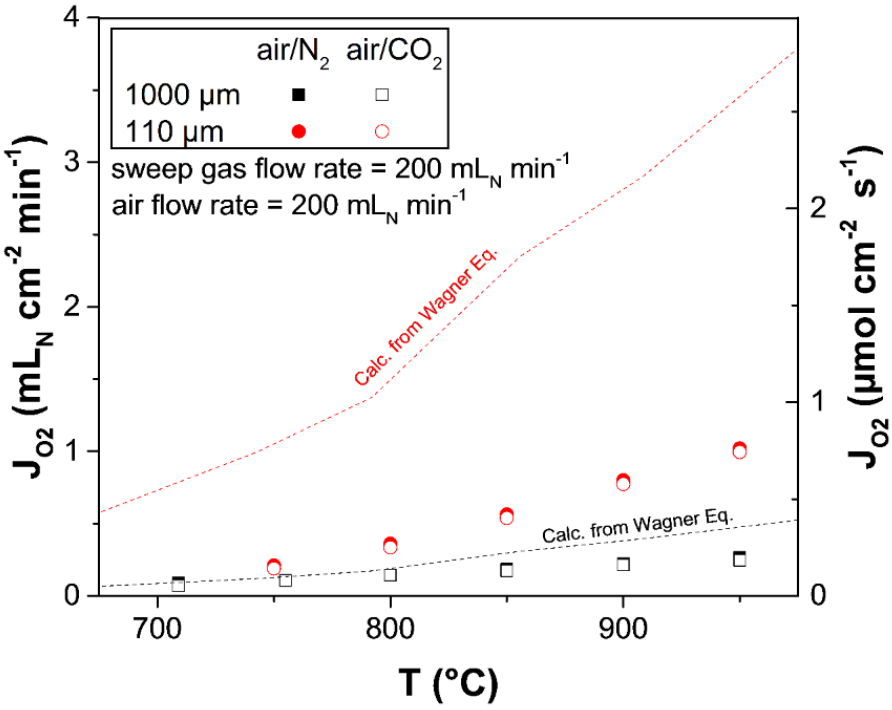

Figure 5. 39: Oxygen permeation fluxes through 1000 µm thick (black symbols) and the 110 µm thick (red symbols) 10Sc1YSZ-LCCN (70-30 vol.%) membranes in the temperature range of 700-950 °C. N_2 (solid symbols) and CO_2 (empty symbols) were used as sweep gases, while air was flowed as feed gas. Dashed lines represent oxygen permeation fluxes calculated thanks to the Wagner equation.

Section S 1: Calculation of theoretical oxygen permeation flux using the Wagner equation

When the permeation flux is mainly limited by the transport of oxide ions and electrons in the bulk of the material (bulk diffusion limitation), the oxygen permeation flux can be characterized by the Wagner equation (3):

$$J_{O_2} = \frac{RT}{16F^2L}\int_{pO_{2,permeate}}^{pO_{2,feed}} \frac{\sigma_e\sigma_i}{\sigma_e+\sigma_i}\,(pO_2)\,d\ln pO_2 \quad (3)$$

where J_{O_2} is the oxygen permeation flux (mol m^{-2} s^{-1}), R is the gas constant (J mol^{-1} K^{-1}), T is the absolute temperature (K), F is the Faraday constant (A mol^{-1}), L is the membrane thickness (m), σ_e and σ_i are the electronic and the ionic conductivities (S m^{-1}), and $pO_{2,feed}$ and $pO_{2,permeate}$ are the oxygen partial pressures at the high-pressure and low-pressure sides (Pa), respectively.

For the calculations of the theoretical oxygen permeation flux through the 1000 µm thick and the 110 µm thick membranes, it was considered that: $\sigma_e \gg \sigma_i$, consequently the integrand in Eq. (3) becomes:

$$J_{O_2} = \frac{RT}{16F^2L}\int_{pO_{2,permeate}}^{pO_{2,feed}} \sigma_i\,(pO_2)\,d\ln pO_2 \quad (4)$$

The ionic conductivity value σ_i was approximated as: $\sigma_{i,10Sc1YSZ} \gg \sigma_{i,LCCN}$ and $\sigma_i = x * \sigma_{ion,10Sc1YSZ}$, where x is the volume percentage of 10Sc1YSZ in the composite membrane. The ionic conductivities of 10Sc1YSZ from 750 to 940 °C were selected in a study by Irvine *et al.* [69]. The values of the temperatures (T), the membrane thicknesses (L) and the oxygen partial pressures P'_{O_2} and P''_{O_2} were determined experimentally for the calculations.

References

[1] O. Edenhofer, R. Pichs-Madruga, Y. Sokona, J.C. Minx, E. Farahani, S. Kadner, K. Seyboth, A. Adler, I. Baum, S. Brunner, P. Eickemeier, B. Kriemann, J. Savolainen, S. Schlömer, C. von Stechow, T. Zwickel, Climate Change 2014: Mitigation of Climate Change: Working Group III Contribution to the Fifth Assessment Report of the Intergovernmental Panel on, 2014. http://www.ipcc.ch/index.htm.

[2] H. Stadler, F. Beggel, M. Habermehl, B. Persigehl, R. Kneer, M. Modigell, P. Jeschke, Oxyfuel coal combustion by efficient integration of oxygen transport membranes, Int. J. Greenh. Gas Control. 5 (2011) 7–15. doi:10.1016/j.ijggc.2010.03.004.

[3] M. Czyperek, P. Zapp, H.J.M. Bouwmeester, M. Modigell, K. Ebert, I. Voigt, W.A. Meulenberg, L. Singheiser, D. Stöver, Gas separation membranes for zero-emission fossil power plants: MEM-BRAIN, J. Memb. Sci. 359 (2010) 149–159. doi:10.1016/j.memsci.2010.04.012.

[4] S.S. Hashim, A.R. Mohamed, S. Bhatia, Oxygen separation from air using ceramic-based membrane technology for sustainable fuel production and power generation, Renew. Sustain. Energy Rev. 15 (2011) 1284–1293. doi:10.1016/j.rser.2010.10.002.

[5] E.S. Rubin, A.B. Rao, M.B. Berkenpas, Technical Documentation : Oxygen-based Combustion Systems (Oxyfuels) with Carbon Capture and Storage (CCS), 2007.

[6] P. Haworth, S. Smart, J. Glasscock, J.C. Diniz da Costa, High performance yttrium-doped BSCF hollow fibre membranes, Sep. Purif. Technol. 94 (2012) 16–22. doi:10.1016/j.seppur.2012.04.005.

[7] R. Kiebach, K. Engelbrecht, K. Kwok, S. Molin, M. Søgaard, P. Niehoff, F. Schulze-Küppers, R. Kriegel, J. Kluge, P.V. Hendriksen, Joining of ceramic $Ba_{0.5}Sr_{0.5}Co_{0.8}Fe_{0.2}O_3$ membranes for oxygen production to high temperature alloys, J. Memb. Sci. 506 (2016) 11–21. doi:10.1016/j.memsci.2016.01.050.

[8] S. Baumann, J.M. Serra, M.P. Lobera, S. Escolástico, F. Schulze-Küppers, W.A. Meulenberg, Ultrahigh oxygen permeation flux through supported $Ba_{0.5}Sr_{0.5}Co_{0.8}Fe_{0.2}O_{3-\delta}$ membranes, J. Memb. Sci. 377 (2011) 198–205. doi:10.1016/j.memsci.2011.04.050.

[9] M. Arnold, H. Wang, A. Feldhoff, Influence of CO_2 on the oxygen permeation performance and the microstructure of perovskite-type $(Ba_{0.5}Sr_{0.5})(Co_{0.8}Fe_{0.2})O_{3-\delta}$ membranes, J. Memb. Sci. 293 (2007) 44–52. doi:10.1016/j.memsci.2007.01.032.

[10] Z. Shao, W. Yang, Y. Cong, H. Dong, J. Tong, G. Xiong, Investigation of the permeation behavior and stability of a $Ba_{0.5}Sr_{0.5}Co_{0.8}Fe_{0.2}O_{(3-\delta)}$ oxygen membrane, J. Memb. Sci. 172 (2000) 177–188. doi:10.1016/S0376-7388(00)00337-9.

[11] L. Ge, W. Zhou, R. Ran, S. Liu, Z. Shao, W. Jin, N. Xu, Properties and performance of A-site deficient $(Ba_{0.5}Sr_{0.5})_{1-x}Co_{0.8}Fe_{0.2}O_{3-\delta}$ for oxygen permeating membrane, J. Memb. Sci. 306 (2007) 318–328. doi:10.1016/j.memsci.2007.09.004.

[12] Z. Taheri, K. Nazari, N. Seyed-Matin, A.A. Safekordi, B. Ghanbari, S. Zarrinpashne, R. Ahmadi, Comparison of oxygen permeation through some perovskite membranes synthesized with EDTNAD, React. Kinet. Mech. Catal. 100 (2010) 459–469. doi:10.1007/s11144-010-0158-2.

[13] F. Schulze-Küppers, S. Baumann, F. Tietz, H.J.M. Bouwmeester, W.A. Meulenberg, Towards the fabrication of $La_{0.98-x}Sr_xCo_{0.2}Fe_{0.8}O_{3-\delta}$ perovskite-type oxygen transport membranes, J. Eur. Ceram. Soc. 34 (2014) 3741–3748. doi:10.1016/j.jeurceramsoc.2014.06.012.

[14] X. Tan, Z. Wang, B. Meng, X. Meng, K. Li, Pilot-scale production of oxygen from air using perovskite hollow fibre membranes, J. Memb. Sci. 352 (2010) 189–196. doi:10.1016/j.memsci.2010.02.015.

[15] J. Gurauskis, Ø.F. Lohne, D.S. Lagergren, E.T. Wefring, K. Wiik, Oxygen permeation in symmetric and asymmetric $La_{0.2}Sr_{0.8}Fe_{0.8}Ta_{0.2}O_{3-\delta}$ membranes, J. Eur. Ceram. Soc. 36 (2016) 1427–1434. doi:10.1016/j.jeurceramsoc.2016.01.004.

[16] E. Bucher, A. Egger, G.B. Caraman, W. Sitte, Stability of the SOFC Cathode Material $(Ba,Sr)(Co,Fe)O_{3-\delta}$ in CO_2-Containing Atmospheres, J. Electrochem. Soc. 155 (2008) B1218. doi:10.1149/1.2981024.

[17] X. Tan, N. Liu, B. Meng, J. Sunarso, K. Zhang, S. Liu, Oxygen permeation behavior of La0.6Sr0.4Co0.8Fe0.2O3 hollow fibre membranes with highly concentrated CO_2 exposure, J. Memb. Sci. 389 (2012) 216–222. doi:10.1016/j.memsci.2011.10.032.

[18] M. Pilar Lobera, S. Escolastico, J. Garcia-Fayos, J.M. Serra, Ethylene Production by ODHE in Catalytically Modified $Ba_{0.5}Sr_{0.5}Co_{0.8}Fe_{0.2}O_{3-\delta}$ Membrane Reactors, ChemSusChem. 5 (2012) 1587–1596. doi:10.1002/cssc.201100747.

[19] S.J. Benson, D. Waller, J.A. Kilner, Degradation of $La_{0.6}Sr_{0.4}Fe_{0.8}Co_{0.2}O_{3-\delta}$ in Carbon Dioxide and Water Atmospheres, J. Electrochem. Soc. 146 (2000) 1305–1309.

[20] M. Schulz, R. Kriegel, A. Kämpfer, Assessment of CO_2 stability and oxygen flux of oxygen permeable membranes, J. Memb. Sci. 378 (2011) 10–17. doi:10.1016/j.memsci.2011.02.037.

[21] S. Engels, T. Markus, M. Modigell, L. Singheiser, Oxygen permeation and stability investigations on MIEC membrane materials under operating conditions for power plant processes, J. Memb. Sci. 370 (2011) 58–69. doi:10.1016/j.memsci.2010.12.021.

[22] J. Gao, L. Li, Z. Yin, J. Zhang, S. Lu, X. Tan, Poisoning effect of SO_2 on the oxygen permeation behavior of $La_{0.6}Sr_{0.4}Co_{0.2}Fe_{0.8}O_{3-\delta}$ perovskite hollow fiber membranes, J. Memb. Sci. 455 (2014) 341–348. doi:10.1016/j.memsci.2013.12.073.

[23] S. Lia, W. Jin, N. Xu, J. Shi, Mechanical strength, and oxygen and electronic transport properties of $SrCo_{0.4}Fe_{0.6}O_{3-\delta}$-YSZ membranes, J. Memb. Sci. 186 (2001) 195–204.

[24] B. Wang, M. Zhan, D. Zhu, W. Liu, C. Chen, Oxygen permeation and stability of $Zr_{0.8}Y_{0.2}O_{0.9}$–$La_{0.8}Sr_{0.2}CrO_{3-\delta}$ dual-phase composite, J. Solid State Electrochem. 10 (2006) 625–628. doi:10.1007/s10008-006-0136-9.

[25] M.M. Hiroaki Yanagida, Kunihiko Koumoto, Kunihito Komoto, The Chemistry of Ceramics, 1996.

[26] X.J. Chen, K.A. Khor, S.H. Chan, L.G. Yu, Influence of microstructure on the ionic conductivity of yttria-stabilized zirconia electrolyte, Mater. Sci. Eng. A. 335 (2002) 246–252. doi:10.1016/S0921-5093(01)01935-9.

[27] V.G. Artemov, I.E. Kuritsyna, S.P. Lebedev, G.A. Komandin, P.O. Kapralov, I.E. Spektor, V.V Kharton, S.I. Bredikhin, A.A. Volkov, Analysis of electric properties of ZrO_2-Y_2O_3 single crystals using teraherz IR and impedance spectroscopy techniques, Russ. J. Electrochem. 50 (2014) 690–693. doi:10.1134/S1023193514070039.

[28] S. Pirou, J.M. Bermudez, P.V. Hendriksen, A. Kaiser, T. Ramirez, M. Millan, R. Kiebach, Stability and performance of robust dual-phase $(ZrO_2)_{0.89}(Y_2O_3)_{0.01}(Sc_2O_3)_{0.}$10-$Al_{0.}02Zn_{0.98}O_{1.01}$ oxygen transport membranes, J. Memb. Sci. 543 (2017) 18–27. doi:10.1016/j.memsci.2017.08.044.

[29] J.G.M. Furtado, R.N. Oliveira, Development of lanthanum chromites-based materials for solid oxide fuel cell interconnects, Mater. Janeiro. 13 (2008) 147–153. doi:10.1590/s1517-70762008000100018.

[30] W.Z. Zhu, S.C. Deevi, Development of interconnect materials for solid oxide fuel cells, Mater. Sci. Eng. A. 348 (2003) 227–243. doi:10.1016/S0921-5093(02)00736-0.

[31] N.. Minh, T. Takahashi, Science and Technology of Ceramic Fuel Cells, Elsevier science, 1995.

[32] T. Nakamura, G. Petzow, L.J. Gauckler, Stability of the perovskite phase $LaBO_3$ (B = V, Cr, Mn, Fe, Co, Ni) in reducing atmosphere I. Experimental results, Mater. Res. Bull. 14 (1979) 649–659.

[33] A. Crucq, ed., Catalysis and Automotive Pollution Control II, 1st Edition, 1991.

[34] M.A. Peña, J.L.G. Fierro, Chemical structures and performance of perovskite oxides, Chem. Rev. 101 (2001) 1981–2017. doi:10.1021/cr980129f.

[35] O. Yamamoto, Solid oxide fuel cells: fundamental aspects and prospects, Electrochim. Acta. 45 (2000) 2423–2435. doi:10.1016/S0013-4686(00)00330-3.

[36] T. Akashi, T. Maruyama, T. Goto, Transport of lanthanum ion and hole in $LaCrO_3$ determined by electrical conductivity measurements, Solid State Ionics. 164 (2003) 177–183. doi:10.1016/j.ssi.2003.08.050.

[37] S.P. Jiang, L. Liu, K.P. Ong, P. Wu, J. Li, J. Pu, Electrical conductivity and performance of doped LaCrO3 perovskite oxides for solid oxide fuel cells, J. Power Sources. 176 (2008) 82–89. doi:10.1016/j.jpowsour.2007.10.053.

[38] R. Xing, Y. Wang, Y. Zhu, S. Liu, C. Jin, Co-electrolysis of steam and CO_2 in a solid oxide electrolysis cell with $La_{0.75}Sr_{0.25}Cr_{0.5}Mn_{0.5}O_{3-\delta}$ –Cu ceramic composite electrode, J. Power Sources. 274 (2015) 260–264.

[39] J.W. Fergus, Lanthanum chromite-based materials for solid oxide fuel cell interconnects, Solid State Ionics. 171 (2004) 1–15. doi:10.1016/j.ssi.2004.04.010.

[40] S. Gupta, M.K. Mahapatra, P. Singh, Lanthanum chromite based perovskites for oxygen transport membrane, Mater. Sci. Eng. R Reports. 90 (2015) 1–36. doi:10.1016/j.mser.2015.01.001.

[41] L.A. Chick, L.R. Pederson, G.D. Maupin, J.L. Bates, L.E. Thomas, G.J. Exarhos, Glycine-nitrate combustion synthesis of oxide ceramic powders, Mater. Lett. 10 (1990) 6–12. doi:10.1016/0167-577X(90)90003-5.

[42] K.A. Nielsen, M. Solvang, S.B.L. Nielsen, A.R. Dinesen, D. Beeaff, P.H. Larsen, Glass composite seals for SOFC application, J. Eur. Ceram. Soc. 27 (2007) 1817–1822. doi:10.1016/j.jeurceramsoc.2006.05.046.

[43] A.J. Samson, M. Søgaard, P.V. Hendriksen, $(Ce,Gd)O_{2-\delta}$-based dual phase membranes for oxygen separation, J. Memb. Sci. 470 (2014) 178–188. doi:10.1016/j.memsci.2014.07.028.

[44] K. Nakamoto, Chapter 2: Application in Inorganic Chemistry, in: Infrared Raman Spectra Inorg. Coord. Compd. Sixth Ed. Part A Theory Appl. Inorg. Chem., 2009: pp. 149–354.

[45] X. Zhang, C. He, L. Wang, Z. Li, Q. Feng, Synthesis , characterization and nonisothermal decomposition kinetics of $La_2(CO_3)_3 \cdot 3.4H_2O$, J. Therm. Anal. Calorim. 119 (2015) 1713–1722. doi:10.1007/s10973-015-4389-3.

[46] D.G. Henry, J.S. Watson, C.M. John, Assessing and calibrating the ATR-FTIR approach as a carbonate rock characterization tool, Sediment. Geol. 347 (2017) 36–52. doi:10.1016/j.sedgeo.2016.07.003.

[47] R. Zhang, H. Alamdari, S. Kaliaguine, SO_2 poisoning of $LaFe_{0.8}Cu_{0.2}O_3$ perovskite prepared by reactive grinding during NO reduction by C3H6, Appl. Catal. A Gen. 340 (2008) 140–151. doi:10.1016/j.apcata.2008.02.028.

[48] P. Roonasi, A. Holmgren, An ATR-FTIR study of sulphate sorption on magnetite; rate of adsorption, surface speciation, and effect of calcium ions, J. Colloid Interface Sci. 333 (2009) 27–32. doi:10.1016/j.jcis.2008.12.080.

[49] G.J. Puts, P.L. Crouse, The influence of inorganic materials on the pyrolysis of polytetrafluoroethylene. Part 1: The sulfates and fluorides of Al, Zn, Cu, Ni, Co, Fe and Mn, J. Fluor. Chem. 168 (2014) 260–267. doi:10.1016/j.jfluchem.2014.05.004.

[50] W. Martens, R.L. Frost, J.T. Kloprogge, P.A. Williams, Raman spectroscopic study of the basic copper sulphates — implications for copper corrosion and “bronze disease,” J. Raman Spectrosc. 34 (2003) 145–151. doi:10.1002/jrs.969.

[51] M. Mizuhata, T. Ohta, S. Deki, Polarized Raman Spectra of Molten Carbonates Influenced by the Surface Acidity of the Coexisting Inorganic Powder, Electrochemistry. 77 (2009) 721–724.

[52] W. Kaabar, S. Bott, R. Devonshire, Raman spectroscopic study of mixed carbonate materials, Spectrochim. Acta Part A Mol. Biomol. Spectrosc. 78 (2011) 136–141. doi:10.1016/j.saa.2010.09.011.

[53] L.J. Bonales, V. Muñoz-Iglesias, D. Santamaría-Pérez, M. Caceres, D. Fernandez-Remolar, O. Prieto-Ballesteros, Quantitative Raman spectroscopy as a tool to study the kinetics and formation mechanism of carbonates, Spectrochim. Acta Part A Mol. Biomol. Spectrosc. 116 (2013) 26–30. doi:10.1016/j.saa.2013.06.121.

[54] E. Turianicová, A. Obut, A. Zorkovská, P. Baláz, M. Matik, J. Briancin, The effects of LiOH and NaOH on the carbonation of $SrSO_4$ by dry high-energy milling, Miner. Eng. 49 (2013) 98–102. doi:10.1016/j.mineng.2013.05.017.

[55] E. Avzianova, S.D. Brooks, Analysis of nickel (II) in particulate matter by Raman microspectroscopy, J. Aerosol Sci. 67 (2014) 207–214. doi:10.1016/j.jaerosci.2013.10.003.

[56] J. Sfeir, $LaCrO_3$-based anodes: stability considerations, J. Power Sources. 118 (2003) 276–285. doi:10.1016/S0378-7753(03)00099-5.

[57] H.C. Graham, H.H. Davis, Oxidation/Vaporization Kinetics of Cr_2O_3, J. Am. Ceram. Soc. 54 (1971) 89–93.

[58] D.B. Meadowcroft, J.M. Wimmer, No Title, Am. Soc. Bull. 58 (1979) 610.

[59] W. Li, T. Tian, F. Shi, Y. Wang, C. Chen, $Ce_{0.8}Sm_{0.2}O_{2-\delta}$ -$La_{0.8}Sr_{0.2}MnO_{3-\delta}$ dual-phase

composite hollow fiber membrane for oxygen separation, Ind. Eng. Chem. Res. 48 (2009) 5789–5793. doi:10.1016/j.memsci.2012.03.026.

[60] K. Zhang, L. Liu, Z. Shao, R. Xu, J. Diniz da Costa, S. Wang, S. Liu, Robust ion-transporting ceramic membrane with an internal short circuit for oxygen production, J. Mater. Chem. A. 1 (2013) 9150–9156. doi:10.1039/c3ta11427a.

[61] V. Esposito, M. Søgaard, P.V. Hendriksen, Chemical stability of $La_{0.6}Sr_{0.4}CoO_{3-\delta}$ in oxygen permeation applications under exposure to N_2 and CO_2, Solid State Ionics. 227 (2012) 46–56. doi:10.1016/j.ssi.2012.08.015.

[62] H. Luo, H. Jiang, K. Efimov, F. Liang, H. Wang, J. Caro, CO_2-Tolerant Oxygen-Permeable Fe_2O_3-$Ce_{0.9}Gd_{0.1}O_{2-\delta}$ Dual Phase Membranes, Ind. Eng. Chem. Res. 50 (2011) 13508–13517. doi:10.1021/ie200517t.

[63] J.M. Serra, J. Garcia-Fayos, S. Baumann, F. Schulze-Küppers, W. a. Meulenberg, Oxygen permeation through tape-cast asymmetric all-$La_{0.6}Sr_{0.4}Co_{0.2}Fe_{0.8}O_{3-\delta}$ membranes, J. Memb. Sci. 447 (2013) 297–305. doi:10.1016/j.memsci.2013.07.030.

[64] S. Pirou, J. Gurauskis, V. Gil, M. Søgaard, P.V. Hendriksen, A. Kaiser, S. Ovtar, R. Kiebach, Oxygen permeation flux through 10Sc1YSZ-$MnCo_2O_4$ asymmetric membranes prepared by two-step sintering, Fuel Process. Technol. 152 (2016) 192–199. doi:10.1016/j.fuproc.2016.06.019.

[65] J. Nielsen, J. Hjelm, Impedance of SOFC electrodes : A review and a comprehensive case study on the impedance of LSM:YSZ cathodes, Electrochim. Acta. 115 (2014) 31–45. doi:10.1016/j.electacta.2013.10.053.

[66] M. Ghatee, M.H. Shariat, J.T.S. Irvine, Investigation of electrical and mechanical properties of 3YSZ/8YSZ composite electrolytes, Solid State Ionics. 180 (2009) 57–62. doi:10.1016/j.ssi.2008.10.006.

[67] P. Ried, C. Lorenz, A. Brönstrup, T. Graule, N.H. Menzler, W. Sitte, P. Holtappels, Processing of YSZ screen printing pastes and the characterization of the electrolyte layers for anode supported SOFC, J. Electrochem. Soc. 28 (2008) 1801–1808. doi:10.1016/j.jeurceramsoc.2007.11.018.

[68] N.M. Sammes, Z. Cai, Ionic conductivity of ceria/yttria stabilized zirconia electrolyte

materials, Solid State Ionics. 100 (1997) 39–44.

[69] J.T.S. Irvine, J.W.L. Dobson, T. Politova, S.G. Martín, A. Shenouda, Co-doping of scandia-zirconia electrolytes for SOFCs., Faraday Discuss. 134 (2007) 41–49; discussion 103–118, 415–419. doi:10.1039/b604441g.

[70] R. Kiebach, C. Knöfel, F. Bozza, T. Klemensø, C. Chatzichristodoulou, Infiltration of ionic-, electronic- and mixed-conducting nano particles into $La_{0.75}Sr_{0.25}MnO_3$–$Y_{0.16}Zr_{0.84}O_2$ cathodes – A comparative study of performance enhancement and stability at different temperatures, J. Power Sources. 228 (2013) 170–177. doi:10.1016/j.jpowsour.2012.11.070.

[71] T. Klemensø, C. Chatzichristodoulou, J. Nielsen, F. Bozza, K. Thydén, R. Kiebach, S. Ramousse, Characterization of impregnated GDC nano structures and their functionality in LSM based cathodes, Solid State Ionics. 224 (2012) 21–31. doi:10.1016/j.ssi.2012.07.011.

[72] V. Gil, K. Kammer Hansen, High performance infiltrated backbones for cathode-supported SOFC's, ECS Trans. 64 (2014) 41–51. doi:10.1149/06402.0041ecst.

[73] C. Tsai, A.G. Dixon, W.R. Moser, Y.H. Ma, Dense Perovskite Membrane Reactors for Partial Oxidation of Methane to Syngas, AIChE J. 43 (1997) 2741–2750.

5.5. Development and characterization of supported $(ZrO_2)_{0.89}(Y_2O_3)_{0.01}(Sc_2O_3)_{0.10}$-$LaCr_{0.85}Cu_{0.10}Ni_{0.05}O_{3-\delta}$ oxygen transport membranes

This sub-chapter describes the main challenges encountered to develop supported, thin film 10Sc1YSZ-LCCN membranes and the most advanced results obtained. The challenge with this part of the work was the well-known difficulty to fully densify lanthanum chromite based perovskite materials at temperatures below 1400 °C in a multilayer system [1]. Furthermore, $LaCrO_3$-based materials have a poor sinterability due to volatilization of chromium vapor species above 1000 °C creating pores on the sides of the membranes [1 – 3]. As a result, conventional sintering to obtain gastight membrane layer with the desired ratio of the ionic/electronic conductor is difficult or impossible for many membrane geometries and sintering arrangements.

During the co-firing of the thin 10Sc1YSZ-LCCN membrane on a 3YSZ porous support, different types of defects were formed, such as cracks, delamination and curvature of the membranes (Figure 5. 40). It is believed that these defects are formed due to the different sintering behavior of the YSZ and LCCN materials used in the different layers (dense membrane and porous support). To overcome this problem, the YSZ as support material was replaced by ScYSZ-LCCN, so that the support and membrane were of the same material. Nevertheless, the ratio of the electronic conducting phase (LCCN) in the porous support structure was increased (10Sc1YSZ- LCCN (40-**60** vol.%)) compared to the dense membrane layer (10Sc1YSZ-LCCN (70-**30** vol.%)). The main reason for this choice is that EIS measurements performed on 10Sc1YSZ-$MnCo_2O_4$ porous backbones (**sub-chapter 5.2.**) demonstrated that such porous structures containing higher amount of electronic conducting phase were better performing as catalytic layers than porous structures containing only 30 vol.% of electronic conducting phase.

The supported 10Sc1YSZ-LCCN membranes were developed using two architectures (symmetric and asymmetric supported membranes). Asymmetric membranes were made of a thin dense layer (10Sc1YSZ-LCCN (70-30 vol.%), 10 – 15 µm) supported on a thick porous support (10Sc1YSZ-LCCN (40-60 vol.%), 200 µm) (Figure 5. 42), while symmetric membranes consisted of a dense membrane layer (10Sc1YSZ-LCCN (70-30 vol.%), 30-60 µm) sandwiched between two porous layers (10Sc1YSZ-LCCN (40-60 vol.%), 60 µm)

(Figure 5. 43). Both architectures included 3 vol.% of NiO as sintering aid to help the densification of the composite membrane layer. 10Sc1YSZ, LCCN and NiO powders were mixed by ball-milling for 48 h with appropriate amounts of solvents (ethanol, acetate) and organic additives (plasticizer, binder, dispersant) to form the required slurry to tape-cast the dense membrane layer. Different pore formers (graphite, PMMA, carbon black), different pore former particle sizes and different volume quantities were used for the slurries preparation nevertheless further R&D is required to obtain highly porous 10Sc1YSZ-LCCN (40-60 vol.%) structures.

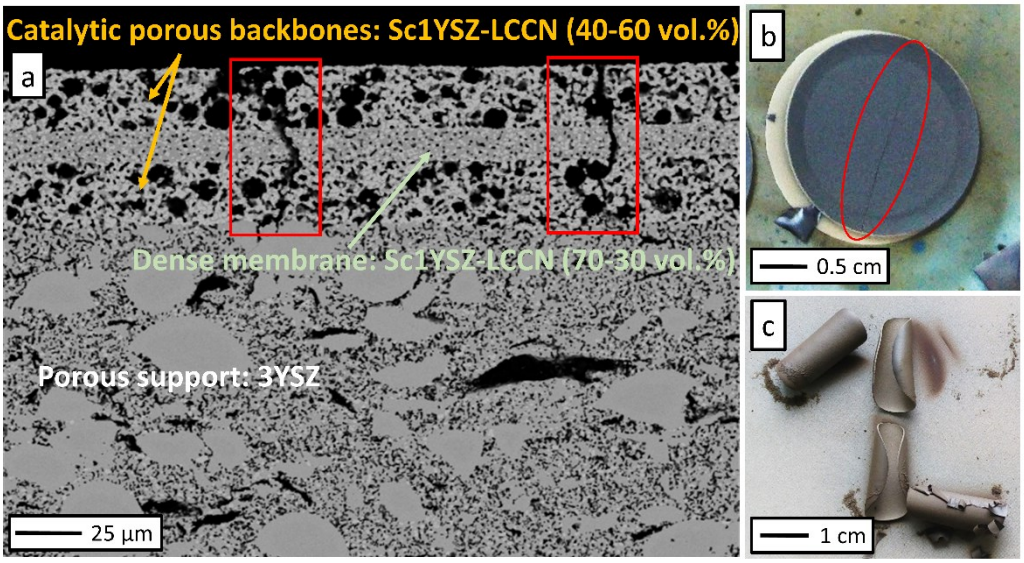

Figure 5. 40: Examples of observed cracks, curling and delamination of thin 10Sc1YSZ-LCCN membranes supported on 3YSZ porous support. (a) SEM image of a cross-section of a membrane after sintering, (b) and (c) Images of membranes after sintering.

De-binding and sintering are among the most critical steps in ceramic processing of multilayers with different material composition and different targeted microstructure/density of resulting layers. For the de-binding step, the heating profile was optimized with the help of thermogravimetric measurements that were performed on tape-casted porous supports (in this layer thermal removal of organics and formation of decomposition gases is most critical due to the thickness of the samples). As presented Figure 5. 41, the optimized de-binding profile comprises five dwell temperatures (3 h at 120 °C, 3 h at 180 °C, 5 h at 220 °C, 3 h at 280 °C and 2 h at 700 °C), an heating ramp of 60 °C min, a cooling ramp of 120 °C min^{-1}. The de-binding process was performed in N_2.

Due to the difficulty of densifying LCCN, the sintering step can be a challenge in the fabrication of 10Sc1YSZ-LCCN thin supported membranes. For the pressing of fully dense 1000 µm thick 10Sc1YSZ-LCCN membranes conventional sintering cycles could be applied because the pressed powders have a very high green density that helps densification. However, tape-cast membranes have a significantly lower green density due to organic additives, and require higher temperatures for densification that the pressed counterparts and chromium evaporation is a problem. For these reasons, a two-step sintering process, including a peak temperature of 1500 °C (3 min) and a dwell temperature of 1450 °C (3 h) was used in order to fully densify the 10Sc1YSZ-LCCN membranes while at the same time avoiding the loose of the LCCN phase. Heating ramps of 60 °C h^{-1} and 300 °C h^{-1} were used from room temperature to 1200 °C and from 1200 °C to 1500 °C, respectively. Cooling ramps of 300 °C h^{-1} and 180 °C h^{-1} were applied from 1500 °C to 1450 °C, and from 1450 °C to room temperature. Figure 5. 41 summarizes the de-binding and sintering cycles used for the preparation of the supported 10Sc1YSZ-LCCN membranes presented in Figures 5. 42 and 5. 43.

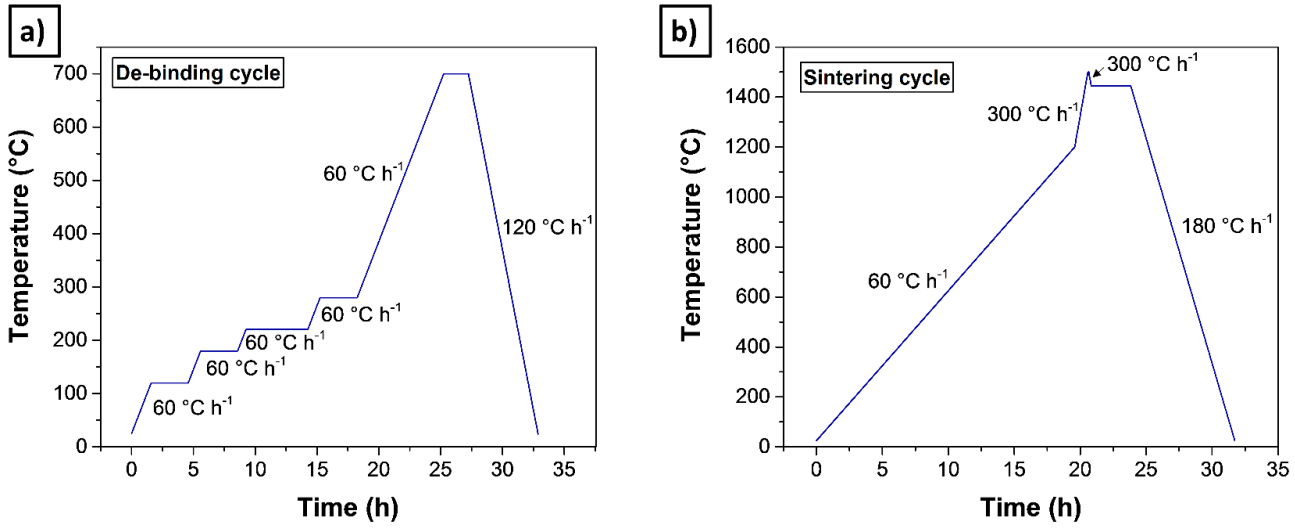

Figure 5. 41: De-binding cycle (a) and sintering cycle (b) used to optimize the microstructure of the 10Sc1YSZ-LCCN (70-30 vol.%) supported membranes.

Figures 5. 42 and 4. 43 present the SEM images of polished cross-sections of the asymmetric and symmetric supported membranes, respectively. In both cases, the dense 10Sc1YSZ-LCCN (70-30 vol.%) membrane layers are sufficiently dense to be gastight. Nevertheless, after the high temperature sintering the 10Sc1YSZ-LCCN (40-60 vol.%)

supports are too dense to allow the diffusion of the feed and sweep gases through the support or the infiltration of aqueous solutions of oxygen oxidation/reduction catalysts into the three phase boundary region close to the membrane.

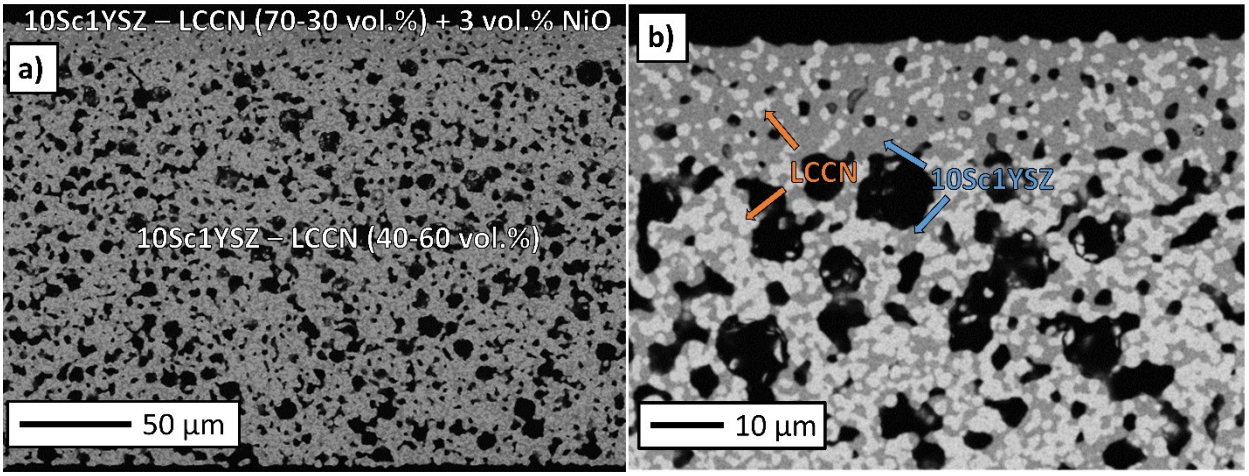

Figure 5. 42: SEM images of a polished cross-section of an asymmetric membrane made of a thin dense layer (10Sc1YSZ-LCCN (70-30 vol.%), 10-15 µm) supported on a thick porous support (10Sc1YSZ-LCCN (40-60 vol.%), 200 µm). (a) Overview of the membrane, and (b) zoomed view on the dense membrane layer.

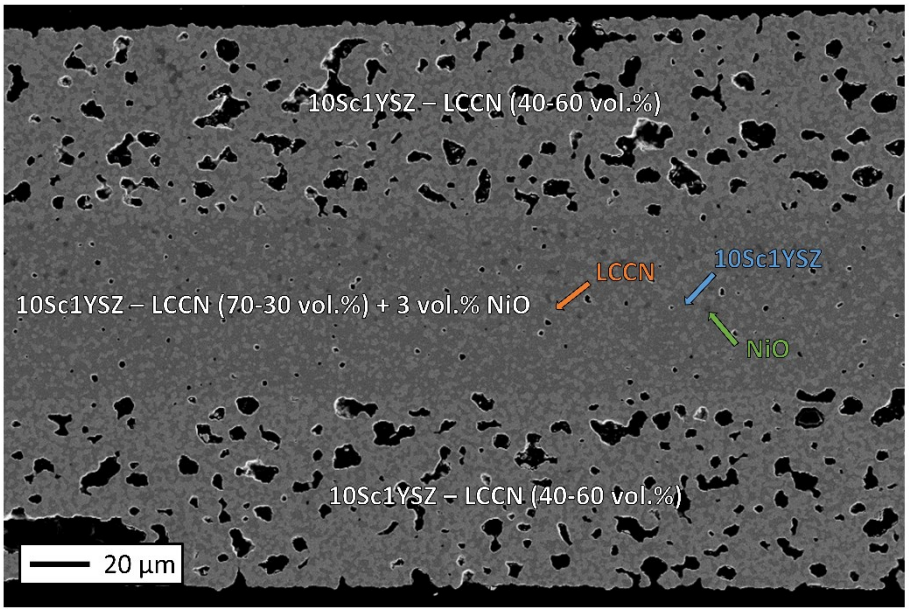

Figure 5. 43: SEM image of a polished cross-section of a symmetrical supported membrane made of a dense membrane layer (10Sc1YSZ-LCCN (70-30 vol.%), 30-60 µm) sandwiched in between two porous layers (10Sc1YSZ-LCCN (40-60 vol.%), 60 µm).

Even though a perfect microstructure of the 10Sc1YSZ-LCCN (70-30 vol.%) symmetrical supported membrane has not been achieved within this work, the membrane has been

characterized by oxygen permeation measurement after catalyst infiltration. As catalyst, a $(Ce_{0.8}Gd_{0.2})_{0.8}Pr_{0.2}O_{2-\delta}$ aqueous solution (concentration 1.4 M) was prepared by dissolving the corresponding nitrate solid solutions in water. The solution was supplemented with a wetting agent (Triton X-100) and a complexing agent (Urea), and was infiltrated in both 10Sc1YSZ-LCCN (40-60 vol.%) porous layers to serve as oxygen oxidation/reduction catalyst. The $(Ce_{0.8}Gd_{0.2})_{0.8}Pr_{0.2}O_{2-\delta}$ catalytic solution was poured in excess onto the surfaces of the porous layers at atmospheric pressure. Afterwards the infiltrated samples were heat-treated at 350 °C for 1 h. This infiltration process was repeated 3 times.

Figure 5. 44 displays the results of oxygen permeation flux measurements as a function of the ratio between the oxygen partial pressures of the feed and permeate sides ($\ln(pO_2^{feed}/pO_2^{permeate})$) using N_2 or CO_2 as the sweep gas, and air or pure oxygen as the feed gas. The oxygen permeation through the membrane was measured from 750 °C to 950 °C. The highest fluxes in air/N_2 and O_2/N_2 were measured at 950 °C and correspond to 1.11 $mL_N\,cm^{-2}\,min^{-1}$ and 2.32 $mL_N\,cm^{-2}\,min^{-1}$, respectively. The oxygen permeation flux measured using CO_2 as the sweep gas was slightly lower than the ones measured in N_2 at an equivalent driving force. The oxygen flux permeating through the membrane does not scale in direct proportion to the driving force across the membrane, indicating that the oxygen permeation flux is mainly limited by the surface exchange kinetics and/or by gas diffusion limitations. Such results were expected due to the non-optimized microstructure of the porous supporting layers.

To lead to better microstructures of the 10Sc1YSZ-LCCN supported membranes additional pore former will be added in the 10Sc1YSZ-LCCN (40-60 vol.%) porous structures. Once ideal microstructure will be obtained, the performances of the membranes for transporting oxygen will be evaluated by oxygen permeation measurements in clean atmosphere (inert gas as a sweep gas) and in simulated oxy-fuel combustion conditions (SO_2 CO_2 and H_2O).

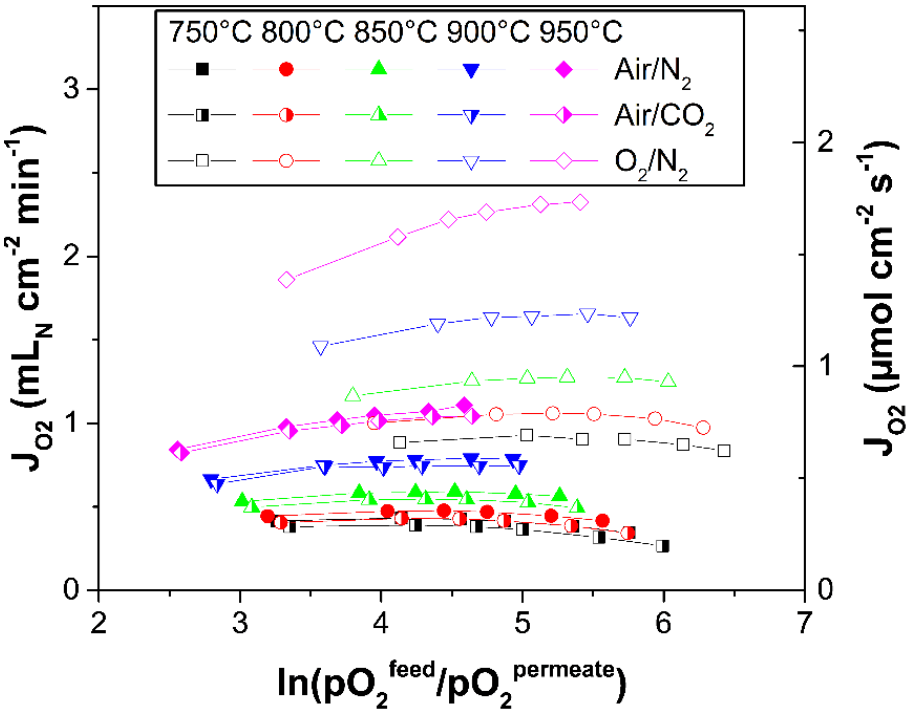

Figure 5. 44: Oxygen permeation flux of 10Sc1YSZ-LCCN (70-30 vol.%) supported membrane as a function of the natural logarithm ratio between the oxygen partial pressure of the feed and the permeate side using N_2 or CO_2 as the sweep gas and air or pure oxygen as the feed gas.

References

[1] S. Gupta, M.K. Mahapatra, P. Singh, Lanthanum chromite based perovskites for oxygen transport membrane, Mater. Sci. Eng. R Reports. 90 (2015) 1–36. doi:10.1016/j.mser.2015.01.001.

[2] J. Sfeir, $LaCrO_3$-based anodes: stability considerations, J. Power Sources. 118 (2003) 276–285. doi:10.1016/S0378-7753(03)00099-5.

[3] H.C. Graham, H.H. Davis, Oxidation/Vaporization Kinetics of Cr_2O_3, J. Am. Ceram. Soc. 54 (1971) 89–93.

Chapter 6: Summary and outlook

The objective of this thesis was to develop high-performing and chemically stable planar asymmetric oxygen transport membranes (OTMs) for direct operation (4-end mode membrane module) in oxy-fuel combustion power plants. In practice, the development of planar asymmetric membranes entails the parallel development of (i) stable porous supports, (ii) thin dense membrane layers, (iii) porous catalytic backbones and (iv) meso-porous nano-particulate catalytic coatings. For the dense membrane layer, dual-phase composite membranes consisting of a stable ionic and a stable electronic conductor were used to overcome the stability limitations commonly observed with single-phase membrane materials (e.g. $La_{1-x}Sr_xCo_{1-y}Fe_yO_{3-\delta}$ (LSCF), $Ba_{1-x}Sr_xCo_{1-y}Fe_yO_{3-\delta}$ (BSCF)) in CO_2 and SO_2 [1 – 7]. Three composite materials, $(ZrO_2)_{0.89}(Y_2O_3)_{0.01}(Sc_2O_3)_{0.10}$ - $MnCo_2O_4$ (10Sc1YSZ-MCO), $(ZrO_2)_{0.89}(Y_2O_3)_{0.01}(Sc_2O_3)_{0.10}$ - $Al_{0.02}Zn_{0.98}O_{1.01}$ (10Sc1YSZ-AZO) and $(ZrO_2)_{0.89}(Y_2O_3)_{0.01}(Sc_2O_3)_{0.10}$ - $LaCr_{0.85}Cu_{0.10}Ni_{0.05}O_{3-\delta}$ (10Sc1YSZ-LCCN) were pursued in parallel to develop and characterize planar asymmetric oxygen transport membranes.

Stability of OTMs in oxy-fuel conditions: The stability of the three composite membranes was studied in conditions relevant for oxy-fuel combustion (CO_2, SO_2, H_2O containing atmospheres). The stability of 10Sc1YSZ-AZO and 10Sc1YSZ-LCCN composites was tested on loose powder at 850 °C for 8 h. Under the harshest test conditions, the powders were in contact with up to 2000 ppm of SO_2, 30 vol.% of H_2O balanced by CO_2. Analyses using several characterization techniques (XRD, XRF, ATR-FTIR, Raman spectroscopy and SEM-EDX) underlined the excellent stability of these materials under application-relevant atmospheres. For the 10Sc1YSZ-MCO case the thermochemical stability of the composite was studied on a 7 µm thick asymmetric membrane. The test was performed at 850 °C for 7 days using a gaseous mixture containing 250 ppm of SO_2, 3 vol.% of H_2O, and 5 vol.% of O_2 balanced with CO_2. The analyses of the exposed membrane by XRD, Raman spectroscopy and SEM revealed excellent stability. In addition to these tests, longer stability tests (250-1700 h) were performed on membranes at 850 °C using pure CO_2 as sweep gas. All the tests showed stable oxygen permeation performances in CO_2. Overall, all the tests confirmed, that in terms of stability, the three composites studied are good candidates for use in OTMs directly integrated in oxy-fuel combustion processes.

10Sc1YSZ-MCO membranes: Thin dual-phase membranes (7 µm) made of 70 vol.% 10Sc1YSZ and 30 vol.% $MnCo_2O_4$ were successfully prepared and characterized by oxygen permeation tests. The decomposition of $MnCo_2O_4$ spinel known to occur by formation of cobalt oxide above 1200 °C [8] made the development of a thin and fully dense 10Sc1YSZ-MCO (70-30 vol.%) membrane layer challenging. The use of a two-step sintering process, including a peak temperature of 1250 °C (3 min) and a dwell temperature of 1075 °C (6 h), was found to be a feasible solution to this challenge. The method allowed manufacture of fully dense 7 µm thick 10Sc1YSZ-$MnCo_2O_4$ dual-phase membrane while at the same time avoiding excessive Co and Mn diffusions and ensuring sufficient mechanical strength of the YSZ/Al_2O_3 support structure. Similar results could not be obtained by conventional sintering. The two-step sintering cycle was optimized, thanks to separate dilatometry measurements performed on the support and on the membrane layer materials. Oxygen permeation tests performed on 7 µm thick 10Sc1YSZ-$MnCo_2O_4$ dual-phase membrane resulted in oxygen fluxes of 1.41 $mL_N\ cm^{-2}\ min^{-1}$ and 2.23 $mL_N\ cm^{-2}\ min^{-1}$ at 940 °C in air/N_2 and O_2/N_2 atmospheres, respectively. Calculated values corresponding to the characteristic membrane thickness (L_c) of the dual-phase membrane strongly indicated that the main rate-limiting factor for the oxygen permeation was the surface exchange kinetics; therefore, further studies were performed to improve the catalytic surface layers on the membrane. Electrochemical impedance spectroscopy (EIS) measurements were performed to study the performances of (i) 8YSZ, (ii) 8YSZ-MCO (40-60 vol.%), (iii) 10Sc1YSZ-MCO (40-60 vol.%), (iv) 10Sc1YSZ-MCO (70-30 vol.%), and (v) $Ce_{0.8}Tb_{0.2}O_{2-\delta}$ (CTO) - $NiFe_2O_4$ (NFO) (40-60 vol.%) as surface catalysts (in form of porous layers). The tests were carried out under different atmospheres: (i) 21 % O_2 in N_2, (ii) 5 % O_2 in N_2, (iii) 5 % O_2 in CO_2 and (iv) 250 ppm SO_2 in 5 % O_2 in CO_2, and (v) 5 % O_2 in N_2 (recovery step after exposure to CO_2 + SO_2). Polarization resistances (R_p) were deduced from the EIS measurements to compare the performance of the five coatings. The lowest R_p values were acquired with 10Sc1YSZ-MCO (40-60 vol.%) and CTO-NFO (40-60 vol.%) porous backbones, demonstrating the importance of ensuring both good ionic and electronic conductivities in the catalytic porous structures. Oxygen permeation tests were realized on 0.5 mm thick 10Sc1YSZ-MCO membranes coated with different porous backbones ((i) 8YSZ, (ii) 10Sc1YSZ-MCO (70-30 vol.%) and (iii) CTO-NFO (40-60 vol.%)) and infiltrated with a Ce-Pr containing catalytic solution. The good catalytic performance of the CTO-NFO backbone resulted in an increase

of about 50 % of the oxygen permeation flux (0.28 $mL_N\ cm^{-2}\ min^{-1}$, 850 °C, air/Ar) when compared to the membrane coated with the 8YSZ backbone (0.19 $mL_N\ cm^{-2}\ min^{-1}$, 850 °C, air/Ar).

10Sc1YSZ-AZO membranes: Dual-phase composite membranes consisting of 50 vol.% $(ZrO_2)_{0.89}(Y_2O_3)_{0.01}(Sc_2O_3)_{0.10}$ (10Sc1YSZ) and 50 vol.% $Al_{0.02}Zn_{0.98}O_{1.01}$ (AZO) were developed and characterized as thick (1 mm) self-standing membranes and thin (8 µm) supported membranes. Due to the high volatility of the Zn in the AZO phase under mildly reducing atmospheres ($pO_2 \sim 10^{-4}$ atm), the development of thin supported membranes was complicated and had to be performed under sufficiently high oxygen partial pressure to keep the AZO phase in the composite. This was not easily achieved as, even when pure oxygen was applied during the sintering, a thin dense layer (1-2 µm) depleted in AZO was formed at the interfaces between the dense layer and the infiltration layers. Very limited oxygen permeation fluxes were measured through the 8 µm thick 10Sc1YSZ-AZO (50-50 vol.%) supported membrane (0.16 $mL_N\ cm^{-2}\ min^{-1}$ at 925 °C in air/N_2) due to these layers that were without a percolating electronic conducting phase. When preparing 1 mm thick self-standing membranes, the problem of low stability of the AZO phase under mildly reducing atmospheres was overcome by removing the 10Sc1YSZ porous phase on both sides of the membrane by polishing. Accordingly, higher oxygen permeation fluxes were measured (0.33 $mL_N\ cm^{-2}\ min^{-1}$ at 925 °C in air/N_2). Nevertheless, the performances of thick self-standing membranes are clearly too limited to be commercially interesting and further efforts will be required to realize thin and highly performing 10Sc1YSZ-AZO asymmetric membranes.

10Sc1YSZ-LCCN membranes: Self-supported dual-phase membranes made of 70 vol.% of $(ZrO_2)_{0.89}(Y_2O_3)_{0.01}(Sc_2O_3)_{0.10}$ (10Sc1YSZ) and 30 vol.% of $LaCr_{0.85}Cu_{0.10}Ni_{0.05}O_{3-\delta}$ (10Sc1YSZ-LCCN) were prepared and characterized by oxygen permeation tests. Fully dense 1000 µm thick membranes were obtained by powder pressing and conventional sintering (1400 °C/ 6 h in air). After sintering, a $(Y_2O_3)_{0.08}(ZrO_2)_{0.92}$ - $(La_{0.80}Sr_{0.20})MnO_{3-\delta}$ (8YSZ-LSM (50-50 vol.%)) layer was screen-printed on both sides of the membrane to serve as oxygen oxidation/reduction catalyst. An oxygen permeation flux up to 0.27 $mL_N\ cm^{-2}\ min^{-1}$ was obtained at 950 °C in air/N_2 atmosphere. The analysis of the results demonstrated that the oxygen permeation is mainly limited by the bulk diffusion into the membrane. To reduce bulk diffusion limitation, thinner membranes (110 µm thick) were prepared by tape-casting. Unlike the 1000 µm thick membranes prepared by powder pressing, thin tape-cast

membranes have relatively low green density and require higher sintering temperatures. In addition, $LaCrO_3$-based materials have poor sinterability due to the volatilization of chromium vapor species above 1000 °C [9 – 11]. As a result, conventional sintering cannot be used to obtain a gastight membrane layer with the desired ratio of the ionic/electronic conductor. A two-step sintering process, including a peak temperature of 1500 °C (3 min) and a dwell temperature of 1450 °C (3 h) was used in order to maximize the density of the 10Sc1YSZ-LCCN membranes while at the same time avoiding the loss of chromium. A membrane with 93.5 % of density was obtained and tested. A 8YSZ-LSM (50-50 vol.%) composite was coated on both sides of the membrane to serve as a catalyst for the oxygen oxidation/reduction reactions. Oxygen permeation fluxes-up to 1.02 $mL_N\ cm^{-2}\ min^{-1}$ were obtained at 950 °C placing the membrane between an air flow and a N_2 sweep flow. The analyses of the test demonstrated that the oxygen permeation was mainly limited by the surface exchange processes at low temperatures (T < 900 °C) and by bulk diffusion in the membrane at high temperatures (T > 900 °C). Accordingly, to further improve the oxygen permeation through 10Sc1YSZ-LCCN membranes, it is necessary to both decrease the bulk limitations and improve the surface exchange kinetics. To achieve this goal, a significant amount of work was dedicated to the development of thin supported 10Sc1YSZ-LCCN membranes. Asymmetric membranes made of a thin dense layer (10Sc1YSZ-LCCN (70-30 vol.%), 10-15 µm) supported on a thick porous support (10Sc1YSZ-LCCN (40-60 vol.%), 200 µm), and symmetrically supported membranes made of a dense membrane layer (10Sc1YSZ-LCCN (70-30 vol.%), 30-60 µm) sandwiched in between two porous layers (10Sc1YSZ-LCCN (40-60 vol.%), 60 µm) were prepared. Fully dense thin membrane layers (10-60 µm) were obtained, but the porous structures (support and activation layers) in the process became too dense. Consequently, further research and development are required to realize highly performing 10Sc1YSZ-LCCN supported membranes.

In summary; three composite materials (10Sc1YSZ-MCO, 10Sc1YSZ-AZO and 10Sc1YSZ-LCCN) were successfully prepared and characterized as planar dual-phase asymmetric OTMs for direct operation (4-end mode membrane module) in oxy-fuel combustion power plants. Stability tests performed under conditions relevant for oxy-fuel combustion (SO_2, CO_2, H_2O) underlined the excellent stability of the three composites. The highest oxygen permeation performance was obtained on a 7 µm thick 10Sc1YSZ-$MnCo_2O_4$ dual-phase membrane (1.41 $mL_N\ cm^{-2}\ min^{-1}$ at 940 °C in air/N_2).

Future work: Above summarized results are promising, but further improvements are still needed to reach the flux targets considered required for further up-scale and industrialization of the technology. For all the pursued materials systems optimization of effective and stable catalytic materials for the oxygen reduction/oxidation reaction could significantly improve the performances of asymmetric membranes. Specifically on the YSZ/AZO system, the utilization of a "protective" porous layer with a high AZO content covering the dense membrane could likely prevent the undesired depletion of the zinc oxide phase and allow the realization of thin 10Sc1YSZ-AZO asymmetric membranes. Finally, an increase in the amount of pore former added in the 10Sc1YSZ-LCCN (40-60 vol.%) porous structures is recommended to lead to better microstructures of the 10Sc1YSZ-LCCN supported membranes possibly improving performance.

Besides above suggestions of development efforts that can improve the membrane performance a number of other initiatives are called to bring this technology to commercialization. As a first step, oxygen permeation tests of planar asymmetric membranes should be performed under simulated oxy-fuel combustion conditions (250 ppm of SO_2, 5 % O_2, 3 % H_2O balanced with CO_2). Preferably, these tests should last for, at least, 1000 h in order to verify the stability of the membranes over a long exposure time. The next steps of development should include an up-scaling of the membrane area (as a next immediate step in this upscale something on the order of to 10 x 10 cm^2 is suggested) and subsequently a membrane module with multiple planar membranes should be developed.

References

[1] M. Arnold, H. Wang, A. Feldhoff, Influence of CO_2 on the oxygen permeation performance and the microstructure of perovskite-type $(Ba_{0.5}Sr_{0.5})(Co_{0.8}Fe_{0.2})O_{3-\delta}$ membranes, J. Memb. Sci. 293 (2007) 44–52. doi:10.1016/j.memsci.2007.01.032.

[2] X. Tan, N. Liu, B. Meng, J. Sunarso, K. Zhang, S. Liu, Oxygen permeation behavior of $La_{0.6}Sr_{0.4}Co_{0.8}Fe_{0.2}O_3$ hollow fibre membranes with highly concentrated CO_2 exposure, J. Memb. Sci. 389 (2012) 216–222. doi:10.1016/j.memsci.2011.10.032.

[3] S. Engels, T. Markus, M. Modigell, L. Singheiser, Oxygen permeation and stability investigations on MIEC membrane materials under operating conditions for power plant processes, J. Memb. Sci. 370 (2011) 58–69. doi:10.1016/j.memsci.2010.12.021.

[4] J. Gao, L. Li, Z. Yin, J. Zhang, S. Lu, X. Tan, Poisoning effect of SO_2 on the oxygen permeation behavior of $La_{0.6}Sr_{0.4}Co_{0.2}Fe_{0.8}O_{3-\delta}$ perovskite hollow fiber membranes, J. Memb. Sci. 455 (2014) 341–348. doi:10.1016/j.memsci.2013.12.073.

[5] E. Bucher, A. Egger, G.B. Caraman, W. Sitte, Stability of the SOFC Cathode Material $(Ba,Sr)(Co,Fe)O_{3-\delta}$ in CO_2-Containing Atmospheres, J. Electrochem. Soc. 155 (2008) B1218. doi:10.1149/1.2981024.

[6] S.J. Benson, D. Waller, J.A. Kilner, Degradation of $La_{0.6}Sr_{0.4}Fe_{0.8}Co_{0.2}O_{3-\delta}$ in Carbon Dioxide and Water Atmospheres, J. Electrochem. Soc. 146 (2000) 1305–1309.

[7] M. Schulz, R. Kriegel, A. Kämpfer, Assessment of CO_2 stability and oxygen flux of oxygen permeable membranes, J. Memb. Sci. 378 (2011) 10–17. doi:10.1016/j.memsci.2011.02.037.

[8] E.J. Yi, M.Y. Yoon, J.W. Moon, H.J. Hwang, Fabrication of a $MnCo_2O_4$/gadolinia-doped Ceria (GDC) dual-phase composite membrane for oxygen separation, J. Korean Ceram. Soc. 47 (2010) 199–204. doi:10.4191/KCERS.2010.47.2.199.

[9] S. Gupta, M.K. Mahapatra, P. Singh, Lanthanum chromite based perovskites for oxygen transport membrane, Mater. Sci. Eng. R Reports. 90 (2015) 1–36. doi:10.1016/j.mser.2015.01.001.

[10] J. Sfeir, $LaCrO_3$-based anodes: stability considerations, J. Power Sources. 118 (2003)

276–285. doi:10.1016/S0378-7753(03)00099-5.

[11] H.C. Graham, H.H. Davis, Oxidation/Vaporization Kinetics of Cr_2O_3, J. Am. Ceram. Soc. 54 (1971) 89–93.